THE ROLE OF TURBULENCE ON THE INITIATION OF SEDIMENT MOTION

by

Athanasios N. Papanicolaou

Dissertation submitted to the Faculty of the

Virginia Polytechnic Institute and State University

in partial fulfillment of the requirements for the degree of

Doctor of Philosophy

in

Civil Engineering

APPROVED:

_____

P. Diplas, Chairman

_____ _____

C. L. Dancey D. F. Kibler

_____ _____

R. D. Kriz J. A. Schetz

May, 1997

Blacksburg, Virginia

THE ROLE OF TURBULENCE ON THE INITIATION OF SEDIMENT MOTION

By

Athanasios N. Papanicolaou

Committee Chairman: Panayiotis Diplas
Civil Engineering

(ABSTRACT)

The present study examines the role of turbulence on the incipient motion of sediment. For this purpose, well-controlled experiments are performed at the laboratory in a tilting flume. In these tests glass beads of the same size and density are used as the testing material to isolate the role of turbulence. State of the art equipment are used during the course of this study. Specifically, a 3-D Laser Doppler Velocimetry system is employed to measure the instantaneous velocity components at different points near the vicinity of a ball while the ball motion is monitored with a video camera. An image analysis program is developed here to analyze the motion of the particles within a test area.

To examine the importance of the different stress components in the entrainment of sediment, five tests of different packing configuration are performed. Specifically three different roughness regimes are examined namely, the isolated, the wake interference, and the skimming flow. The results reveal that the instantaneous normal stress in the streamwise direction is the most dominant component of the instantaneous stress tensor.

The backbone of this study is the development of a methodology to link the effects of turbulence with the commencement of sediment motion. It is considered that the metastable bursting cycle (i.e. sweeps, ejections, inward and outward interactions) is responsible for the sediment entrainment. And that the sediment entrainment, if any, occurs within a bursting period.

The main concept behind the determination of the critical conditions is that the probability of the entrainment of sediment (effect) is equal to the probability of occurrence of these highly energetic turbulent events that have magnitude greater than the critical (cause). The probability of sediment entrainment is computed by means of the image analysis tool.

The balance of moments is obtained here to determine the minimum moment that is required for the commencement of sediment motion. The balance of moments yields the deduction of a new variable that is used to describe the probability of occurrence of the different turbulent events. This variable is the summation of the instantaneous normal stresses in the streamwise and vertical direction. It is shown here that a two-parameter gamma density function describes quite well the statistical behavior of this variable.

The results that are obtained from the existing model suggest that the present methodology can adequately describe the commencement of sediment motion. It is shown here that the traditionally used shear stress term uw may not be the appropriate measure for the determination of the critical conditions.

Acknowledgments

I have many to thank for their help and guidance during the course of this study.

I would like to thank my advisor, Dr. Panayiotis Diplas, for the opportunity to work with him, and for his assistance and encouragement over the course of this study.

I thank the members of this committee, Dr. C. L. Dancey, Dr. F. A. Kibler, Dr. R. Kriz, and Dr. J. A. Schetz for their assistance during my graduate studies and in the preparation and refinement of this dissertation.

I thank Dr. W. Knocke, Head of the Civil Engineering Department, for his support over the last years of my studies at Virginia Tech.

I thank the staff of the Scientific Visualization laboratory of Virginia Tech for letting me use their facilities.

I thank my parents for their encouragement and support over the years. I would like to thank, also, my project mate Mahesh Balakrishnan for his advice, support, and for listening.

The support of this work by the United States Geological Society (Grant # 14-08-0001-G2271) is gratefully acknowledged.

Table of Contents

List of Tables

List of Figures

Symbols

The following list includes abbreviations and symbols that are frequently used in this work. Units are expressed in terms of length (L), time (t), and mass (M).

A	Area. [L^2]
A_1, A_2	Constants in the moment equation. [M]
B	Width of the flume. [L]
B_r (&)	Constant in the log law equation.
C_L &	Coefficient of lift.
d	Diameter of the particle. [L]
d_f	Mean fringe spacing. [L]
d_i	Mean diameter of particles in ith size fraction. [L]
f_a	Average frequency of sediment entrainment. [1/t]
f_d	Frequency of the Doppler signal. [1/t]
f_i &	Proportion of fraction i in the bed.
F_D	Net drag force. [ML/t^2]
F_L	Net lift force. [ML/t^2]
f_{mi} &	Proportion of the ith size fraction present on the bed surface.
Fr &	Froude number
g	Acceleration due to gravity. [L/t^2]
G	Submerged weight of the particle. [ML/t^2]
G	Mass rate of sediment "disturbed" particles. [M/L/t]
G_{ij}	Fraction of particles that cross a line within a subreach i in the jth bursting period.
Δh	Pressure difference between the two legs of the manometer. [L]
H	Flow depth. [L]
H &	Hole size.

& Non-Dimensional Variable or Constant.

K_0	Modified Bessel function of zeroth order.
$K^{\&}$	Lift factor.
n	Number of grains that are displaced from an area over a period of time, t. $[1/L^2/t]$
n_i	Number of grains of ith fraction displaced from an area over a period of time, t. $[1/L^2/t]$
$N^{\&}$	Non-Dimensional number of transported particles.
N_E	Number of particles entrained in Δt_{obs}.
N_T	Total number of particles placed in the test area at the beginning of Δt_{obs}
Q	Volumetric flow rate. $[L^3/t]$
Q_b	Bed load transport rate. [M/L/t]
q_{bi}	Transport rate of a fraction i per unit width.
P_E	Probability of entrainment of a particle.
P	Instantaneous pressure. $[M/L/t^2]$
$P^{\&}$	Probability.
$\overline{P}$	Time-averaged pressure. $[M/L/t^2]$
p	Fluctuating pressure. $[M/L/t^2]$
R	Correlation coefficient.
Re	Reynolds number.
Re_p	Particle Reynolds number.
S	Slope of the flume.
t	Particle transit time to cross the 8 fringes, or time. [t]
T_B	Mean bursting period. [t]
Δt_{obs}	Period of sediment entrainment observation. [t]
U	Depth-Average velocity.
U	Instantaneous stream-wise velocity. [L/t]
U_B	Mean velocity at the particle bottom. [L/t]
U_T	Mean velocity at the particle top. [L/t]
U_f	Mean flow velocity at the particle centerline. [L/t]
u_*	Friction velocity. [L/t]
u	Fluctuating stream-wise velocity. [L/t]

u’	Root mean square value of the fluctuating stream-wise velocity. [L/t]
$U^{+\&}$	Normalized stream-wise velocity.
U_N	Standard normal definition of U.
V	Instantaneous span-wise velocity. [L/t]
v	Fluctuating span-wise velocity. [L/t]
v’	Root mean square value of the fluctuating span-wise velocity. [L/t]
$V^{+\&}$	Normalized span-wise velocity.
W	Instantaneous normal velocity. [L/t]
W_i^*	Fractional sediment transport parameter.
w	Fluctuating normal velocity. [L/t]
w’	Root mean square value of the normal velocity. [L/t]
W_i	Velocity bias correction factor. [t/L]
$W^{+\&}$	Normalized normal velocity.
x, y, z, or x_i	Cartesian stream-wise, span-wise, and normal coordinates. [L]
z_o	Zero-Plane displacement height. [L]
$( )^{+(\&)}$	The + sign denotes normalized variables. Thus, u^+, l^+, k_s^+, etc. are defined.
$\overline{( )}$	The overbar denotes time-averaging operation.

Greek Symbols

α	Shape parameter in the gamma distribution.
α_s	Saffman lift coefficient.
β	Scaling parameter in the gamma distribution.
λ	Wavelength of the laser light. [L]
λ	Porosity of the bed.
$\theta^{(\&)}$	Angle between two coherent laser beams. [radians]
ν	Fluid kinematic viscosity. [L^2/t]
$\kappa^{(\&)}$	von Karmann constant.
ρ	Fluid density. [M/L^3]

& Non-Dimensional constants or variable(s).

ρ_s	Particle density. [M/L^3]
μ	Fluid absolute viscosity. [M/L/t]
τ	Average bed shear stress. [$M/L/t^2$]
τ^*	Non-Dimensional average bed shear stress.
τ^*_{cr}	Non-Dimensional critical bed shear stress.
τ_{xx}, τ_{zz}	Normal stress components. [$M/L/t^2$]
τ_{xz}	Shear stress component. [$M/L/t^2$]
ω	Normalized instantaneous shear stress.
Φ	Variable from the moment equation. [ML^2/t^2]
Φ_N	Normalized Φ.
$\Gamma(x)$	Denotes the gamma value x.

Chapter 1

Introduction

1.1 **Definition of the Incipient and Bedload Motions of River Bed Material.**

Incipient motion of bed material in a river due to flowing water refers to the beginning of movement of bed particles that previously were at rest. It is implied that the particles, once disturbed, will continue to move over some unspecified distance during some unspecified time. For flow conditions close to incipient the particles tend to slide or role atop of other particles while for higher flow conditions particle motion is dominated by saltating steps. The material that is transported with the above modes of motion constitutes the bedload material over a stream bed. The current study focuses on the bedload motion. The condition of incipient motion is needed to set a lower bound on the bedload transport.

Incipient motion is associated with changing river flow conditions. This is generally due to increasing water discharge, such as on the rising limb of a hydrograph during a runoff event. Causes for such events include storms, snowmelt and increased releases of water from upstream reservoirs.

1.2 **Importance of the Incipient Motion of Sediment.**

Incipient motion of sediment in gravel bed streams is a very important process because it represents the difference between bed stability and bed mobility. Incipient motion is a basis for the analysis and design of stable river beds. One use is for determining maximum flows at which a contaminated bed will remain stable and retain

toxic substances that otherwise might contaminate the water and affect aquatic organisms and human health at downstream sections. Another use is to establish "flushing flows" to maintain a clean, pervious bed in rivers. Without sufficient flushing, fine material and organic substances may accumulate in the voids among bed particles and cause oxygen depletion. As a result fish eggs buried in the gravel bed may suffocate. An understanding of incipient motion conditions is also used in general sediment transport studies for computing the bedload transport rate because a lot of bedload formulas are based on the bed shear stress in excess of the critical value (Yalin, 1977). The incipient motion conditions can be used to define a lower limit on the bedload transport function.

1.3 **Prediction of Incipient Motion Conditions.**

Prediction of incipient motion conditions is difficult. Lack of a clear view of the incipient motion concept is one of the reasons. For many, incipient motion is a deterministic process. According to this view a time-mean bottom stress moves the particles (e.g. Shields, 1936; Carling, 1983). The stochastic view is that turbulent stresses are responsible for the initiation of particles motion (e.g. Einstein, 1949; Sumer and Deigaard, 1981; Grass, 1983). This may provide an explanation to the observation made by many researchers that motion of particles occurs even for low flow conditions (e.g. Paintal, 1971). However, there are additional difficulties to the problem of defining the incipient conditions precisely. The accurate water discharge at which incipient motion occurs in a channel is a subjective criterion. Some researchers consider incipient motion to occur at the time that the first few particles start moving (e.g. Kramer, 1935; Vanoni

1966; and Fenton and Abbott, 1977). Others believe that it occurs when there are particles moving over a significant portion of the bed surface (e.g. Neill and Yalin, 1969).

Another factor that makes the problem more complicated is that the bed material is typically non-uniform in size, shape and sometimes in density. Typically, a wide range of particle sizes is present in the sediment found in gravel bed rivers. Bed - material size distribution can affect the hydrodynamic forces acting on a given particle in two significant ways: (1) smaller particles are hidden in the turbulent wake of relatively larger particles while larger particles tend to be overexposed into the flow and (2) the force necessary to start a larger grain rolling over smaller particles is much less than that required to start a smaller grain rolling over larger particles. Wide variation also occurs in particle shapes. A sample of bed material may contain a mixture of shapes such as well-rounded, flat, oval, disk-like, pencil-shaped, angular, and block-like. These are not likely to be entrained in identical manner during transport nor to start moving at the same flow condition. The density of particles may also vary in bed material samples. Fortunately, the range is relatively narrow for most gravel bed streams. Nevertheless, this might require prior knowledge of the material density whenever the conditions of incipient motion need to be accurately predicted.

1.4 **Methods of Predicting Incipient Motion**

The concept of critical stress has long occupied a central position in sediment transport theory. Numerous journal articles have been published in the past that study the incipient motion of sediment. Most of these studies are built on the experimental work and analysis of Shields (1936), although the idea of critical conditions was first

introduced by DuBoys (1879). Shields' work is prominent because he introduced similarity theory to describe the incipient motion of sediment.

Several studies, theoretical and experimental, attempted to explain Shields' analysis. Theories that were derived by White (1980) and Egiazaroff (1965), among others, considered the balance of fluid drag with the submerged weight of a sediment particle. Coleman (1967) and Wiberg and Smith (1987) incorporated the lift force with the drag force and submerged weight in their balance of moments. Ling (1995), based on previous studies, developed separate criteria for rolling and lifting by treating the lift force as the sum of the Saffman shear lift, the magnus spin, and the centrifugal force.

The experimental work that deals with the threshold issue of non cohesive sediments is large. Lavelle and Mofjeld (1987) provided a summary with the most important experimental studies on threshold of motion. They categorized them into two groups, based on the criterion that is used to define the critical stress. In the first category the critical condition is considered to be reached when a minimum sediment flux is obtained. For example, Shields (1936) considered as his definition of critical stress the value of bottom shear stress at which the extrapolated bedload transport rate went to zero. The second category of studies is based on the visual observations of particle motions on a flume bed. In this case visual observations of the flume bed are made and the number of transported particles over an area is noted for a certain period of time. Vanoni (1964), for example, adopted as threshold the condition of grain movement every two seconds at any bed position. Neill and Yalin (1969), and later Yalin (1977), indicated the need to establish a criterion that defines the critical condition in a more consistent and objective way. They suggested that some subjectivity in the above methods could be eliminated if

the area and duration of observations, friction velocity, diameter of unisize sediment, and the number of particles in motion were incorporated into a dimensionless parameter $N=(nd^3/u_*)$ that has a fixed value (10^{-6}) for all experiments (n denotes the number of grains that are transported over an area and period of time, d is the diameter of a particle and u_* is the friction velocity). This value corresponds to a rate of transport that is 10 times less than the expected Shields' threshold value. Wilcock (1988), extended their work by suggesting a threshold criterion for non - uniform sediments that satisfies similarity arguments and provides for each fraction on the bed a representative critical stress. While the above criteria have been defined based on similarity considerations, there are models (e.g. Ackers and White, 1973; and Parker et al., 1982) that involve estimation of the critical stress value for each individual fraction of sediment. For this purpose a constant (reference) low value of dimensionless transport rate was chosen arbitrarily. It has been shown by Kuhnle (1995) that although the criteria of Ackers and White (1973) and Parker et al. (1982) provide different reference shear stress for a set of data, they yield similar results regarding the variation of the reference shear stress with grain size.

Recently, Moore (1994) provided a summary of the studies that extended the Shields diagram to account for the effects of grain size non uniformity, relative protrusion, shape (other than spherical), bed slope, and low ratios of water depth to grain size. Selectively we can refer to the work of the following researchers: Komar and Li (1986), who presented a pivoting angle analysis to examine the selective entrainment of sediments according to shape and size; Fenton and Abbott (1977) who examined the role of relative protrusion on the initiation of particles motion; Mantz (1980) who investigated

the influence of particle shape on transport by using artificial lightweight discs as sediment while Magalhaes and Chau (1983) examined the initiation of motion for shale sediments having a low density and platy shape; Bettess (1984) who suggested an extension to the Shields' curve to account for small flow depth - particle diameter ratios; and Wang and Shen (1985) who expanded the Shields diagram to be valid for large and small size particles. A modified version of the Shields curve based on the results obtained from the above studies is shown in figure 1.

Finally, several researchers have expressed the opininon that no absolute stress threshold value exists. The experimental investigation of Graf and Pazis (1977), Paintal (1971) and others, indicated that there is no mean bed shear stress below which no particle motion occurs. Specifically Paintal (1971) reported dimensionless bedload rates as low as 6.9×10^{-9} for conditions well below the critical Shields stress while He and Han (1982) concluded that the notion of an incipient condition is artificial.

1.5 **Limitations of the Existing Methods.**

The methods that are described above have the following limitations:

a. They ignore the role of turbulent flow (instantaneous stresses) on the initiation of motion. Instead, they treat the particle entrainment problem as a time average problem and use the mean bed shear stress value to determine the critical stress.
b. Several theoretical models for threshold conditions (e.g. Wiberg and Smith, 1987) are based on the assumption that the time average lift force acts at the same instant with the time average drag force, which is not in general true.
c. Some of the existing methods consider that the particle sizes, shapes, and positions in the bed surface are deterministic parameters. In reality, these parameters are

distributed within a given channel reach. Therefore, spatial variations in the local critical stress value would be expected.

d. The existing transport models are site specific or can be used for one type of stream.

e. The methods which are based on visual observations of the particles' entrainment are rather qualitative.

f. The incipient motion criteria of Neill and Yalin (1969) and Yalin (1977) are limited to unisized sediments. The criterion proposed by Wilcock (1988) is valid for non uniform sediments, however, in practice it is very difficult to be implemented for most mixed - sized sediments due to scaling problems (Wilcock, 1988). These scaling problems are less severe with the reference transport models (e.g. Parker at al., 1998; Ackers and White, 1973) and therefore are easier to use in practice.

g. The above models do not account for the effects of bed surface packing conditions on the initiation of motion. The bed surface packing condition defines the percentage of the area of the bed that is covered with particles without including the porosity that exists among the particles.

h. The existing experimental data on incipient motion, which are used to test the theoretical models, have some inaccuracies. These are mainly attributed to the methodological problems that are involved in defining critical conditions and to the conditions under which these tests were conducted. Most of the experimental data do not provide detailed information for the bed conditions that existed during the tests. For example the term "flat bed", that has been used very often in different reports, is a very ambiguous term since it depends on the leveling technique and the type of the grains that are used. If the bed is not flat, then protrusion effects must be considered

in the study of critical stress. Also, by using different types of sediment particles the role of size, shape and density becomes important in the study of sediment motion. Very few studies are consistent in reporting the above information. The experimental studies of Fenton and Abbot (1972) and Coleman (1966) fall in this category. Fenton and Abbot examined the role of particle protrusion by observing the motion of a sphere placed on a rod that is raised vertically to the flow at different locations until motion of the ball is observed. Coleman performed tests by placing isolated spheres atop a tightly packed layer of spheres.

1.6 **The Role of Turbulent Flow on the Initiation of Motion.**

The effects of turbulent flow on the initial entrainment of sediment were recognized as far back as 1939 by Lane and Kalinske. The two investigators did not overlook the statistical aspects of the near bed flow and later Kalinske (1947) proposed a model of bedload transport that incorporated fluctuations in friction velocity. Subsequently, a number of studies (e.g. Gessler, 1965; Nakagawa and Nezu, 1981; Grass 1983, Sekine and Kikkawa, 1988; and Naden, 1987) focused on the statistical nature of the entrainment problem. Grass (1983) hypothesized that the value of instantaneous bed shear stress follows a Gaussian distribution, while the values of the critical shear stress required for the movement of individual grains can be described by a log Normal distribution. The overlapping region between the two distributions defines the critical shear stress values that correspond to particles' initiation of motion. Naden (1987) considered the balance of instantaneous drag, lift, and gravity forces operating on a particle. To accommodate the temporal variation in bed shear stress, the model is based

on the assumption that the turbulent velocity fluctuation in the vertical direction, w, is proportional to the longitudinal velocity fluctuation, u.

The discovery of the so called bursting phenomenon in turbulent flows by Kline et al. (1967) (i.e. the cycle of sweeps ($u>0$, $w<0$), ejections ($u<0$, $w>0$), inward ($u<0$, $w<0$), and outward interactions ($u>0$, $w>0$), where, u is the fluctuating velocity component in the longitudinal direction and w is the fluctuating velocity component in the vertical direction) (figure 2) generated a new interest in studying further the structures of boundary layer turbulence and then apply this new knowledge to the initiation of sediment motion problem. An essential precursor to the examination of the role of flow turbulence on the sediment motion is a good understanding of the characteristics of boundary turbulence itself.

There are numerous studies in the literature that focus on turbulent flow over smooth surfaces, fewer investigations, however, deal with flows over rough surfaces. A comparison of these two different cases by Clifford et al. (1991), Grass et al. (1991), and Sumer and Deigaard (1981), among others, have indicated that the metastable sweep-burst cycle, which is responsible for periodic stress fluctuations, is present in flows over rough and smooth surfaces and occurs with the same sequence of events. The mechanisms, however, that generate these events are different for flows over smooth surfaces than flows over rough surfaces. In flows over smooth surfaces the sweep - burst cycle relies on the presence of a continuous viscous sublayer in the near bed vicinity, which retards and organizes fluid motion in the form of low speed streaks (e.g. Offen and Kline, 1974). In the case of rough surfaces the presence of these low speed streaks becomes less conspicuous (Sumer and Deigaard, 1981; Grass et al., 1991). In rough

boundaries the most likely reason for the occurrence of the sweep-burst cycle is vortex shedding from individual particles, particle clusters, and bedforms (Gyr, 1983).

Also, Sumer and Deigaard (1981) studied the particle trajectories in rough boundaries. They concluded that in rough walls, the particles gain much higher elevations than in the case of the smooth walls. From their partially quantitative results, they concluded that the longitudinal fluctuating velocity, u, decreases while the upward fluctuating velocity, w, increases. Finally, it was shown that the burst duration decreases with increasing bed roughness. Krogstad et al. (1992) obtained similar results with those of Sumer and Deigaard's (1981). They demonstrated that there is significant increase in the vertical turbulent intensity w´, which is defined as the r.m.s. of the velocity fluctuation w, and a moderate increase in the Reynolds shear stress ($-\overline{uw}$) over the rough wall. The longitudinal turbulence intensity, u′, distribution is essentially the same for both surfaces.

The scaling of "bursting" events over smooth and rough walls has been a source of controversy. Different opinions have been expressed by many researchers in the past. Lu and Willmarth (1973) pointed out that the "bursting" events should scale with the outer variables. Blackwelder and Haritonidis (1983) suggested that the "bursting" events scale with inner variables. Alfredson and Johansson (1984) introduced a mixed scaling. Recently, Wark and Nagib (1991) showed that there is strong correlation between the outer flow and the "bursting" process. The mean streamwise spacing, l_X , between two "bursting" events for smooth walls is determined experimentally to be 1.4 to 2.7 times the average water depth, H (Nakagawa and Nezu, 1978).

In an attempt to link the characteristics of the Reynolds stress ($-\overline{uw}$) with the entrainment of sediment, different researchers (e.g. Bridge and Bennett, 1992; Diplas and Parker, 1992; Grass, 1983; Leeder, 1983; Sumer and Deigaard, 1981; and Wei and Willmarth, 1991) have considered that the sweeps might cause the initiation of bedload motion in a stream bed, while the ejections are responsible for the particles suspension motion. The reasoning behind this consideration is that the sweeps and ejections are the only events from the burst - sweep cycle that contribute positively to the Reynolds shear stress and therefore, contribute significantly to the production term of turbulence. To detect the contributions of these two events to the time average Reynolds stress ($-\overline{uw}$) and isolate them from the outward and inward interactions, different detection techniques have been suggested. Lu and Willmarth (1973), for example, determined the above contributions by conducting a conditional sampling technique, known as quadrant method. By using this technique, over smooth bed surface, they indicated that the ejections account for 77% of the total contributions to the time average Reynolds stress and that the sweeps contribute 55%. The excess percentage over 100% is due to small negative contributions from the outward and inward events, to the Reynolds stress. There are two other detection algorithms available in literature: the variable internal time average technique (VITA), developed by Blackwelder and Kaplan (1976), and the modified u-level algorithm constructed by Luchic and Tiederman (1987). The quadrant method provides significant advantages over the other two methods (i.e. it has the greatest reliability, a high probability of detecting the ejections and a low probability of making false detections) and so it has been extensively used by many researchers (e.g. Nakagawa and Nezu, 1978; and Antonia, 1981). Significant attention was given also to

the statistical properties of the uw term. The probability density function (p.d.f.) of uw fluctuations were measured at different distances form the wall by Gupta and Kaplan (1972), Lu and Willmarth (1973), Nezu and Nakagawa (1993) and others. This distribution has long tails for extreme values of uw, and a sharp peak at uw = 0. The normalized $\frac{uw}{\overline{uw}}$ can be described by the joint probability of the u, w components. A typical probability density function plot of the uw stress for a rough wall is shown in figure 3. (Balakrishnan, 1997).

Recently, a second school of thought (e.g. Williams et al., 1989a; and Nelson et al., 1995) has supported the opinion that the sweeps are not the only events responsible for bedload transport of gravel but also the outward interactions. Nelson et al. (1995) indicated that when the magnitude of the outward interactions increases comparatively to the other events the sediment flux increases too, although the magnitude of the Reynolds stress decreases. Nelson et al. (1995) have shown a poor correlation between the sediment flux and the Reynolds stress (-uw). Instead they indicated a very significant positive correlation between the streamwise velocity and the sediment flux for flow conditions well above the critical.

From the above description it can be concluded that the linkage of the sediment flux with the turbulent flow components responsible for the initiation of motion remains an open case. Specifically, it is questionable as to whether the distributional characteristics of the uw term are of the greatest importance in the prediction of the initiation of sediment motion. Also, despite the good correlation between the sediment flux and the streamwise instantaneous velocity U (where, U= $\overline{U}$ +u and $\overline{U}$ is the local time average velocity) for flow conditions well above the critical, U may not be the only

parameter responsible for the sediment entrainment near the threshold conditions. Next, several shortcomings in the approaches presented above are described.

1.7 **Comments on the Existing Stochastic Incipient Motion Criteria**

a. The majority of the existing theoretical models (e.g. Gessler, 1965; Nakagawa and Nezu, 1981; Grass, 1983; and Sekine and Kikkawa, 1988) are rather qualitative.

b. Naden's (1987) study is based on the assumption that a simple proportionality exists between the velocity fluctuations in the vertical and longitudinal direction (i.e. w = 0.77 u). This assumption, however, does not represent the reality and has been made simply for mathematical expedience. A simple proportionality exists only between the r.m.s values of the fluctuating velocity components (McQuivey, 1973).

c. During the last twenty years misplaced emphasis has been given to the turbulent shear stress term (-uw). Nowadays, it is shown (e.g. Clifford, 1991; Leeder, 1983) that the dominant components of the turbulent stress are the normal stresses in the longitudinal and vertical direction, u^2 and w^2. Although the (-uw) term remains the principal shear stress, its contributions to the total average turbulent stress are much less than those of the u^2, w^2, and of the stresses involving mixed products (e.g. $\overline{U}$ w) (Clifford et al., 1991).

d. A reason that attention over these years has been directed towards the term uw could be the fact that this is the only term which does not get eliminated after time averaging of the momentum equation. Thus, different conditional

techniques have been developed to isolate the contributions of the events of the burst - sweep cycle to ($-\overline{uw}$). However, if the argument stated above has been indeed used as the criterion for the exclusion of the mixed stress products from the study of the entrainment problem then this criterion does not hold any validity. Because it is not reasonable and consistent to consider the role of instantaneous Reynolds stress on the initiation of motion and at the same time use the time averaging process as the basis for the elimination of the mixed products in the Reynolds stress tensor. A similar view has been expressed by Corrsin (1973) who indicated that studies referring to instantaneous Reynolds stresses are incomplete if they do not include the mixed term product. According to Corrsin (1973), it is likely that the mixed terms might significantly contribute to the initiation of sediment motion.

1.8 **The Role of Surface Packing Conditions on the Initiation of Motion.**

The need to examine the role of surface packing conditions on the incipient motion of sediment has been expressed by several researchers (e.g. Billi, 1988; Naden, 1987; Reid et al., 1992; and Ling, 1995). The above investigators have suggested that the criterion for the incipient motion depends on how tightly packed the surface layer is. How far apart the particles of the top surface are located affects the roughness conditions near the boundary layer and essentially the turbulent flow structure within its proximity. For example, Schlichting (1960) found that for the same sphere diameter the values of equivalent sand roughness k_s increased substantially when the particles were positioned closer to each other. Lee and Soliman (1977) studied the effect of surface packing

condition on the mean drag force acting on the roughness elements. On this basis, they proposed three different roughness regimes: i) the "isolated roughness" regime that corresponds to a surface packing condition of up to 8 %, ii) the "wake interference flow" regime that corresponds to a surface packing condition that lies within the range of 16 % to 40 %, and iii) the "skimming flow" regime that corresponds to a surface packing condition that is greater than 40 %.

Reid and Frostick (1988) and Papanicolaou et al. (1995, 1996), among others, indicated the formation of cluster microforms for "loose" bed surfaces based on observations made in natural streams and in the laboratory. Preliminary results (Papanicolaou et al., 1995) have shown a variation in the value of the critical stress for different surface packing conditions. In relatively high surface packing conditions the particles get trapped in the cluster structures which persist until a "nucleous particle" is removed (Billi, 1988). The importance of the surface packing conditions on the initiation of sediment motion is examined next.

1.9 Objectives

The present work intends to remedy the deficiencies of the previous studies, that are indicated in Chapter 1 (see sections 1.5, 1.7, and 1.8), and provide a quantitative criterion for the incipient motion of sediment. One of its primary goals is to examine the role of different surface bed packing conditions on the incipient motion of sediment. For this purpose several tests with different packing configurations are

performed. Also, in this study the changes in the magnitude of the turbulent stress components (i.e., normal and shear), for different packing conditions, are examined.

Another objective of this study is the examination of the role of the normal and shear stresses on the commencement of sediment motion. Specifically, the main emphasis is placed here on the coupling of the turbulent stress components with the rate of the entrained sediment. This is possible here by using the distributional characteristics of the instantaneous stresses and the consideration that the probability of the entrained particles should be the same with the probability of the stress events that have magnitude higher than the critical stress value. The final outcome of this methodology is the development of an incipient motion model that accounts for the role of turbulence and is applicable for different bed configurations.

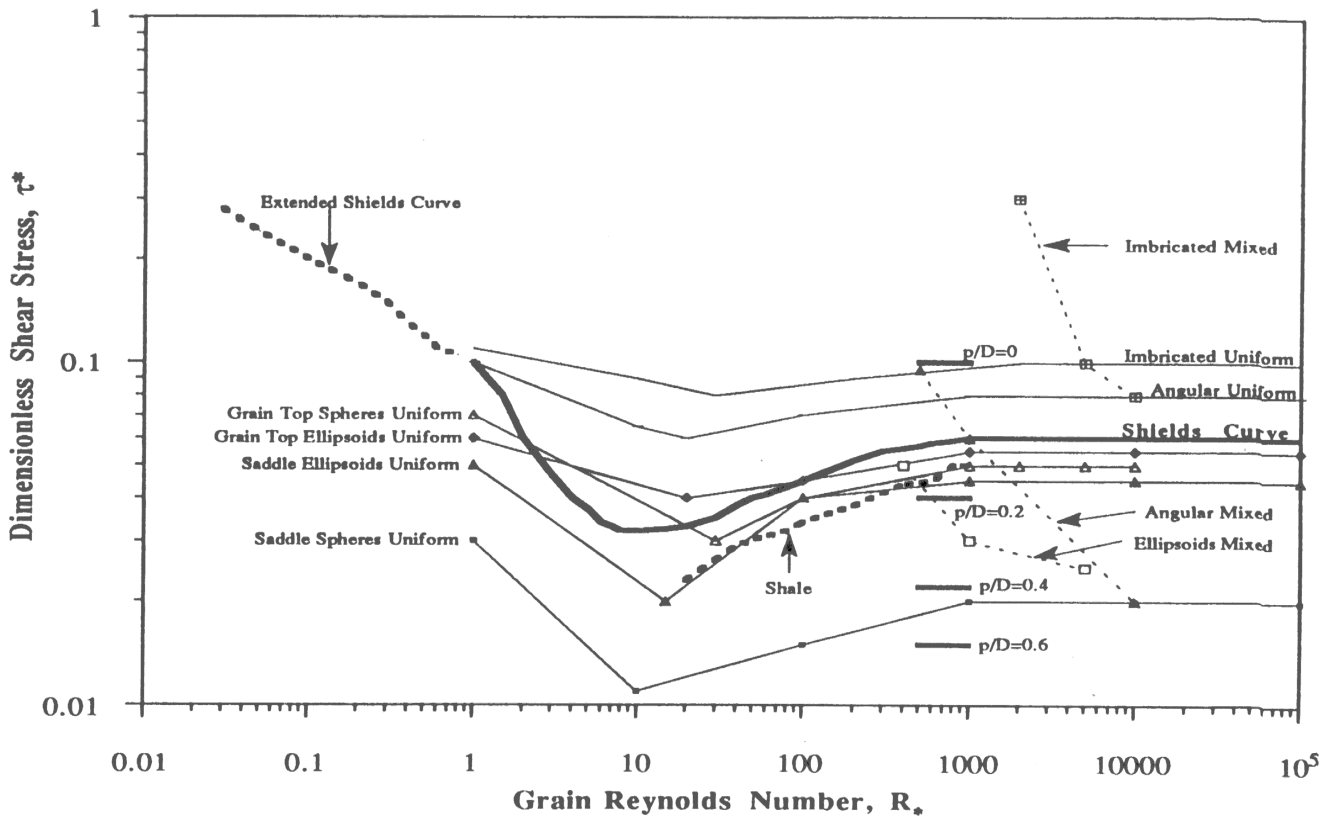

Fig. 1. Modified Shields curve including the extended region for $R_* < 1$ proposed by Mantz (1977) and Yalin and Karahan (1979), the effects of grain size, shape, and imbrication proposed by Komar and Li (1986), the effects of relative protrusion, p/D, proposed by Fenton and Abbott (1977), and the results of a shale study by Magalhaes and Chau (1983).

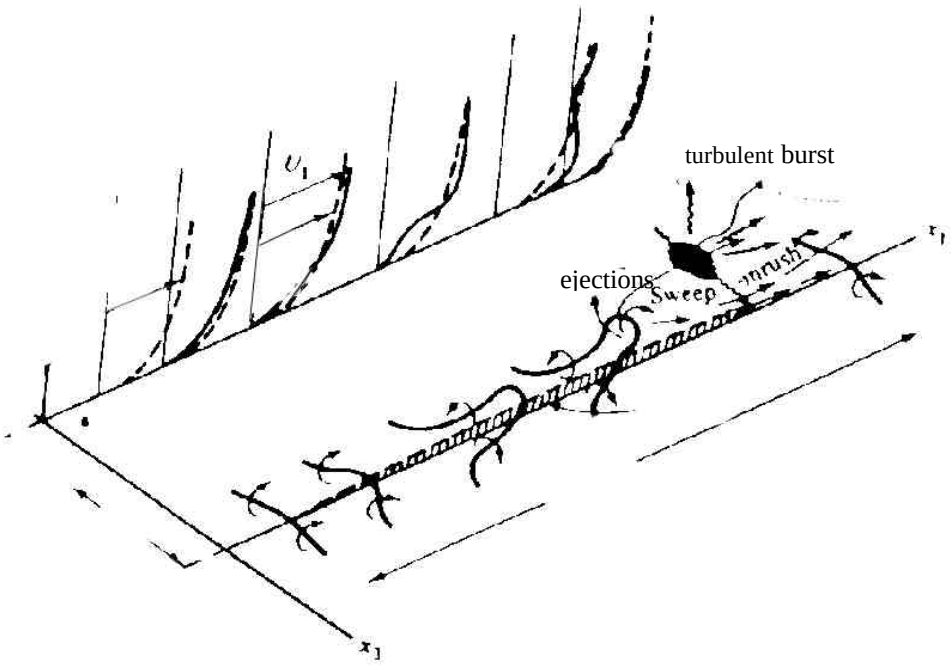

Figure 2. Conceptual model of turbulence near the wall during a cyclic process (from Hinze 1975).

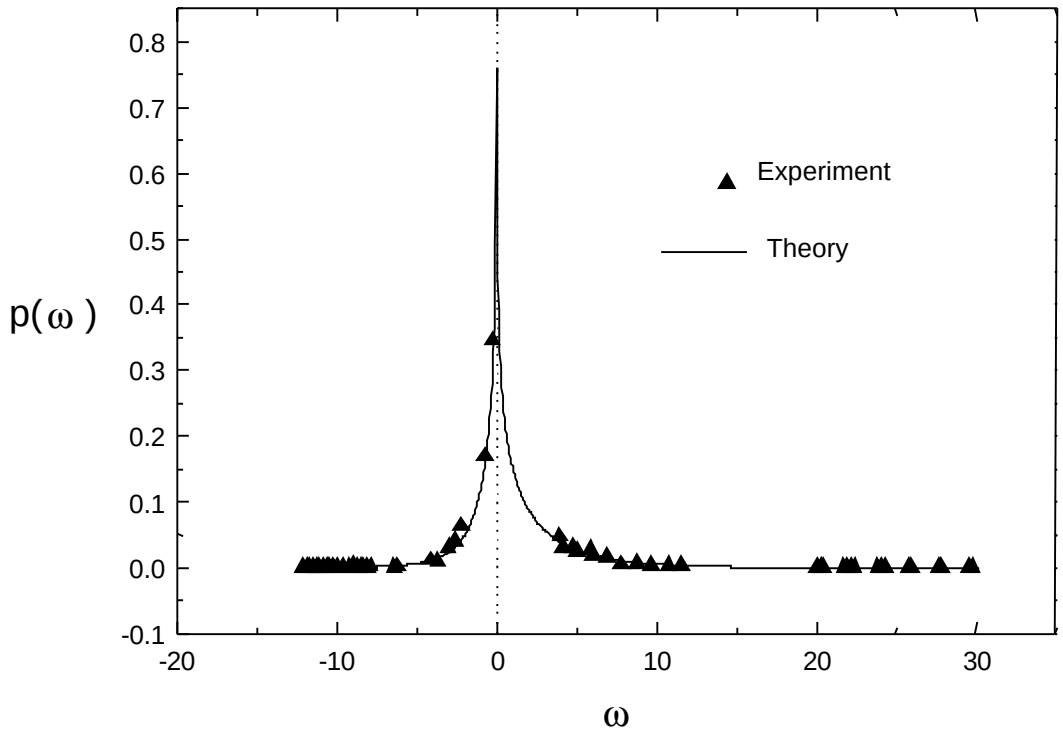

Figure 3. The probability density function of the ω=uw/<uw> term.

Chapter 2

Experimental Procedure

2.1 Laboratory Facilities

The experimental work in this study takes place in a tilting water flume of rectangular cross section. Figure 4(a) constitutes a sketch of the flume and figure (4b) provides a side view of the flume. The flume is 14.4 m long, 0.6 m wide, and 0.3 m deep. The flume at its entrance is equipped with a honeycomb structure to provide a rectilinear flow. The water from the channel is discharged into a 400 ft^3 tank located at its downstream end and it is recirculated to the channel entrance with the use of two centrifugal pumps. The pumps are of the closed impeller type, with 7 ½ HP, and have 3 phase motors. One of the pumps is equipped with a Transistor Inverter Variable Frequency speed controller for adjusting the water flow. The flume is also equipped with a tailgate that is located at the downstream end of the flume. Underneath the main body of the flume a Venturi meter is located that is made from fiberglass material. An air/water and a water/mercury U tube manometer are furnished as readouts for the Venturi meter. A "knife" type gate valve is installed in the pipe downstream of the Venturi meter to regulate the channel flow. A motor located at the side of the flume is used to adjust the slope of the flume from 0% to 5 %. Near its downstream end, the flume has a sediment trap that can be used to collect bedload material, which in turn can be fed to its upstream end with the help of a ½ hp pump. The flume is also equipped with rails upon which a trolley is moving along the channel. At the trolley are placed a pressure transducer Schaevitz P3091-5Wd and a Prandtl tube that are used to obtain the

average velocity profile, a point gauge and a tube that is used for the seeding of the water with metal coated glass beads of average diameter 4 μm. The pressure transducer is connected with a Macintosh PC that has a data acquisition card and software for data analysis.

The flow measurements are obtained with the use of a three-component LDV system, manufactured by TSI (System 9100-12) (figure 5). This system is a six-beam (it has three pairs of green, blue and violet beams), non-orthogonal, color separated, fringe-mode, off-axis backscatter system with counter-based signal processing. This particular system uses three independent optical channels to measure three non-orthogonal components of the velocity (Balakrishnan and Dancey, 1994). Two of these components are approximately coplanar with a coupling angle, the angle between the measured components, of approximately 30 degrees. A laser beam is produced by a 5 Watt Argon-Ion laser and is, then, split into various, monochromatic beams, by a dispersion prism. Three of these beams are guided to two different optical trains by means of high efficiency mirrors. The green (514.5 nm) and the blue (488 nm) beams form one path, whereas the violet, the weakest beam, is led to a different train. All beams are split by beamsplitters and three pairs of beams are formed. One of the two beams of each pair is shifted 40 MHz by acousto-optic "Bragg" cells. Frequency shifting is necessary for measuring low-velocity flows as well as high frequency turbulence. After the beams are expanded by a beam expander, two focusing lenses, one for each optical, are used to focus all six beams to the same spot. To improve optical access and facilitate near-wall measurements near the center-line of the flume, the LDV system, which is mounted on a traverse table, is tilted from the horizontal by 3.8 degrees. The measurement volume is

ellipsoidal in shape with dimensions 87 μm in the horizontal direction and 318 μm in the vertical. The measurement volume is located 0.97 m upstream of the tailgate of the flume. To systematically position the LDV measurement volume within the flume a traverse system is employed. When optically probing from air into water, adverse laser beam refraction effects are likely to occur. This problem is rectified here by using a water filled, acrylic vessel rigidly attached to the optical table and coupled to the flume sidewall with a flexible rubber (figure 6). The flexible rubber permits traversing the LDV measurement volume in the three coordinate directions. The vessel is open to the atmosphere so that the water level within it can adjust as the LDV is traversed. This design permits good quality signals with adequate data rate (typically 30 measurements per second), independent of LDV movement and measurement volume location within the flume.

The changes of the particles' position with time are monitored by means of a camcorder (Minolta Master series V 2000). The maximum recording capability of the camera is 30 frames per second. During the tests the camera is mounted on a tripod over the test section at a distance of 1.30 m from the downstream end of the flume (figure 7). The filming process takes place from above the flume's bed (figure 7) by setting the camera in the macro-focus mode. The macro-focus mode allows the focal length of the camera to be within a range of 2.54 cm to 3.6 m. The typical area of view during the experimental runs is about 0.084 m^2 (0.28 m length and 0.30 m width). These dimensions are chosen such, as the resolution that is assigned to each sediment particle is sufficient to allow the particles' identification in the post processing process. The illumination conditions that exist during the recording process play an important role in the quality of

the movie. Sufficient illumination of the control area is required to obtain movies with small noise. However, excessive amount of light can cause saturation in the shape of the sediment particles and lead to errors in the particle recognition process during the analysis of the film. In this study two high-intensity tungsten lamps (DVY GE 650W, 120V quartz halogen lamps) are used as light sources and they are placed 1 m upstream of the camera. This location of lamps has been found by trial and error to be the most suitable because no saturation or significant noise in the film was observed during the digitization process.

A Panasonic videocassette recorder model AG-7750 is used for the digitization of the film (figure 8). The configuration of the Panasonic recorder during the timing process of the movie is given in Appendix 1. The Panasonic recorder is connected with a Macintosh Quadra 900 computer that allows the capturing of the movie in an automatic fashion. Different commercial programs (developed by Adobe Systems Inc.) are used to perform the digitization process. During this process the movie is converted to individual frames. The frames are gathered in sequential manner and at a rate of 30 frames per second. Next, the frames are imported electronically to a Sun Sparc 2 workstation (with 65Mb RAM, 1.2 GB Disk and a 650 MB Read/Write Optical drive) for the midlevel and post processing image analysis (figure 9). More details on the digitization and image analysis processes are provided in Chapter 4.

2.2. Experimental Design

A major effort is placed during this study in the area of experimental design. The issues examined as part of this design process are: the choice of particle shape, size and

density, the location and length of the test section, the morphology of the bed throughout the flume length, the identification of the particles from the image analysis system, the number of tests that are performed in this study, the number of balls used in the tests, the feeding process of the material, the flow conditions during the tests, the collection method of the particles at the downstream end of the flume, and the collection period of the sediment.

During the tests spherical particles of the same diameter and density (glass beads) are used to isolate the role of turbulent flow on the initiation of particle motion. To reduce further the number of parameters affecting the entrainment of sediment particles, it was decided that the critical stress should be independent of the particles Reynolds number. This requirement is satisfied when (Vanoni, 1975):

$$\frac{d}{\nu}\sqrt{0.1Rgd} \geq 500 \qquad (1)$$

where, d is the particle diameter, ν is the kinematic viscosity of water, $R=\frac{\rho_s}{\rho}-1$ is the particle submerged weight, ρ_s is the density of the glass beads (2540 kg/m^3), ρ is the water density, and g is the acceleration of gravity. Equation (1) identifies the lower limit of the particle size that satisfies the above requirement. The upper limit of the particle size is determined by the relative depth ratio, H/d. We need to have an H/d≥6 so that the sides wall effect is not pronounced within the central 40 cm section of the channel. Based on these criteria the particle diameter is chosen to be 0.008 m. The specific gravity (s.g.) of glass beads is 2.54.

The test section is located at 11.4 m downstream of the flume entrance where fully developed turbulent flow conditions exist during the tests. To ensure fully developed flow conditions for the case of a rough boundary the following relation must be satisfied: $\frac{x}{4R_h} \geq 45$ (Nezu and Nakagawa, 1986) where, x denotes the channel length that fully developed conditions start to exist and R_h is the hydraulic radius of the flume cross section. Naturally worn gravel ($d_{50} \approx 25$ mm) is used for the first 10.4 m reach (figure 10). The remaining 1 m reach before the test section is covered with three layers of colorless glass beads (the glass beads is a product of Jaygo Inc.) of diameter 0.008 m and a fourth layer of lead balls (s.g. = 12.4) with the same diameter (figure 10). The last 3.0 m reach, which is considered as the test section, is covered with four layers of colorless glass beads (figure 10). The thickness of the flume bed is constant throughout its length and is equal to 2.9 cm. To maintain the same thickness in the roughness bed layer along the gravel section a flat surface is attached to the trolley that moves along the flume. This surface is positioned vertically towards the flume bed and at a distance of 2.9 cm.

Depending on the experiment, a number of Painted glass beads of colorless beads are painted and placed atop the fourth layer of the test section (figure 10). It is the movement of these balls that is examined during the experiments. The balls are painted to make easier their identification from the image analysis tool. Specifically, they are painted in green color because this color overall enhances the quality of images and does not cause any blur to the movie. The painting process of the balls is a time consuming process. For this reason a Wagner sprayer is used here to minimize the labor that is required. The balls are placed on horizontal meshes that allow the paint to dry fast at the

surface of the balls. The green color paint that is used here (which is a product of the Dykem Co.) can stick on glass surfaces.

The length of the area of view of the camera is 28 cm (figure 11). This length is considered sufficient for monitoring the particle motion (Sekine and Kikkawa, 1992) because the average step of the saltating glass beads (at the fifth layer) for conditions well above the critical does not typically exceed the diameter of the particles several times. The green color glass beads are distributed uniformly, atop the fourth layer, during the experimental runs throughout the 3.0 m test section. The reach of the test section that is upstream of the area of view and has length of 1.54 m (figure 11) is used to feed the glass beads to the area of view. The width of the test section is 40 cm. The wall effects are considered minimal at a distance greater than 10 cm away from the flume walls. Lead balls are placed at both sides of the flume within a distance of 10 cm from the two walls (figure 11). The lead balls are distributed the same way as the glass beads to maintain bed uniformity throughout the area of the test. Downstream of the test section, a plexiglas surface is placed at the bottom of the flume. This surface is 0.60 m wide and 0.18 m long and is used to facilitate the collection of the balls in the basket that is located at the downstream end of the flume.

The total number of glass beads that is used in the test section as roughness elements is equal to 74,232. These balls are tightly packed to avoid local anomalies in the morphology of the bed surface (figure 12). The porosity of the tightly packed bed is 30 %. A flat wooden surface is used to make the bed surface as plane as possible. Figure 13 shows the different sections of the flume. Depending on the surface packing condition case that is chosen to be examined during the experimental runs, different number of

green glass beads is used in the test section. The criterion for the selection of different surface packing conditions during the experimental runs is based on the suggestion of Lee and Soliman (1977). Specifically, the surface packing conditions, that are chosen here, correspond to the packing conditions that typically exist in the three distinct roughness regimes (i.e. the isolated roughness regime (the 2% packing condition test), the wake interference regime (the 20% and 35% packing condition tests), and the skimming flow regime (the 50% and 70% packing condition tests)) that have been defined by the above investigators. Table 1 summarizes the surface packing condition cases that are examined during the course of this study and the corresponding number of balls. Figures 14(a), (b), (c), (d), and (e) show the different surface packing configurations.

The number of balls for the different surface packing conditions in table 1 is calculated by taking into account that the porosity of a tightly packed layer of spheres is 30 %. The 2 % packing condition in Table 1 represents the theoretical case where one isolated sphere is situated on top of other spheres. The 70 % packing condition represents the case where the surface layer is tightly packed.

2.3. Experimental Procedure

Prior to the commencement of the tests, the slope of the flume is calibrated. For this purpose a precise optical micrometer is used. The optical micrometer (model Wild no.3) provides readings with a mean error of less than 10 mm over a distance of 80 meters. The preparatory work for the tests involves the following subtasks: 1) Examine the alignment of the six Laser beams. If the beams are out of position (due to thermal expansion of the table and minor vibrations of the ground) steering of the beams is

required. For this reason, the system is equipped with beam steering modules and adjustable mirrors for minor adjustments of the beam directions. A common way to adjust the beams is by using a tiny, 50 μm diameter pinhole. To make sure that the beams are crossing, the pinhole is placed inside the flume and the measuring point is guided towards the position of the pinhole with the traverse mechanism. A detailed description of each one of the optical and electronic components as well as the alignment procedure can be found in the system's instruction manual (System 9100-12 3 Color, 3 Component Laser Doppler Velocimeter Instruction Manual, TSI Incorporated, St. Paul, Minnesota 1985). Finally, the beam angle measurements are obtained. The beam angle values are used in the postprocessing process of the Laser data to obtain the orthogonal components of the velocity vector. 2) Find the pump frequency that is required to reach the desirable flow depth for the particular test. To ensure flow uniformity the depth is measured at seven different locations along the flume. To avoid a drawdown curve at the downstream end of the flume and maintain uniform flow depth, steel rods are placed at the downstream end of the flume. The rods are mounted horizontally at the rails of the tailgate structure and are easily removed. Depending on the flow conditions that need to be reached, rods are added or removed from the existing structure. A gap of 3 cm exists between the bed surface of the flume and the lowest rod at the tailgate to allow the balls to reach the basket at the downstream end of the flume. 3) Position the green balls as uniformly as you can in the test section. 4) Position the camcorder vertically atop the flume. The focus of the camera is adjusted to obtain the dimensions of the area of view. 5) Increase the pump frequency gradually to avoid any displacement of the balls prior to the commencement of the testing period. When the discharge that is required for the

testing conditions is reached, manipulate the gate - rod configuration until uniform depth prevails throughout the flume. Do not consider the balls that are collected in the basket during this time as part of the bedload transport. 6) Feed the water in the flume with seed to obtain flow measurements by using the LDV system. 7) Activate the timer when the flow conditions of the test are reached. Collect the particles from the basket every 5 minutes. Before the termination of the test get the manometer reading. At the conclusion of the run the bedload collected in the basket is dried and weighted.

The data collected in each run are the discharge, the flow depth, the flume slope, and the total number of the balls that are transported. The data acquisition of the laser Doppler velocimetry, the digitization process of the movie and the image analysis of the images are described next.

Table 1. Different surface packing conditions.

Surface packing conditions in percentage.	Number of green glass beads	Number of lead balls at the side walls of the test section.
2 (isolated case)	530	258
20 (wake interference case)	5300	2586
35 (wake interference case)	9275	4526
50 (skimming case)	13250	6466
70 (skimming case)	18558	9052

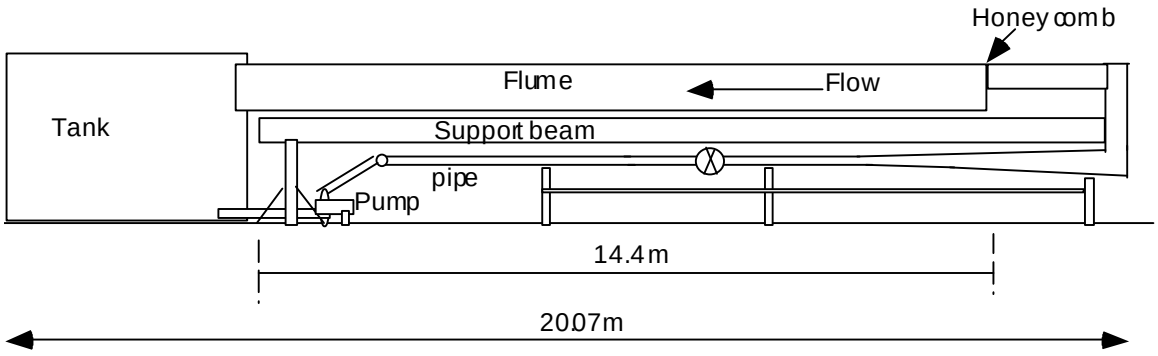

Figure 4(a). A sketch of the flume.

Figure 4(b). A side view of the flume.

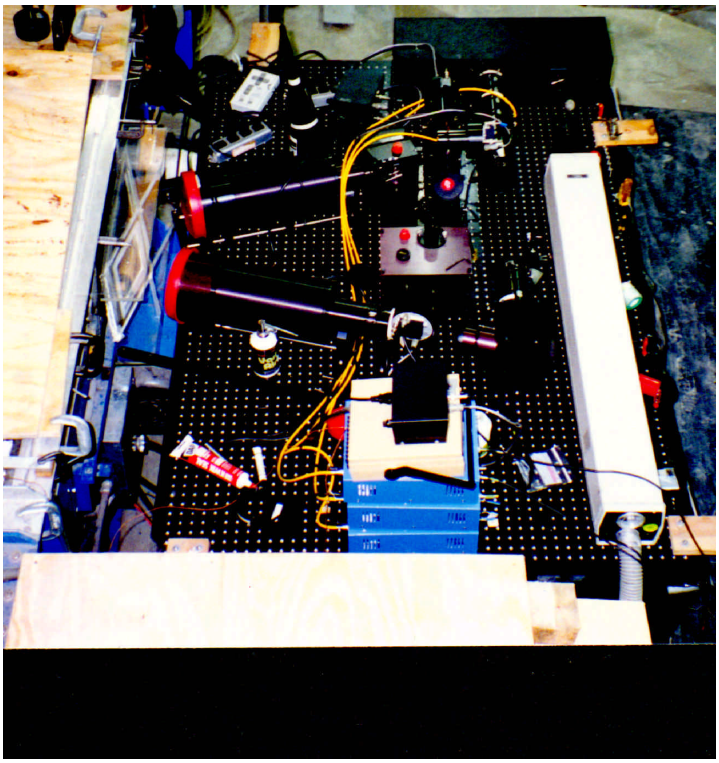

Figure 5. A top view of the L.D.V. system and the traverse table.

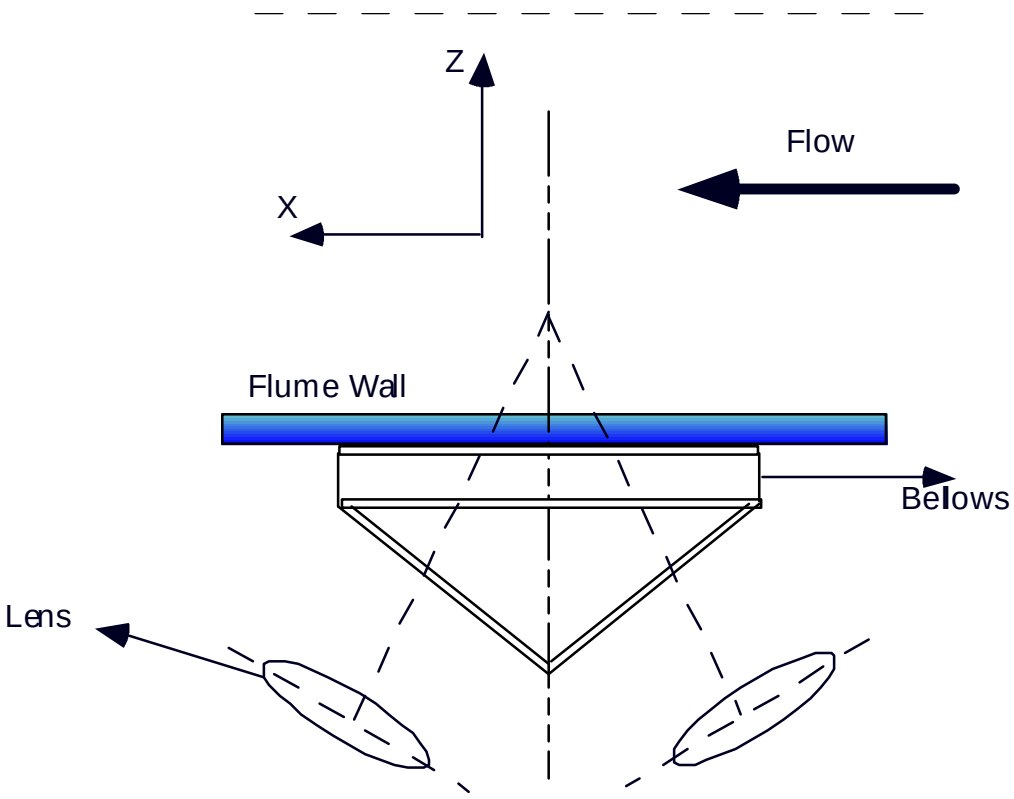

Figure 6. A view of the optical window

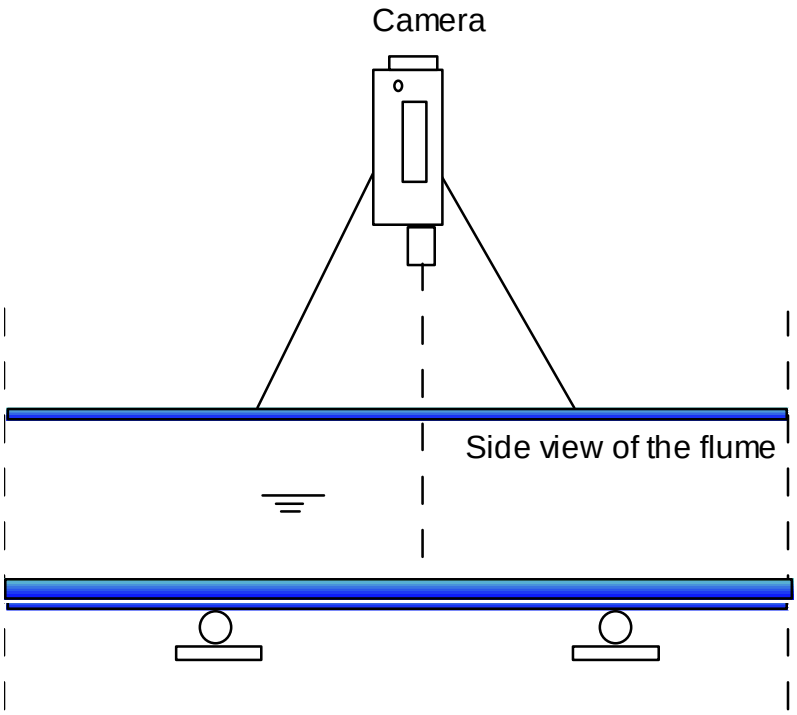

Figure 7. The filming process

Figure 8. The Panasonic video cassette recorder

Figure 9. The Sun Sparc 2 workstation

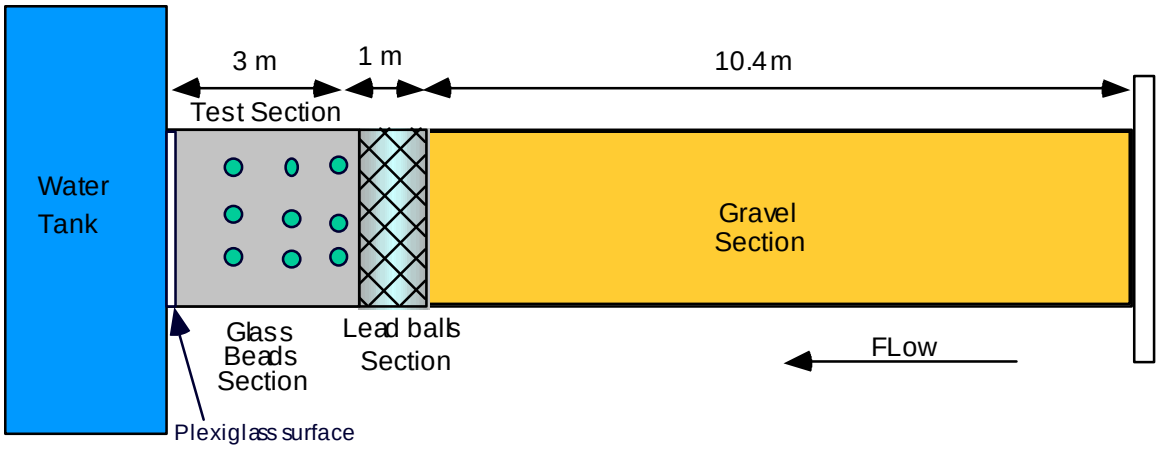

Top view of the differentsections of the flume

Figure 10. A sketch of the different sections of the flume.

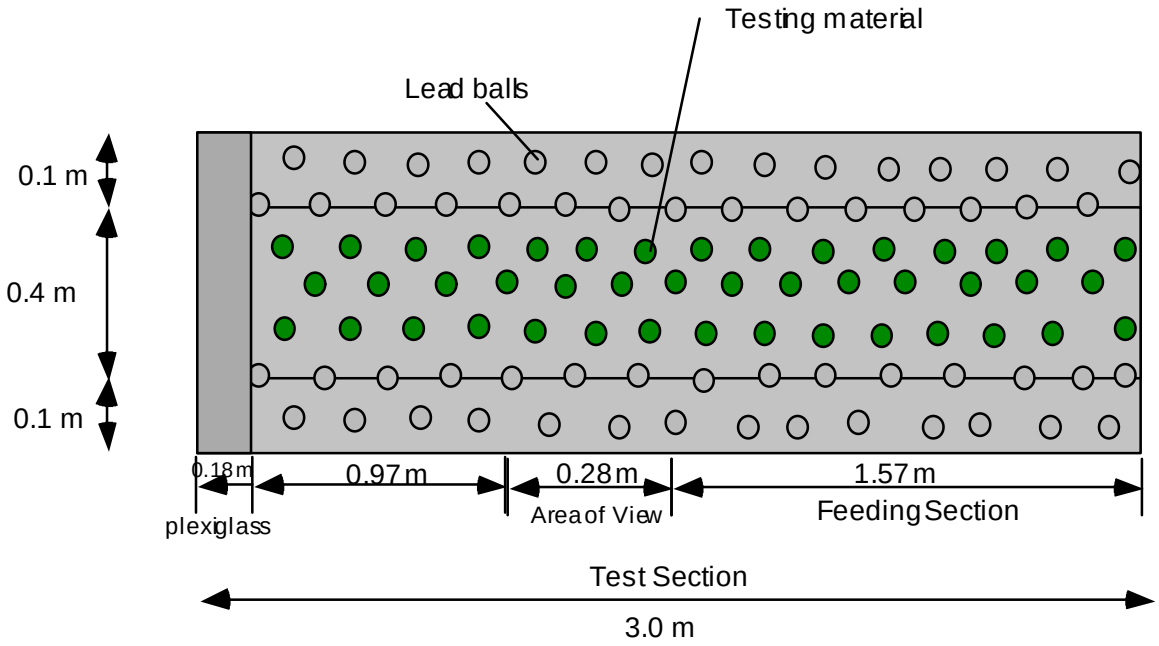

Figure 11. The test section.

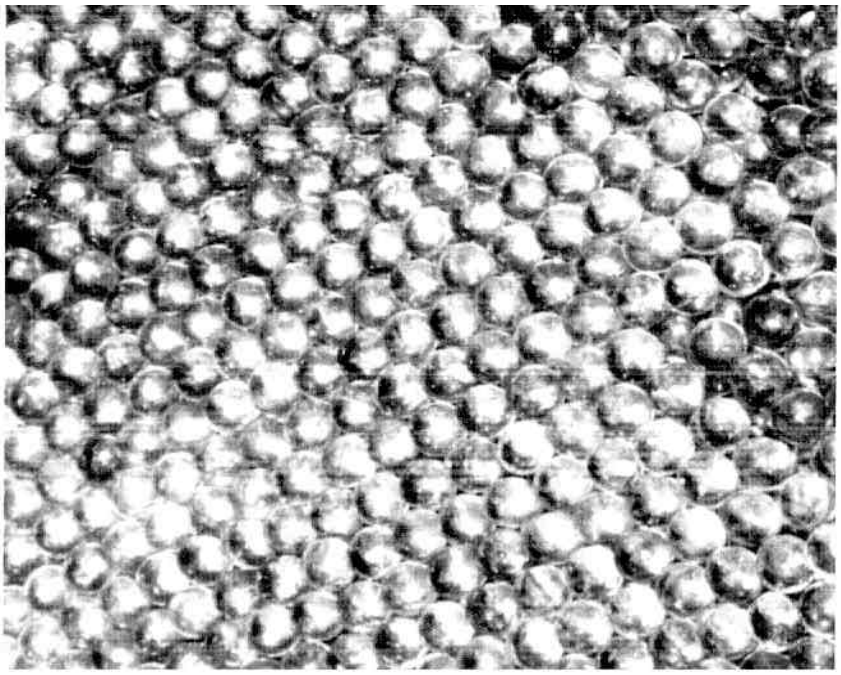

Figure 12. Top view of the tightly packed glass beads at the fourth layer of the flume.

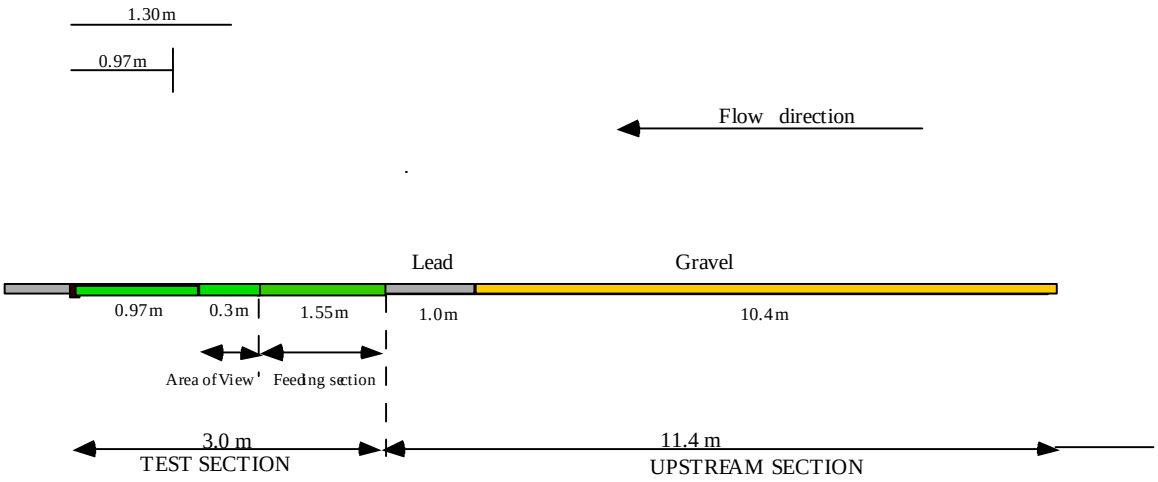

Figure 13. A summary of the several sections of the flume.

Figure 14(a). The 2% packing condition

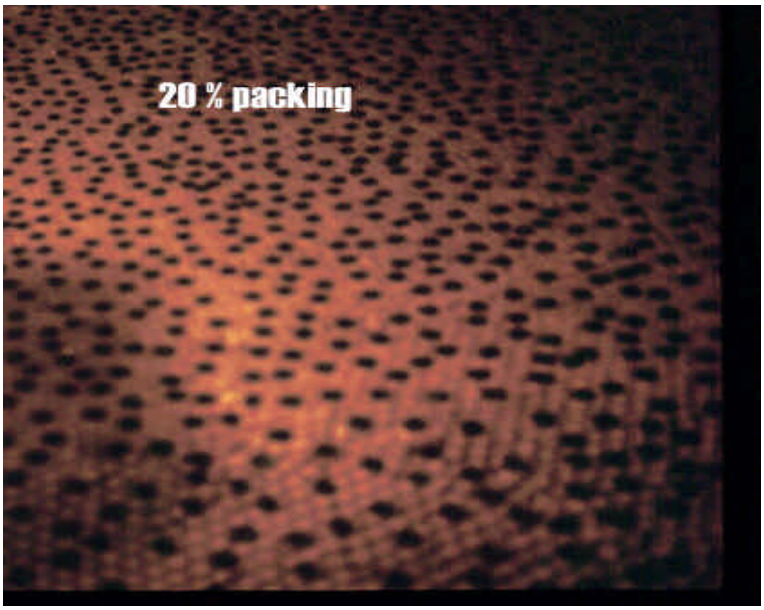

Figure 14(b). The 20% packing condition

Figure (14)c. The 35% packing condition.

Figure 14(d). The 50% packing condition

Figure 14(e). The 70% packing condition.

Chapter 3

Data Acquisition and Image Processing

The first part of this chapter refers to the steps involved in the analysis of the data obtained from the Laser Doppler Velocimetry (LDV) system. Specifically, in this part the procedure by which the information in the raw data files is converted to physical quantities at each measuring point is described. The second part demonstrates the importance of a "visual system" (a "visual system" is defined as the system that consists of a camcorder and a computer system where the movie digitization, processing and analysis take place) to the study of sediment motion and refers to the information that is obtained by its use. The development of the "visual system" has been one of the major elements of this work and therefore a detailed description of the hardware, software, and methodology is provided.

3.1. The LDV Data Acquisition Process.

The LDV data acquisition process is implemented here with the use of the commercial software package FIND (Flow Information Display Software). FIND has been developed by TSI to acquire data from the signal processors. FIND, which runs in DOS environment, allows the collection of data from three different counters (one for each measuring direction), saves the data into raw type of format, and shows real-time statistics associated with the measurements taken at the measurement point.

The program FIND here is used to calculate the frequency of the scattered light, f_d, from the silicon carbide particles (i.e. the seeding material) and the fringe spacing d_f. From the LDV theory when two beams are crossing, a set of fringes appears in the ellipsoidal probe that is formed. This set of fringes consists of alternating lighter and darker regions. A particle that crosses this region emits light of higher intensity when it encounters the lighter regions. The fringe spacing and the frequency of the scattered light are needed to compute the velocity of a particle in a direction normal to the fringes. The average velocity $u_n(t)$ of the n-th particle for the time interval during which the particle crossed a specified number of fringes within the measuring volume is given by the formula:

$$u_n(t) = f_{dn}\, d_f \qquad (2)$$

where, f_{dn} is measured in MHZ, d_f in μm, and $u_n(t)$ in (m/sec).

Because the measuring volume is very small, the time interval is very small and the velocity is treated as the instantaneous velocity of the particle. To compute the time average velocity and the turbulent quantities at one location a set of measurements is required at this location. The number of data points for every position in the cross-section is specified in the FIND program by the user (typically 3000 measurements are obtained at a point during our tests). The larger the number of data points, the smaller the statistical errors in the estimated mean velocities and turbulence quantities. The fringe spacing d_f is calculated with the following formula (Drain, 1980):

$$d_f = \frac{\lambda}{2\sin(\frac{\theta}{2})} \qquad (3)$$

where λ is the wavelength of the beams and θ is the angle that two coherent beams form with one another at their intersection point. For the three colors used by the present laser

system, λ is known. The procedure for estimating the beam angle was described in Chapter 2.

Finally, the frequency of the scattered light is obtained if the time t_n needed by a particle to cross a preselected number of fringes is known (in the present study, 8 fringes are used). This information is provided by FIND. Then, the average frequency is given by

$$f_{dn} = \frac{8}{t} \tag{4}$$

Based on the above equations, FIND calculates the velocity statistics for every measuring point with respect to the traverse table coordinate system. Namely, the mean velocities, standard deviations (i.e. the turbulent intensities), and the correlation between the fluctuating velocity components. Because the measurements are taken in three non-orthogonal directions, an initial transformation is required that will transform each individual measurement to the traverse table coordinate system. Finally the measurements of the turbulent quantities are transformed to the flume coordinate system. More details about the formulas and the transformation process used in this study can be found in Balakrishnan (1997).

3.2.The Role of Image Analysis in the Study of Sediment Transport.

The traditional approach of digitizing sequential pictures to obtain quantitative information of bedload transport is a time-consuming method even for fairly short periods of time. Nowadays, the advances that have been made in high resolution cameras and the development of hardware and software suitable for image analysis allow for a more sophisticated approach to the study of bedload processes in a stream or any other

complicated fluid flow problem. More specifically, state of the art computer vision techniques exist that process and analyze images in automated fashion. These techniques, which are known in the literature as image processing and analysis techniques, enhance the quality of the images but at the same time provide quantitative information regarding the geometrical characteristics of the objects that are depicted in the images. The need to use the image analysis methods in the study of incipient and bedload motion has been recently expressed by many researchers (e.g. Drake et al., 1988 and Browand and Plocher, 1985). Such methods can provide an objective and reliable approach for identifying the time and location of the movement of a sediment particle.

The effort that is placed in this study goes far beyond the image manipulation that is normally available in the scientific visualization field. The purpose of this work is to develop an imaging workspace to study the entrainment of the green glass beads that are located atop the flume bed. Specifically this workspace is chosen to be developed in the Khoros 1.0.5 image analysis environment and provides the entrainment rate of the particles within the area of view and the distance that the particles travel when they get entrained by the flow.

Khoros is an interactive visual tool and constitutes the backbone of the program that is developed here. The reasons for selecting Khoros as the image analysis package in this study are: 1) Its functionality is better than some other packages (e.g. HIPS, LaboImage, and Global Imaging Software); 2) Khoros' capabilities suit the needs of our research; 3) Khoros seems to have the highest number of built - in operations than any other imaging tool (e.g. AVS, Global Imaging); 4) Khoros is a public domain software package and therefore it can be downloaded free of charge from the network; and 5) there

is a support group in the Khoros community that provides most of the time free consulting. More information about Khoros and the workspace that is developed here are provided next.

The image work consists of four major steps: the digitization, the low-level image processing, the high-level image processing, and the image analysis (figure 15).

The purpose of the digitization process is to convert the movie to digital images. Subsequently, the digital images are imported to Khoros for their low-level processing. During this level of processing the images are converted from tiff type of format to visual (with the use of the "tiff2viff" subroutine). Their original size is reduced by extracting the regions that do not provide any useful information regarding the bed morphology (with the use of "vextract"). And finally, their calibration takes place to calculate the corresponding number of pixels per ball (with the use of "vcalibr").

The purpose of the high level image processing is to enhance the quality of the images in order to make easier the identification of the balls from Khoros during the image analysis. Initially the images are thresholded (by using the "vthresh") to isolate the entrained green particles from the image background. The filtering of the images is necessary to remove the "noise" (with the use of the "vqmed") that exists in their background.

The purpose of the image analysis, in this study, is to provide quantitative information regarding the sediment motion in sequential images. The number of particles present in the images is computed by means of 'vlabel" and "vshape" while the entrainment rate of particles and the distance that they travel are computed by taking the

absolute difference of two sequential frames. Each of these steps is analyzed below in detail.

3.2.1. Digitization Process

The primary role of the digitization process is to convert the movie, that is the outcome of the recording process during the experimental runs, to individual digital images. A digital image or digitized image is a spatial representation of an object in a computer (Haralick and Spapiro, 1991). It may be abstractly thought as a "mosaic" of small squares that are called pixels. Each pixel is represented in the computer as an integer.

During the digitization process the sampling and quantization of images takes place (Jain et al., 1995). The sampling refers to the number of pixels that are used per image to reproduce an isolated object in the image. The number of pixels assigned to the image is known as image resolution and depicts how well an object is represented in the image. The quantization refers to the brightness intensity of a pixel. Typically each pixel is represented as an unsigned 8-bit integer in the range (0 to 255), with 0 corresponding to black, 255 corresponding to white, and shades of gray distributed over the intermediate values.

The movie is captured by a frame grabber, which is installed in the Macintosh Quadra 900. For this purpose, the commercial program, Adobe premiere 4.0 is used. Prior to the launching of the program the settings on the Panasonic recorder are adjusted to enhance the quality of the capturing process of the movie. The settings on the Panasonic recorder are described in Appendix 1. At the Adobe premiere the image resolution is selected to be 640 x 480. The contrast level of the image is adjusted to

separate the green glass beads from the image background. The contrast level value here is chosen to be 40. This value is found, after some testing, to provide images with high quality contrast level. Because the digital images are color images the color reflectance of different objects in the image is examined. The quantities that determine how surfaces reflect color are the hue and saturation. Hue is determined by the dominant wavelength in the spectral distribution of light wavelengths. Spectral hues are the primary colors (red, green, and blue). Non spectral hues are mixtures of wavelengths. The hue quantity in Adobe premiere is by default 50. Saturation is the magnitude of the hue relative to the other wavelengths. The maximum saturation of an image occurs when its parameter becomes equal to 1 and the minimum when the saturation parameter is set equal to 100. In this study the saturation value is set to 100.

In the Adobe premiere interface three windows pop-up. The recording window, where the movie is played, the project window, where the movie clip is developed (the movie clip is essentially a video image and is defined here as video vision studio file), and the construction window, where the individual frames are obtained. These frames are files of Pict type of format and each of them typically occupies memory of 66 Kb. The steps that are followed during the digitization process are illustrated in Appendix 2.

The images should have the appropriate type of format in order to be imported to the image processing and analysis software. For this purpose the commercial program Debabilizer 1.5 is used. The Debabilizer allows the auto naming of the images to take place in a sequential manner, “remaps” the images, and saves them as Tiff color uncompressed files which typically occupy 330 Kb of memory. The byte order of the files should be of the Motorolla type (because this is the only type that Khoros accepts).

The procedure of using the Debabilizer software is given in Appendix 3. The images are transferred electronically via the FTP (file transfer protocol) site to the Sun-Sparc workstation for their further analysis.

3.2.2. Image Processing and Analysis Software.

3.2.2.1. Description of the Khoros 1.0.5 Package.

Khoros is a software environment for research, which uses visual programming as a tool for scientific visualization. The Khoros infrastructure consists of several layers of interacting subsystems. A user interface development system (UIDS) combines a high-level user interface specification with methods of software development and maintenance that are embedded in a code generation tool set. An inter-operable data exchange format (Visual Information File Format, VIFF) and algorithm library contain the application specific layer. The UIDS is used here to create three user interface styles: 1). A command line user interface, 2) A graphical form menu based user interface, and 3). The basic operations of a visual programming environment. The result is a visual programming environment. The current version of Khoros facilitates a library of over 260 routines that relate to image processing, signal processing, pattern recognition, machine vision, and geographic information systems.

Khoros is not an acronym. It is the Greek spelling of the word “chorous”. A combination of a “chorous” is “a company of singers or dancers who sing or dance in concert”. The name Khoros is symbolic of the objectives of this software. The “singers or dancers” are the interacting systems of Khoros; the objective is to provide a group of systems that will provide a harmonious environment for its many different kind of users.

These same themes are expressed in the definition: “a composition to be sung by a number of voices in concert”. For more information about Khoros there is a Web site at the network (the address is http://www.khoros.unm.edu).

The Khoros license is provided free via ftp from “ftp.khoros.unm.edu” in /pub/khoros. Khoral Research, Inc. (KRI) owns the Khoros copyrights and trademarks. The prerequisites for using the khoros software are the following: 1) the availability of the X windows system (X11R4) and the window manager ‘twm” or the “Open Win” windows manager in a Unix machine. In this study the “Open Win” manager is used; 2) a C language compiler, the “gcc” compiler, is used here; 3) a Fortran compiler , Fortran 97; and 4) About 128 Mb of hard-disk space.

The compilation process of Khoros for the Sun Sparc architecture requires about 5 to 6 hours to be completed. Before starting the compilation process the “imake” files in the Khoros directory are modified to meet the requirements of the machine architecture (different workstations have different architectures). Once the “imake” configuration files have been modified, the compilation process of Khoros is ready to start. The compilation process is automated by using the program “installit”. Khoros provides a frequent asked Questions (FAQ) file regarding the problems that are encountered during the compilation process. More information regarding the Khoros installation is provided in Chapter 1 of the Khoros users manual. The configuration of the system follows right after its installation. During the configuration the following issues are addressed: 1) the Khoros environment variables are defined. This is done here by modifying the “Khoros_env” file that is provided with the Khoros package; and 2) the path is set to include the Khoros binaries. This is done by sourcing the “cshrc” file.

Khoros consists of two types of programs, the “vroutines” and the “xvroutines”. An “xvroutine” is an application, which has its own graphical user interface and has to link at least with one of the shared libraries of the X windows program. A “vroutine” does not have its own interface. It can be opened only through its inclusion into a graphical user interface. In this study both types of programs are used. The graphical user interface in Khoros is provided by the visual programming language, “cantata” (figure 16).

To create a visual program using “cantata”, you begin with a blank cantata workspace. Selecting the desired Khoros routines to perform various tasks, you then create icon representations of the Khoros routines called “glyphs” (figure 16). Next, you connect the “glyphs” together with lines to go from one glyph’s output arrow to another glyph’s input arrow. This is the equivalent of running the program from the command line. A complete cantata workspace is a visual program made up of glyphs representing Khoros programs, with lines representing the flow of data between routines. The entire program can be run using a “Run” button located on the cantata form, or the program may be run step by step by clicking on the little “on/off” switches that appear at the upper left hand corner of each glyph representing an executable khoros program (figure 16). At any time, a cantata workspace may be saved as an “ascii” file and then be restored for any future use.

3.2.2.2. The Khoros Workspace

The purpose of developing the Khoros workspace that is shown in figure 16, is to quantitatively describe the motion of sediment (i.e. green glass beads) atop the flume bed.

Specifically, the rate at which sediment is entrained and the distance that the particles travel are computed. The Khoros workspace, “probability”, consists of three parts, namely, the low level image processing, the high level image processing, and the image analysis.

The low level image processing part is performed here by using the “tiff2viff”, the “vextract”, and the “vcalibr” subroutines. The “tiff2viff” does not support tiff images that contain more than 8 bit per sample and provides viff images with 3 data bands (one for red, one for green, and one for blue). The “vextract” routine allows a coordinate input image to specify the region to extract. The output image is of the same data type as the input image. The dimensions of the extracted images are 520 x 330 and thus occupy less memory in the computer system (the original images have dimensions 640 x 480). At the same time, they require less computational time during their analysis. The “vcalibr” computes the number of pixels that correspond per unit length of the test section. For the calibration of the system, a grid with fixed dimensions is placed in front of the camera. The grid defines the real world coordinate system in which the calibrated measurements are reported. From the “calibr” routine is found that the diameter of glass beads, d = 0.008 m, corresponds to 14 pixels. This number of pixels allows accurate determination of the center of the balls. The minimum number of pixels that is necessary for the recognition of a ball is about 9 pixels.

The role of the high level image processing is to convert the viff images to binary images, to remove the background noise, if any, from the binary images, to label the objects in the images and compute the number of glass beads that are present in the image.

The routine “vthresh” in the Khoros workspace is used to obtain the binary images. The binary images contain only two gray levels of intensity. Typically object pixels have the value of 1 and background pixels have the value of 0. Thus, in binary images, the background is white and the objects are black (figure 17). The separation of the objects form their background is achieved here by performing thresholding. For the thresholding process to be effective, it is necessary that the objects and background have sufficient contrast and that we know the intensity levels of either the objects or the background. In this study the intensity level of the green glass beads is 135. This value is found by trial and error and is a function of the illumination and the reflectance characteristics of the green glass beads.

The next step after thresholding is to remove the noise that exists at the background of the image. For this reason the subroutine “vqmed” is used. The “vqmed” computes in this study a two dimensional median filter of width 7 pixels and height 7 over the given image. The median is computed by moving a mask with dimensions 7 by 7 pixels over the image and sorting the masked values. The dimensions of the mask in pixels can vary from 1 to 9. By increasing the dimensions of the mask more noise is removed from the background of the image; however, the computational time that is required to “clean” the image increases. In this study the size of the mask is chosen to be 7 by 7 pixels (which is relatively high) to minimize the error that is involved in the identification of balls. The reason for using median filters instead of linear filters (e.g. convolution mask) is that the later tend to blur sharp discontinuities in intensity values in an image (Economicos et al., 1990). The median filter approach replaces each pixel value with the median of the gray values in the local neighborhood. Finally, median

filters are very effective in removing “salt and pepper” and impulse noise while retaining image details (compare figures 17 and 18). The “salt and pepper” noise is caused by uneven illumination and the reflectance of the light on the surface of the water, and is typically a low frequency noise. The impulse noise is a high frequency noise and is principally caused during the digitization process. The “striped” effect that is shown in figures 17 and 18 is caused by “beating” between the illumination and the digitization rate of the video studio during the digitization process (Perkins and Hunt, 1989).

To accurately find the edge placement of the balls in the images, higher sensitivity techniques may need to be used in the high level image processing stage. These techniques can be region splitting or merging and they are used to differentiate or combine regions respectively. Region merging is used to join together neighbored regions of the same pixel intensity while region splitting to break apart regions that should be multiple objects (Advanced Imaging, 1995). A component labeling algorithm in the Khoros workspace, “vlabel”, finds all connected components in an image and assigns a unique label to all points in the same component. The algorithm that is used here is a sequential algorithm (Jain et al., 1995). It uses the fourth connectivity scheme to label the pixels in the image. Specifically it looks at only four of a pixel eight neighbors, the ones above and to the left of it, and assigns the same labels to them if they have the same pixel intensity. During the labeling process the distance between two pixels is computed based on the Euclidean distance function. The effectiveness of the labeling process depends on the values of two parameters, namely, the “merge and split factor” and the “minimum size region”. The default value of the “merge and split factor” is 0.07. This value allows “vlabel” to pick up many objects in the image that are harder to

see. However, in our case the green balls have a fixed pixel intensity (135) and therefore can be easily distinguished from the background of the image. This factor here is chosen to be 0.5 to reduce the number of iterations that is required from the program to label the pixels of an image. The "minimum region factor" indicates the percentage of pixels that the balls occupy in the image. The "minimum region factor" is given by the product: 100 x 14^2 /(480 x 640)= 0.063 % (14^2 pixels are assigned to each ball). Typically the minimum region factor is chosen to be (1/2) or (1/3) of the above value because some balls come out from the filtering process with smaller size than the original. The "minimum region factor" is equal here to 1/3 (0.063) ≅ 0.02.

The image analysis part consists of two subroutines: the "vshape" and the "vabsdiff". The role of the vshape is to compute the centroid of the particles in pixels coordinates with respect to the image coordinate system. The origin of the digital orthogonal system of a Khoros image is located at its upper left corner. The coordinates of the origin are (-1,-1). This origin is chosen to coincide with the origin of the geometric coordinate system in the area of view. A simple transformation relation is then used to convert the pixel coordinates of the particles to geometrical coordinates.

The purpose of the "vabsdiff" routine is to determine changes in the particles' location in two successive frames of a sequence. It computes the absolute difference of the two images by comparing the corresponding pixels of the two frames. Specifically, two binary images $F_i(x,y)$ and $F_j(x,y)$ are used as the input files in the "vabsdiff" glyph. The "difference picture" $Df_{ij}(x,y)$ is a binary image and is described as follows:

$$Df_{ij}(x,y) = 1, \text{ if } \quad |F_i(x,y)-F_j(x,y)| > \sigma \qquad (5)$$

$$Df_{ij}(x,y) = 0, \text{ otherwise.}$$

Where, σ is the threshold pixel intensity value and is equal here to 135. In the difference image, pixels that have the value of 1 are considered to be the result of object motion. The idea of using the absolute difference of two sequential images to detect the motion of objects constitutes the most widely used method in dynamic visual image analysis. Figure 19 illustrates the image that is obtained by taking the difference of two sequential images. From this figure the number of balls that are entrained by the flow during a time period is shown to be four (Four couples of black circles are shown in figure 19. These circles depict the original and final location of the balls). Finally the routine "vabsdiff" provides the travelling distance of the balls in the area of view.

The analysis of a significant number of frames in this study suggests that the error rate in locating particles is less than 5 %. Also it takes about 1 minute to digitize an image, 10 seconds to perform its thresholding, 1.5 minutes to filter the image, 20 seconds to identify the particles and their coordinates and about 30 seconds to compute the absolute difference of two sequential images. The total time that is approximately required for the digitization, image processing, and analysis of a frame is 3.1 min.

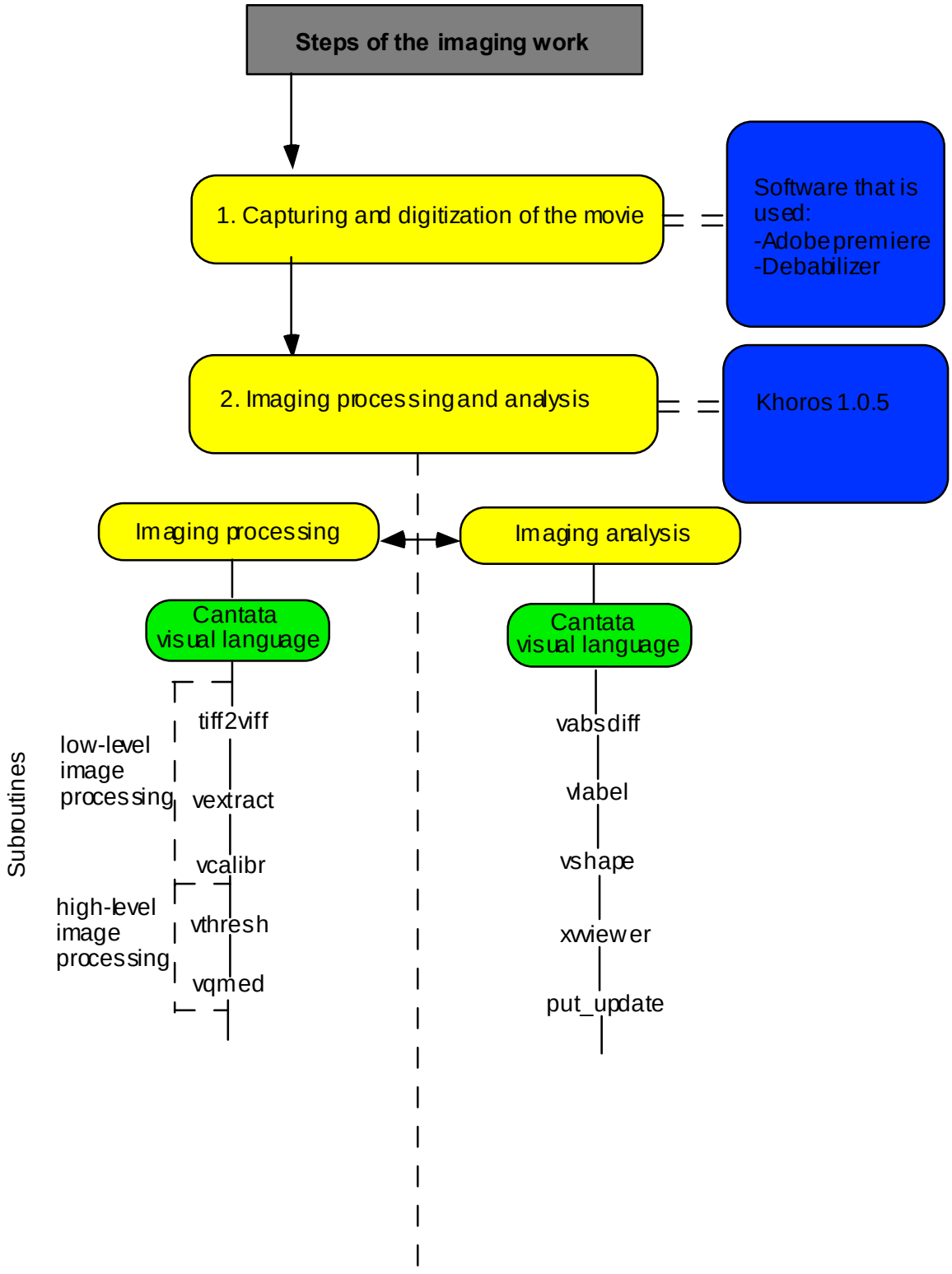

Figure 15. The steps of the image processing and analysis.

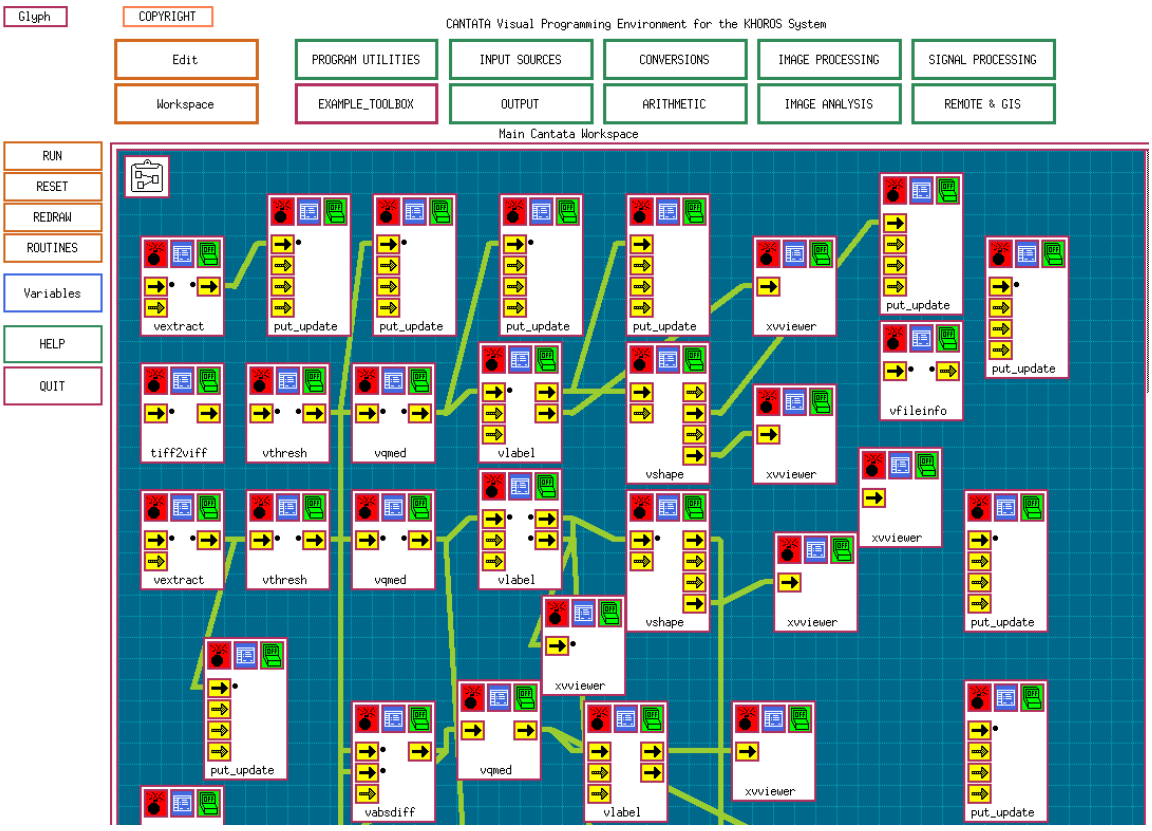

Figure 16. The “probability” workspace.

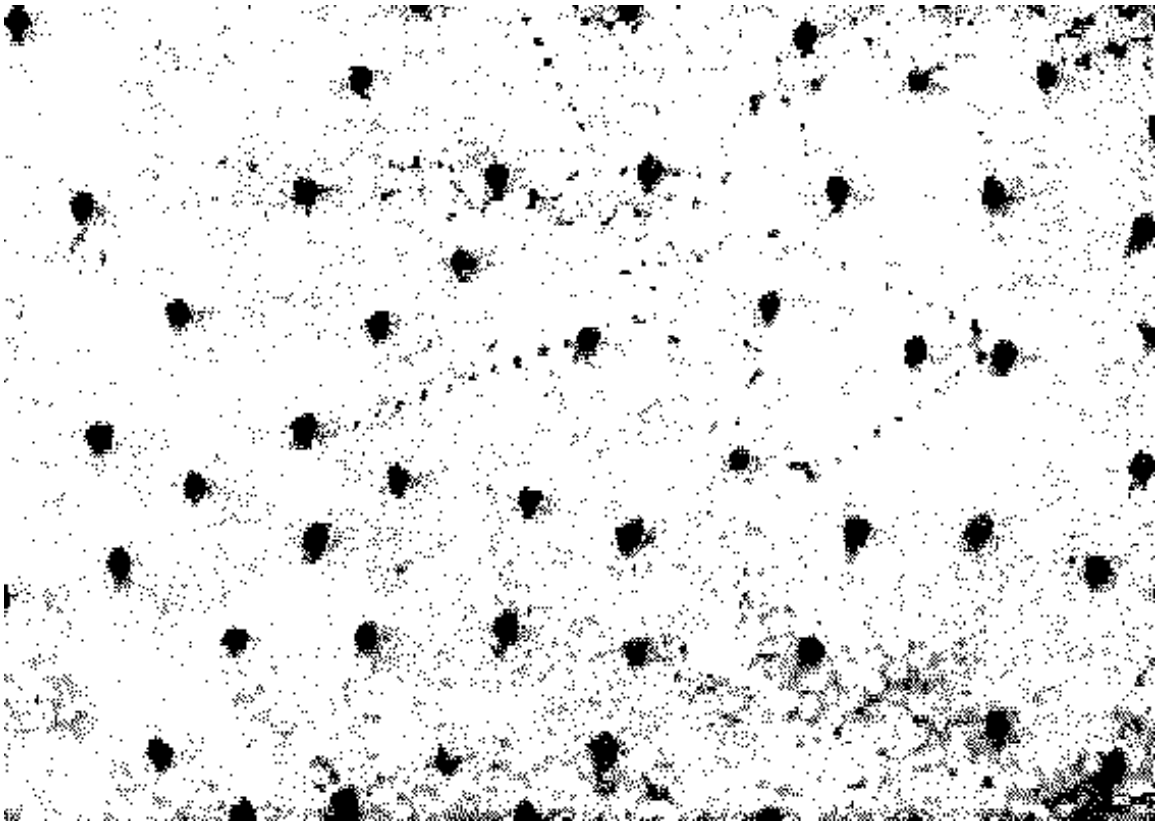

Figure 17. The image after the thresholding process takes place.

Figure 18. The image after the filtering process.

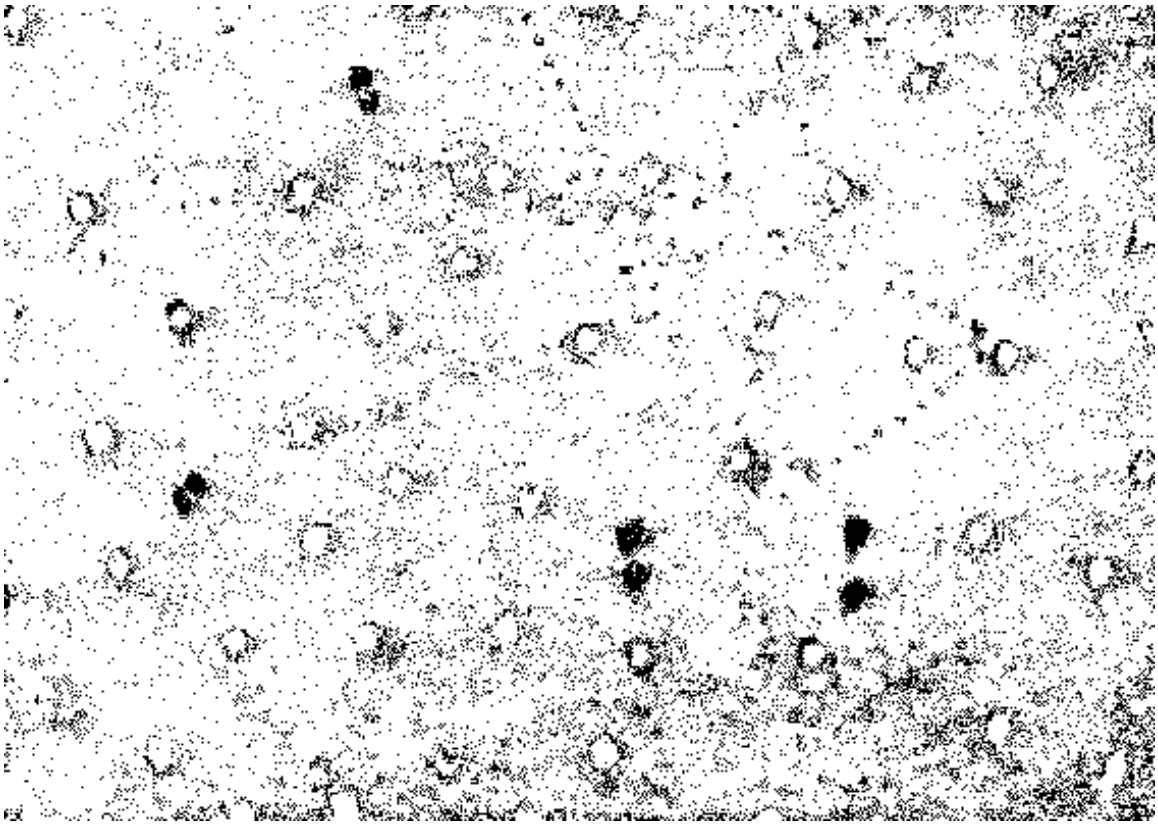

Figure 19. An image that is obtained from the subtraction of two sequential images.

Chapter 4

Incipient Motion Conditions-Methodology

4.1. Introduction

The incipient conditions of sediment motion are typically determined by measuring the rate of particles that cross a line over a period of time. Subsequently, critical conditions are reached when the flux of particles crossing a line approaches to zero (e.g. Shields, 1936; Paintal, 1971). The observations made by Kramer (1935), Vanoni (1964), Fenton and Abbott (1977), and others, during the performance of different incipient motion tests, indicate that in some cases the number of particles that is collected (in a sediment trap) is relatively small, however, the motion of particles over an area is rather significant and occurs sporadically at different spots of the bed. Thus, critical conditions that are based on crossing a line criteria tend to be less rigorous.

Learning from these observations, a different method is proposed here to define the incipient motion conditions of the green glass beads for the five different packing conditions that are examined in this study. According to this method, a more rigorous criterion to determine the threshold of motion will be the one that accounts for the "first displacement" of particles over an area than the number of balls crossing a line. The term "first displacement" of particles is defined by Fenton and Abbott (1977) as the particles' dislodgment from their original position. The "first displacement" of particles is detected here by using the image analysis workspace "probability" for the five packing condition tests.

Because the availability of particles in the test area varies for each packing condition test (see table 1), it is more appropriate here to calculate the fraction of the displaced particles in the test area than their number. This approach is independent of the availability of particles in the test section, since it refers to the fraction of sediment that is entrained by the flow than the number of particles.

Thus, if N_T denotes the total number of particles that are initially placed in the test area, for a certain packing condition, and N_E denotes the number of particles that are entrained within a period Δt_j the fraction of the displaced particles is equal to the ratio $\frac{N_E}{N_T}$. The frequency, f_j, with which the fraction of sediment $\frac{N_E}{N_T}$ is displaced within the area of view is equal to,

$$f_j = \frac{N_E}{N_T}\frac{1}{\Delta t_j} \tag{6a}$$

For k subsequent periods Δt_j of observations the average frequency of entrainment f_a is given by,

$$f_a = \frac{\sum_{j=1}^{k} f_j}{k} \tag{6b}$$

It is suggested here that the metastable bursting cycle (i.e., sweeps, ejections, outward, and inward interactions) is the mechanism responsible for the commencement of the sediment motion and its sporadic nature. Therefore, the frequency of the occurrence of the bursting events affects the rate of displacement of sediment particles. During a bursting period T_B the probability that a particle is displaced within the area of view is equal to P_E. P_E is computed as the product of the average frequency of the

sediment entrainment, f_a, (that is given in equation 6(b)) with the mean bursting period, T_B, viz.

$$P_E = f_a T_B \qquad (7)$$

The mean period of bursts is typically defined as (Cantwell, 1981),

$$T_B = 6 (H/\mathbf{U}) \qquad (8)$$

where, H is the flow depth and **U** is the depth average flow velocity.

Entrainment of sediment particles is governed by flow and particle characteristics. In the tests that are proposed in this study (see table 1), spheres of the same weight are used to isolate the role of turbulence on the initiation of sediment motion. Although spherical grains are not very common in natural streams, the well-controlled experiments of this study lead to the determination of the hydraulic conditions necessary to entrain the spherical particles in a known geometric packing configuration. The concept behind the determination of the critical hydraulic conditions for the different packing condition tests is that the probability of the entrained sediment, P_E, should be the same when incipient motion conditions are reached for the different packing configurations. The experiments that are conducted provide useful information regarding the clustering process and its role on the sediment entrainment problem.

The methodology that is followed to determine the critical hydraulic conditions for the different surface packing arrangements is illustrated here. The effects of the different

packing arrangements on the magnitude of the turbulent stress components are studied in Chapter 6. Chapter 6 also focuses on the role of turbulence on the initiation of sediment motion.

4.2. Determination of the Critical Flow Depth

The idea behind the determination of the critical hydraulic conditions is that the probability of particles' displacement P_E must be the same for the different surface packing configurations. The steps that are involved in the calculation of the probability P_E are the following:

1. The 2% packing condition is considered as the benchmark experiment for the computation of the probability P_E. The main reason for this choice is that the 2% condition closely represents the case of an isolated ball that resting on the top of a layer of similar balls and is fully exposed to the flow. This case has been extensively studied by several researchers (e.g. Coleman, 1966; Fenton and Abbot, 1972; Wiberg and Smith 1985; Ling, 1995) and therefore, data are available for comparison with the results that are obtained here.
2. For the 2% case, several preliminary tests are performed, for a fixed flume slope, to find the lowest bound of the critical flow depth. Initially, the depth H is chosen arbitrarily to be equal to 4 cm because no significant displacement of sediment is observed for this depth. The depth is increased gradually, up to 5.8 cm, to observe the rate of the sediment entrainment for different flow conditions (specifically, the depth obtains the values of 5, 5.3, and 5.8 cm). The entrainment of sediment in the 5cm and 5.3cm cases is infrequent and sporadic while, in the 5.8 cm case an

appreciable amount of sediment movement occurs. The 5 cm depth is chosen to be the critical depth for the 2% packing condition for the following reasons: a. It presents the lowest entrainment rate than the other cases ; b. The ratio H/d is greater than 3 (d is the particles diameter), thus the critical stress value is independent of H/d (Bettess, 1984); c. It is greater than the minimum depth (3.8 cm) that is required by the LDV system for conducting flow measurements in the 2% packing condition. The laser beams may cross first the water surface and be reflected if the depth is less than 3.8 cm.

3. The movie that is obtained for the 5 cm depth case is digitized to obtain digital images. The obtained images are imported to Khoros 1.0.5 for their image processing and analysis. The steps that are involved in the above processes are described in detail in Chapter 4. The calculation of the frequency of particle's displacement f is possible here with the use of the Khoros workspace “probability," that is described in section 4.2.2.2. The “Probability” program, by means of the subroutine “vabsdiff”, determines the particle's location in the images and provides accurately the changes in the bed morphology of the test section with an error of less than 5%. Khoros has the capability to detect relatively small particles' motions (e.g., motions that are of the order of one particles diameter) which are typically hard to detect by eye. Specifically, when the subroutine “vabsdiff” is used, a time step is chosen to find the absolute difference of two images that are obtained at the beginning and at the end of the time step. During the analysis we make sure that: a. Within the chosen time step, a ball does not experience a second movement. For this purpose, the movie is reviewed several times to ensure that the balls do not get entrained more than once

within this step. The time step of the image analysis is not the same for the different bed configurations that are examined here; and b. The number of particles that enter or exit the test section is not considered in the calculations of the frequency. Only the particles' displacements that occur within the test section are counted.

In the 2% case, subsequent images taken from the movie at one-minute intervals are compared with each other. Figure 20 illustrates several pictures that are obtained from the subtraction of two subsequent images during different time periods for the 2% packing condition. During the first time step, 4 balls out of 52 are displaced from their initial position. The black balls in figure 20(a) show the balls that are entrained by the flow, at their original and final location. Similarly, figures 20(b), (c), and (d) show respectively that 3 out of 51 balls are entrained during the 10^{th} time step, 0 balls out of 48 within the 15^{th} time step, and 0 balls out of 49 during the 20^{th} time period. The frequency of entrainment for different periods in the 2% case is illustrated in table 2 while table 3 shows the average frequency of sediment entrainment, the average depth velocity, and the mean bursting period. The probability of entrainment P_E that is shown in table 3 is computed by means of equation (7).

4. A trial and error method for computing the critical hydraulic conditions for the remaining surface packing configurations is performed next. Specifically, for each surface packing condition, several preliminary tests are conducted to obtain probability values of entrainmnent that are close to the one computed for the 2% case. The Khoros workspace "probability" is used to compute the probability P_E.

Figure 21 illustrates the pictures that are obtained from the subtraction of sequential images at the fifth time period in the 20% packing condition. The time step that is chosen

in the image analysis is equal to 1 minute because no second displacement of particles occurs within this period. Table 4 illustrates the frequency of entrainment for all the time steps that are included in the 20% analysis and table 3 provides the average frequency of entrainment, the average depth velocity, and the mean bursting period for this test.

In both 2% and 20% packing conditions the frequency of the particles entrainment is calculated for the first 20 minutes of the tests (the total testing period is 30 minutes) because the availability of particles does not alter significantly as the test progresses. The critical depth value for the 20% is shown in table 3.

Figure 22 shows the absolute difference of two sequential images that are obtained for the second time period in the 35% packing test. The time step in the image analysis process is 0.5 minutes to ensure that a ball does not move twice during this period. The image analysis is performed here only for the first eight minutes of the test (i.e. the total duration of the test is 30 minutes). The reason is that after the 8^{th} minute the bed configuration differs significantly from the initial bed setting due to the formation of clusters. Table 5 provides the frequency f_j for the eight minutes of the analysis while table 3 illustrates the average frequency of entrainment, the depth average velocity, the mean bursting period and the critical depth for this test.

Finally, figure 23 illustrates the image for the 50% case for the second time step. In this case only the first three minutes of the movie are analyzed. The reason is that the clustering process, which occurs after the third minute, alters significantly the initial bed morphology. The average number of balls found in the area during the first 3 minutes is 1,035 while it was reduced to 837 for the last 17 minutes. Table 6 includes the frequency

of entrainment for the first six time steps while table 3 shows the average frequency of entrainment, depth average velocity, mean bursting period and the critical depth. The use of Khoros program to determine the critical hydraulic conditions for the 70% packing is not possible. The surface waves that are observed in this case do not allow the program to identify the particles in the images. In this case the conditions are determined by counting the number of particles that are displaced from the tightly packed layer at the end of a run. For this purpose, ten runs with one-minute duration are performed. The results of this experiment are summarized in table 3.

4.3 Analysis of the Tests

Table 7 summarizes the hydraulic parameters for the packing conditions that are examined here. Specifically, in this investigation the slope of the flume varies between $0.2<S[\%]<1.2$. The slope of the flume is adjusted to attain critical water depth values within the range of $0.05<H[m]<0.076$. This is important in this study to ensure that two dimensional conditions exist during the tests (i.e., here the ratio B/H is greater than 5, where B is the width of the flume and is equal to 0.6096 m); and that the critical stress is independent of the H/d ratio (i.e., H/d is greater than 3, where d is the particle diameter and is equal to 0.008 m). The depth velocity **U** varies within the range of $0.4<\mathbf{U}(m/s)<1.19$; and the discharge Q is calculated from an air/water manometer calibration equation,

$$Q = 0.00306\sqrt{\Delta h} \qquad (9)$$

where, Δh is the differential pressure in cm. The discharge varies within the range of $0.0122<Q[m^3/s]<0.054$. The friction velocity u_* is computed from the hydraulic relation for uniform flows,

$$u_* = \sqrt{gHS} \tag{10}$$

where, g is the gravitational acceleration. The range of the friction velocity is $0.03131< u_*(m/s)<0.093$. The expression for the dimensionless critical stress τ^* is given by,

$$t* = \frac{t}{(r_s - r)gd} \tag{11}$$

where, $\tau=\rho gHS$, ρ is the density of the water (1000 Kg/m^3), and ρ_s is the density of solids (2540 Kg/m^3). The dimensionless critical stress obtains values in the interval [0.008,0.074]. The values of the Reynolds number $Re = \frac{4HU}{n}$ that are shown on table 7 ensure the existence of turbulent flow conditions. For the first 3 packing conditions tests subcritical flow conditions exist since the Fr number is less than 1. Near critical flow conditions exist in the 50 % case and supercritical at the 70% test. Finally, the bed load transport Q_b varies within the range of $2.52\ 10^{-6}<Q_b[kg/m/s]<9.46\ 10^{-4}$. Next the role of the clustering process on the entrainment problem is illustrated for the different bed packing configurations.

a. The 2% packing condition.

Initially the balls are distributed uniformly atop the bed of the test area (the green balls in figure (24a)). The average distance of the balls is about six ball diameters. Within the first twenty minutes of the experiment no clustering occurs. Instead, this

testing period is characterized from a sporadic motion of particles; more specifically, the particles move along a straight line in the longitudinal direction of the flume bed. Steidtman (1984) has reported similar observations regarding the pathlines of the particles in motion. The histogram in figure 25 provides the traveling distance in the streamwise direction of the balls during the 2% run. This information is obtained from the image analysis package for the first twenty minutes of the testing period. The majority of the balls cover a distance of one ball diameter (figure 25). Their average traveling distance is equal to 1.5 of a ball diameter and their maximum distance is equal to 4 balls diameter. The average traveling period of the displaced particles is almost 0.622 s and their displacement speed is 0.02 m/s. During the last five minutes of the run some of the entrained balls tend to group together (figures 24 (e)). Very few clusters are formed that typically consist of two balls. The spheres in these clusters are positioned in line in the direction of the flow. This remark is consistent with the observations of Brayshaw et al. (1983) that were made on hemispheres positioned in line.

b. The 20% packing condition.

The distance of the balls from their neighboring particles at the beginning of the 20% case is approximately two balls diameter (figure 26(a)). The bed configuration of the test section does not change significantly during the first twenty minutes of the experiment (figures 26(a)-(c)). The motion of particles during this period is sporadic and eventually leads to the formation of clusters that consist of three balls each. Some of these structures are very stable and remain unchangeable as the test progresses.

The view of the test section changes at the twenty-fifth minute. Figure (26 (d)) illustrates different types of particles' groupings. Few particles are positioned in line parallel to the flow direction, while most of the particles become part of clusters with four or more spheres. It is also observed that several of the balls that are entrained by the flow tend to find protection at the perimeter of the existing clusters. It is viewed that the particles that are in-groups of two or three are more susceptible to entrainment than in-groups of four balls. The most stable clusters consist of four particles and have a rhomboid shape (figure 26 (d)). Similar remarks have been made by Reid and Frostick (1987). Figure (27) illustrates the histogram with the particle distance for the first twenty minutes of the test. The average traveling distance of the balls in the streamwise direction is 1.9 of a ball diameter and the maximum distance is 4.5 balls diameter. The average traveling period of the displaced particles is almost 0.958 s and their displacement speed is 0.016 m/s.

c. The 35% packing condition.

In the 35% packing condition, it is practically impossible to avoid some initial clustering of the balls prior to the commencement of the run due to the wake interference that exists among the particles. Thus, in the process of reaching the critical hydraulic conditions the particles tend to approach their neighboring particles and in some cases to group with them. Initially, when the balls are distributed in the test section their average distance from the surrounding particles is almost 1.2 of a ball diameter. This distance varies as the test progresses (Figure 28(a)). During the first five minutes of the testing period a frequent displacement of particles is noted. The particles tend to find their way

among other particles by moving longitudinally and transversely to the flow. The average distance of the balls in the longitudinal direction is 2.17 of a ball diameter and the maximum distance that a ball travels in this direction is equal to 6 balls diameter. In the spanwise direction the maximum distance that a ball travels is 3.5 ball diameters. The average traveling period of the displaced particles is almost 0.78 s and their displacement speed is 0.022 m/s (figure 29).

At the end of the fifth minute clusters that consist of at least 20 balls are formed (figure 28(b)). Most of these microforms are connected with each other throughout the test section. The formation of the cluster microforms inhibits the entrainment of sediment during the remaining period of the test and yields more stable bed conditions (figures 28(c), and (d)). In this case entrainment of sediment occurs only when a particle that belongs to a cluster gets displaced. This results to the break-up of the cluster microforms and to their continuous rearrangement with time. At the 20^{th} minute two parallel stripes of clusters are formed in the area of view (figure 28(e)).

d. The 50% packing condition.

The initial distance of the balls in the 50% case is less than a ball diameter (figure 30(a)). The average distance that is traveled by the entrained balls in the longitudinal direction is 2.5 ball diameters, while their maximum traveling distance is 10 ball diameters (figure 31). At the beginning of the third minute clusters with size of about 30 balls are formed. Similar conditions exist at the 5^{th} minute of the test (figure 30(b)). During the remaining testing period the entrainment of sediment is rather infrequent, however, when it occurs an appreciable amount of sediment gets displaced. For example

at the 15th minute ten balls are entrained simultaneously by the flow from the perimeter of a cluster (figure 30(c)). The transported particles tend to override the particles that are found in different cluster microforms or they move transversely to the flow. The maximum distance of the balls in the transverse direction is 3.6 of the ball diameter. Similar behavior in sediment entrainment is observed throughout the test. The massive displacement of particles results in the disintegration of the clusters that are initially shown in figure 30(d) and changes drastically the bed morphology at the end of the testing period (figure 30(e)). The average traveling period of the displaced particles is almost 0.692 s and their displacement speed is 0.028 m/s.

e. The 70% packing condition.

The balls are tightly packed in the 70% packing condition. Specifically in this case, 70% of the test section is covered with green glass beads while the remaining 30% represents the porosity that exists among the particles. Figure 32(a) illustrates a top view of the test area prior to the commencement of the test. The surface waves that are generated in this run due to the extreme flow conditions (see figures 32(b) and (c)) do not allow the use of the Khoros software to determine the frequency of the sediment entrainment. For this purpose ten different experimental runs with duration of 1 minute are performed to determine the critical flow conditions. At the end of each run the number of particles that are dislodged from their pocket is counted. The average frequency of entrainment is computed here as the ratio of the number of particles that are dislodged from the test area with the total number of particles placed in the test section over a period of 1 minute. During the test most of the entrained material reaches the

basket at the downstream end of the flume. Very few balls get trapped at the empty pockets that exist at different locations of the bed. Also, it is observed that when the balls get entrained, they tend to loose their contact with the bed. Ling et al. (1992) reported a similar behavior in particles' transport for a particle Reynolds number greater than 500.

4.4. Summary

In this chapter a new criterion of defining the critical hydraulic conditions for different surface packing conditions is introduced. This criterion requires the calculation of the probability of the entrainment of a particle P_E within a bursting period. The probability P_E must be the same for all the packing configurations when the critical conditions are reached. Also, it is shown that the critical stress value is remarkably different for a ball that is fully exposed to the flow compared to a tightly packed arrangement (table 7).

The image analysis program that is developed here, plays a significant role throughout the process of determining the critical conditions since it allows the computation of the frequency of sediment entrainment, the traveling distance of the entrained material, and its displacement speed. During the runs the formation of clusters is observed. Different cluster configurations are present at the test section. It is shown that clustering inhibits entrainment and has a significant effect on bedload motion. Thus, although the rate of displacement of particles is significant the number of particles crossing a line is comparatively small. The most stable clustering structures are the ones that follow a rhombohedral pattern. It is observed that as the packing density increases

the size of clusters increases too. In the following chapter it will be demonstrated why the criterion that accounts for the first displacement of balls is more rigorous than other criteria that focus on the number of particles crossing a line.

Table 2. Frequency of the sediment entrainment in the 2% packing condition (E-2 test).

ΔT(min)	Fraction of balls displaced	F 10^{-4}(1/s)
0-1	4/52	12.8
1-2	3/50	10
2-3	0	0
3-4	4/54	12.3
4-5	0	0
5-6	0	6.4
6-7	2/52	0
7-8	0	0
8-9	0	3.14
9-10	1/53	9.8
10-11	3/51	3.26
11-12	1/51	6.94
12-13	2/48	0
13-14	0	0
14-15	0	0
15-16	0	0
16-17	1/47	3.54
17-18	1/47	3.54
18-19	0	0
19-20	1/49	3.4

Table 3. Summary of the average frequency of sediment entrainment, mean bursting period, and probability of entrainment.

Test	Average depth, H (m)	Average depth Velocity, U (m/s)	Average frequency of particles entrainment, f (1/s)	Bursting period, T_B (s)= $6\frac{H}{U}$	Probability of particles entrainment, P_E
E-2	0.05	0.4	$2.86\ 10^{-4}$	0.75	$2.15\ 10^{-4}$
E-20	0.068	0.527	$3.145\ 10^{-4}$	0.74	$2.32\ 10^{-4}$
E-35	0.057	0.708	$4.21\ 10^{-4}$	0.48	$2.02\ 10^{-4}$
E-50	0.057	0.76	$4.67\ 10^{-4}$	0.45	$2.10\ 10^{-4}$
E-70	0.076	1.19	$5.5\ 10^{-4}$	0.38	$2.035\ 10^{-4}$

Table 4. Frequency of sediment entrainment in the 20% packing condition (E-20 test).

Δt	Fraction of sediment that is displaced	F 10^{-4}(1/s)
0-1(30 s)	3/270	3.7
1-2(30 s)	6/269	7.4
2-3 (30 s)	8/268	9.9
3-4 (30 s)	9/268	11
4-5 (30 s)	3/268	3.7
5-6 (30 s)	7/268	8.7
6-7 (30 s)	7/268	8.7
7-8 (30 s)	7/268	4.9
8-9 (30 s)	4/268	3.7
9-10 (30 s)	3/269	4.9
10-11 (30 s)	4/269	7.4
11-12 (30 s)	6/269	4.3
12-13 (60 s)	7/270	3
13-14 (60 s)	5/269	1.8
14-15 (60 s)	3/268	3.7
15-16 (60 s)	6/267	2.49
16-17 (60 s)	4/267	4.3
17-18 (60 s)	7/267	2.4
18-19 (60 s)	4/268	3.7
19-20 (60 s)	6/268	4.3

Table 5. Frequency of sediment entrainment in the 35% packing condition (E-35 test).

Δt(min)	Fraction of the displaced particles	F 10^{-4}(1/s)
0-0.5	12/553	7.23
0.5-1	10/553	6.027
1-1.5	11/553	6.63
1.5-2	6/553	3.616
2-2.5	7/553	4.219
2.5-3	7/552	4.219
3-3.5	5/551	3.013
3.5-4	4/551	2.411
4-4.5	7/552	4.219
4.5-5	7/552	4.219
5-5.5	3/552	1.8083
5.5-6	3/552	1.8083
6-6.5	5/553	3.013
6.5-7	7/552	4.219
7-8	4/553	2.41

Table 6. Frequency of the sediment entrainment in the 50% packing condition (E-50 test).

Δt(min)	Fraction of particles displaced	f 10^{-4}(1/s)
0-.5	16/1035	6.387
0.5-1	18/1035	7.186
1-1.5	12/1035	4.790
1.5-2	12/1035	4.790
2-2.5	14/1033	5.588
2.5-3	15/1033	5.988

Table 7. Summary of the flow parameters

Tests	Slope S, %	Depth H, m	Average depth velocity U, m/s	Discharge Q, m^3/s	Aspect ratio B/H (width, B=0.6m)	H/d (d=0.008m)	Friction velocity, u^* (m/s)	Dimensionless critical stress, τ^*_{cr}	Reynolds number	Froude Number $Fr=U/(gH)^{0.5}$	Sediment collected per unit time per unit width, Q_b (kg/m/s)
E-2	0.2	0.05	0.4	0.0122	12	6.25	0.0313	0.008	$8\ 10^4$	0.57	$2.52\ 10^{-6}$
E-20	0.2	0.068	0.527	0.02185	9	8.5	0.036	0.01087	$1.4\ 10^5$	0.645	$3.78\ 10^{-6}$
E-35	0.8	0.057	0.708	0.02462	10.7	7.125	0.067	0.037	$1.6\ 10^5$	0.946	$4.9\ 10^{-5}$
E-50	1	0.057	0.76	0.0264	10.7	7.125	0.075	0.048	$1.7\ 10^5$	1.01	$1.13\ 10^{-5}$
E-70	1.2	0.076	1.19	0.054	8	9.5	0.093	0.074	$3.6\ 10^5$	1.37	$9.46\ 10^{-4}$

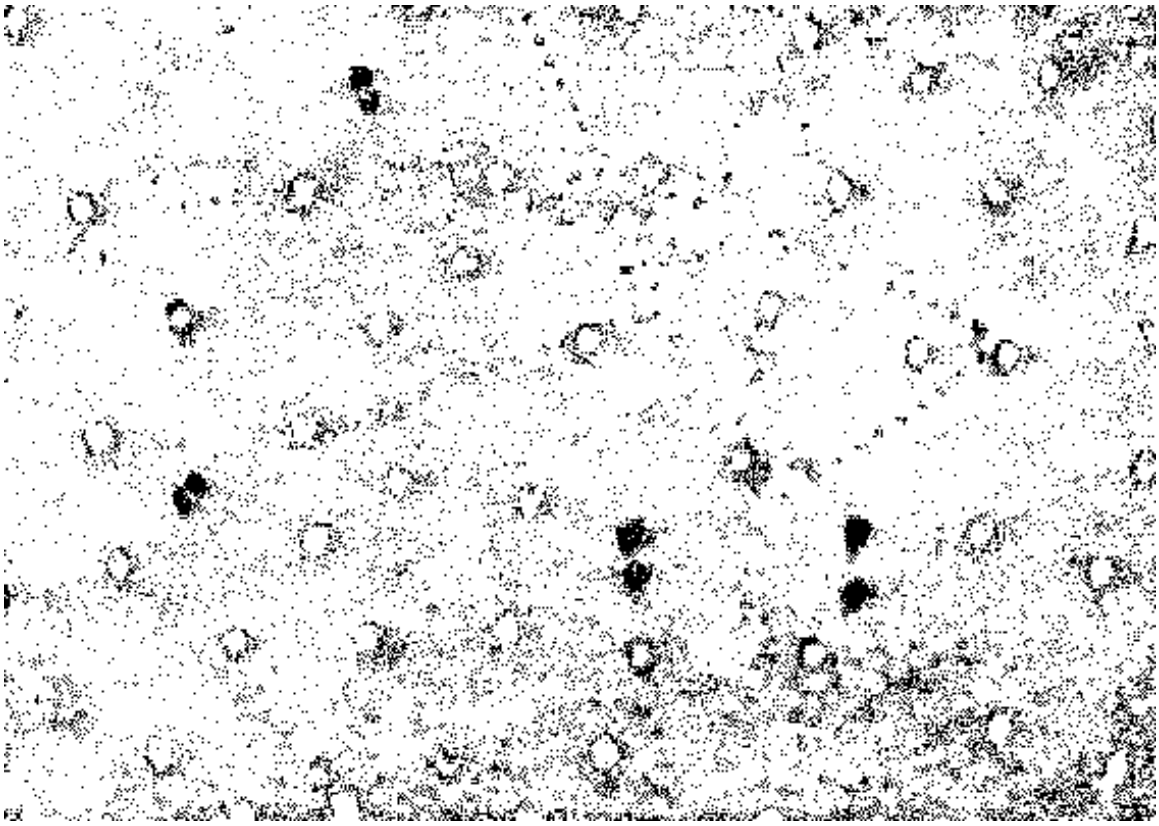

Figure 20(a). An image obtained from the subtraction of two images (the flow direction is from top to bottom).

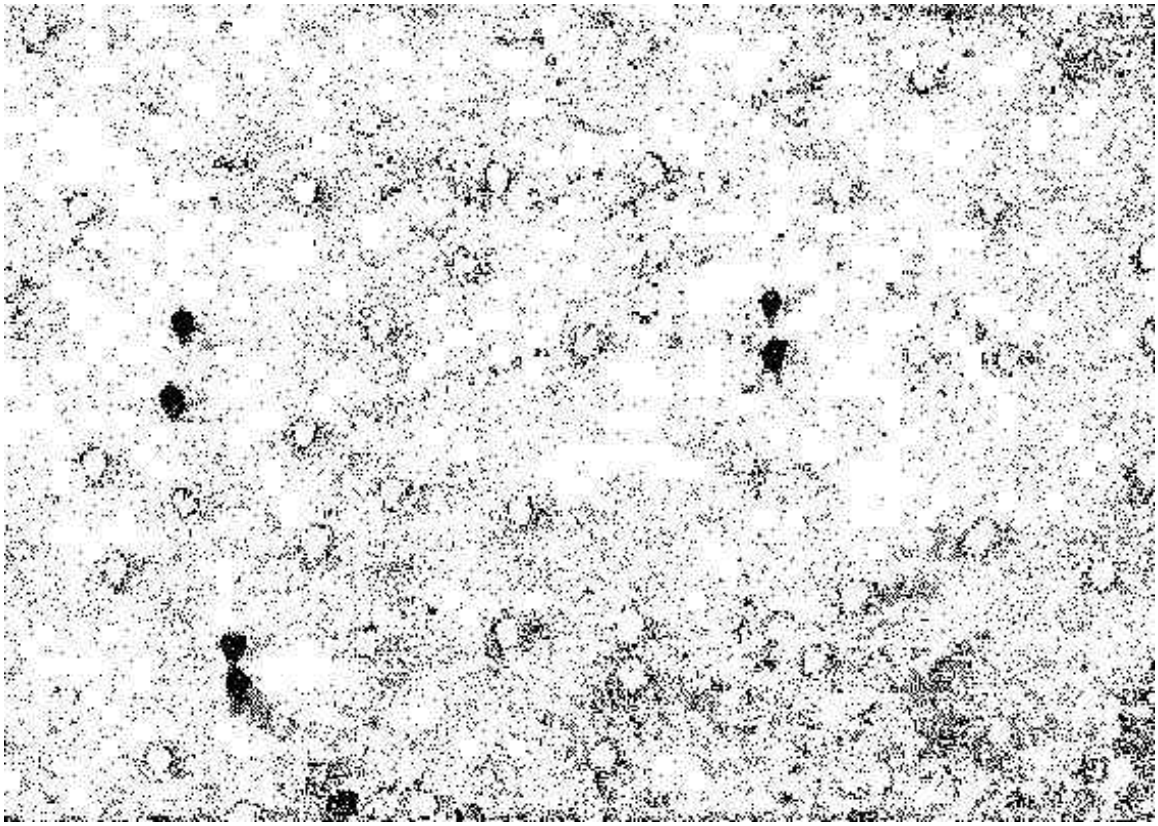

Figure 20(b). An image obtained from the subtraction of two images (the flow direction is from top to bottom).

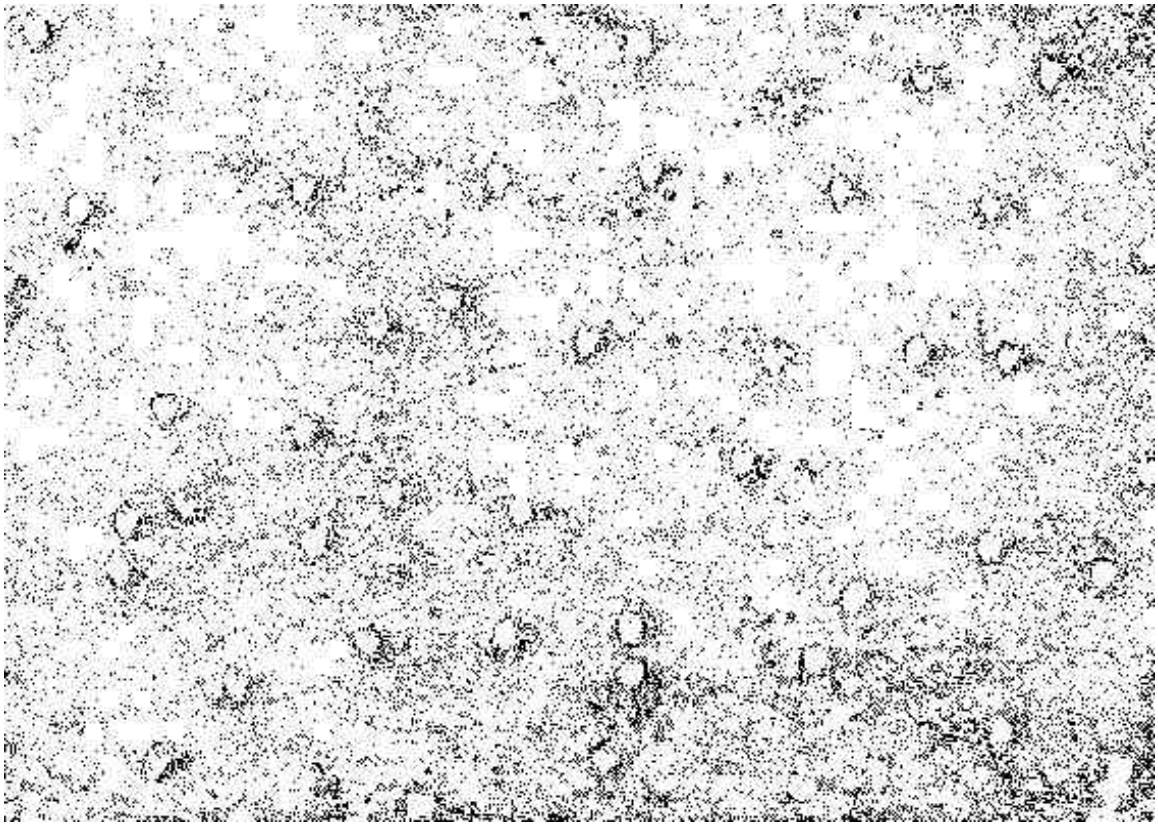

Figure 20(c). An image obtained from the subtraction of two images (the flow direction is from top to bottom).

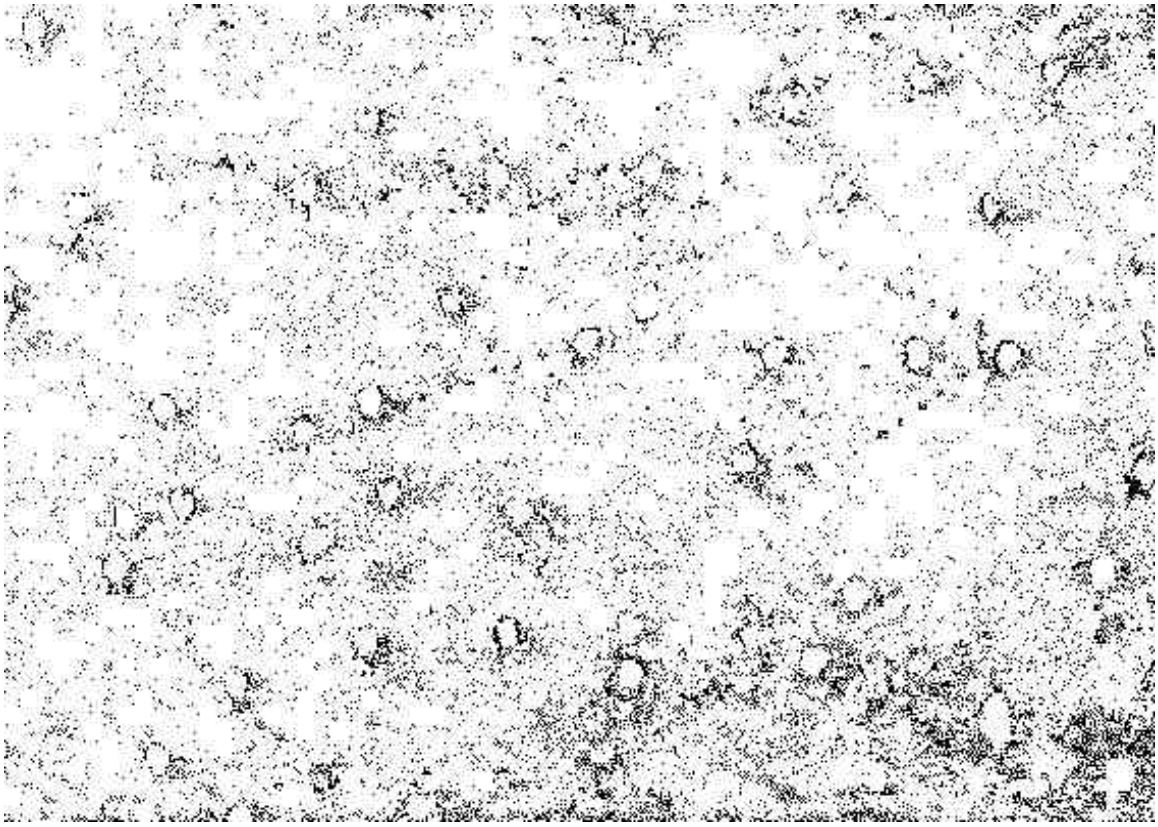

Figure 20(d). An image obtained from the subtraction of two images (the flow direction is from top to bottom).

f

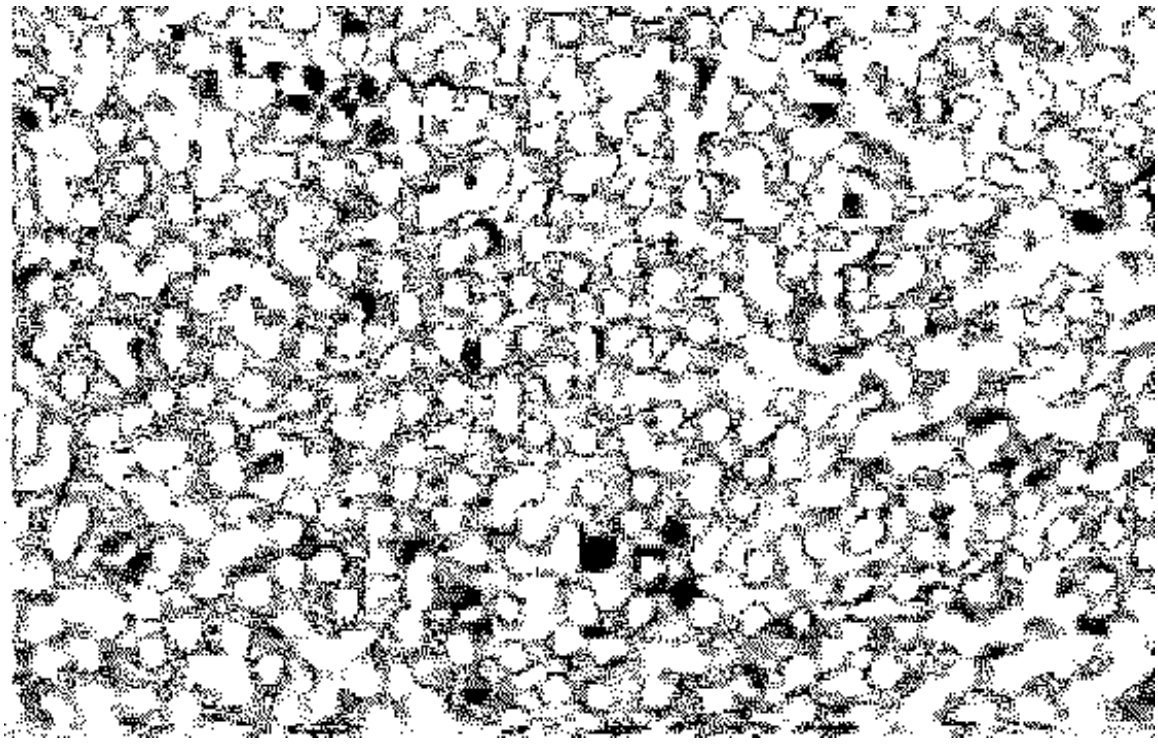

Figure 21. An image obtained from the subtraction of two images
(the flow direction is from top to bottom).

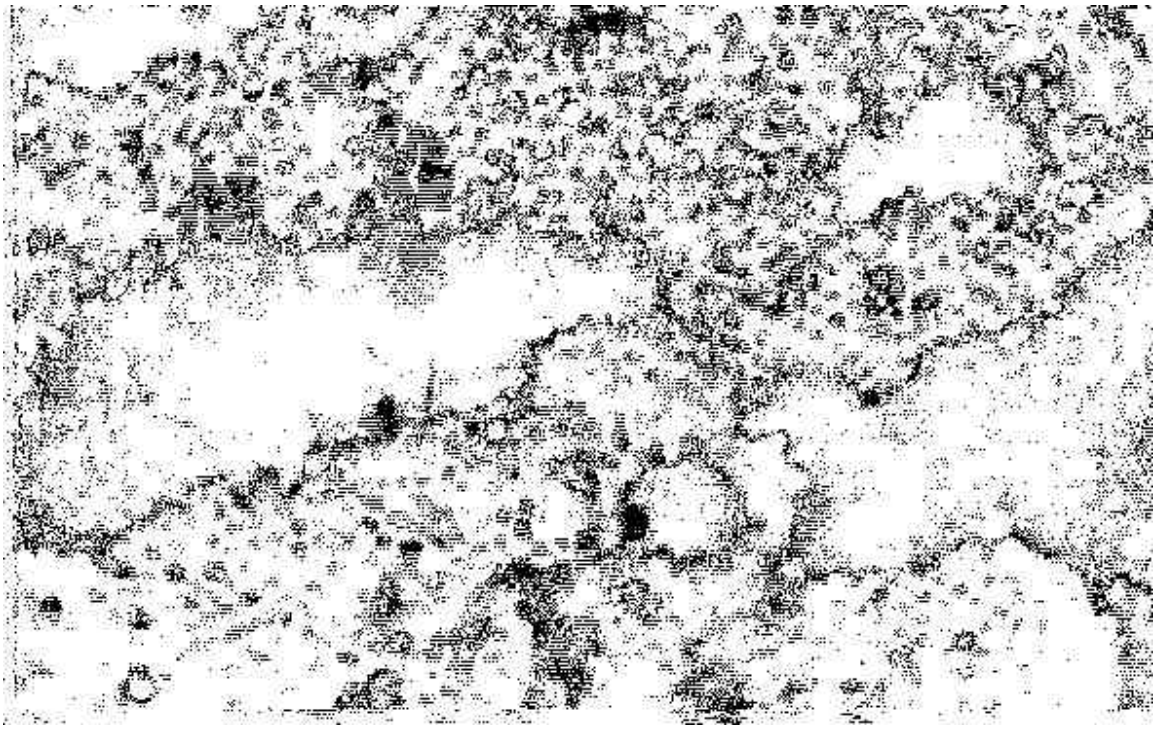

Figure 22. An image obtained from the subtraction of two images (the flow direction is from top to bottom).

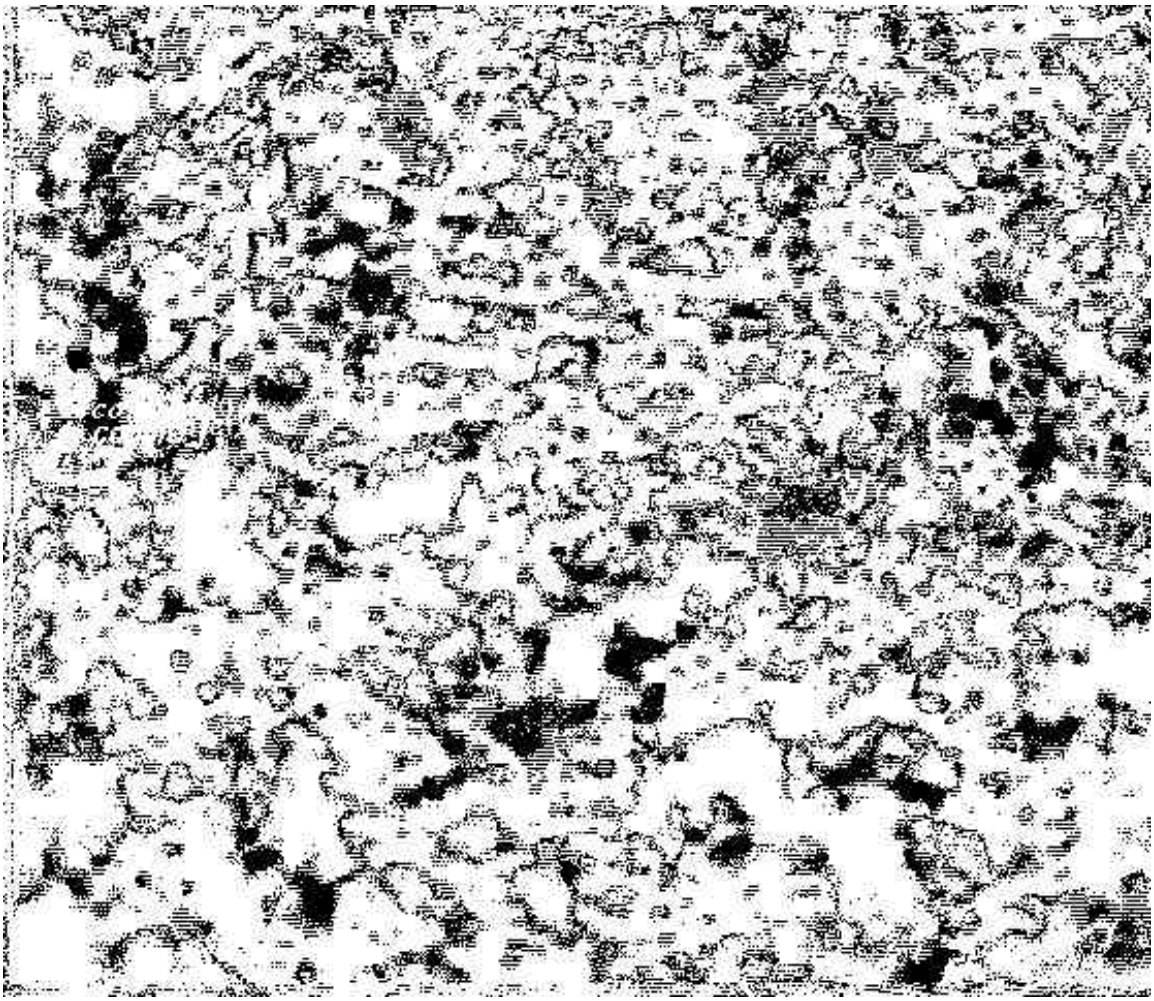

Figure 23. An image obtained from the subtraction of two images (the flow direction is from top to bottom).

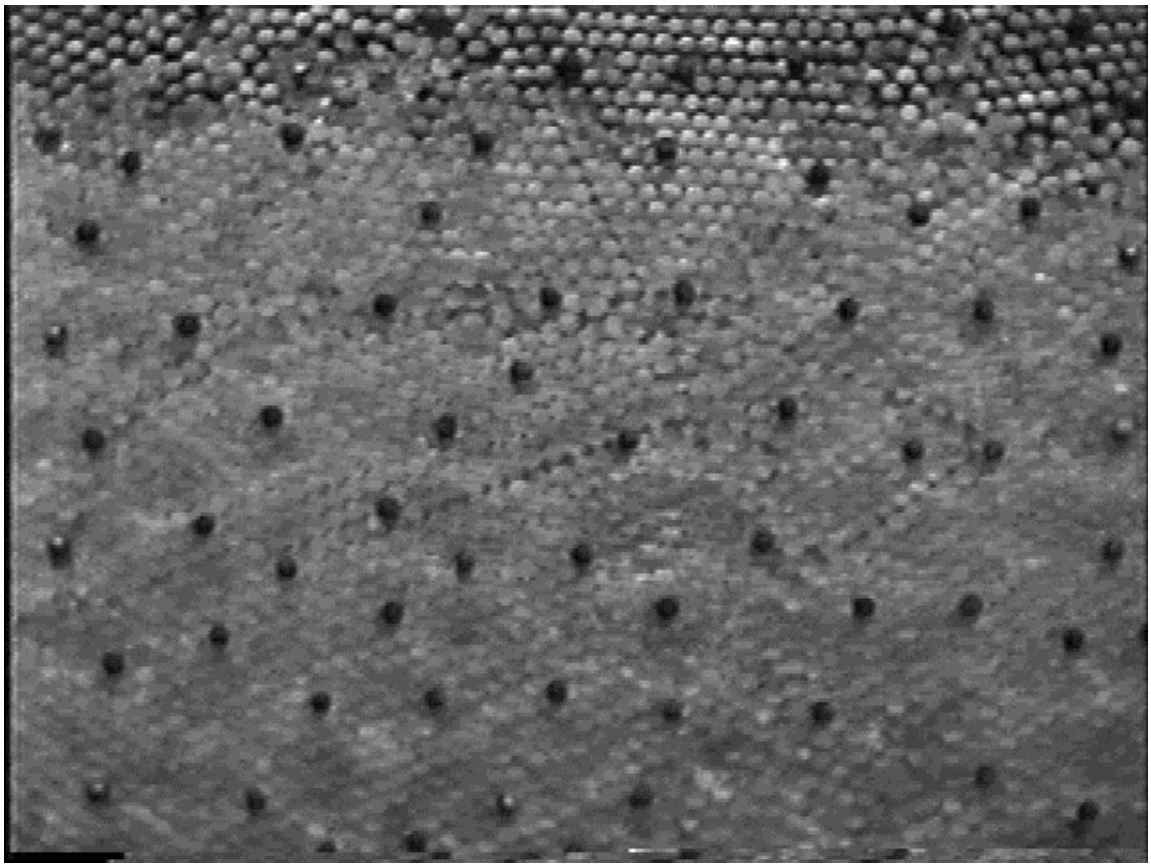

Figure 24(a). A top view of the test section at t=0 min (2% packing condition). The flow direction is from top to bottom.

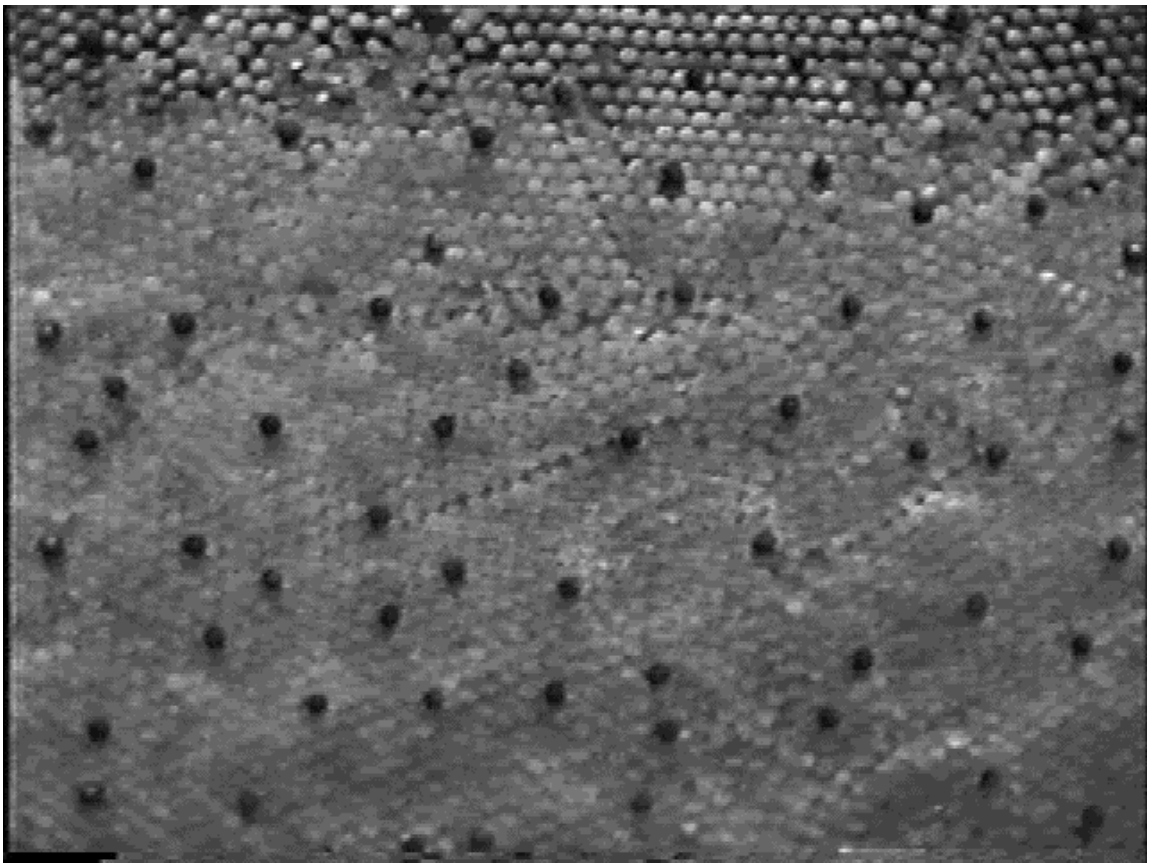

Figure 24(b). A top view of the test section at t=10 min (2% packing condition). The flow direction is from top to bottom.

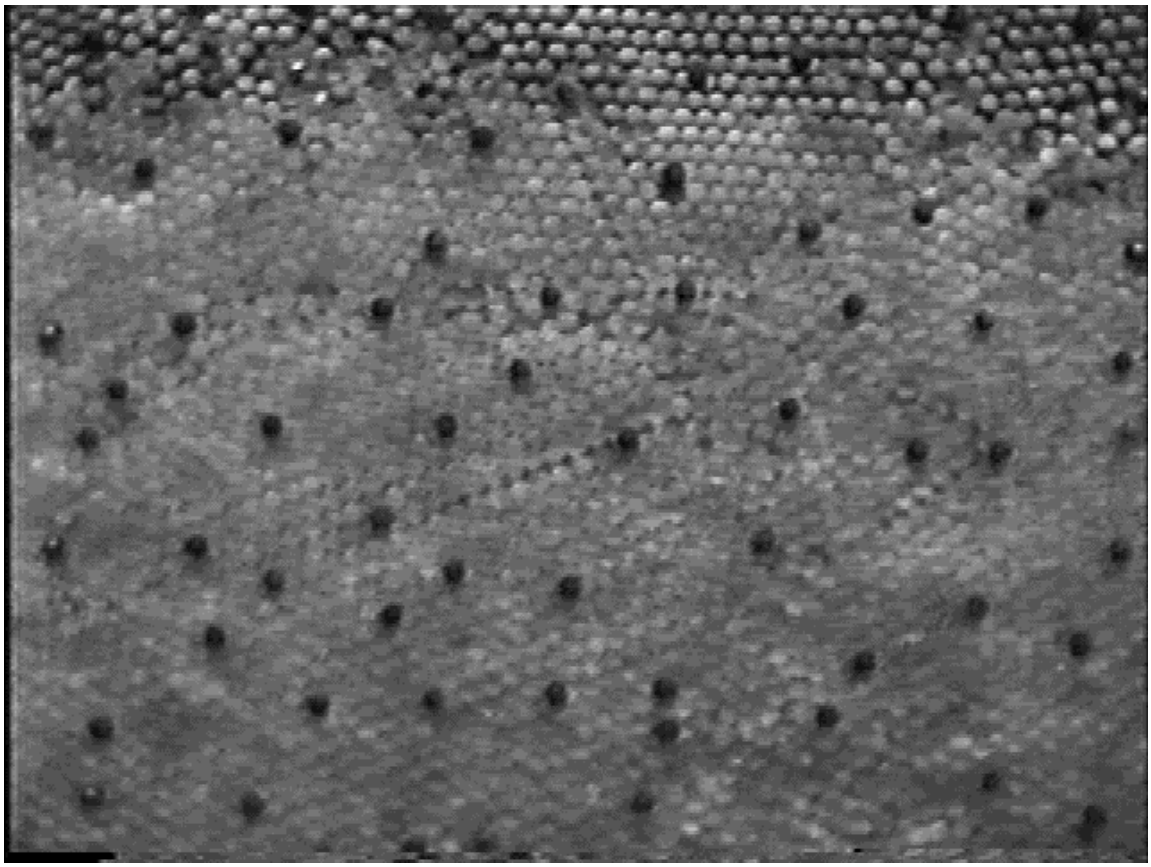

Figure 24(c). A top view of the test section at t=15 min (2% packing condition). The flow direction is from top to bottom.

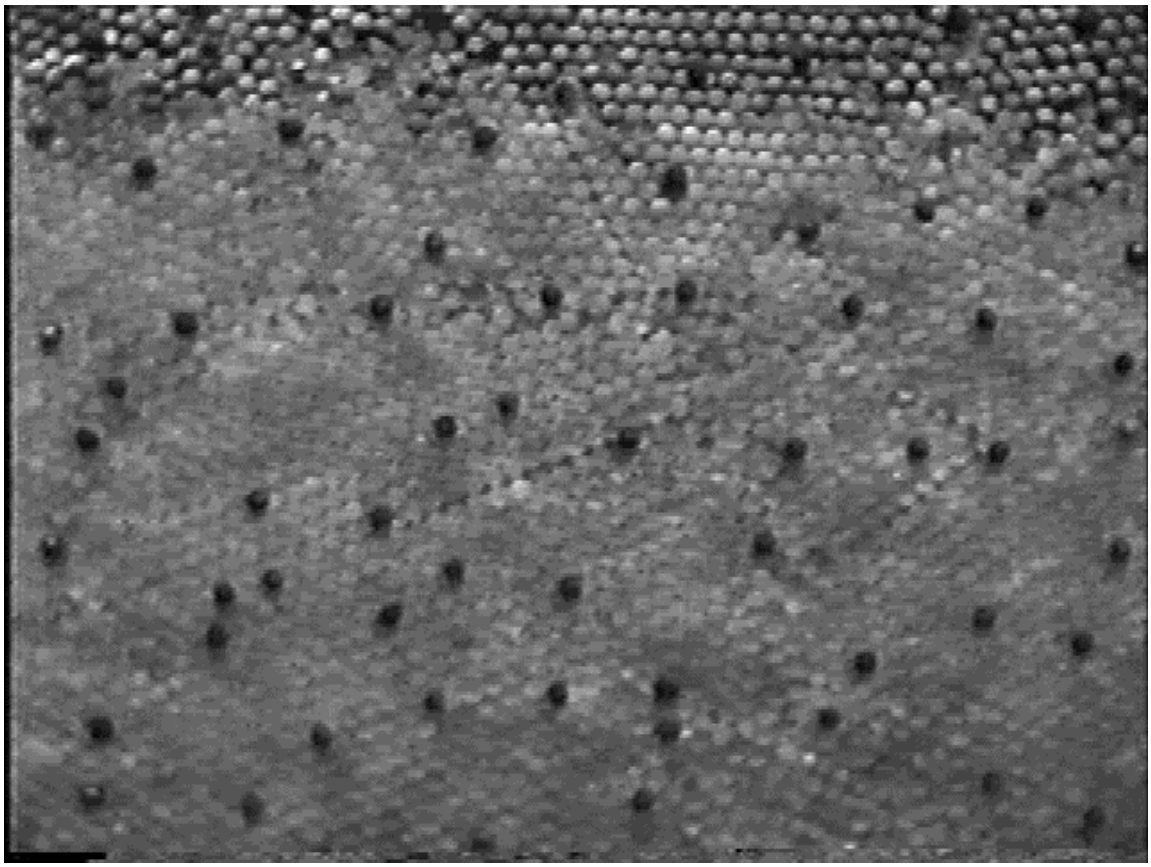

Figure 24(d). A top view of the test section at t=20 min (2% packing condition). The flow direction is from top to bottom.

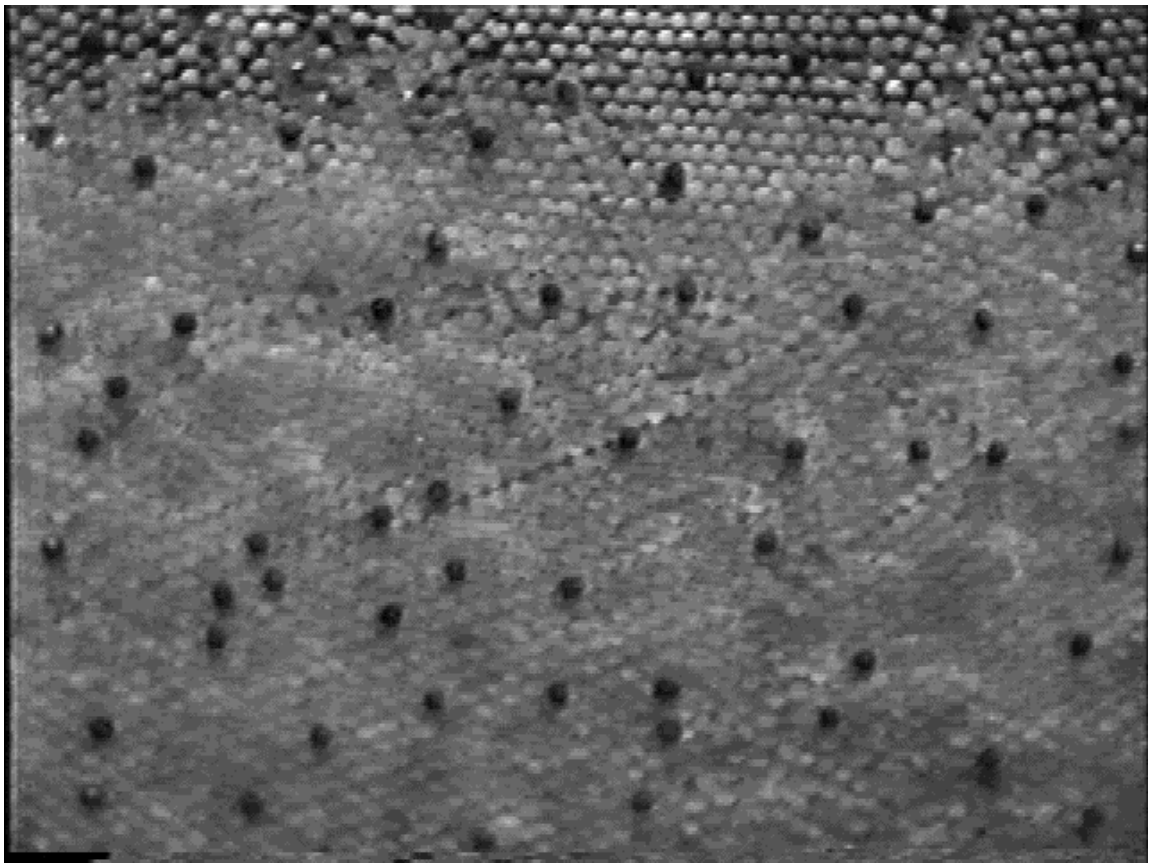

Figure 24(e). A top view of the test section at t=25 min (2% packing condition). The flow direction is from top to bottom.

Number of observations, N=27

Midpoint	Count	
0.5	5	*****
1.0	9	*********
1.5	6	******
2.0	3	***
2.5	3	***
3.0	0	
3.5	0	
4.0	1	*

Figure 25. The histogram of the distance of balls expressed in terms of particle diameters (2% case).

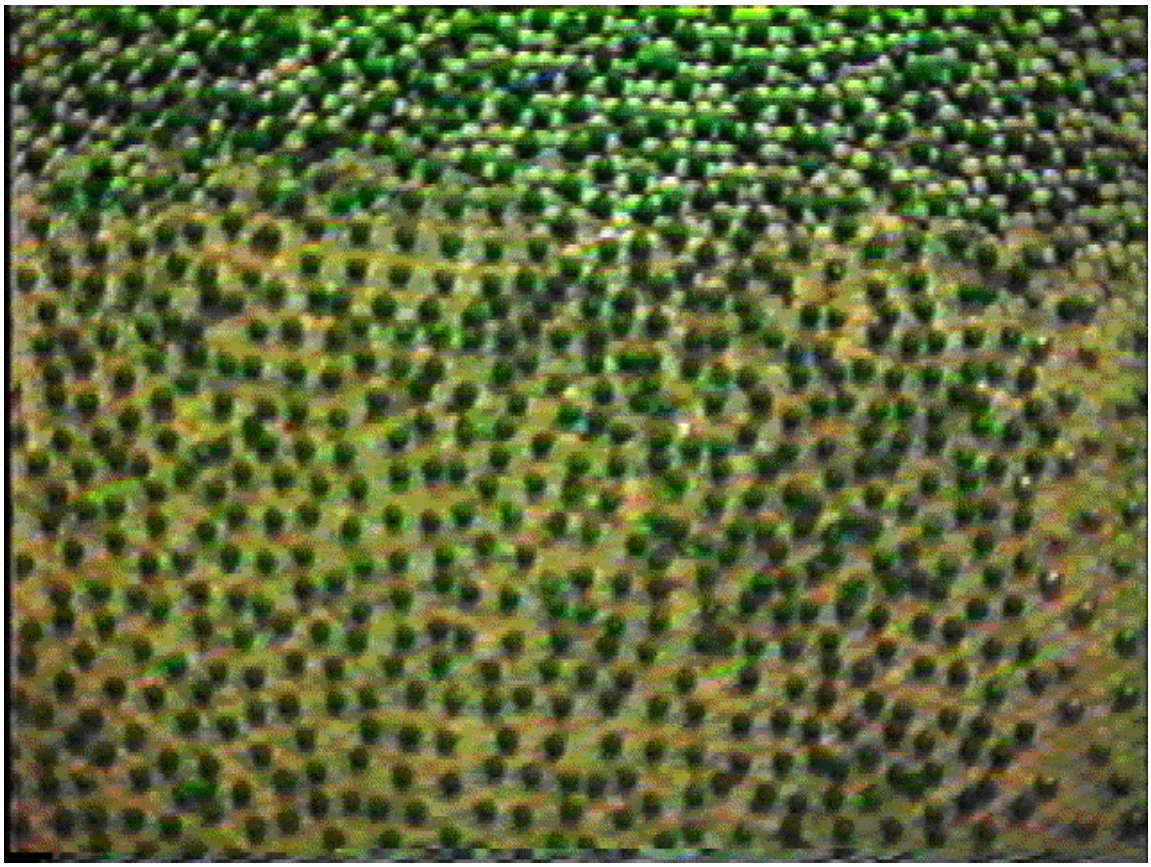

Figure 26(a). A top view of the test section at t=0 min (20% packing condition). The flow direction is from top to bottom.

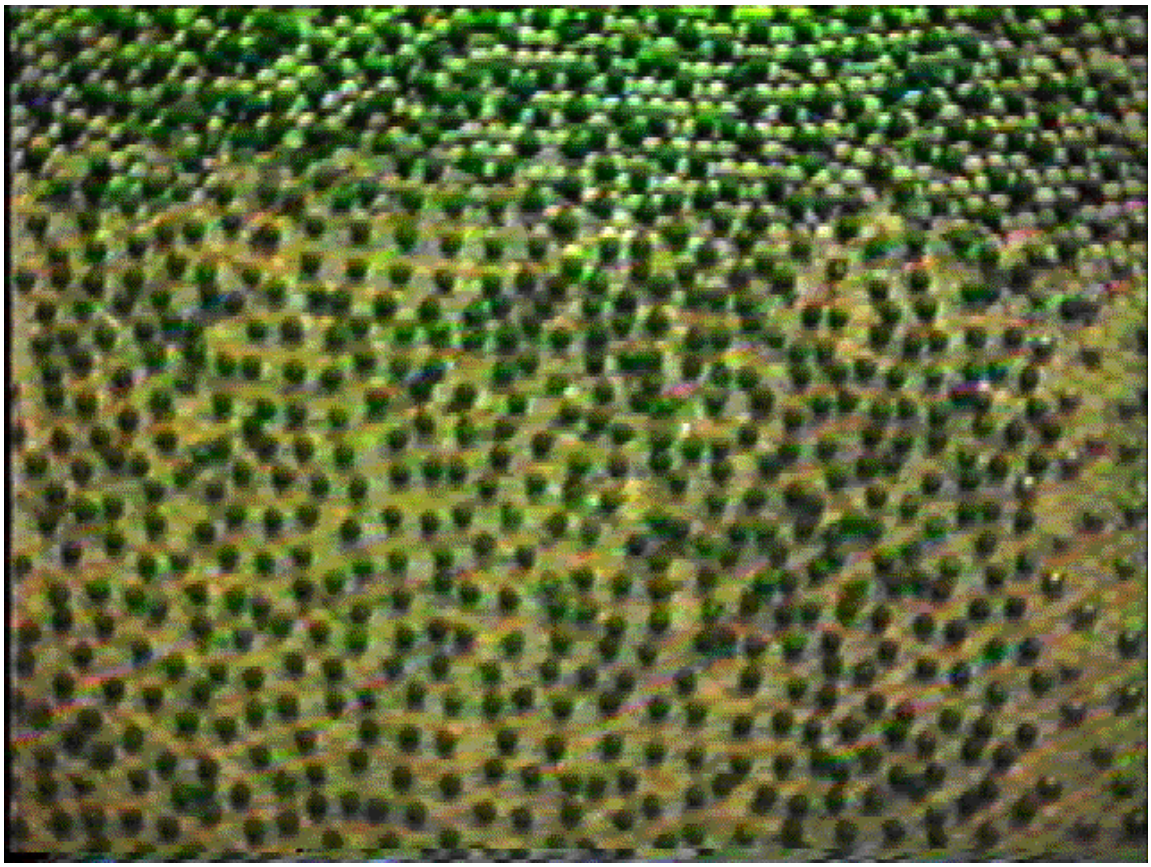

Figure 26(b). A top view of the test section at t=10 min (20% packing condition). The flow direction is from top to bottom.

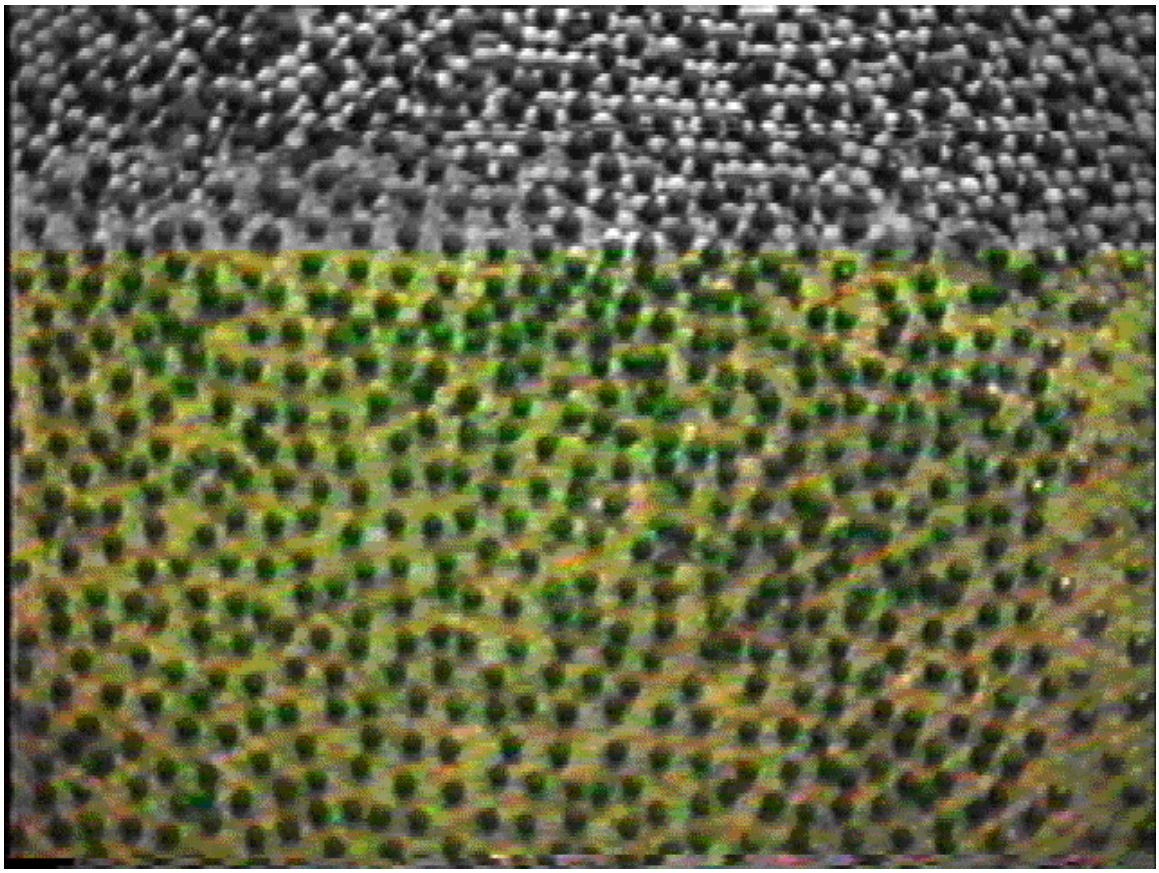

Figure 26(c). A top view of the test section at t=20 min (20% packing condition).

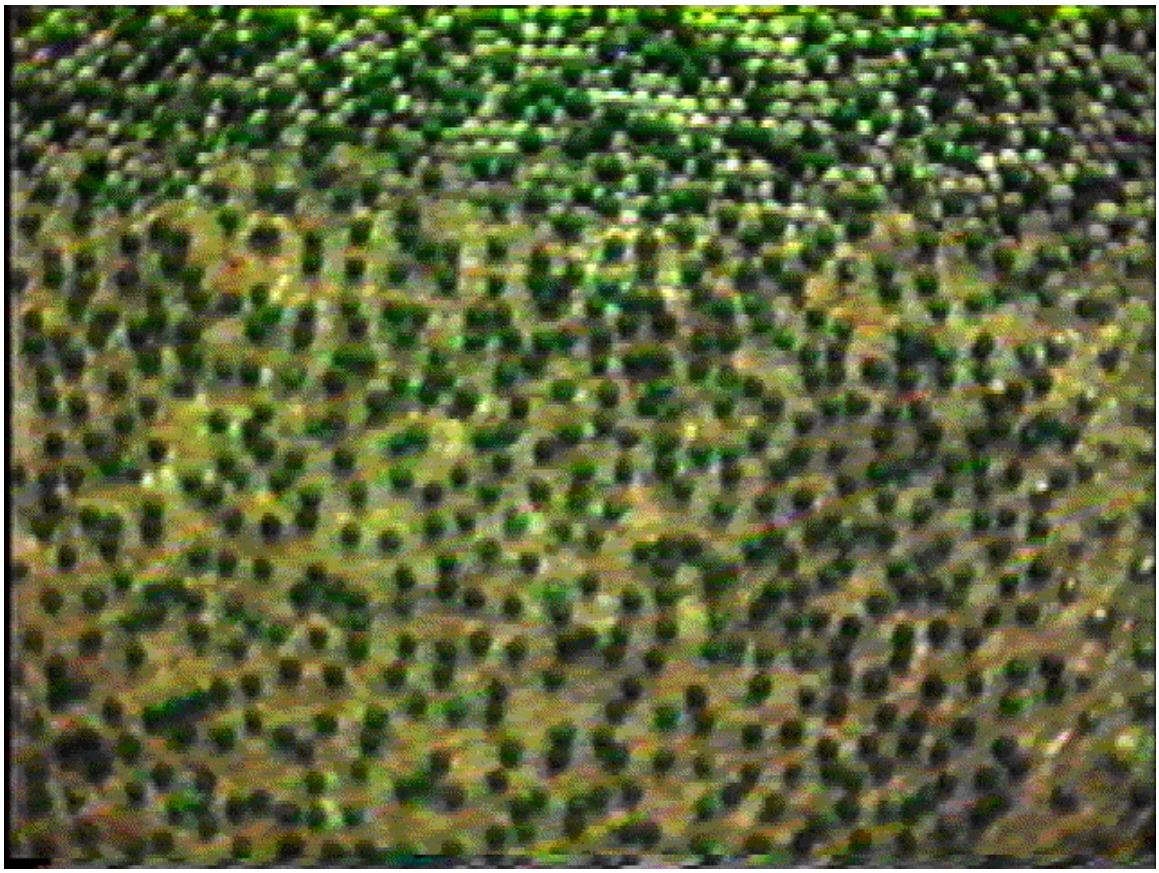

Figure 26(d). A top view of the test section at t=25 min (20% packing condition).

Number of observations, N=56

Midpoint	Count	
0.5	1	*
1.0	23	**********
1.5	6	******
2.0	10	**********
2.5	6	******
3.0	5	*****
3.5	1	*
4.0	2	**
4.5	2	**

Figure 27. The histogram of the distance of balls expressed in terms of particle diameters (20% case).

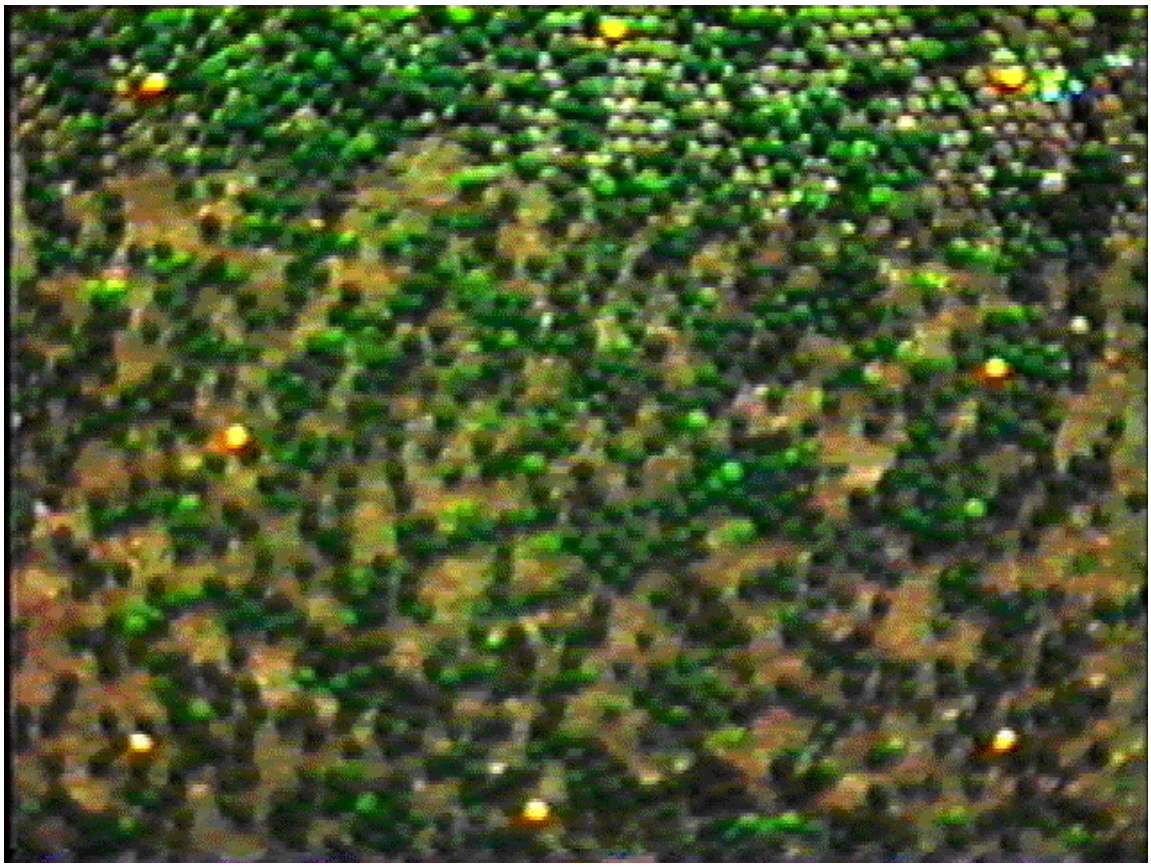

Figure 28(a). A top view of the test section at t=1 min (35% packing condition). The flow direction is from top to bottom

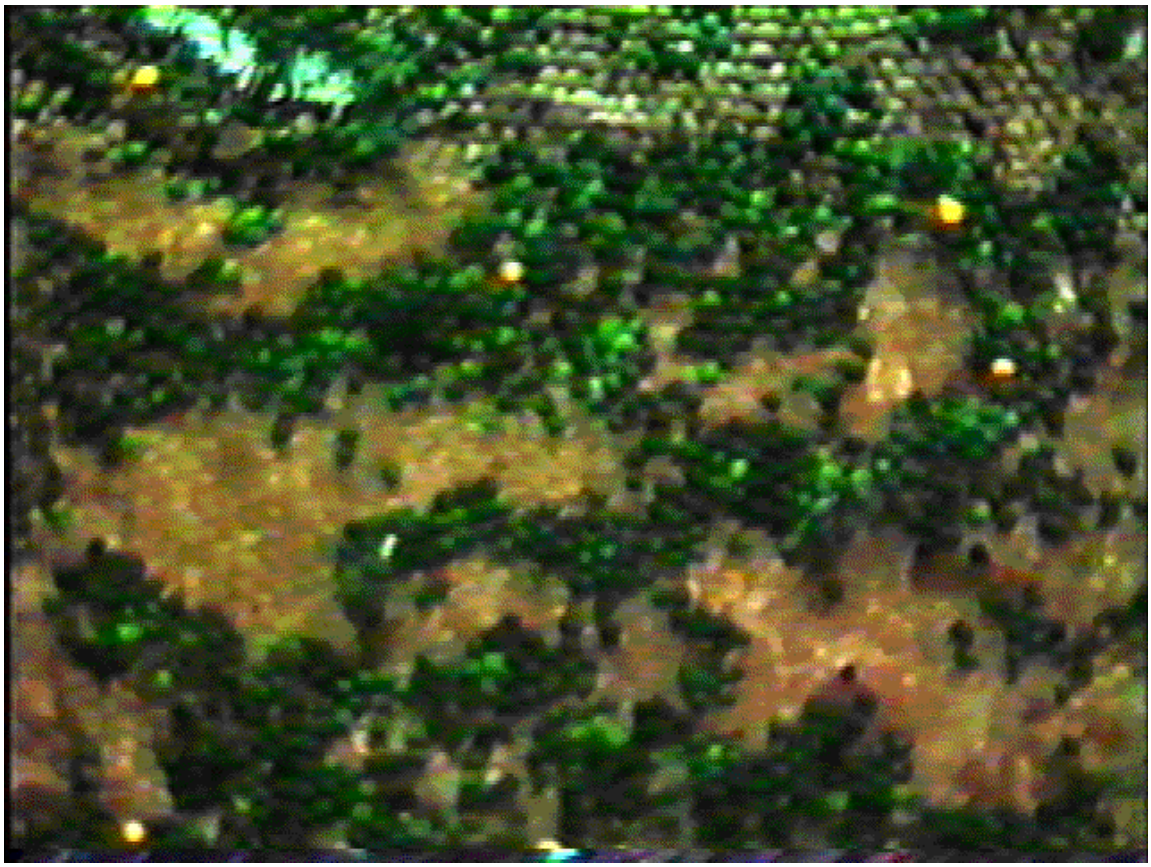

Figure 28(b). A top view of the test section at t=5 min (35% packing condition). The flow direction is from top to bottom

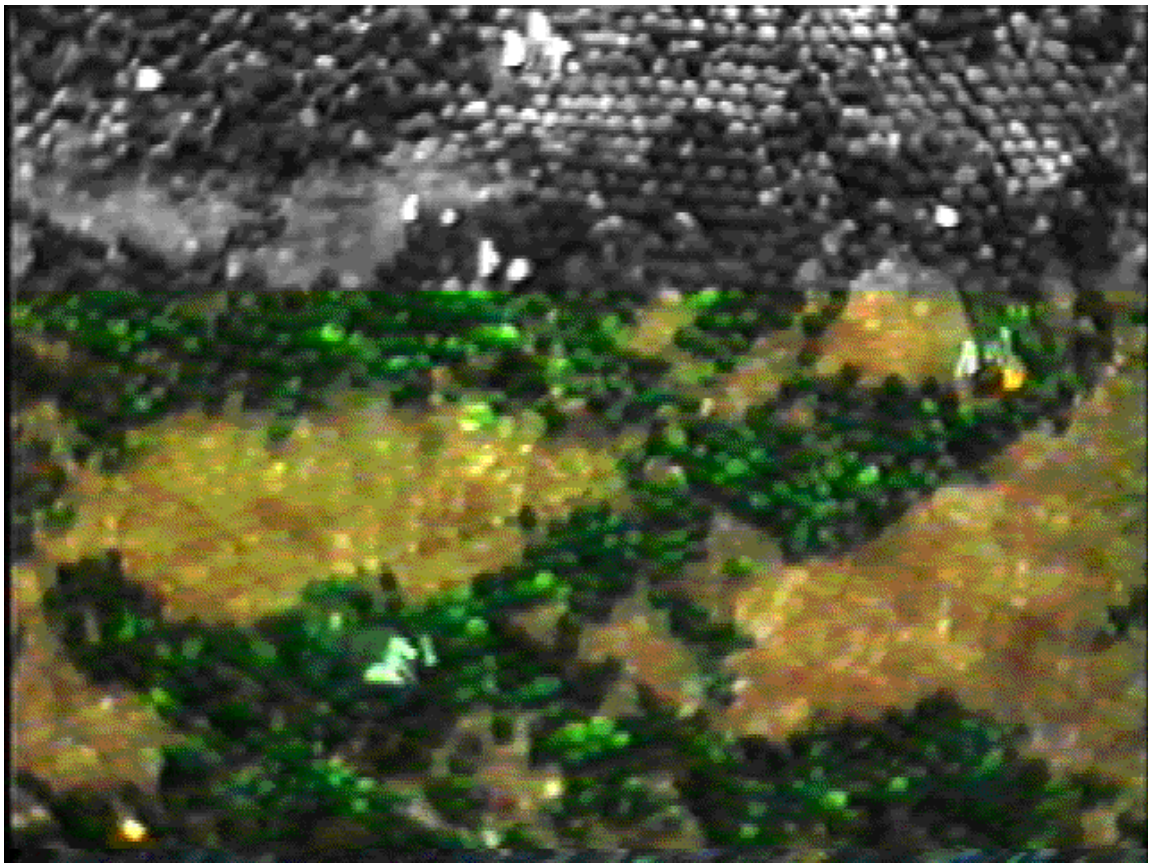

Figure 28(c). A top view of the test section at t=10 min (35% packing condition). The flow direction is from top to bottom

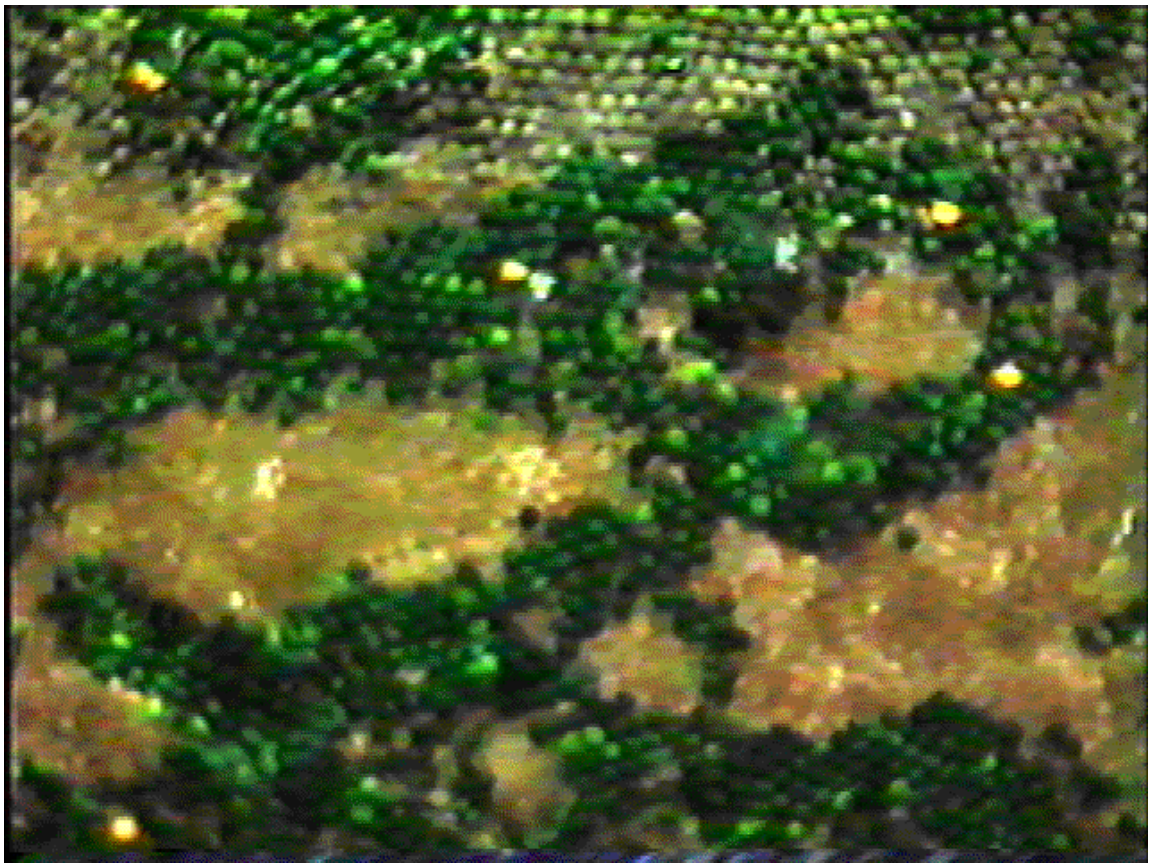

Figure 28(d). A top view of the test section at t=15 min (35% packing condition). The flow direction is from top to bottom

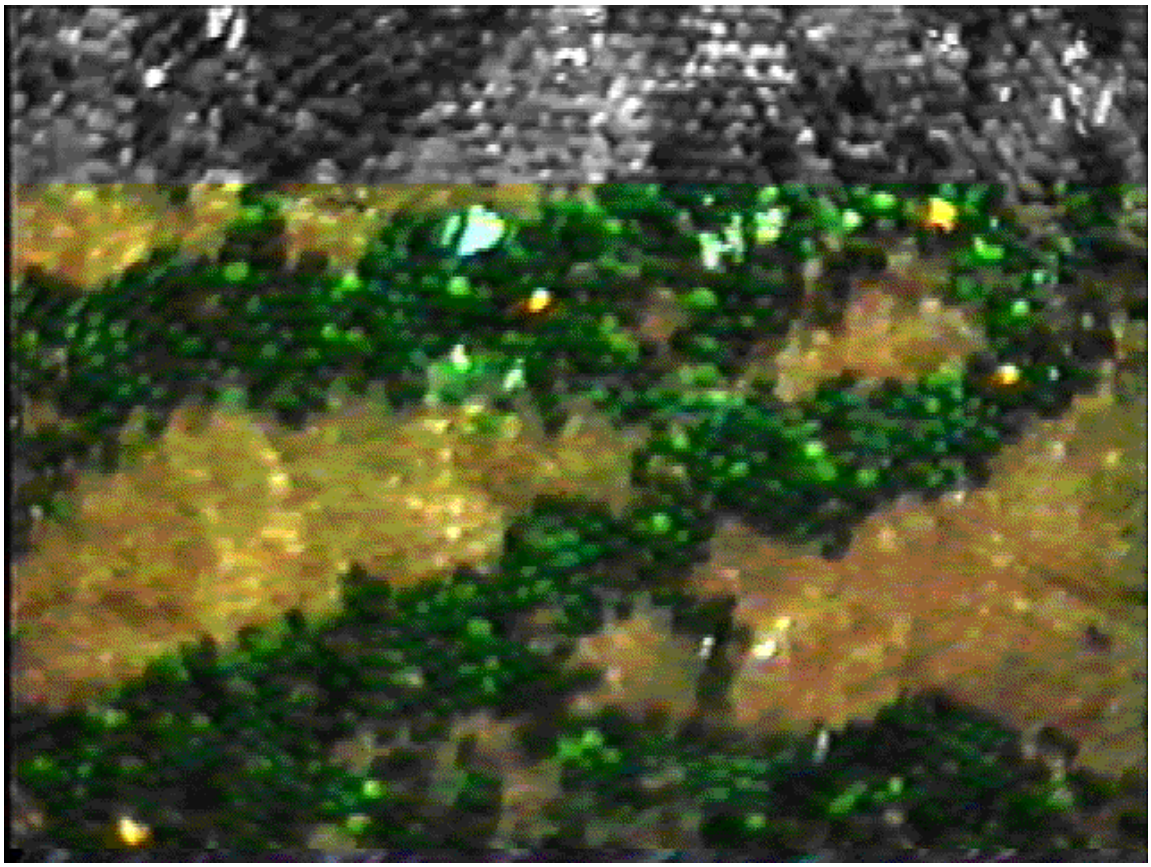

Figure 28(e). A top view of the test section at t= 20min (35% packing condition). The flow direction is from top to bottom

Number of observations, N=62

Midpoint	Count	
1.0	15	**********
1.5	14	**********
2.0	16	**********
2.5	5	*****
3.0	1	*
3.5	4	****
4.0	2	**
4.5	1	*
5.0	0	
5.5	3	***
6.0	1	*

Figure 29. The histogram of the downstream distance of balls expressed as a function of the particle diameter (35% case).

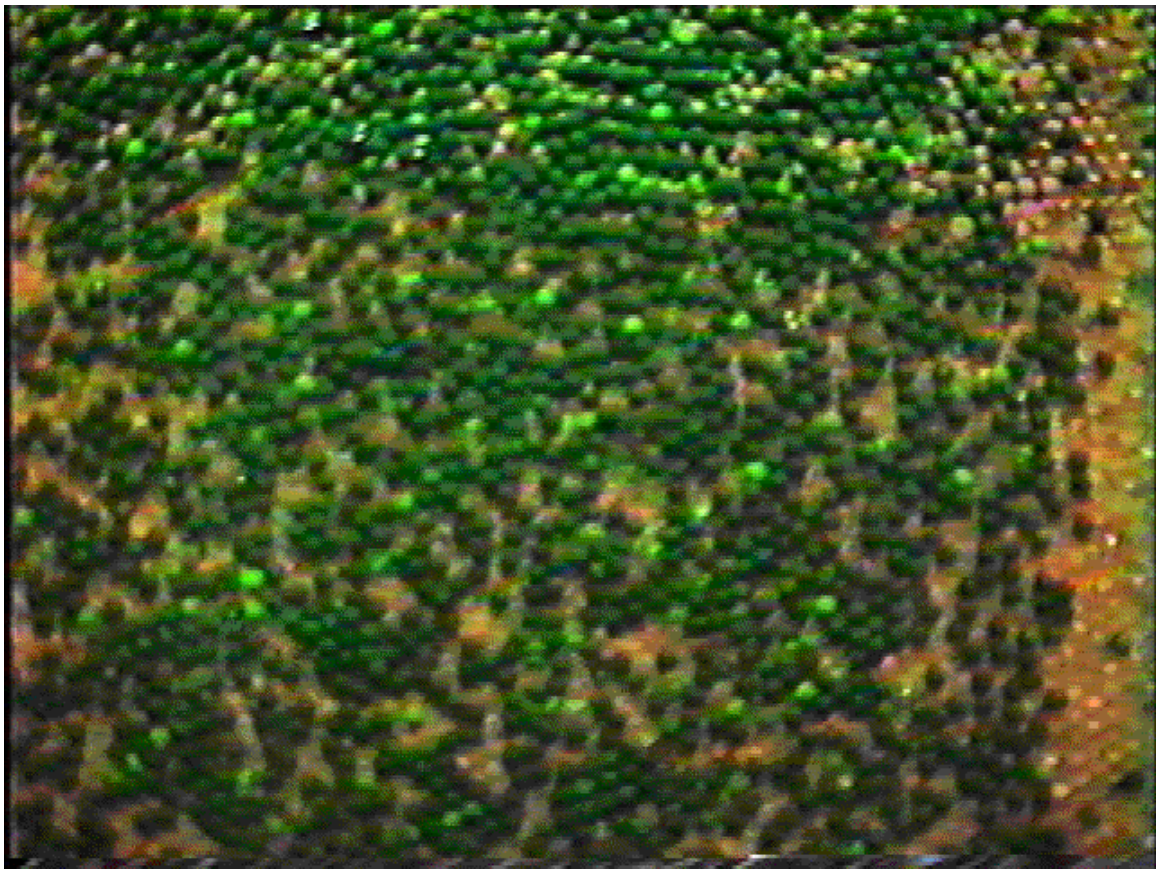

Figure 30(a). A top view of the test section at t= 0 min (50% packing condition).

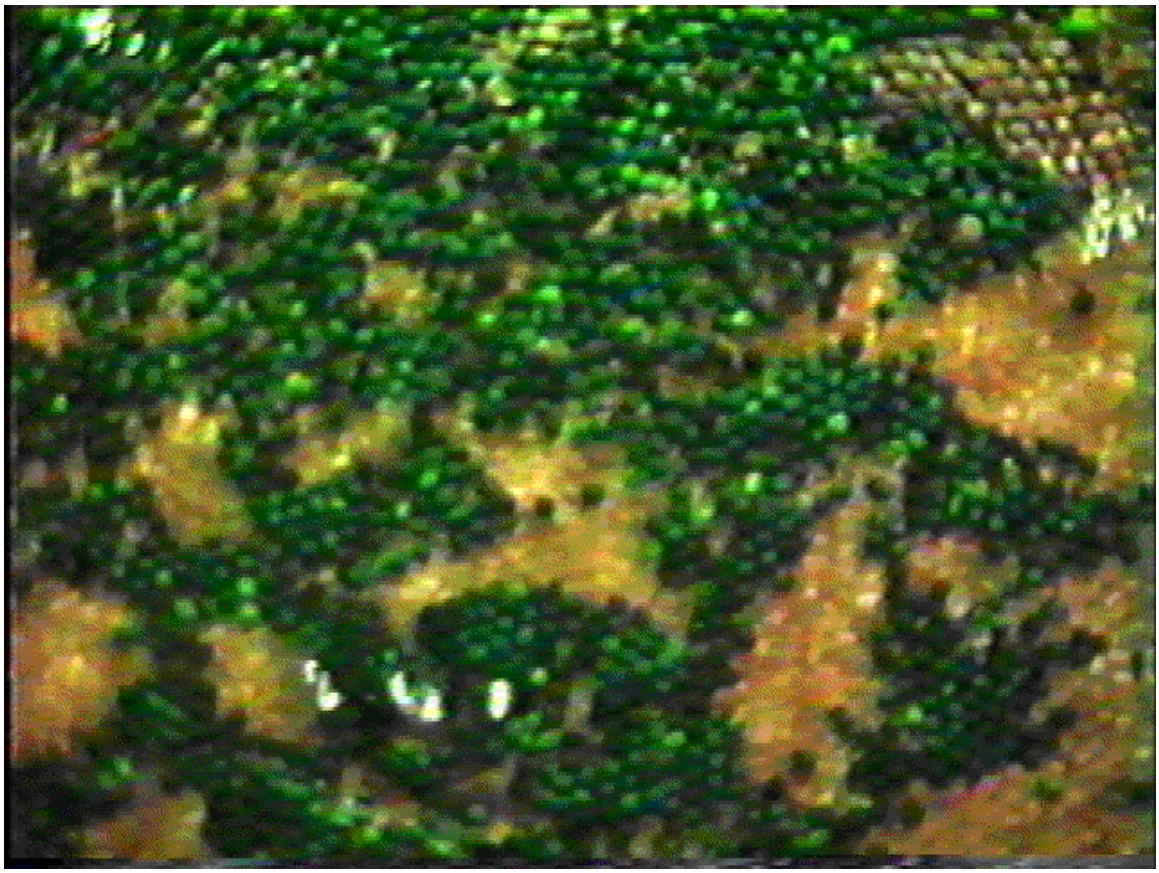

Figure 30(b). A top view of the test section at t= 5min (50% packing condition).

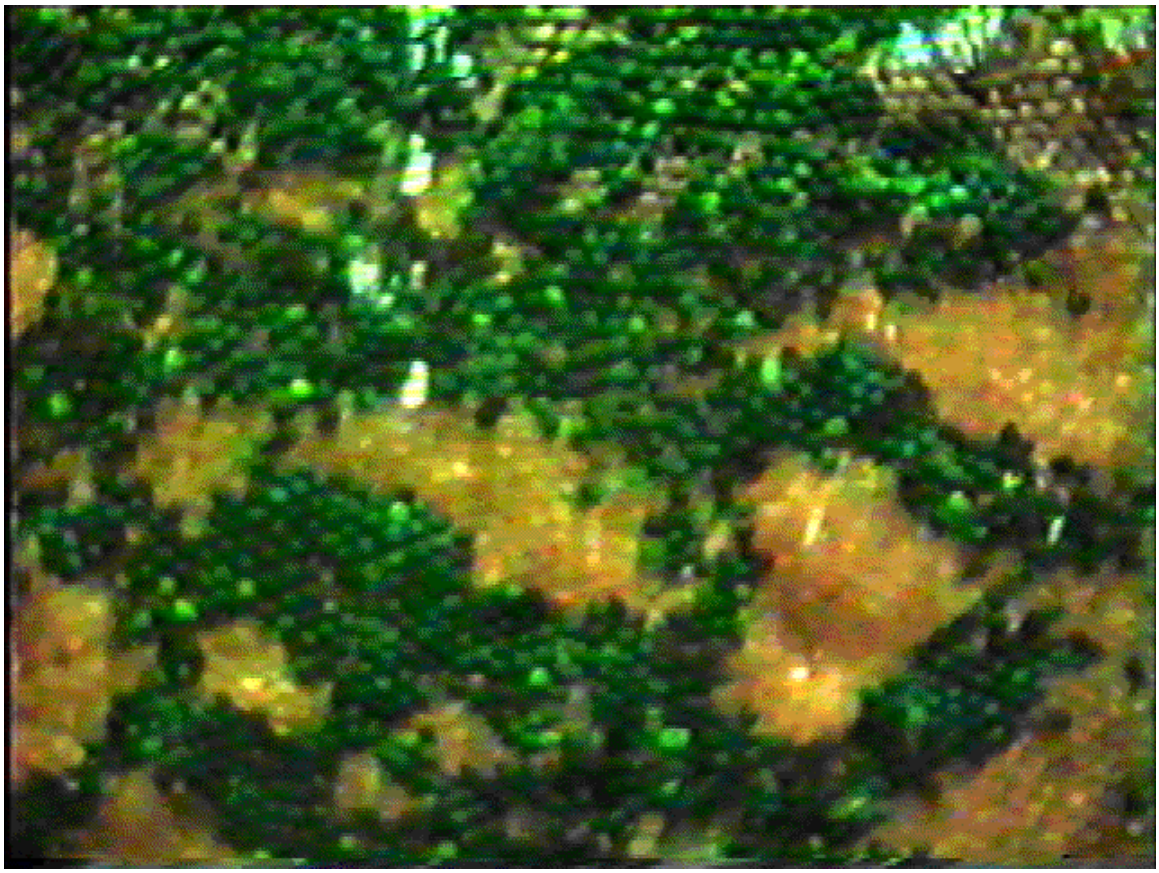

Figure 30(c). A top view of the test section at t= 10min (50% packing condition).

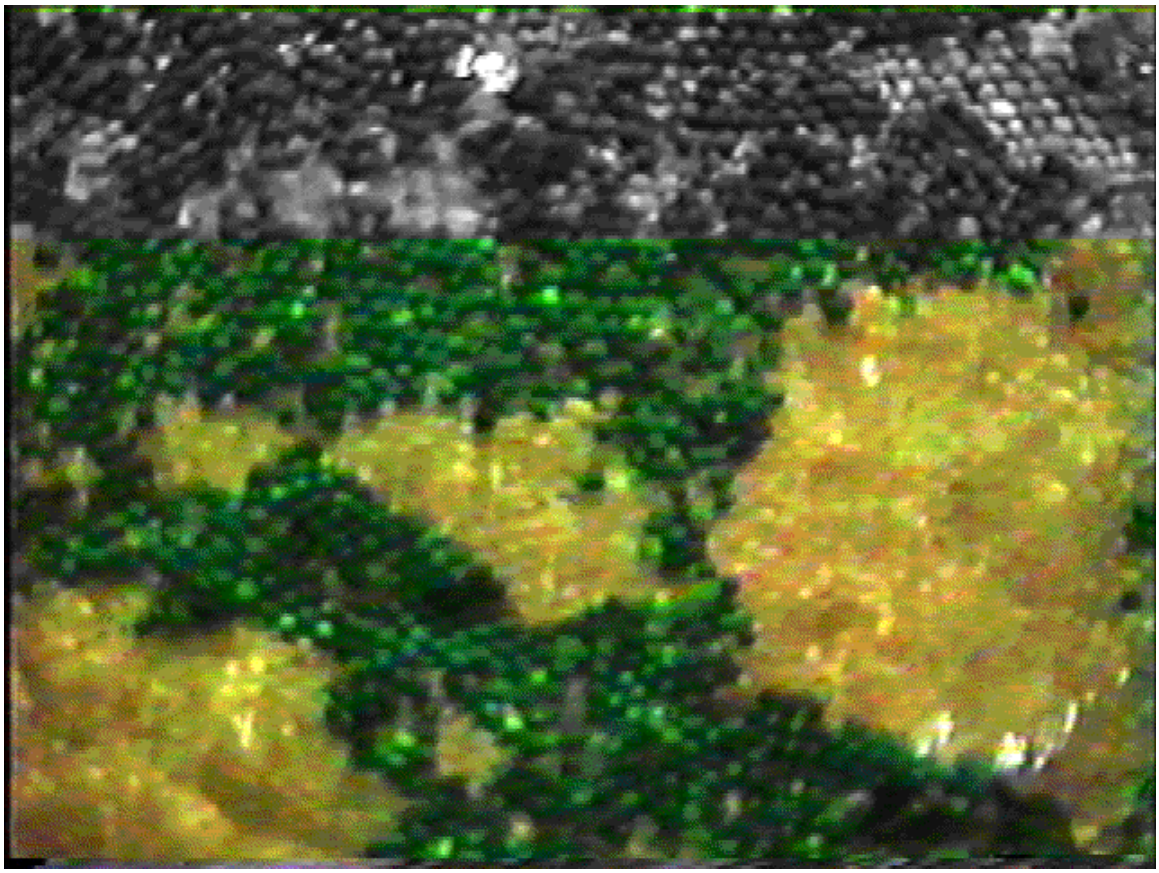

Figure 30(d). A top view of the test section at t= 15min (50% packing condition).

Number of observations, N=48

Midpoint	Count	
1	20	**********
2	12	**********
3	6	******
4	3	***
5	0	
6	5	*****
7	0	
8	0	
9	1	*
10	1	*

Figure 31. The histogram of the downstream distance of balls expressed as a function of the particle diameter (50% case).

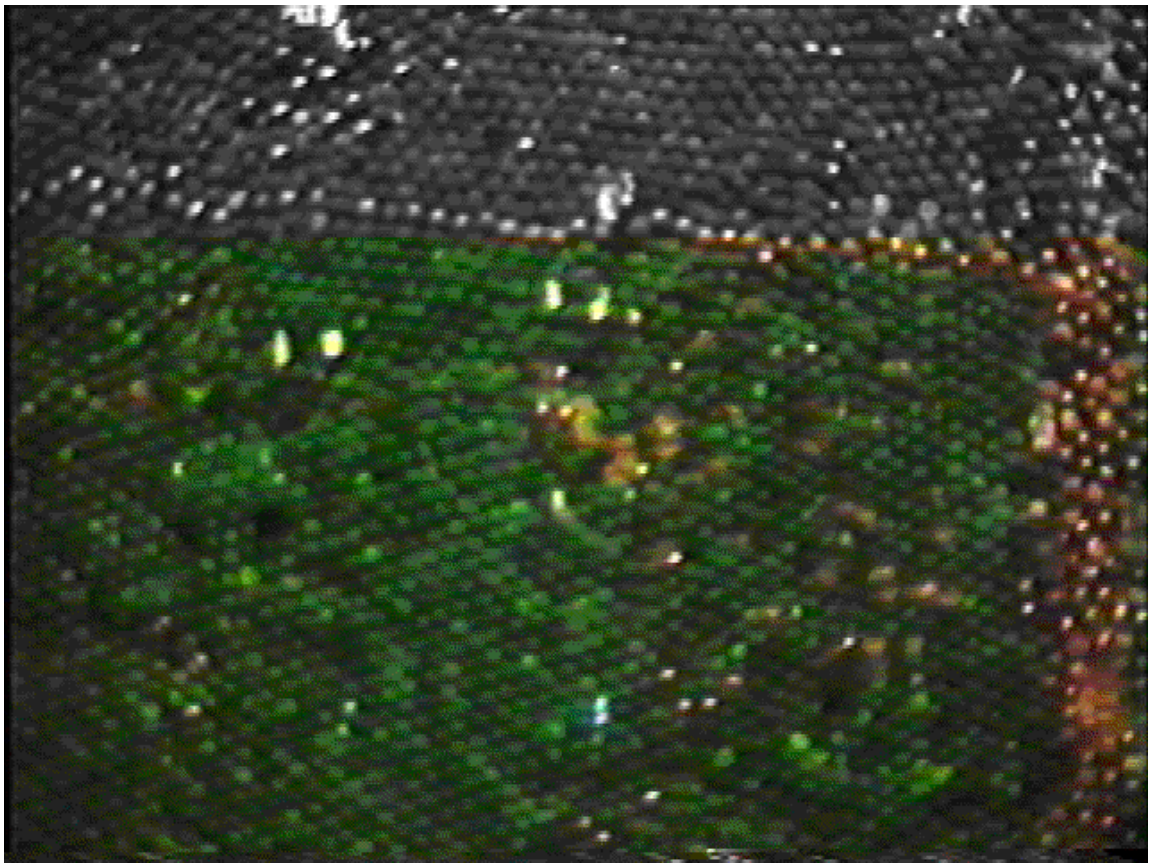

Figure 32(a). A top view of the test section at t=0 min (70% packing condition). The flow is from top to bottom.

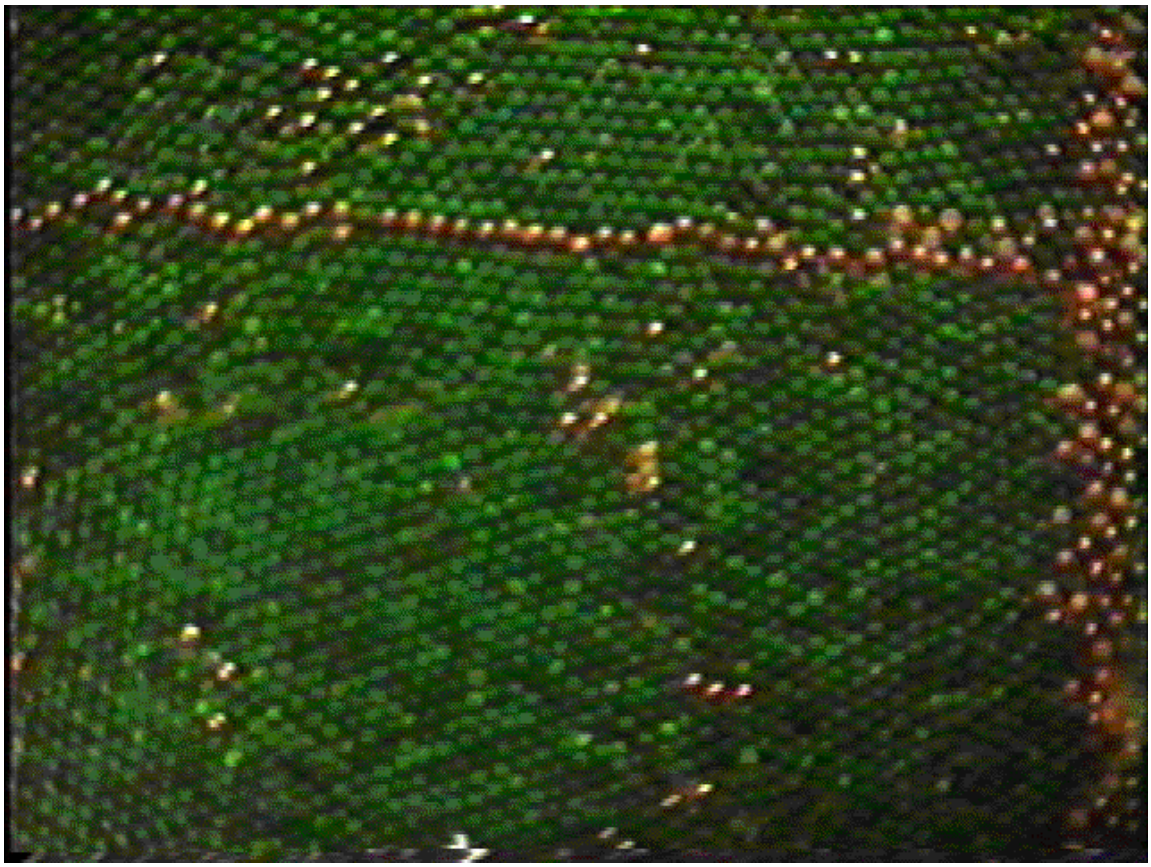

Figure 32(b). A top view of the test section prior to the commencement of the run (70% packing condition). The flow is from top to bottom.

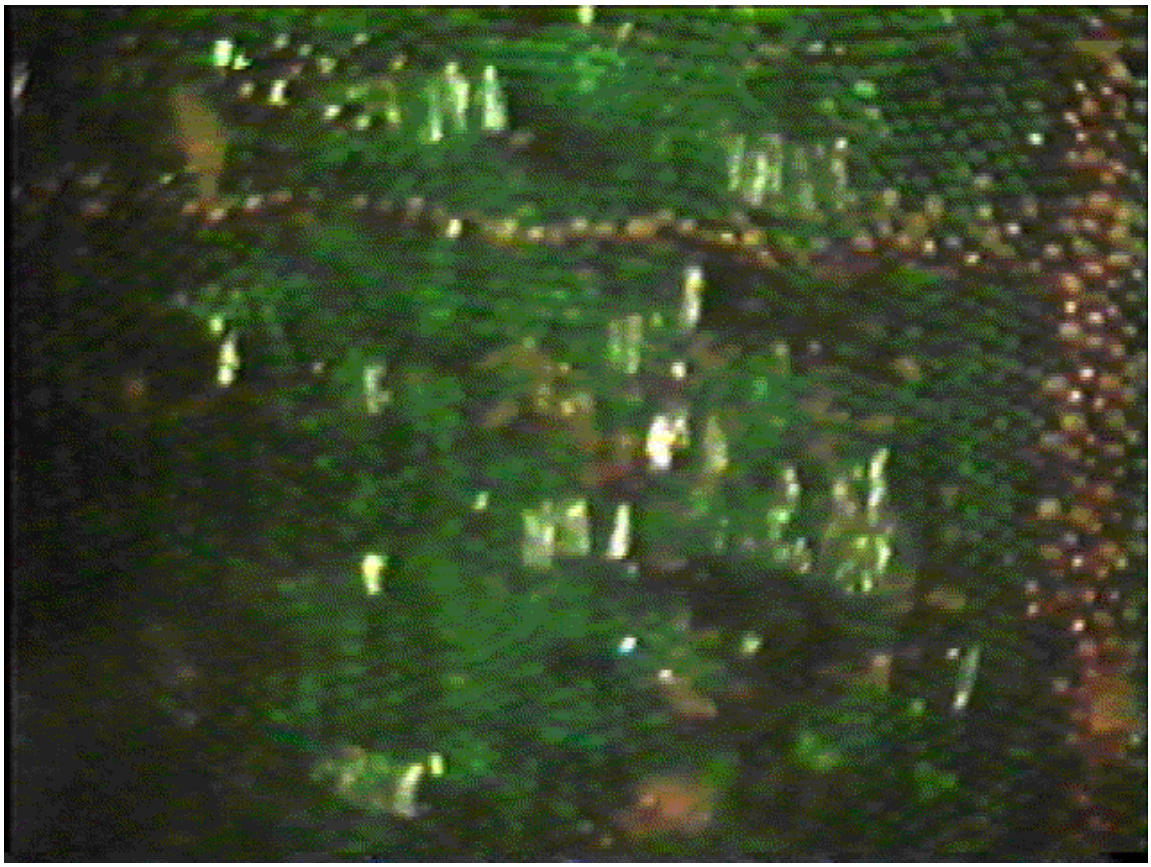

Figure 32(c). A top view of the test section at t=1 min (70% packing condition). The flow is from top to bottom.

Chapter 5

Deterministic Models-Mean Flow Quantities

In the present chapter the performance of several deterministic incipient motion models, which exist in the literature, is examined by comparing their results with the experimental data that are obtained from this study. Also, in this chapter the distributions of the different turbulent flow quantities for different surface packing conditions are provided.

5.1 Models

A common theoretical approach for determining the threshold condition of sediment motion is to consider the balance of moments about a pivot as a single particle moves out of its position. A pioneering study in this area is the work of Coleman (1966). Coleman computed the minimal hydrodynamic force that is required to move a sphere that is located atop a closely packed three dimensional arrangement of spheres of the same size (figure 33). Coleman's moment formulation is given by the following equation:

$$\frac{4}{\sqrt{2}} F_D + F_L = G \qquad (12)$$

where, G is the submerged weight of the sphere and is equal to $G = g\frac{1}{6}\pi(\rho_s-\rho)d^3$, ρ_s is the density of the sphere, ρ is the density of the fluid and d is the sphere diameter; F_D denotes the drag force, which is assumed that is acting on the center of the sphere and is given by the following relation:

$$F_D = \rho \frac{1}{2} C_D d^2 \mathbf{U}_f^2 \qquad (13)$$

where, $\mathbf{U}_f$ is the mean flow velocity at the centerline of the particle, and C_D is the drag coefficient. The lift force, according to Coleman, acts along the line of action of the submerged weight and is equal to:

$$F_L = K\,G \qquad (14)$$

where, K is a lift factor.

To complement his analysis, Coleman performed experiments by using two spheres of the same size and different densities. Coleman indicated that the function of the drag coefficient C_D with the particle Reynolds number, $Re_p=(u_* d/\nu)$, for the sphere at rest, is essentially the same as for a sphere in free fall over a range of Reynolds numbers from about 50 to 9400. Also, according to Coleman, the lift coefficient K (in equation (14)) varies with respect to the particle Reynold number. For $Re_p<100$, K takes negative values while obtains its maximum value ($K_{max} \cong 0.5$) for $Re_p \cong 300$.

Coleman's model is limited to the case of a sediment particle being fully exposed to the flow. His model predicts quite well the corresponding experimental critical stress value for the 2 % packing condition obtained from the present experiments (table 8).

Wiberg and Smith (1987) provided an expression for the critical stress of a sediment particle that is derived from the balance of forces acting on individual particles at the surface of a bed. In their model they define the lift force as follows:

$$F_L = (1/2)\,\rho\, C_L\,(\mathbf{U}_{fT}^2 - \mathbf{U}_{fB}^2)\,\pi\, d^2 \qquad (15)$$

where, C_L is the lift coefficient and is equal to 0.2, $\mathbf{U}_{fT}$ is the longitudinal velocity at the top of the grain and $\mathbf{U}_{fB}$ is the longitudinal velocity at the bottom of the grain. They calculate the velocity at the bottom and top of the grain by extending the logarithmic

velocity profile to $z = z_o$, where, z denotes the vertical direction to the flume bed, and z_o = d/30 is the distance above the zero velocity plane. Typically the zero velocity plane is defined to be at z= 0.2 d below the top surface of a particle (Bridge and Bennett, 1992). The Wiberg and Smith method over-predicts the value of the critical stress for the lower surface packing conditions (for 2% to 35%) but it approximates closely the critical stress value for the 50% and 70 % packing conditions. One reason that this model over-predicts the critical stress values, for the low surface packing densities, is because it considers the sliding of sediment as the initial mode of entrainment instead of the rolling (they consider in their formulation the balance of forces instead of the balance of moments). Also, the way that the lift force is formulated seems to represent closely the entrainment conditions (of a ball by the flow) that exist for the higher surface packing configurations, namely the 50% and 70% cases (see, the discussion by Yalin, 1977 regarding the formulation of the lift force). The Wiberg and Smith model assumes the validity of the logarithmic velocity profile in the ball region.

Ling (1995) based his work on the findings of Coleman (1966) and Wiberg and Smith (1987). He expresses the lift force as follows:

$$F_L = a_s \rho n^{0.5} d^2 \mathbf{U_f} \left(\frac{\partial \mathbf{U_f}}{\partial z}\right)^{0.5} \qquad (16)$$

where, α_s is the Saffman lift coefficient and is equal to 1.615, ν is the fluid viscosity, $\frac{\partial \mathbf{U_f}}{\partial z}$ is the velocity gradient at z_o=d/30. Ling defines two threshold conditions for a sphere, one for rolling and one for lifting. For the rolling condition he uses equation (12), while for the lifting he requires that the lift force is equal to the submerged weight of the sphere. Ling indicates that the lifting and rolling threshold values are far apart at low

Reynolds numbers but they approach each other as the Reynolds number increases. Ling, in his calculations, assumes that the sand roughness k_s is three times the diameter of the particles. This assumption may be the reason for the overestimation, by his method, of the dimensionless critical stress value especially for the low surface packing conditions (table 8). Also, the extension of the logarithmic velocity profile in the ball region may be responsible for the overestimation of the critical stress by his model. Ling recognizes the fact that the criterion of incipient motion depends on the bed surface packing conditions and emphasizes the need to conduct experiments that will examine the interaction of the turbulent flow parameters with roughness. This interaction is discussed at the last section of this chapter for the different surface packing condition data that are collected here.

Table 8, also, demonstrates the critical stress values that are obtained from the Shields (1936) and Paintal (1971) methods. They determined the critical stress by performing tests in which different fluid stresses are applied to a bed that consists of natural sediment. In these tests the bed - load discharge is measured by collecting the transported sediment at the downstream end of the flume. Then by extrapolation to zero transport the critical stress is computed. Paintal computed a dimensionless critical stress of 0.05 value by performing two separate tests for bed material sizes of 2.5 mm and 7.95 mm. Although the material that is used in his study is uniform and the bed is tampered, there is no information on the existing surface packing conditions during his tests. For comparison purposes it is assumed that the bed configuration during the Paintal tests corresponds to the 70% packing. Paintal reports sediment motion even for stress values less than 0.04, however, he considers the value of 0.05 as the critical. Finally, Shields

(1936), for the same range of particle Reynolds numbers that are examined here, obtained critical stress values that vary within the range of 0.048 to 0.06 (Table 8).

Neill and Yalin (1969) stated that is not possible to observe in practice "the real beginning of movement, but only a certain degree of established movement" and defined an initial motion criterion for unisize sediment based on kinematic similarity,

$$\frac{nd^3}{u_*} = N \qquad (17)$$

where, n is the number of grains that are displaced from an area over a period of time, u_* is the shear velocity, d denotes the particles diameter and N is a constant. From practical concerns Neill and Yalin suggested a value of 10^{-6} for N.

The Neill and Yalin semi-empirical model over predicts the number of balls that are transported for the 2%, and 20% packing conditions (table 9). It provides a better estimate of the number of balls that are entrained in the intermediate packing conditions (i.e. 35% and 50 % cases), while it underestimates the number of balls entrained for the 70% case. The significant deviation in the lower packing conditions may be attributed to the following reasons: first, the Neill and Yalin criterion does not account for the effects of packing and thus, the suggested value of N must be too high for these packing conditions; second, equation (17) does not account for the role of clustering on the initiation of motion. Specifically, although the number of balls that are initially displaced from their position is rather significant (tables 2, and 4), the number of balls crossing a line is relatively small. This is due to the fact that most of the displaced balls get trapped within the cluster microforms. Also, in the 20% case the cluster structures are stable and therefore after their formation distrainment of particles dominates over entrainment. The flow conditions are more severe in the 35 %, 50 % and 70 % packing cases and thus,

when the balls get dislodged from their initial position tend to travel for larger distances and longer time periods.

The Neill and Yalin (1977) criterion cannot be directly applied to mixed - size sediments because of the difficulty of defining a common time scale for the individual grain sizes in a bed with mixed sizes. Wilcock (1988) proposed the following criterion to scale the observations for the different sediment sizes in each mixed bed

$$\frac{n_i d_i^3}{f_i} = \text{constant} \qquad (18)$$

where, n_i is the number of grains of ith size fraction displaced per unit bed area, d_i is the grain diameter of the ith size fraction, and f_i is the proportion of the ith size fraction present on the bed surface. Wilcock suggested that a combination of equation (18) with (17) might be a good predictor of the entrainment process of mixed size sediment. Scaling problems, however, make equation (18) very difficult to be implemented for most mixed - size sediments.

One of the most representative reference transport models in the sediment transport area is the Parker et al. model (1982) (known in the literature as the P.K.M model). They defined the reference transport rate in terms of a constant value of the fractional transport parameter W_i^*

$$W_i^* = \frac{(s-1)gq_{bi}}{f_i u_*^3} \qquad (19)$$

where, q_{bi} is the transport rate of a fraction i in terms of volume transport per unit width and time, and f_i is the proportion of a fraction i in the bed surface sediment. The use of $W_i^* = 0.002$, proposed by Parker et al. as a reference transport rate is an arbitrarily value.

The predictive ability of the P.K.M. model is examined here by considering f_i to be equal to 1 and converting the volume transport rate to mass. The Parker et al. model provides bedload transport rates, here in terms of the number of balls entrained per unit time per unit area, that are approximately 12 times larger than the experimental values for the first two packing conditions (table 9). The predictions given by the P.K.M. model for the transported number of particles do not deviate significantly for the intermediate cases (35% and 50%). The model predicts quite well the transport rate for the 70% case. In this case the fraction of displaced particles is almost the same with the fraction of the particles crossing a line (when the balls get entrained tend to accelerate and reach to the basket without any intermediate stops).

Finally, Jain (1992) conducted a very interesting study regarding the entrainment of sediment. His model considers that the "bursting events" are responsible for the entrainment of sediment. His basic concept is that during a bursting period j, a fraction of particles, G_{ij}, crosses a line when particles from a subreach i get transported to a subsequent subreach. The entrained particles are called "disturbed" particles. Jain incorporates into his model the sediment availability factor, which is defined as $(1-\lambda)$, where λ is the porosity of the bed. The sediment G that is transported in terms of mass per unit width of the channel per unit time is equal to,

$$G = \rho_s A d(1-\lambda) G_{ij} / T_B \qquad (20)$$

Where, A denotes the area of the test section, ρ_s is the particles density, and T_B is the bursting period (equation (8)). A comparison between the Jain model and the

experimental data is possible here by assuming that the fraction of particles crossing a line and the fraction of displaced particles over a bursting period is the same. This means that G_{ij} obtains the values of P_E. Based on this consideration the Jain entrainment formula seems to predict quite well the experimental results for the 2%, 35%, 50% conditions, and extremely well for the 70%. Table 9 illustrates, that equation (20) overestimates the bedload transport for the 20%. This indicates that the above assumption, of $G_{ij}=P_E$, is unrealistic in the 20% case. Equation (20) provides considerable advantages compared to the other methods. It accounts for the role of surface packing density on the entrainment of sediment, by including the term $(1-\lambda)$ in equation (20), and considers that the bursting period T_B is indicative of the time scale associated with sediment entrainment. The Jain formula is reconcilable to the Neill and Yalin semiemprirical equation if the $(1-\lambda)$ term is excluded from equation (20) and the bursting period is replaced by a time term $t=d/u_*$, where, d is the particles' diameter and u_* is the friction velocity. In this case G_{ij} is equivalent to N.

5.2. Distributions of the Flow Quantities

To obtain the time-averaged velocity profiles and other statistical characteristics of the flow for the different surface packing conditions that are examined here, measurements at different locations of the bed are carried out. However, for the repeated tests lead balls replace the glass beads. This is to avoid any motion of particles that may cause reflection of the laser beams (i.e. the measurements are obtained in the vicinity of balls) and to deter any clustering that may occur if glass beads are used. The lead balls have the same diameter with the glass beads. For all the packing conditions except the

70% case the measuring location of the laser is chosen to be 1 ball diameter upstream of the center of a lead ball, 1 ball diameter downstream of the ball center, and atop the ball (i.e. the top point at the middle). Figure 34(b) shows the measuring points along the vertical direction z at the locations A, B, and C. Specifically, for the 2% case 30 measurements are obtained for each location A, B, and C. For the 20% case 45 measurements are carried out; and for the 35% and 50% cases 42 measurements. The distance among the measuring points along the vertical direction differs. Typically this distance varies within the range of 0.000254 mm to 0.0254 mm (figure 34(b)). The reference level for the measurements in the 2%, 20%, 35%, and 50% cases is considered to be below the top of the fourth layer balls at a distance of 0.2 d (where, d is the particle diameter). The lowest measuring point at the location A has a ratio of z/d =0.889 and for the locations B and C the ratio z/d is equal to 0.0897.

For the 70% packing condition 40 measurements are obtained at 2 locations, D and E (figure 34(b)). The location D is found in the cavity of the tightly packed balls while the location E at the top of a ball. The reference level of the measurements in the 70% case is considered the top of the balls at the fifth layer. The lowest point in both locations E and D has a ratio of z/d equal to 0.565.

To obtain good estimates of the turbulence statistics 3072 measurements are collected out for each measuring point. Each of these 3072 measurements has three velocity components, which are called triplets. The triplets are instantaneous velocity values.

There are several sources of measurement uncertainty in LDV systems, namely, the digital truncation error, the particle lag, the velocity gradient error, the angular bias, the fringe spacing uncertainty, and statistical sampling error (Balakrishnan and Dancey,

1994). The most frequent errors are introduced by the uncertainty in the LDV fringe spacings on the separate channels and by the uncertainty in the angles that characterize the LDV geometry (i.e., the angular orientation of the LDV beam geometry to the flume coordinate system). Finally, another error is the velocity bias that is introduced by the way measurements are effected by a laser system. Velocity bias is introduced because the scattering particle that is brought to the laser measurement volume depends on the fluid velocity, which means that particles that are enveloped in faster moving parcels of fluid cross the laser volume more frequently, thus biasing the measurements toward higher velocities. Several schemes have been proposed to eliminate velocity bias (Edwards, 1987). Velocity bias schemes are applied through a weighting function, $\hat{W}$. If U is the instantaneous velocity in the streamwise direction then its velocity-bias corrected mean value is:

$$\overline{U} = \frac{\sum_{i=1}^{k} U_i W_i}{\sum_{i=1}^{k} W_i} \tag{21}$$

where, k is the number of measurements per point.

Similar expressions can be written for the other velocity components V and W.

Also, the corrected r.m.s quantity for the streamwise velocity is given by the equation,

$$u' = \sqrt{\frac{\sum_{i=1}^{k} (U_i - \overline{U})^2}{\sum_{i=1}^{k} W_i}} \tag{22}$$

The fluctuating velocity in the longitudinal direction is computed as,

$$u = U - \overline{U} \qquad (23)$$

Similar expressions can be written for the fluctuating velocities in the other two directions. The instantaneous Reynolds stress is computed as the product of the fluctuating velocity components u and w.

The total time-averaged shear stress τ is well represented by the Reynolds stress over a large distance, if the flow Reynolds number is large. Thus,

$$\tau = -\rho \overline{uw} = \rho u_*^2 (1 - z/H) \qquad (24)$$

The friction velocity u_* is calculated here by performing a least squares regression of the experimental stress data about the theoretical linear total stress for all the packing conditions (equation (24)). Table 10 provides a comparison of the values of u_* that are computed by means of equation (24) and from the hydraulic relation $u_*=\sqrt{gHS}$. It is observed that the values of u_* that are computed from equation (24) and from the above relation are very close to each other for certain locations during the tests. For example, in the 20% case (E-20 test) the u_* computed from equation (24) at location B is very close to u_* that is calculated by means of the hydraulic relation. The differences in the values of u_* computed from (24) (for the three locations during the packing condition tests) reveal the effects of roughness to the flow structures around the balls. The values of u_* that are obtained from the hydraulic relation $u_*=\sqrt{gHS}$ are used here to normalize the different flow quantities.

5.2.1. Results

The steps that are involved in the post processing of the laser measurements are summarized in figure 35. More details for the postprocessing of data are given by Balakrishnan (in press). Figures 36-49 present the profiles of the mean velocity components in the three directions, of the turbulent intensities in the three directions, of the time average Reynolds stress, and the correlation coefficient. The mean velocities are normalized with the friction velocity, as well the intensities (i.e. r.m.s. of the velocity quantities) and the time average Reynolds stress. Thus, $U^+ = \frac{\overline{U}}{u_*}$ is the normalized mean velocity in the streamwise direction , $W^+ = \frac{\overline{W}}{u_*}$, is the normalized mean velocity in the vertical direction, and $V^+ = \frac{\overline{V}}{u_*}$ is the normalized velocity in the spanwise direction. The normalized turbulent intensities in the streamwise, vertical, and spanwise directions are defined respectively as u′/u*, w′/u*, and v′/u*, where, $u' = \sqrt{\overline{\overline{U}^2}}$, $w' = \sqrt{\overline{\overline{W}^2}}$, and $v' = \sqrt{\overline{\overline{V}^2}}$. The normalized time average Reynolds stress is defined as $\frac{(\overline{uw})}{u*}$ and the correlation coefficient as R.

Figures 36(a), 39(a), 42(a), 45(a), and 49(a) illustrate the velocity distributions atop the ball (location A) for the packing conditions that are examined here. In the 2% case, U^+ varies within the range of 8 to 10, while W^+ and V^+ obtain positive but small values, with W^+ being larger than V^+. Figure 39(a) reveals the existence of a high velocity gradient in the streamwise direction. The U^+ component varies within the range of (2,14) approximately. Also, in this case V^+ is more dominant than W^+. The velocity

gradient of the streamwise velocity reduces in the 35% case as shown in figure 42(a). In this case $W^+ \approx 0$ and V^+ obtains negative values. Similar velocity distributions are shown in figures 45(a) and 49(a) for the 50% and 70% cases respectively. For the location B (one ball diameter upstream of the center of the ball) figures 37(a), 40(a), 43(a), and 48(a) indicate the same trend for the velocity distributions with the one that is observed for the location A. A noticeable difference between the velocity distributions in A and B locations in the 2% case is that W^+ obtains negative values in location B. Also, the U^+ profile in the 35% case (location B) is less steep than the corresponding profile in the location A. The U^+ distribution in location C (one ball diameter behind the ball) for the 2% case reveals the presence of a high velocity gradient in the streamwise direction (figure 38(a)). Also, W^+ in this case becomes positive (the same sign as in the A location). Finally for the remaining packing cases, the differences that exist in the U^+ distributions, for the locations A and C, are less profound (see figures 41(a), 44(a), and 47(a)).

In the present study we examined if the log law is valid within the vicinity of a ball. Table 11 illustrates that the log law ($U^+=(1/\kappa)\ln(z+z_0) + B_r$) cannot be used to describe the velocity distribution very close to a ball. The values of the constant B_r that are calculated here differ from these reported in the literature, i.e. $B_r=8.42\pm15\%$ (Reynolds, 1974) and the Karman's constant κ does not equal to 0.4. Subsequently, any calculations that are made based on the log law, in the vicinity of a particle, it is expected to yield wrong results.

Figures 36(b)-49(b) provide the distributions of the normalized turbulent intensities. It is illustrated there that u'/u_* and w'/u_* have a tendency to decrease as the

distance of the bed increases. Similar behavior has been reported by Grass (1971) and by McQuivey and Richardson (1969). Also, from the above distributions it is shown that $w' \approx 0.59u'$. McQuivey (1973) indicated a similar relation for the two r.m.s. quantities. He obtained $w'=0.77u'$. The scattering that is observed in the spanwise direction data (for the v' quantity in figures 36(b)-49(b)) reveals the weakness of non-orthogonal LDV systems. Specifically, Dancey (1990) showed that the spanwise component is very sensitive to errors when the coupling angle of the LDV system is small. Finally, the above figures indicate that the values of the v' quantity are high compared to the values of the other two r.m.s quantities. Similar observations have been reported in the literature by Cline and Deutsch (1993), Song et al. (1994), and by Meyers (1985). Cline and Deutsch suggested that the vibration of the probe volume is a likely contributor to these elevated values of v'. According to Meyers the inaccuracies in the measurement of v' can be attributed to the limitations of the non-orthogonal LDV systems. The v' component is known in the literature as the elusive third component (Meyers, 1985).

The distributions of the nondimensional Reynolds stress are shown in figures 36(c)-49(c). The anticipated behavior for the Reynolds stress is that it will vary linearly with respect to z. Figures 36(c.)-49(c.) reveal that the stress distribution very close to the bed is complicated. Similar remarks were made by Steffler et al. (1985). It is also interesting to note that $\overline{uw}$ in the 2% and 20% cases obtains positive values near the ball and negative values for almost z/d >1.4 (figures 36(c)-41(c)). This implies that very close to the ball there is a momentum flux exchange from the boundary to the core of the flow. $\overline{uw}$ does not change sign (i.e., it is always negative) for the rest of the packing cases.

The correlation coefficient R of U and W during the tests varies within the range of (-0.15,-0.45).

5.3 Summary

In this study it is shown that the existing deterministic models (i.e. theoretical and semiempirical) most of the times overpredict the critical stress value that is obtained experimentally here for the different surface packing cases (table 8). Traditionally, the theoretical models (e.g. Wiberg and Smith model) consider that the log law is valid in the ball region. The detailed flow measurements that are obtained here indicate that the log law is not a good predictor of the velocity distribution near the ball (table 11). Also, the existing models do not address the role of packing density on the initiation of sediment motion. However, figures 36-49 illustrate that the changes in the magnitude of the flow quantities for different packing conditions are rather significant and thus, the term of packing density should be included in the formulation of an entrainment model. For example, the behavior of the time average Reynolds stress alters with an increase in the packing density and with the location of the measuring points. The measurements reveal that its behavior is complicated near the ball.

The semiempirical models (e.g. Paintal, 1971) traditionally compute the critical stress value by measuring the sediment that is collected in the basket. The semiempirical models require for their calibration that the following parameters are known: the number of balls that are placed in the test section and the number of the balls that is collected.

The results that are discussed in this chapter suggest that the particles may not necessarily cross a line (i.e., be transported) after their dislodgement. The majority of the

particles after they get dislodged travel for small distances and then stop. The frequency of the displaced particles is significantly higher than the frequency of the particles crossing a line. By ignoring, therefore, the frequency of particles dislodged from their initial position we can deduce the wrong conclusions regarding the entrainability of the bed. To support further this argument table 12 is constructed. This table provides the ratio of the fraction of particles crossing a line with the fraction of particles that are displaced within the test section. The fraction of displaced particles in the 2%, 35%, and 50% cases is almost 80 times larger than the fraction of particles crossing a line. In the 20% case the fraction of displaced particles is almost 500 larger than the fraction of collected sediment and in the 70% case the two fractions tend to approach each other.

Table 8. Predictions of the dimensionless critical stress value from different deterministic models.

Tests	Particles Reynolds Number, $Re_p=(u_*d)/\nu)$	Experimentally determined critical stress	Shields method	Lings' method	Colemans' method	Wiberg - Smiths' method	Paintals' method
E-2	250.56	0.008	0.048	0.072	0.011	0.057	-
E-20	292.21	0.011	0.05	0.08	-	0.05	-
E-35	536	0.037	0.062	0.091	-	0.06	-
E-50	598.22	0.048	0.065	0.096	-	0.06	
E-70	756.69	0.074	0.065	0.12	-	0.06	0.05-

Table 9. Entrainment rate of particles in terms of number of balls per unit area per unit time.

Tests	Number of balls transported over an area per unit time (balls/m^2/s)	Neill and Yalin model (equation (12)) n (balls/m^2/s)	PKM model (q_{bi} in equation (14) is multiplied by the density of solids and the weight of a ball) (balls/m^2/s)	Jains model (equation (20))
E-2	$1.21\ 10^{-3}$	0.061	0.0147	$4.71\ 10^{-3}$
E-20	$1.82\ 10^{-3}$	0.07	0.022	$3.63\ 10^{-2}$
E-35	$2.36\ 10^{-2}$	0.13	0.144	$1.09\ 10^{-2}$
E-50	$5.44\ 10^{-2}$	0.146	0.2	$2.02\ 10^{-2}$
E-70	$4.56\ 10^{-1}$	0.182	0.4	$3.36\ 10^{-1}$

Table 10. A comparison table for the friction velocity.

Tests	Friction velocity u* (m/s) (equation (24))			Friction velocity u*= $\sqrt{gHS}$, u* (m/s)
	Locations			
	A	B	C	
E-2	0.0185	0.0207	0.036	0.0313
E-20	0.0249	0.0381	0.025	0.036
E-35	0.067	0.015	0.014	0.067
E-50	0.054	0.056	0.061	0.075
	Locations			
	E	D		
E-70	0.0778	0.082		0.093

Table 11. The values of the constants in the Log law for all the tests.

Tests	Location	B_r	$1/\kappa$
E-2	A	13.8	5.33
	B	15.7	1.98
	C	8.9	1.28
E-20	A	-1.99	0.17
	B	-2.31	0.28
	C	13.87	5.22
E-35	A	4.55	4.56
	B	24.61	24.6
	C	26.03	24.03
E-50	A	5.7	0.054
	B	6.08	0.056
	C	5.17	0.061
E-75	E	6.96	0.334
	D	6.91	0.336

Table 12. The ratio of the frequency of displaced particles with the frequency of the particles crossing a line.

Tests	ratio, (F_d/F_c)
E-2	68
E-20	499
E-35	89
E-50	67
E-70	12

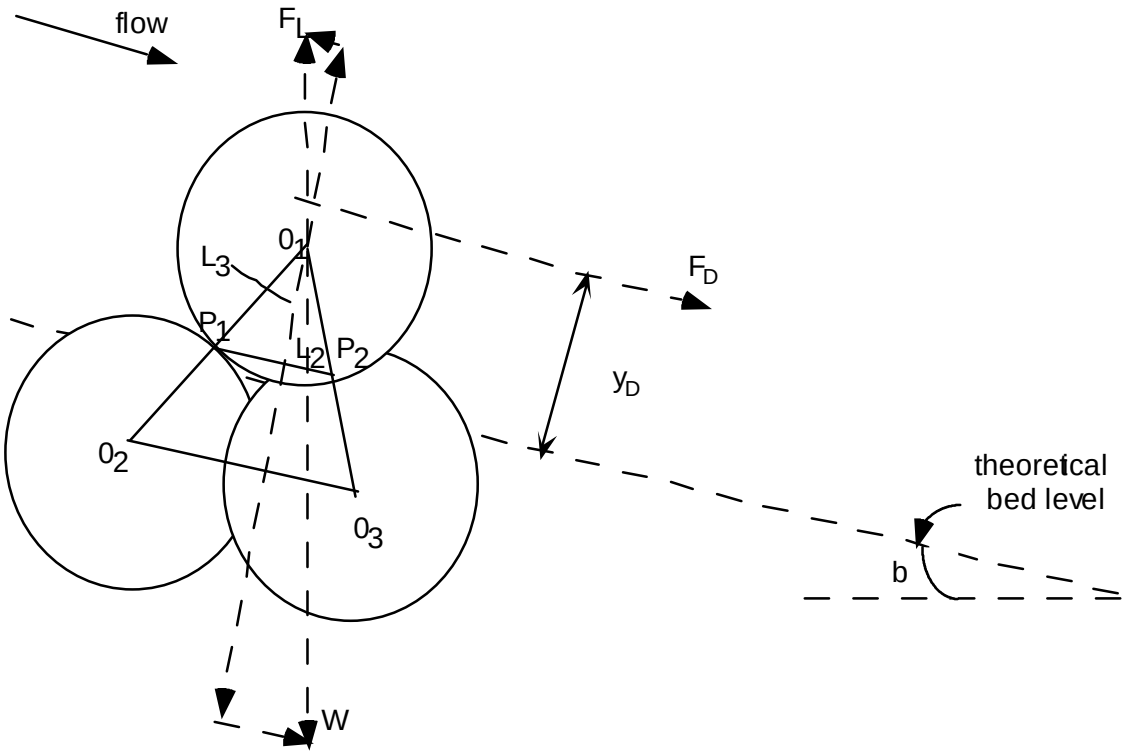

Figure 33. Forces acting on a particle that is fully exposed to the flow

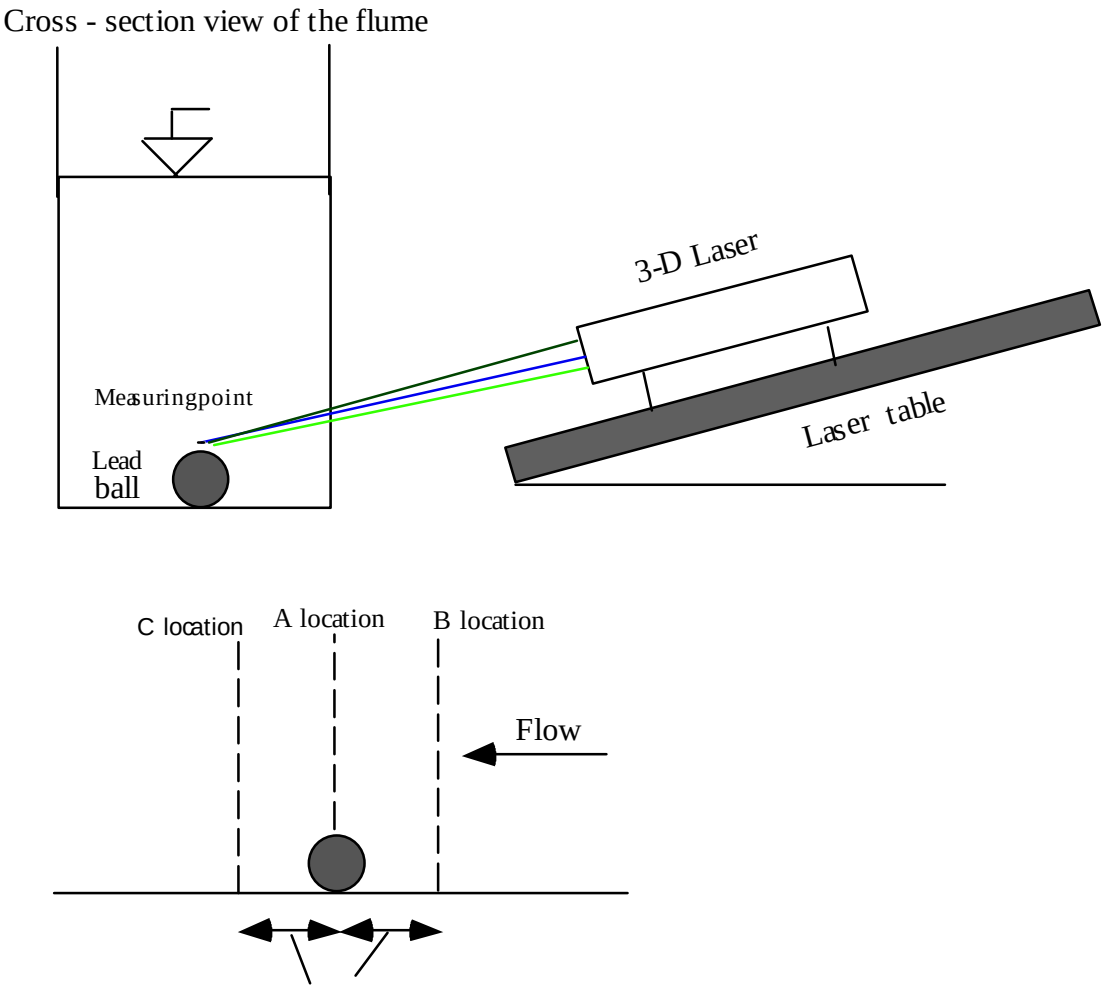

Figure 34 (a). Measuring locations of the LDV system.

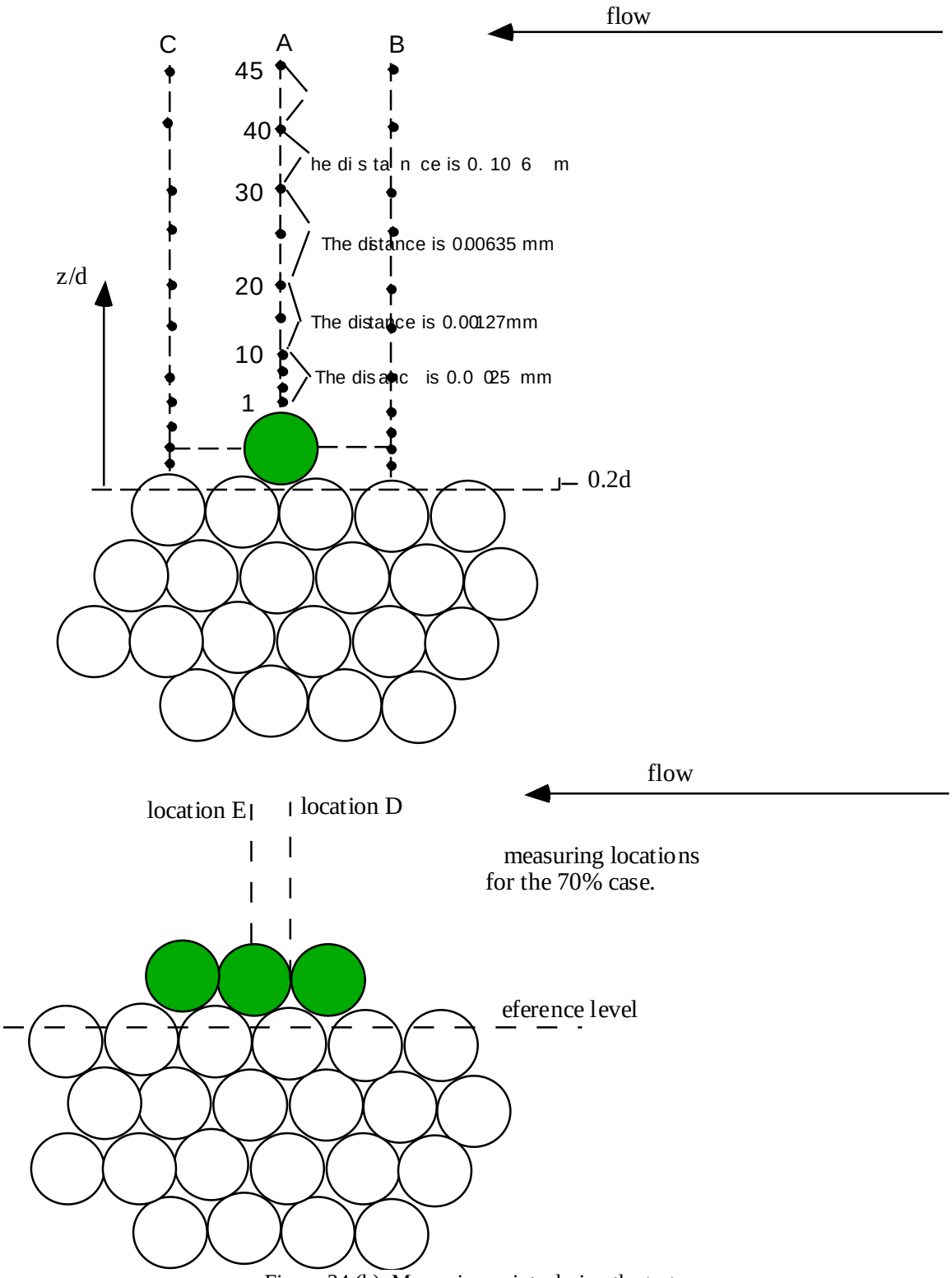

Figure 34 (b). Measuring points during the tests.

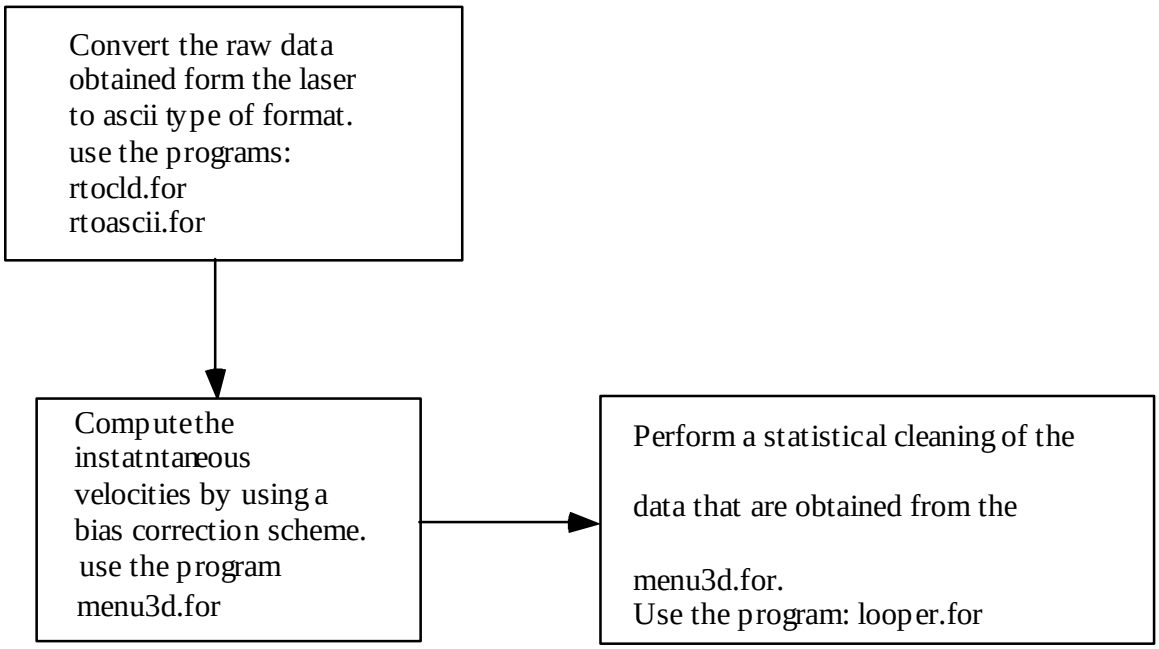

Figure 35. A flow chart of the postprocessing analysis of LDV data.

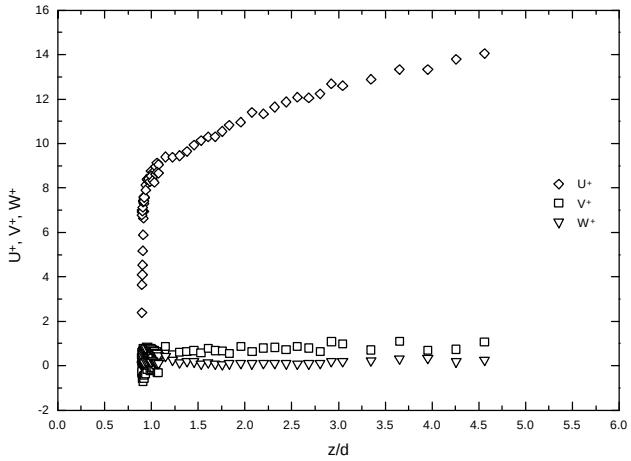

Figure 36(a). The velocity profiles at location A (2% packing condition).

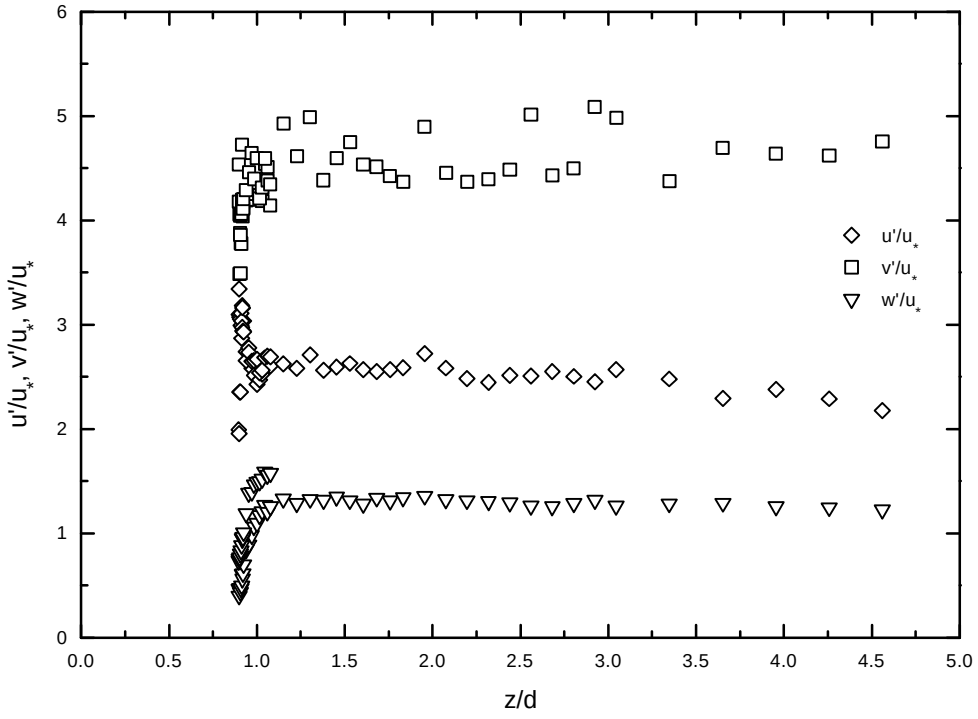

Figure 36(b). Distributions of the turbulent intensities at location A (2% packing condition).

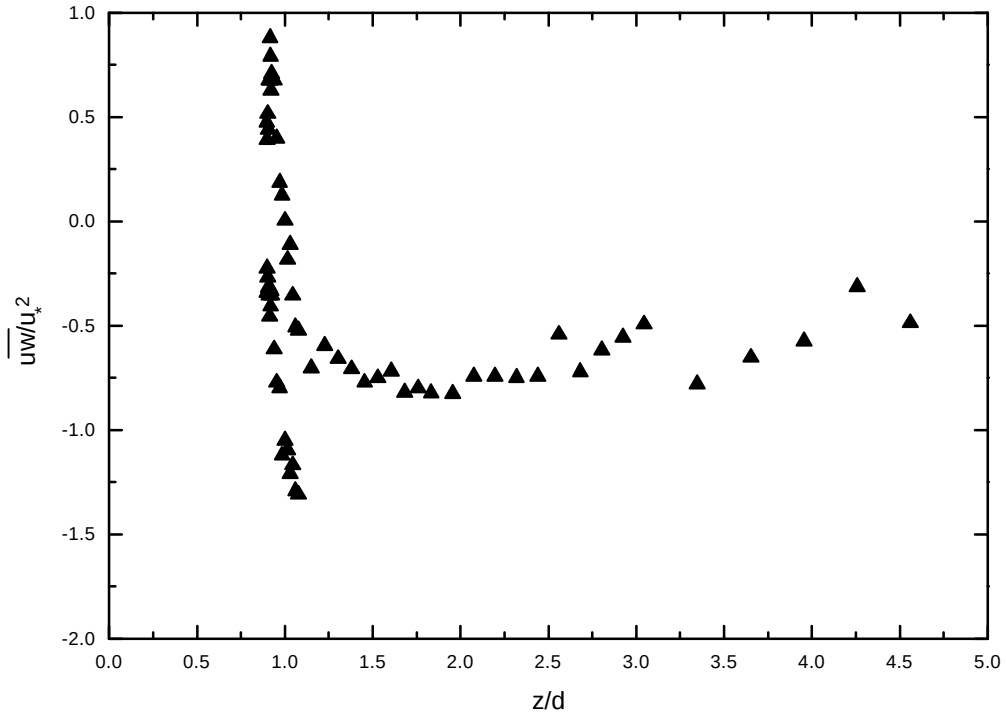

Figure 36(c). The distribution of Reynolds stress at location A (2% packing condition).

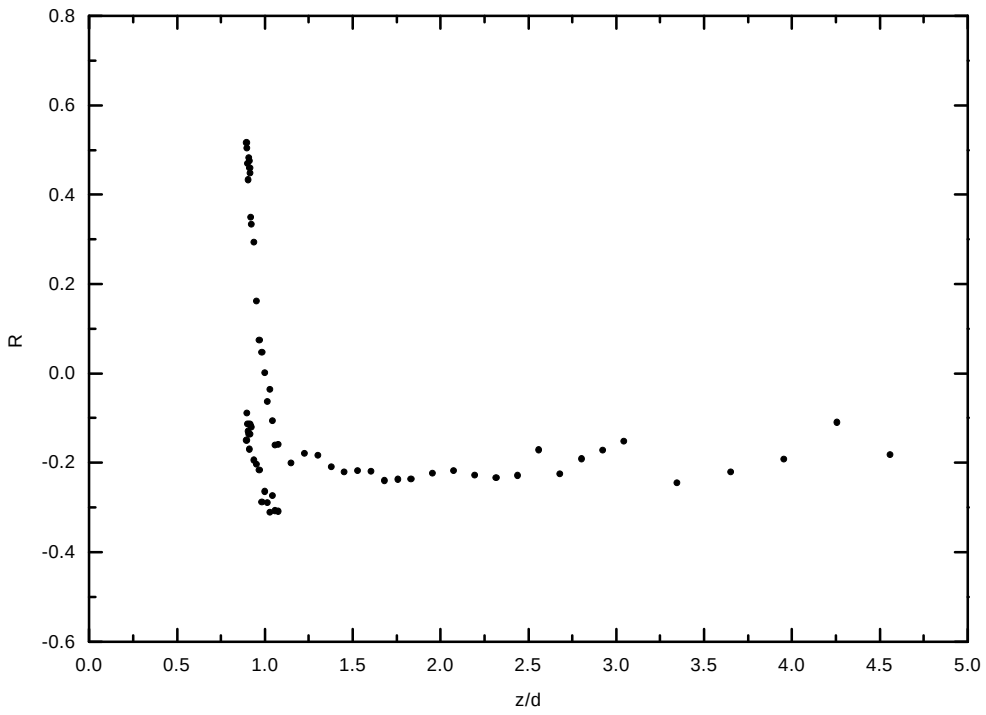

Figure 36(d). The distribution of the correlation coefficient R at location A (2% packing condition)

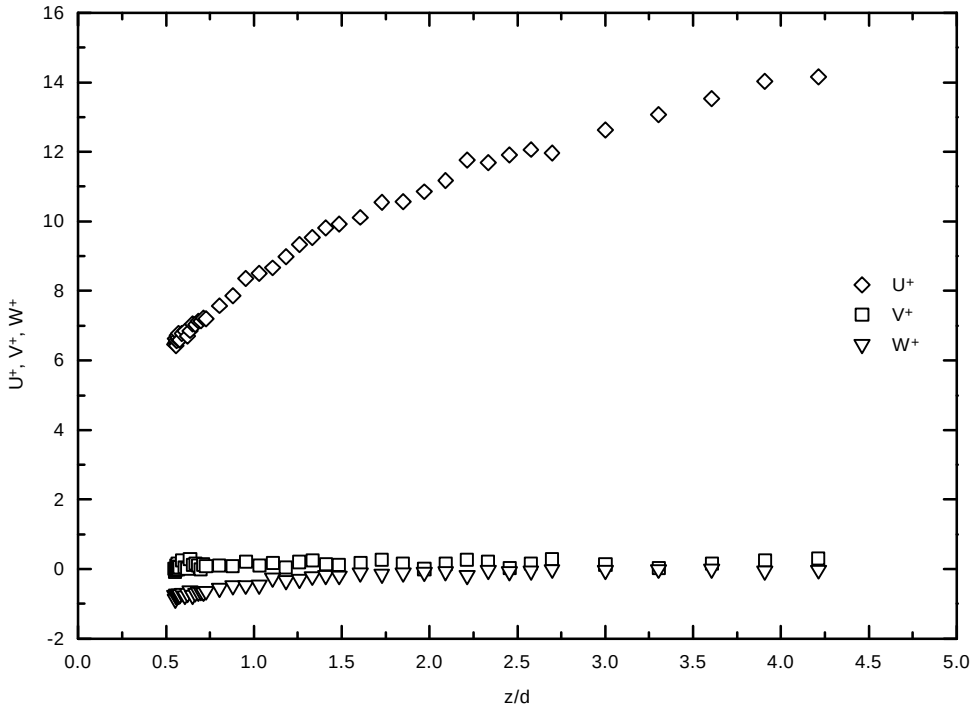

Figure 37(a). The velocity profiles at location B (2% packing condition).

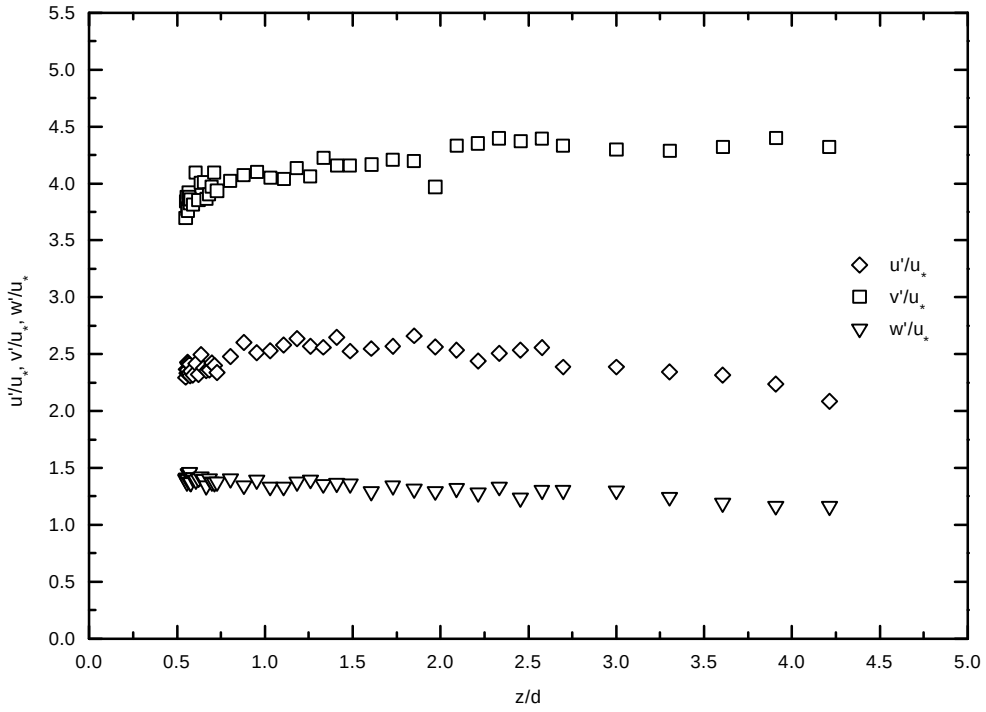

Figure 37(b). Distributions of the turbulent intensities at location B (2% packing condition).

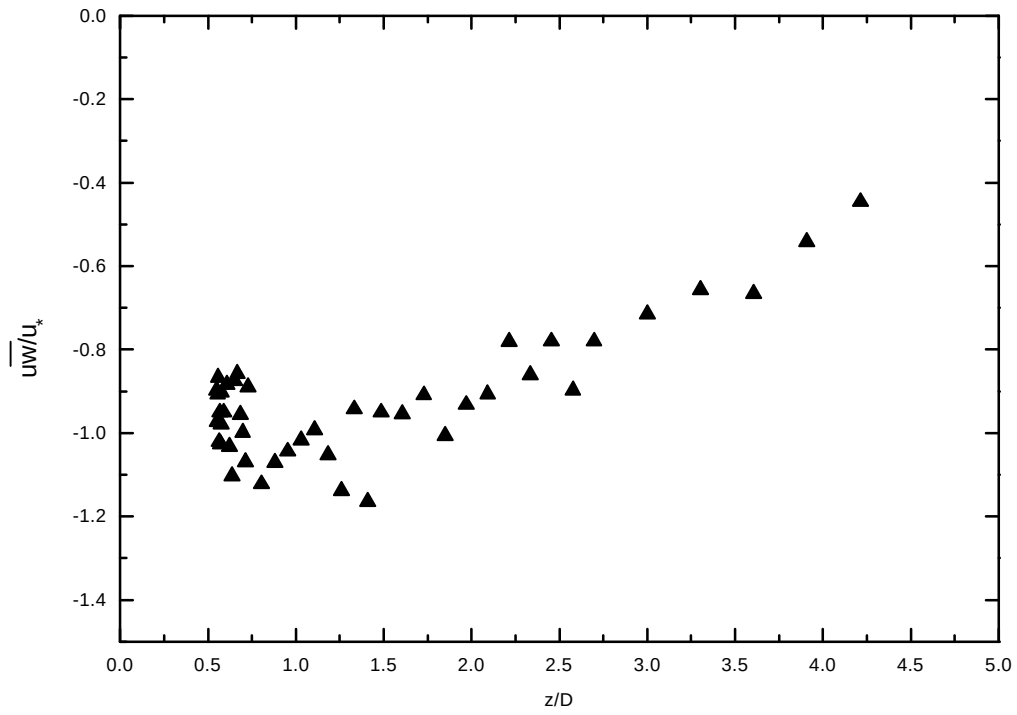

Figure 37(c). The distribution of the time averaged Reynolds stress at location B (2% packing condition).

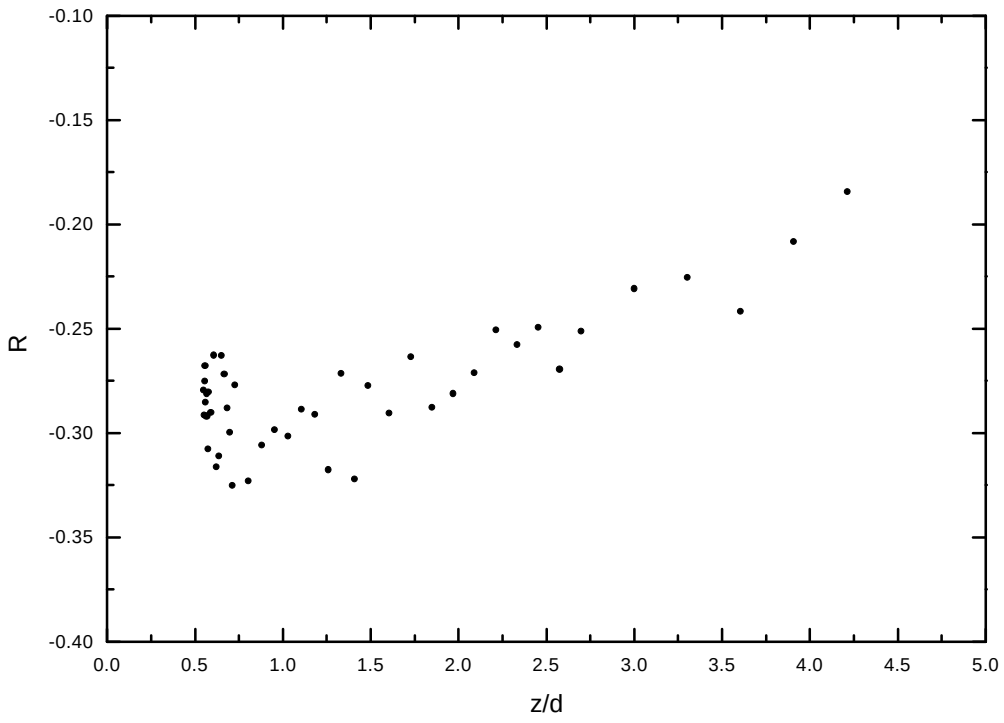

Figure 37(d). The distribution of the correlation coefficient at location B (2% packing condition).

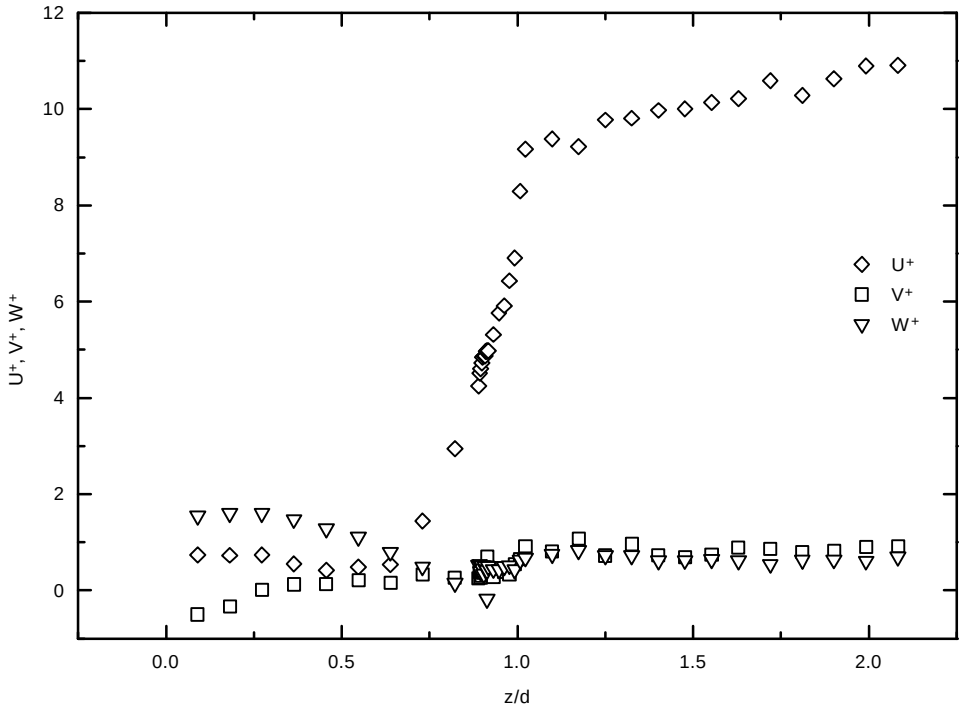

Figure 38(a). The velocity profiles at location C (2% packing condition).

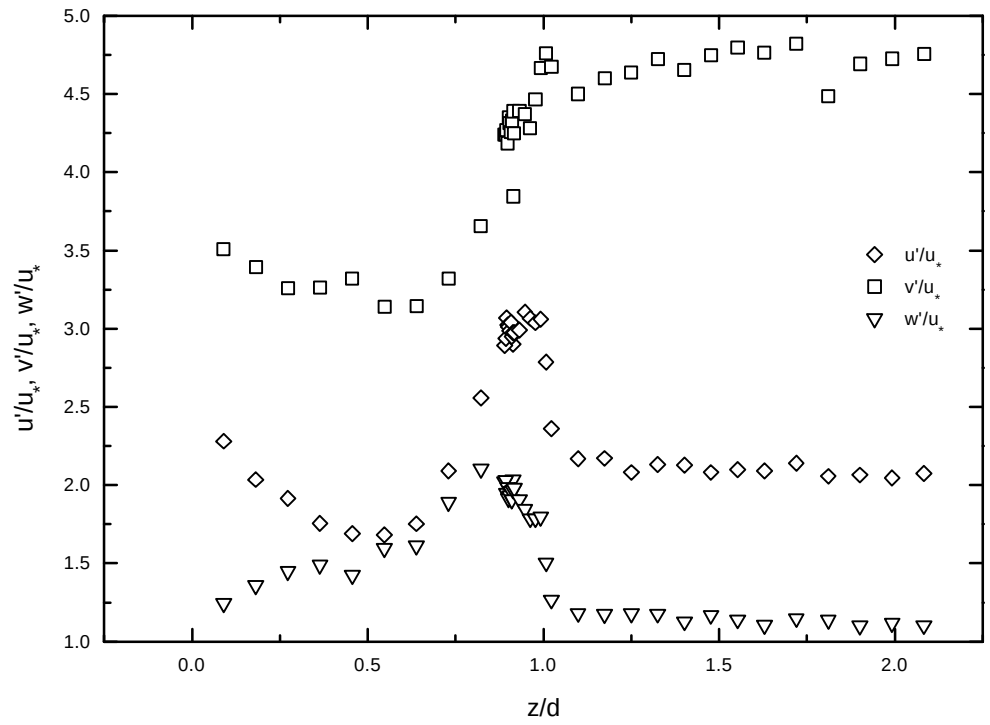

Figure 38(b). Distributions of the turbulent intensities at location C (2% packing

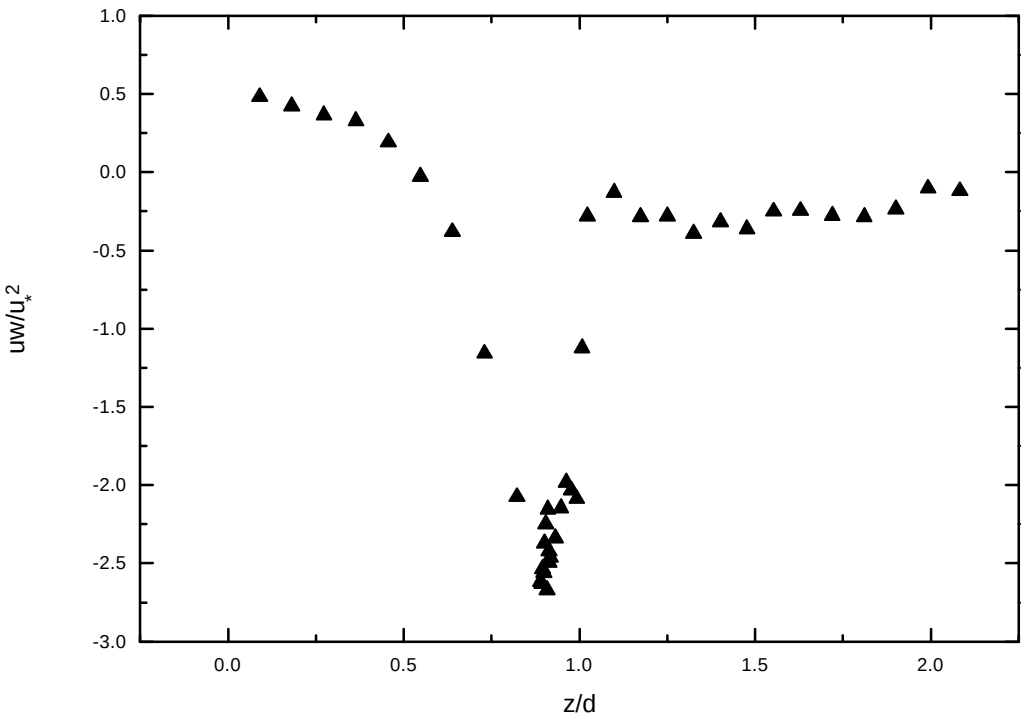

Figure 38(c). The distribution of the time averaged Reynolds stress at location C (2% packing condition).

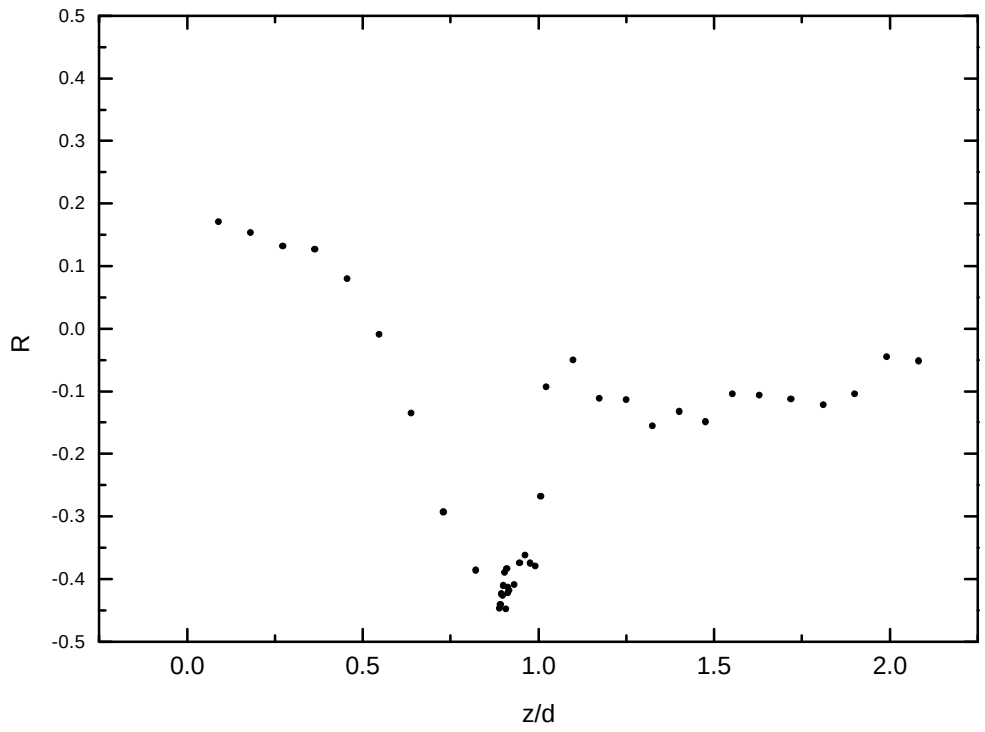

Figure 38(d). The correlation coefficient at location C (2% packing condition).

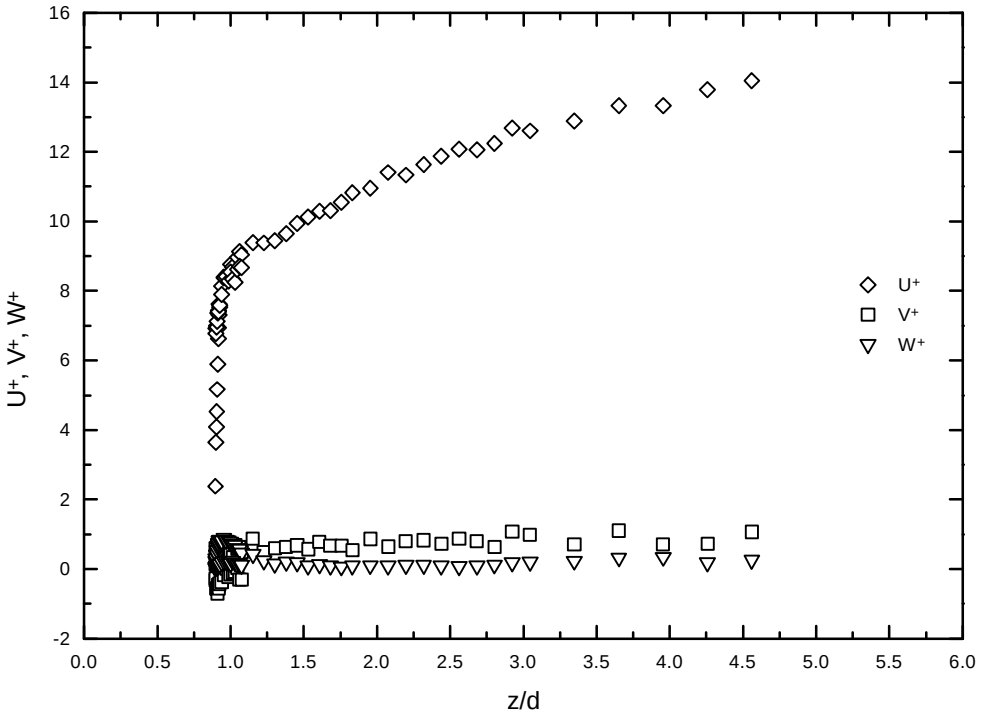

Figure 39(a). The velocity profiles at location A (20% packing conditions).

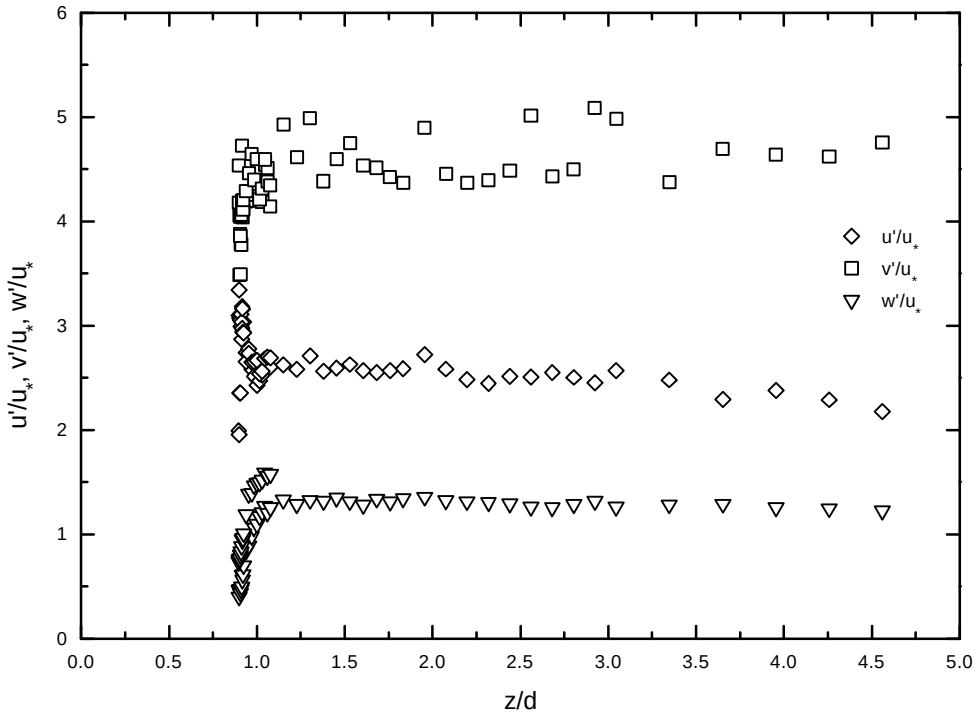

Figure 39(b). Distributions of the turbulent intensities at location A (20% packing condition).

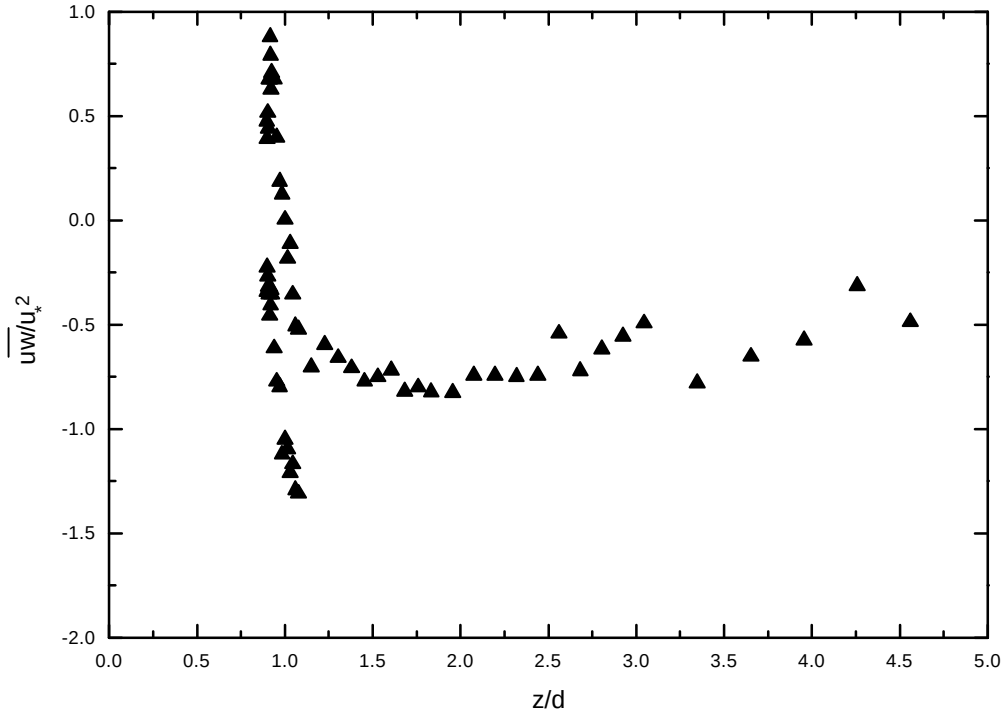

Figure 39(c). The distribution of the time averaged Reynolds stress at location A (20% packing condition).

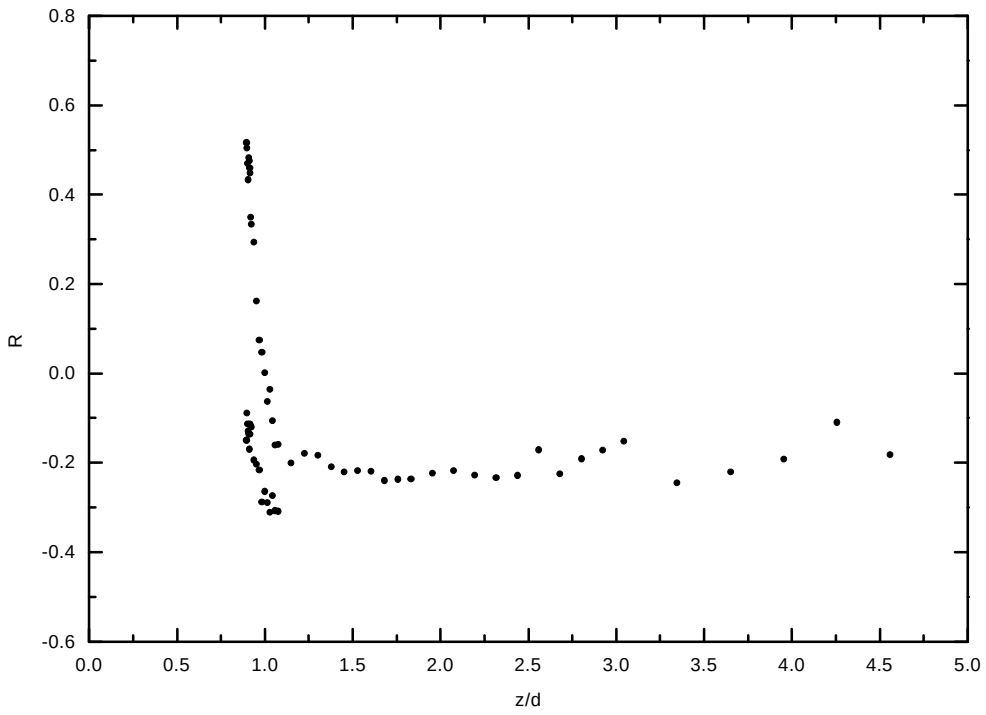

Figure 39(d). The distribution of the correlation coefficient R at location A (20% packing condition).

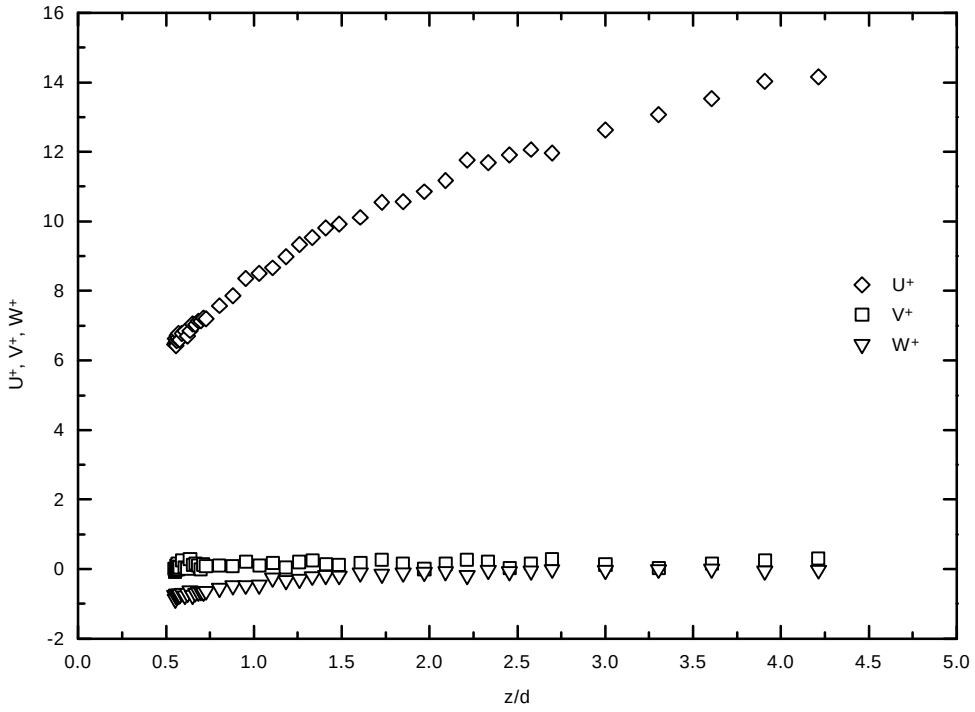

Figure 40 (a) The velocity profiles at location B (20% packing condition).

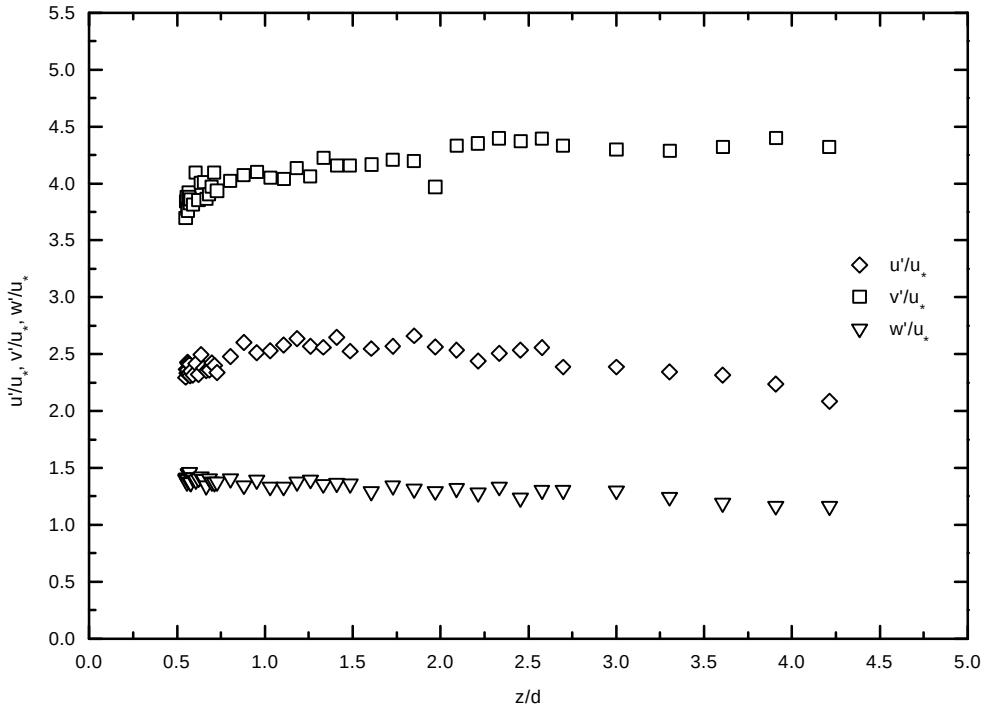

Figure 40(b). Distributions of the turbulent intensities at location B (20% packing condition).

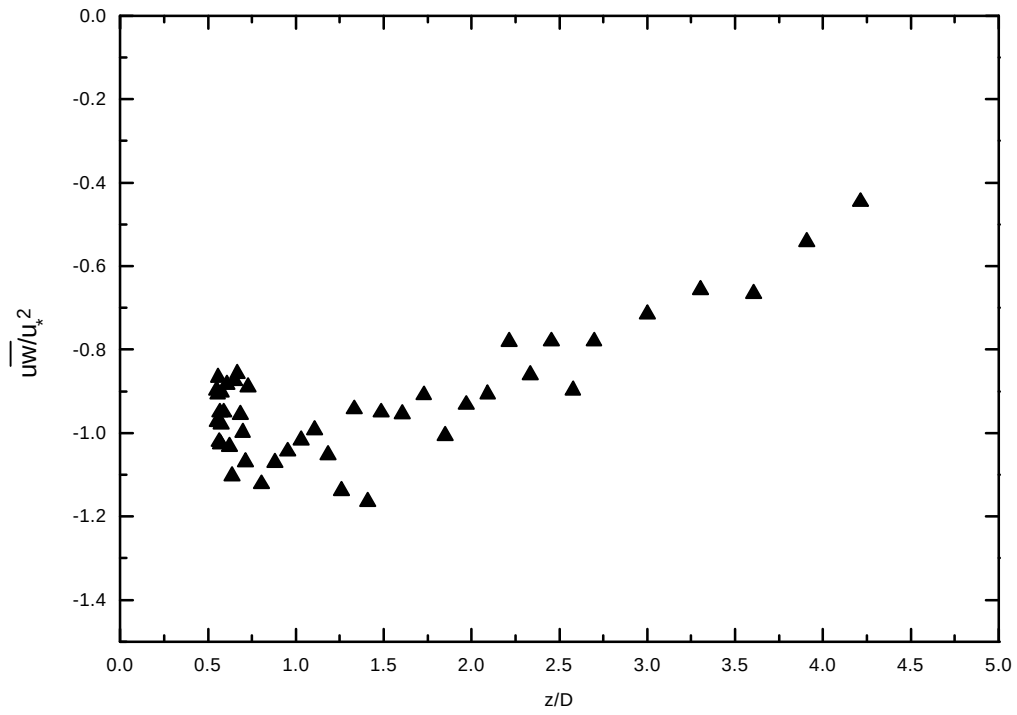

Figure 40(c). The distribution of the time averaged Reynolds stress at location B (20% packing condition).

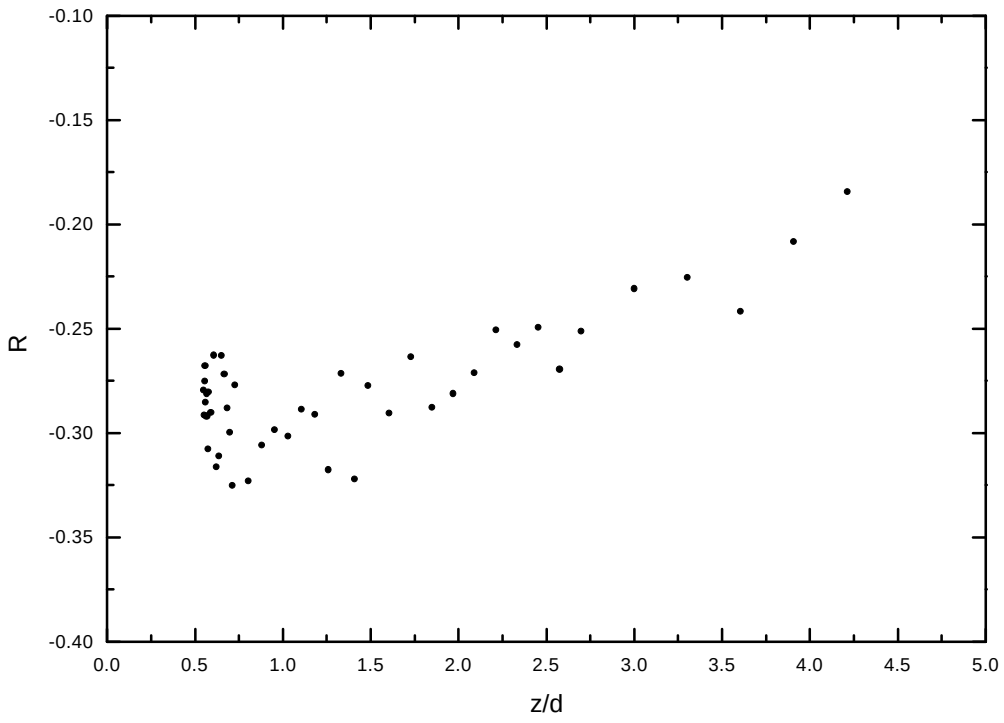

Figure 40(d). The distribution of the correlation coefficient R at location B (20% packing condition).

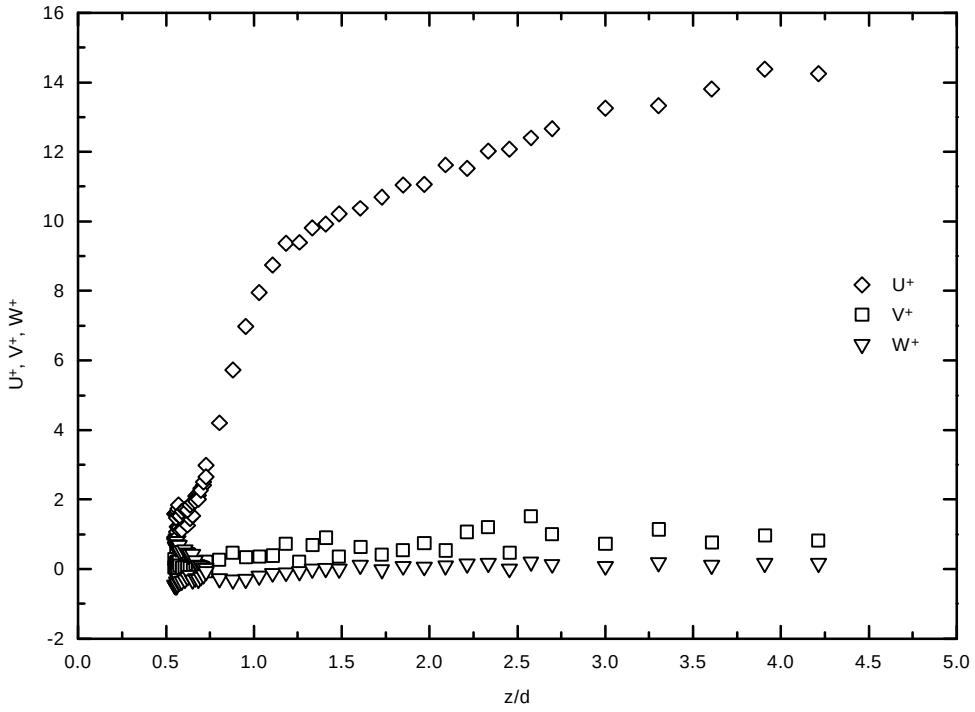

Figure 41(a). The velocity profiles at location C (20% packing condition).

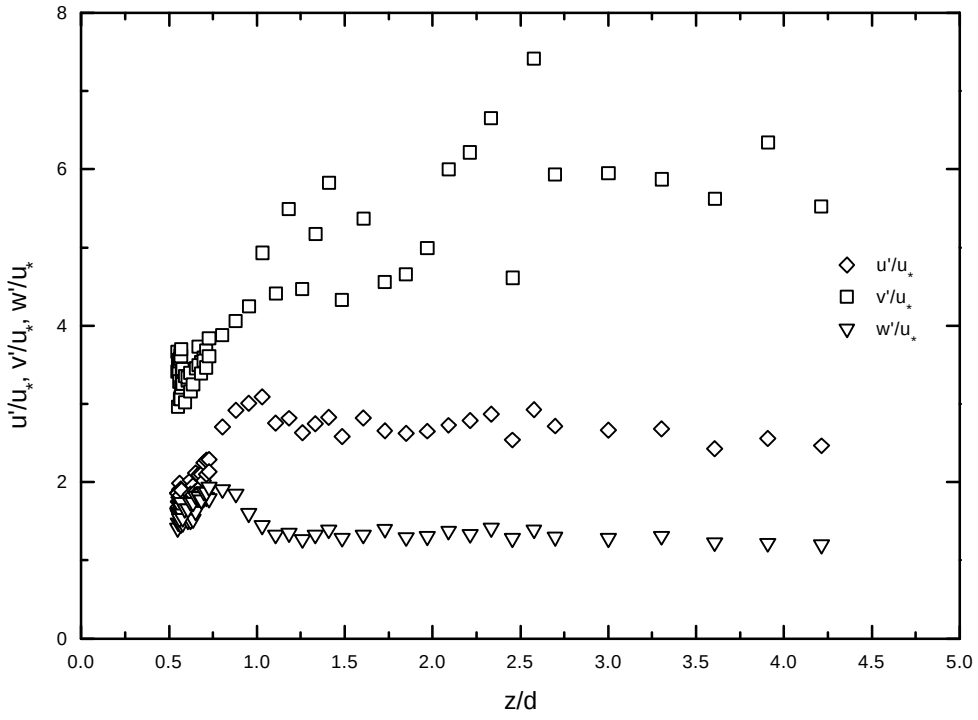

Figure 41(b). Distribution of the turbulent intensities at location C (20% packing condition).

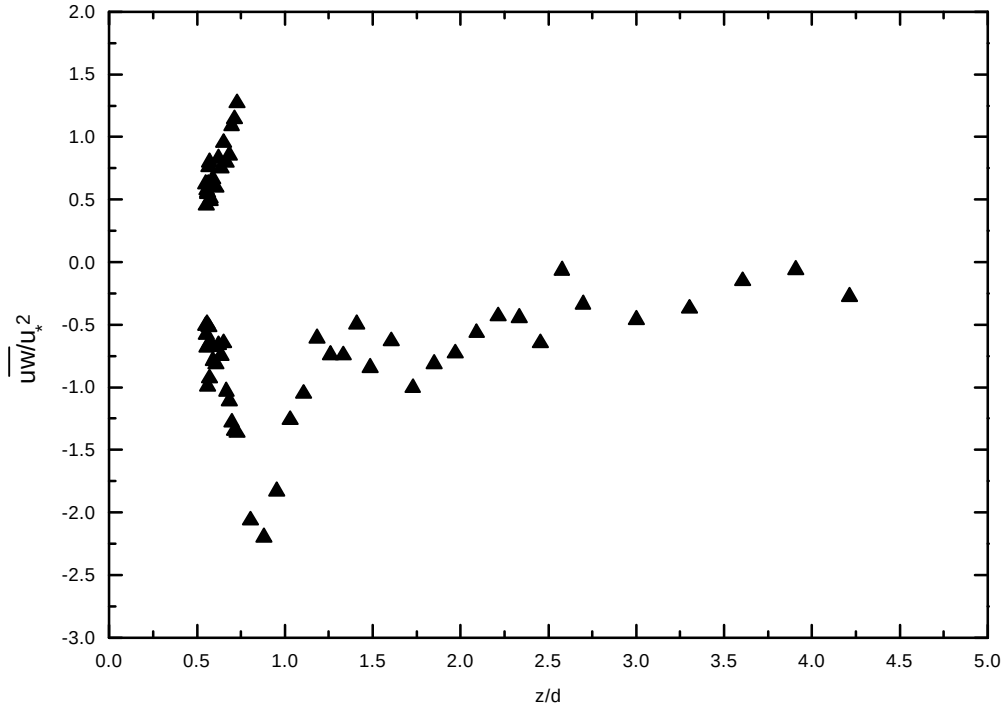

Figure 41(c). The distribution of the time averaged Reynolds stress at location C (20% packing condition).

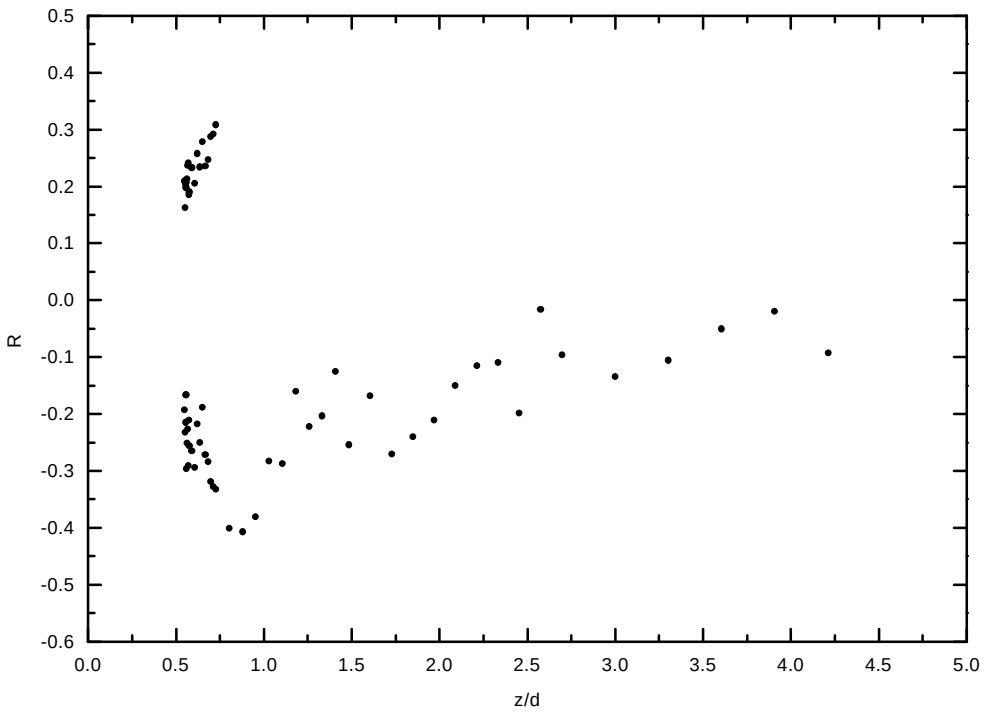

Figure 41(d). The distribution of the correlation coefficient R at location C (20% packing condition).

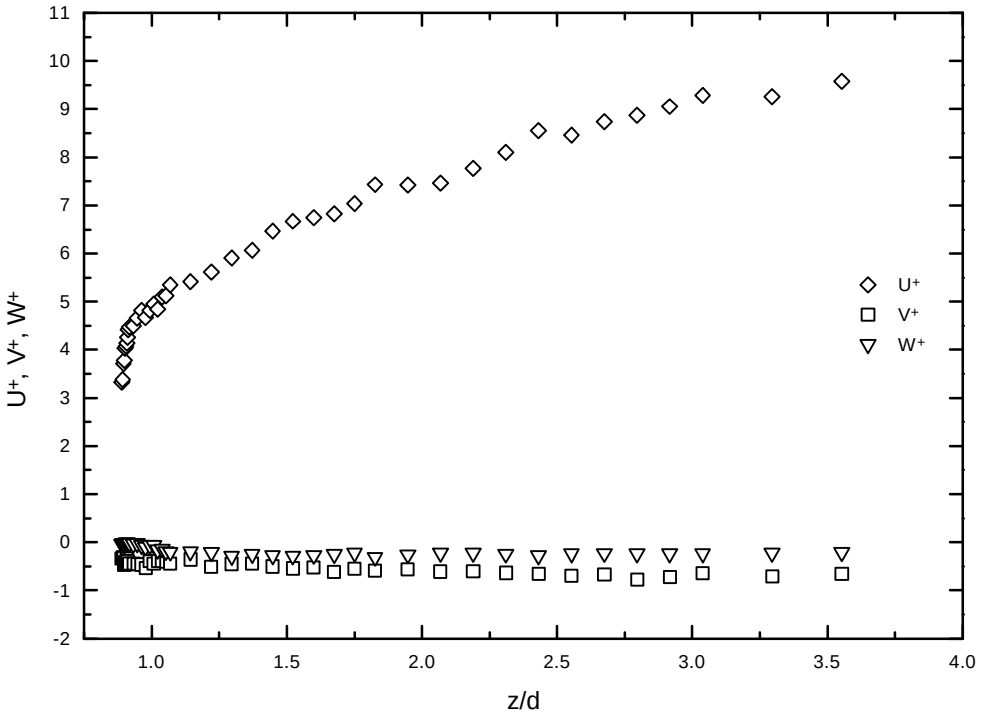

Figure 42(a). The velocity profiles at location A (35% packing condition).

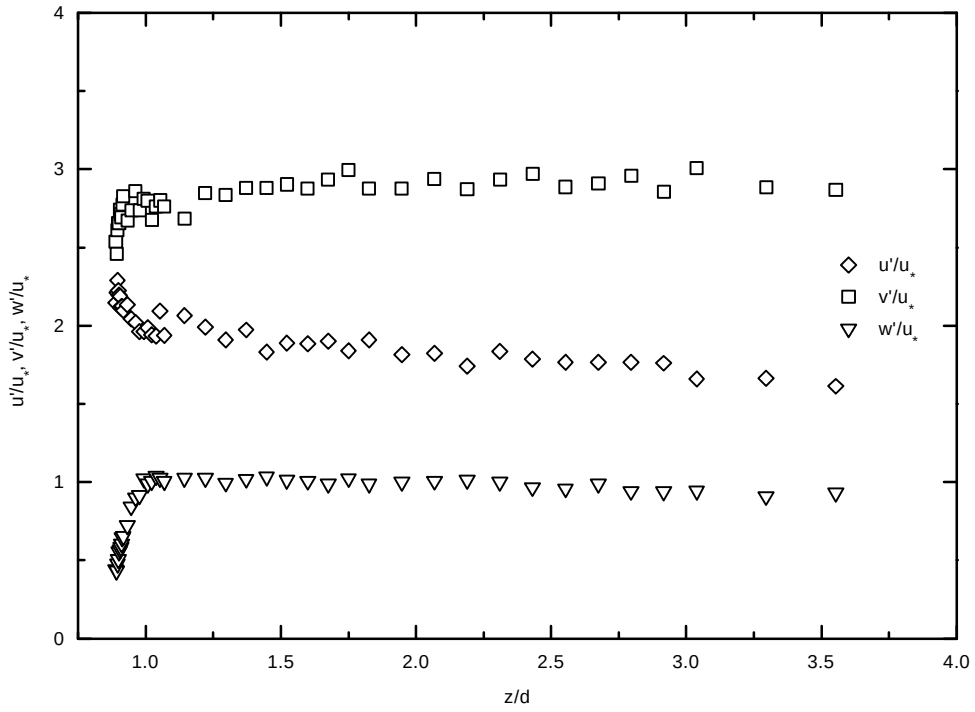

Figure 42(b). Distribution of the turbulent intensities at location A (35% packing condition).

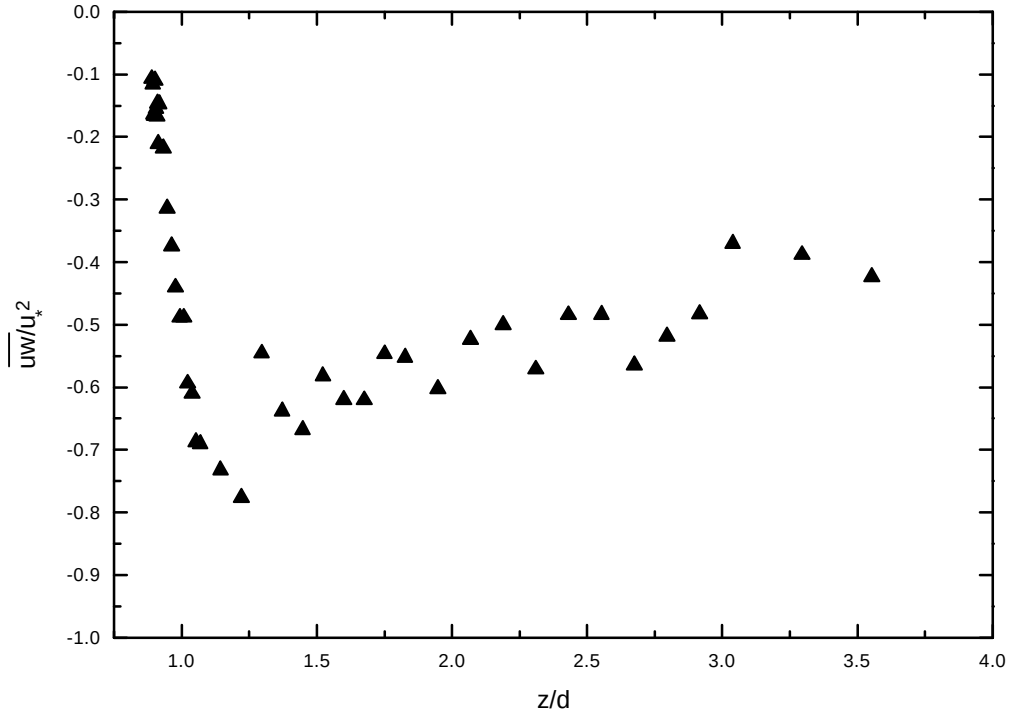

Figure 42(c). The distribution of the time averaged Reynolds stress at location A 35% packing condition).

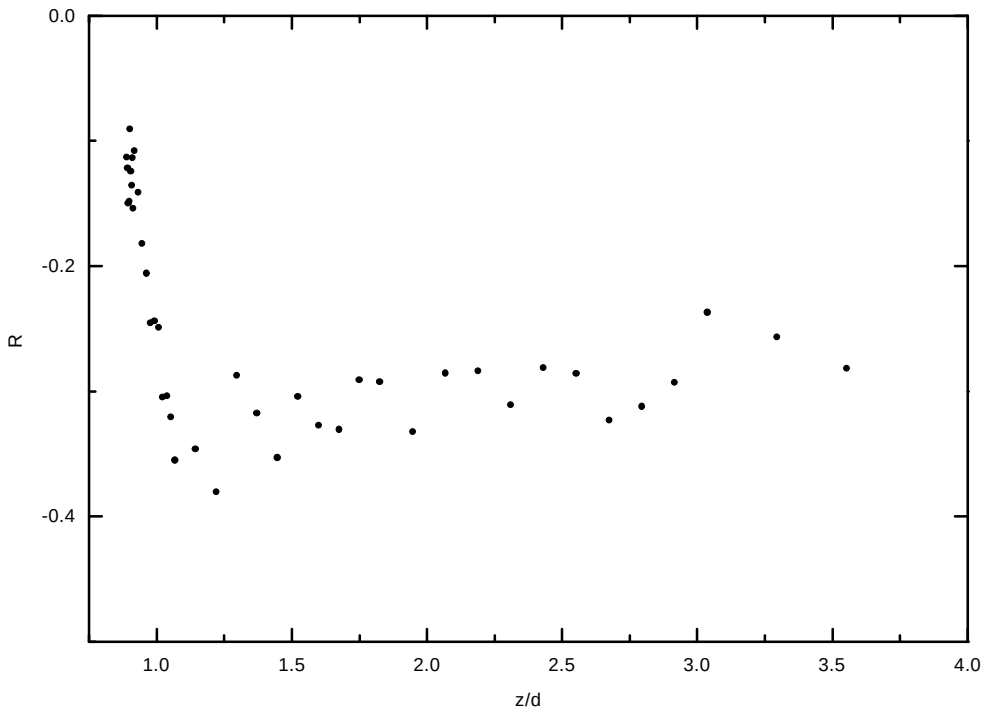

Figure 42(d). The distribution of the correlation coefficient R at location A (35% packing condition).

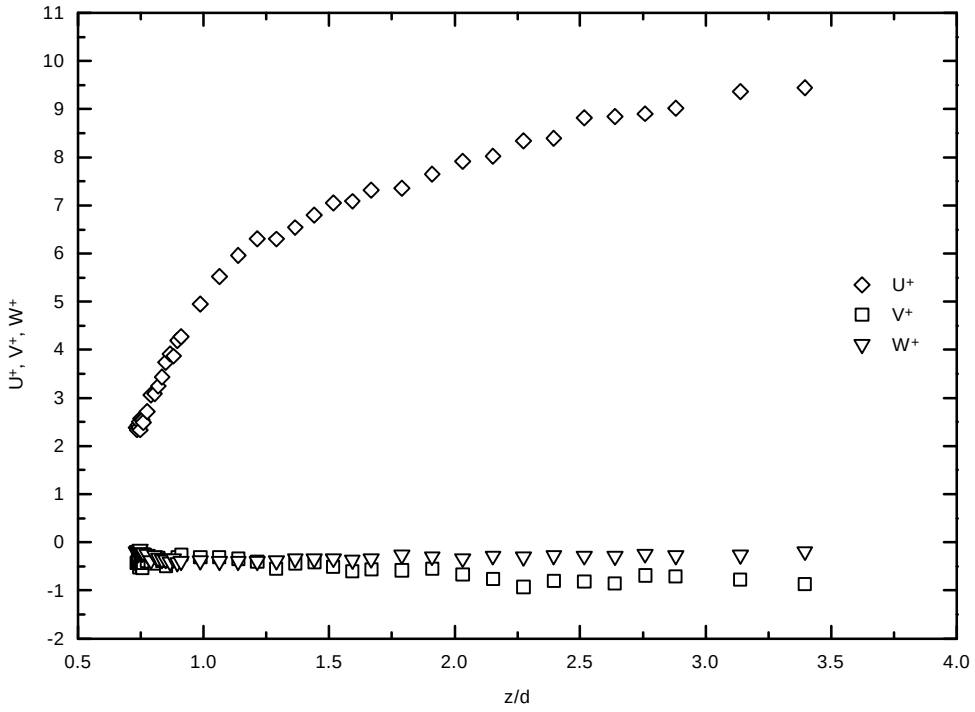

Figure 43(a). The velocity profiles at location B (35%packing condition).

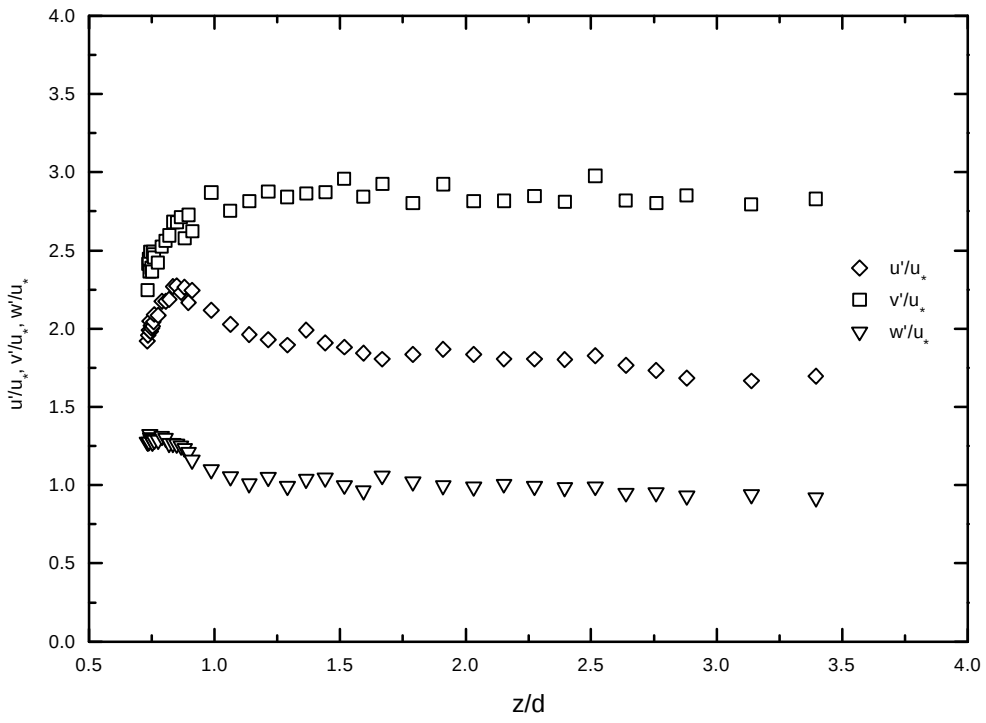

Figure 43(b). Distributions of the turbulent intensities at location B (35% packing condition).

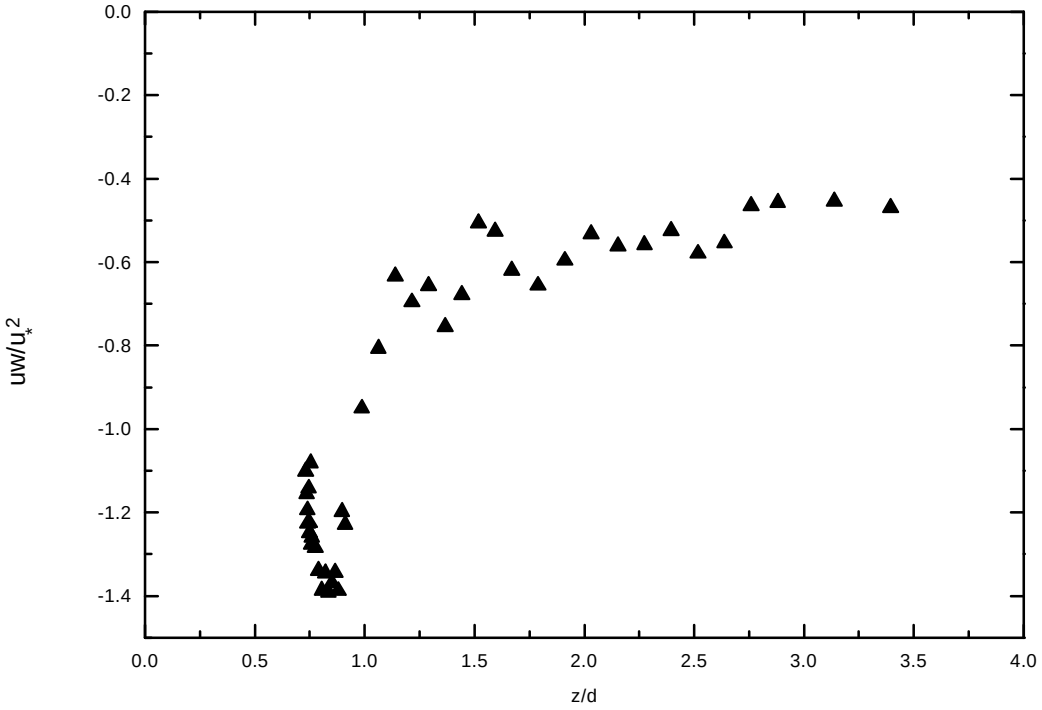

Figure 43(c). The distribution of the time averaged Reynolds stress at location B (35% packing condition).

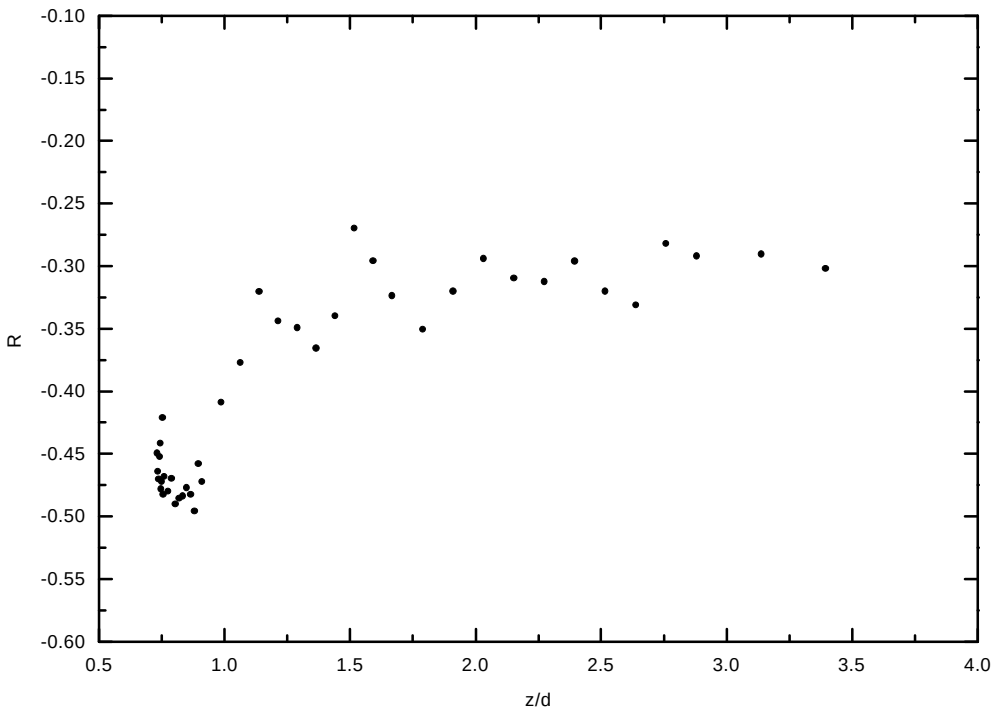

Figure 43(d). The distribution of the correlation coefficient R at location B (35% packing condition).

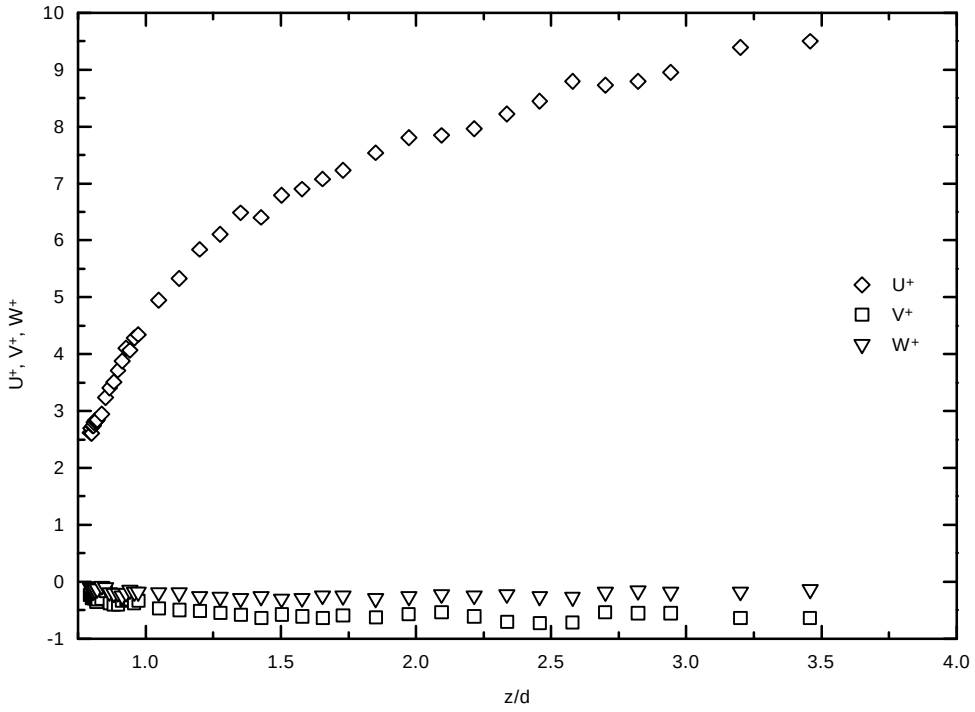

Figure 44(a). The velocity profiles at location C (35% packing condition).

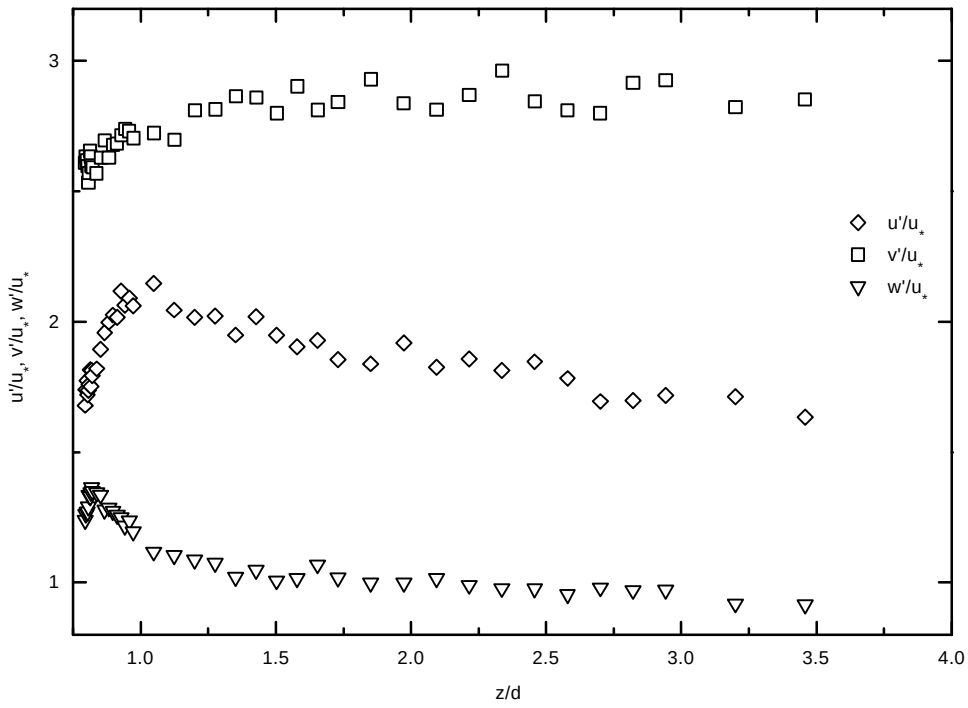

Figure 44(b). Distribution of the turbulent intensities at location C (35% packing condition).

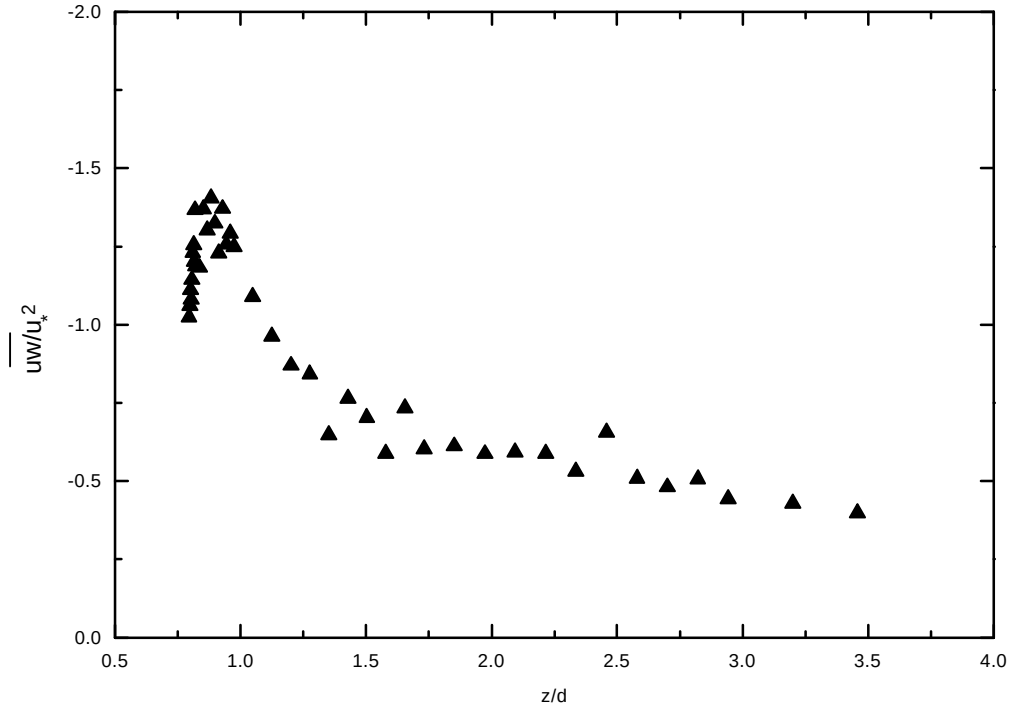

Figure 44(c). The distribution of the time averaged Reynolds stress at location C (35% packing condition).

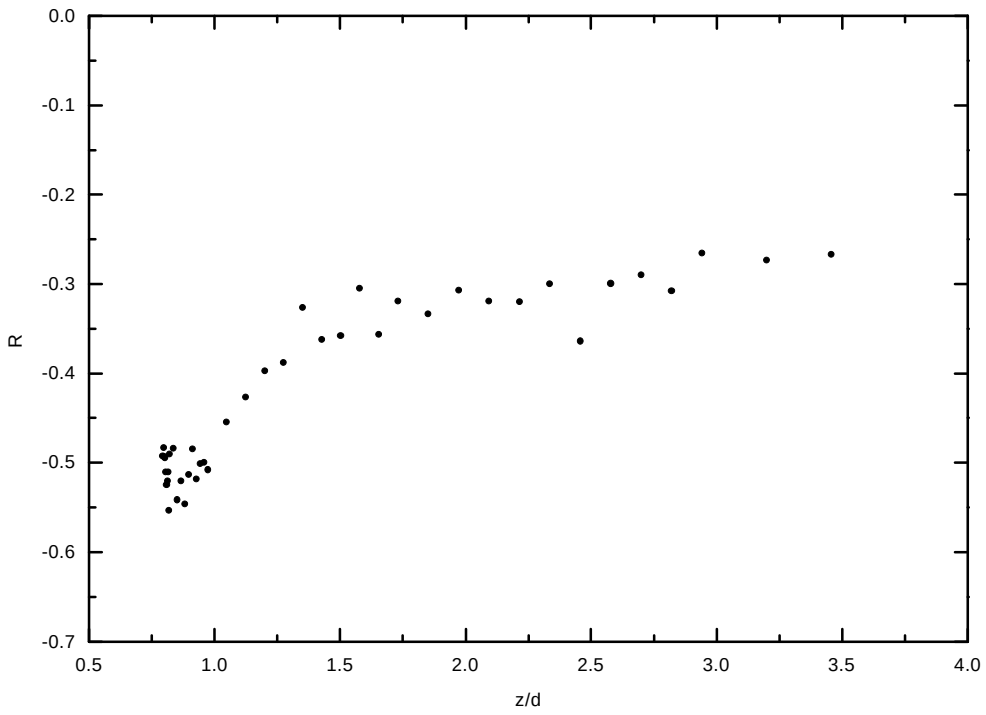

Figure 44(d). The distribution of the correlation coefficient R at location C (35% packing condition).

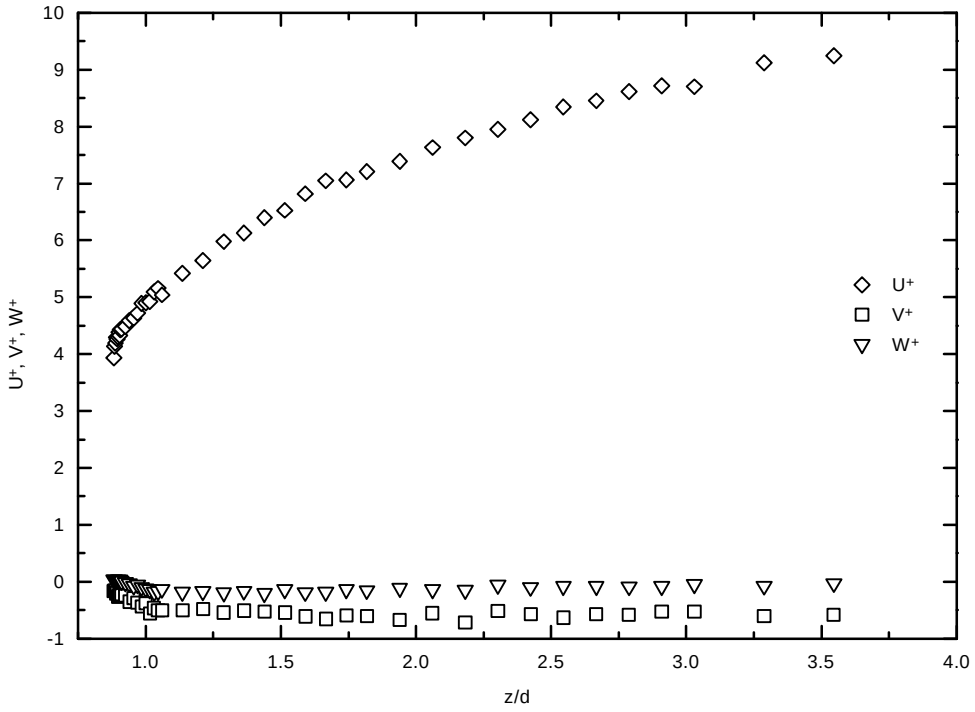

Figure 45(a). The velocity profiles at location A (50% packing condition).

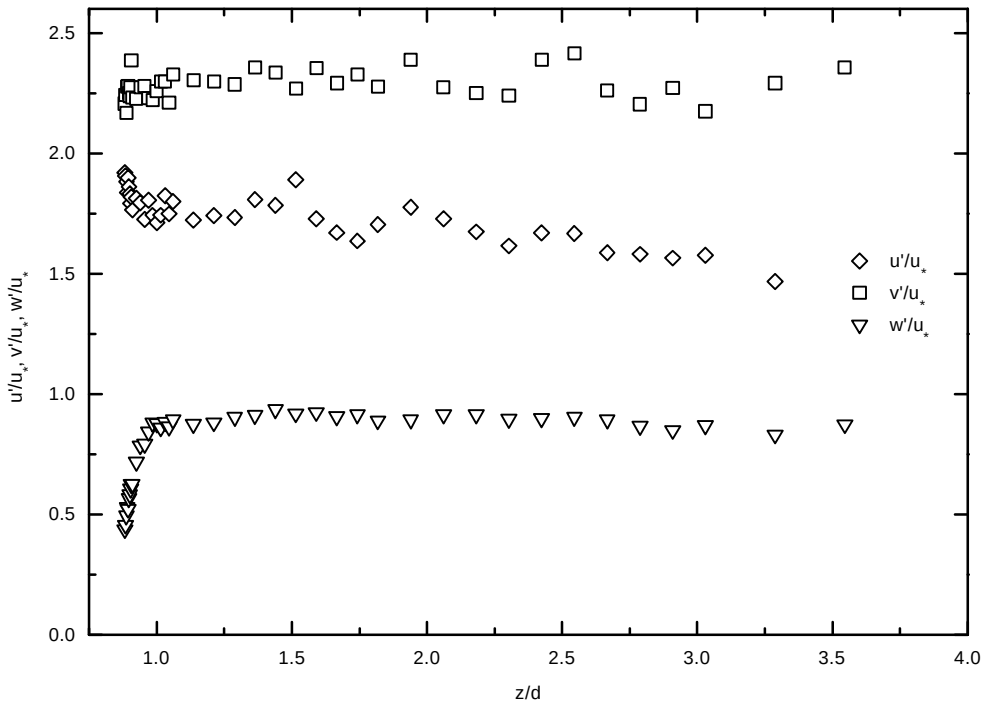

Figure 45(b). Distribution of the turbulent intensities at location A (50% packing condition).

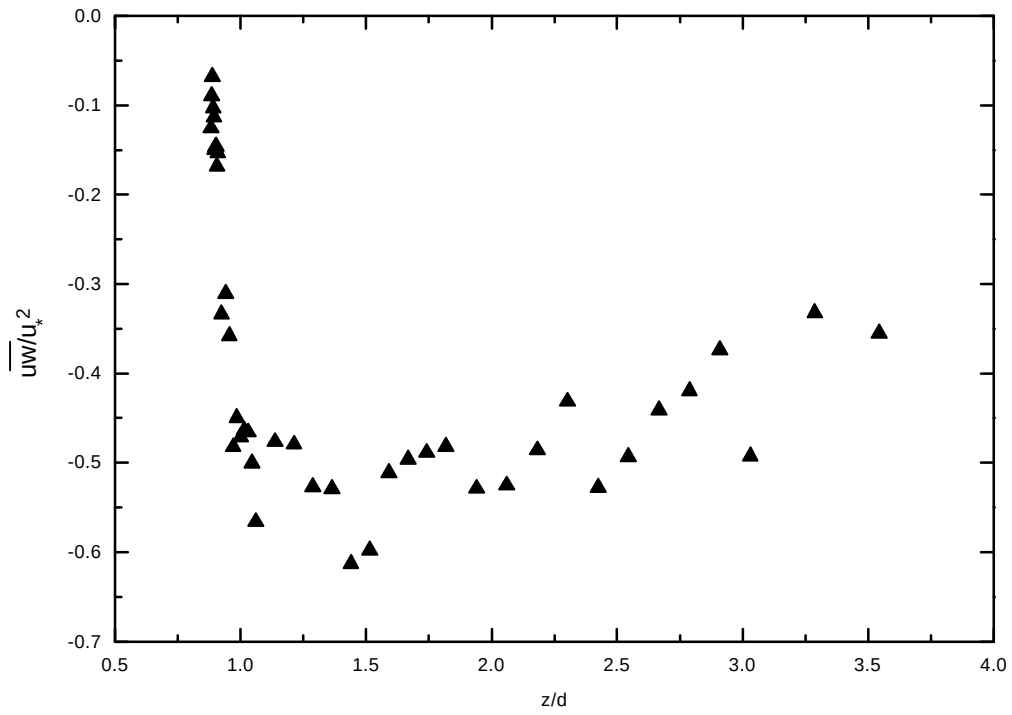

Figure 45(c). The distribution of the time averaged Reynolds stress at location A (50% packing condition).

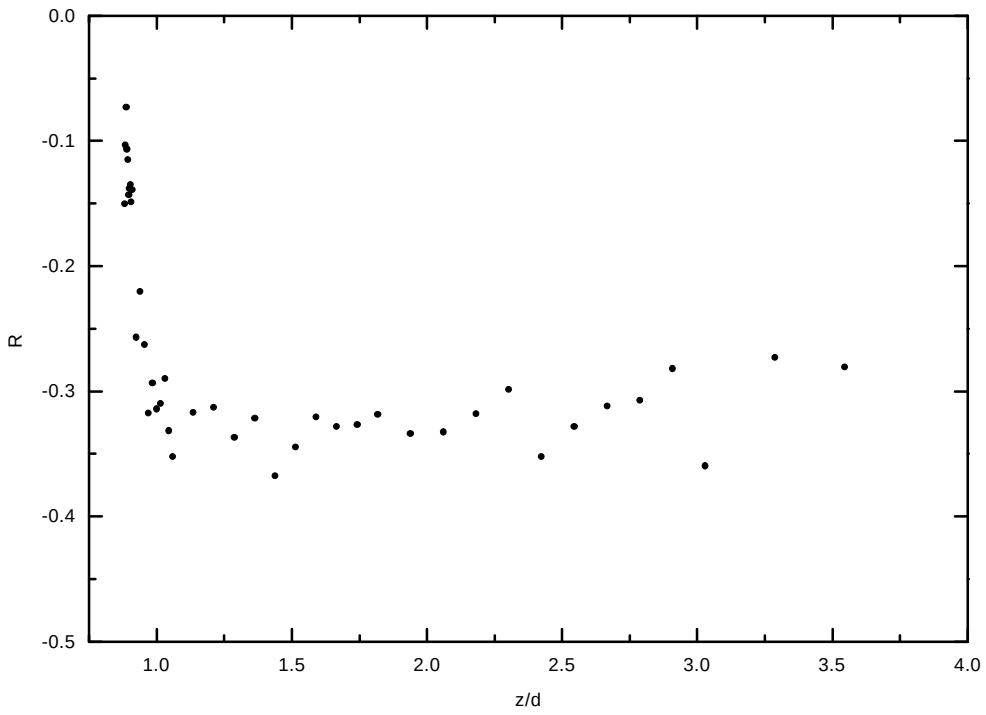

Figure 45(d). The distribution of the correlation coefficient R at location A (50% packing condition).

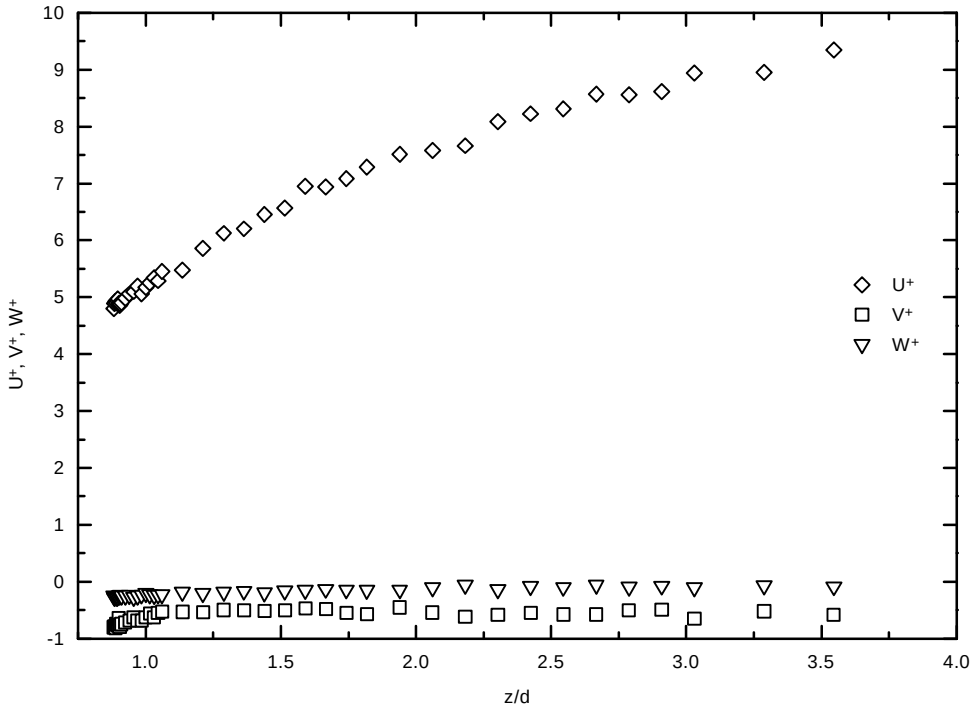

Figure 46(a). The velocity profiles at location B (50% packing condition).

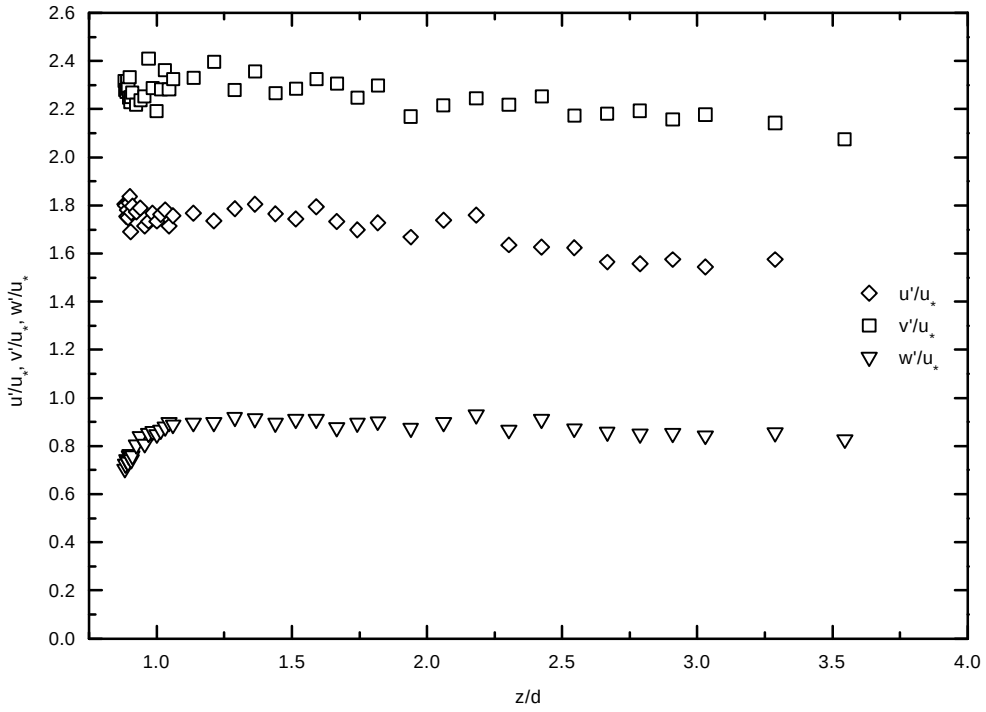

Figure 46(b). Distributions of the turbulent intensities at location B (50% packing condition).

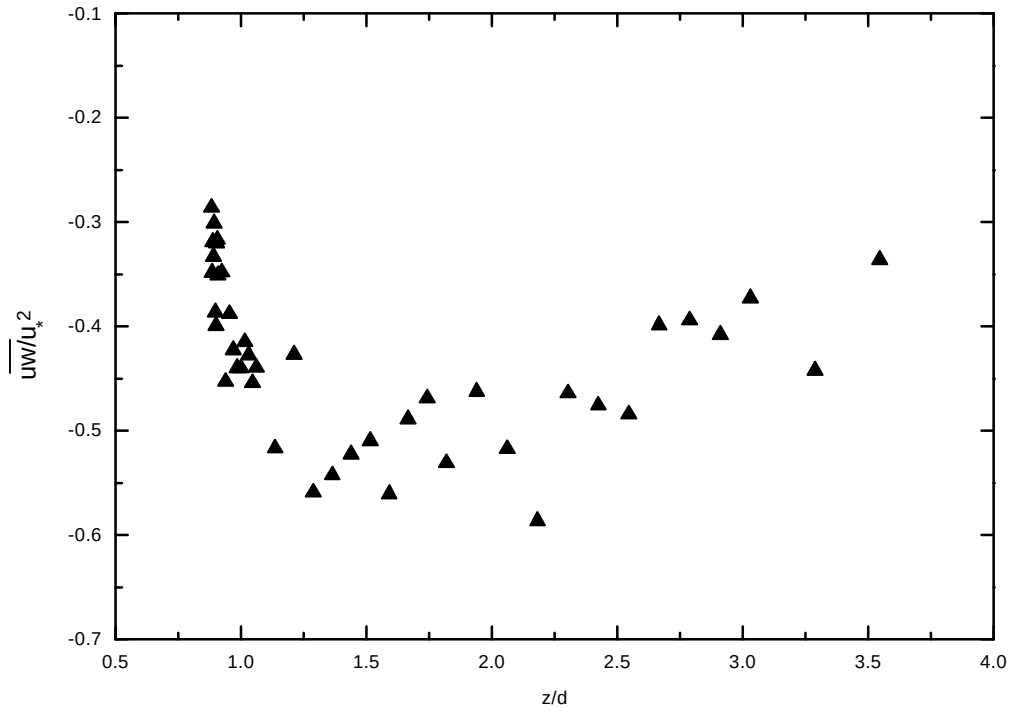

Figure 46(c). The distribution of Reynolds stress at location B (50% packing condition).

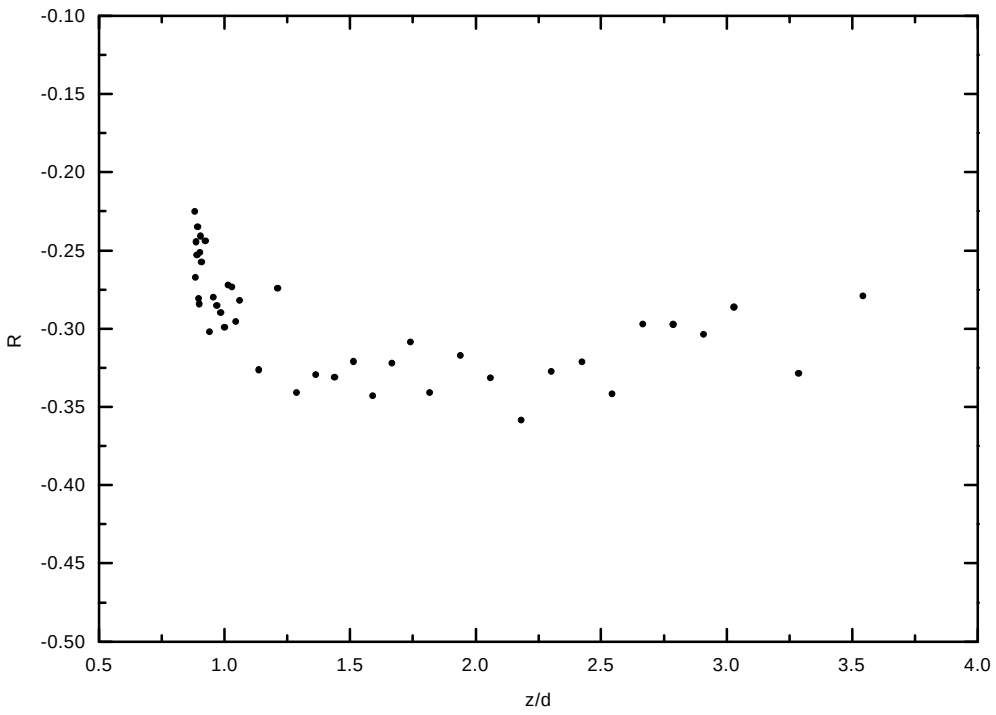

Figure 46(d). The distribution of the correlation coefficient R at location B (50% packing condition).

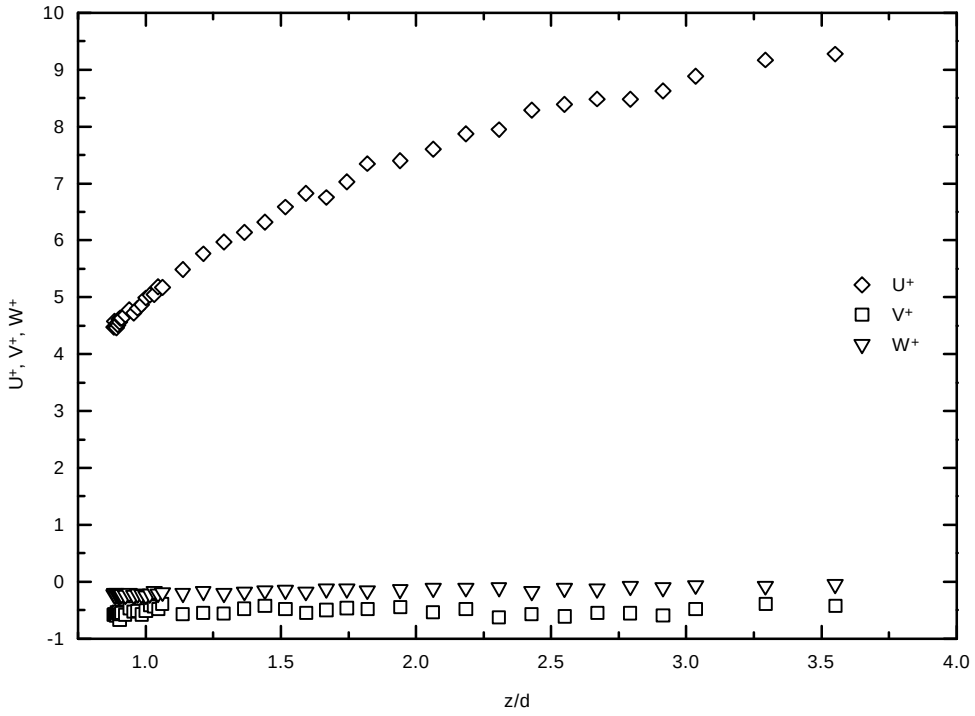

Figure 47(a). The velocity profiles at location C (50% packing condition).

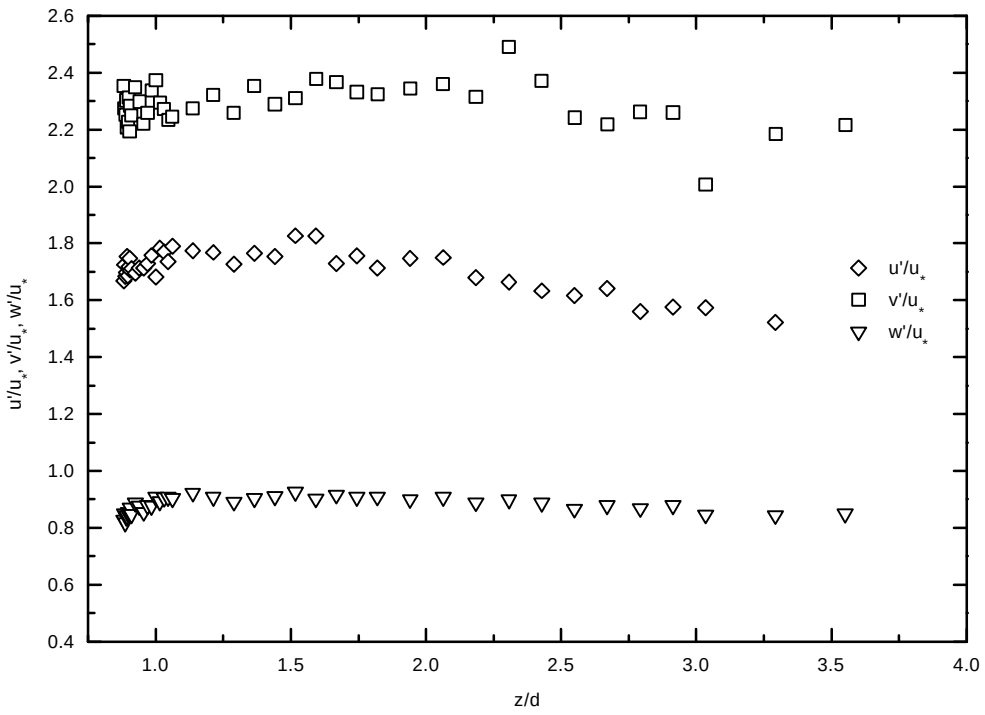

Figure 47(b). Distributions of the turbulent intensities at location C (50% packing condition).

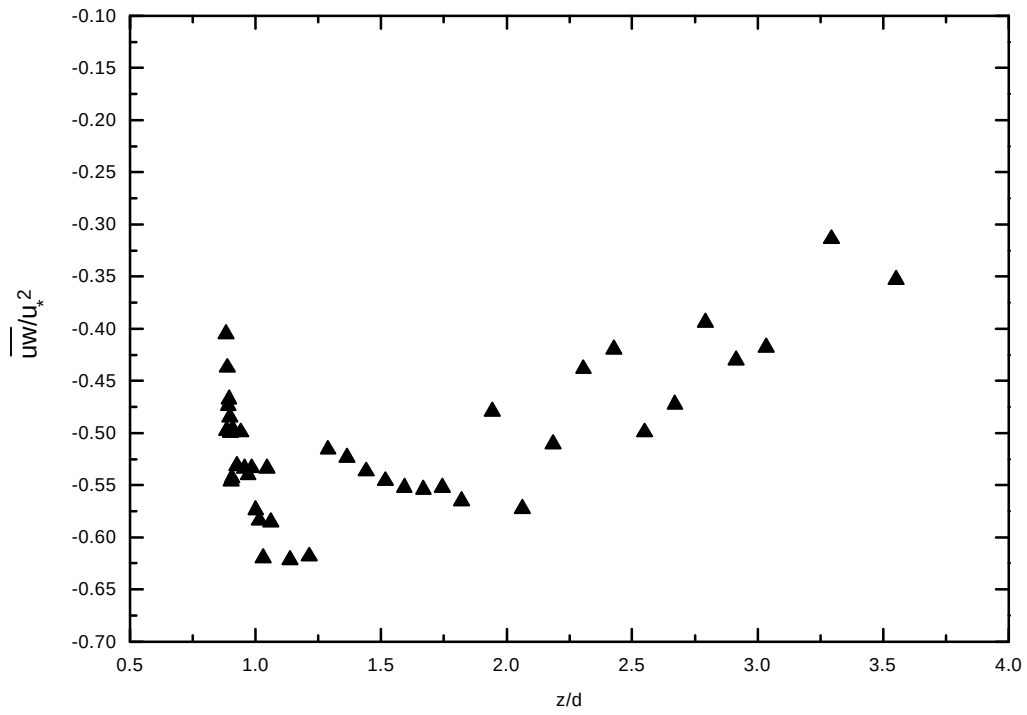

Figure 47(c). The distribution of the time averaged Reynolds stress at location C (50% packing condition).

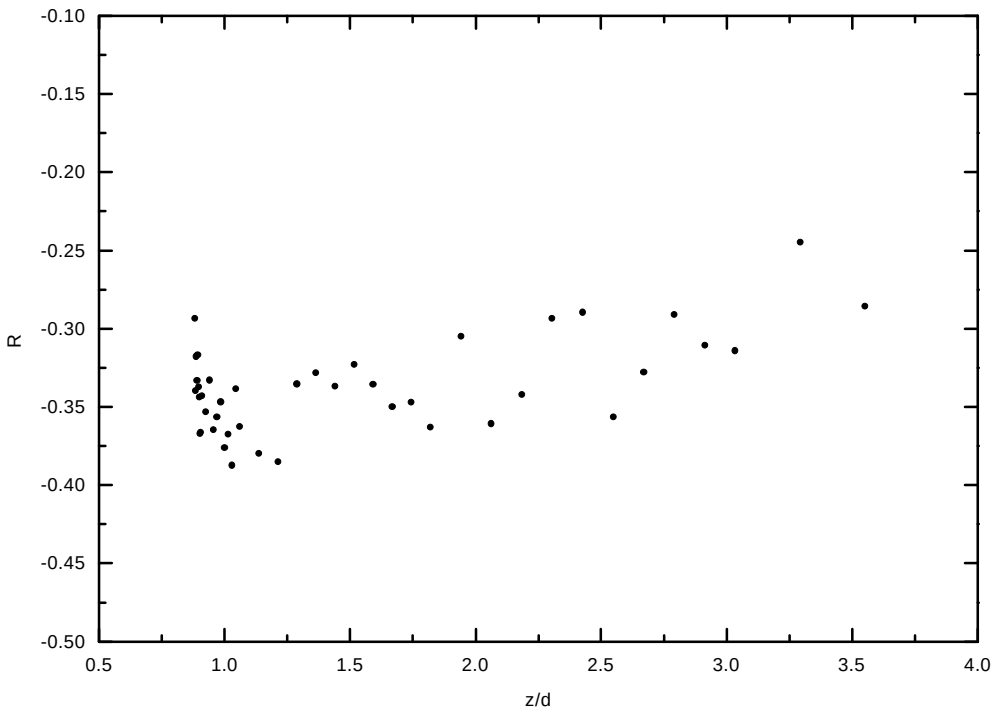

Figure 47(d). The distribution of the correlation coefficient R at location C (50% packing condition).

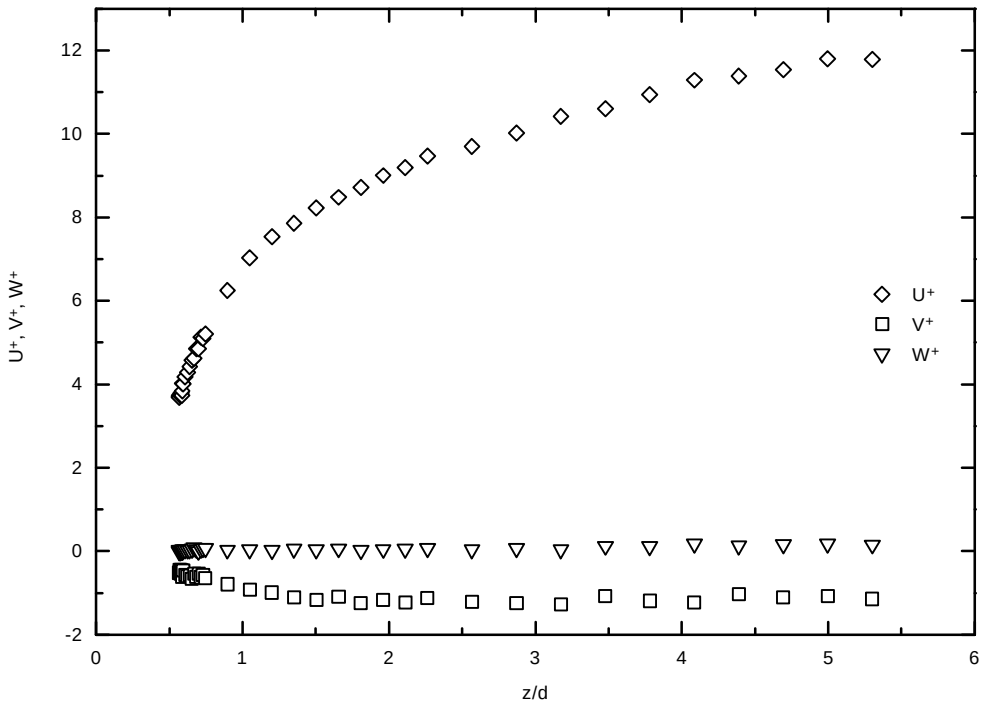

Figure 48(a). The velocity profiles at location E (70% packing condition).

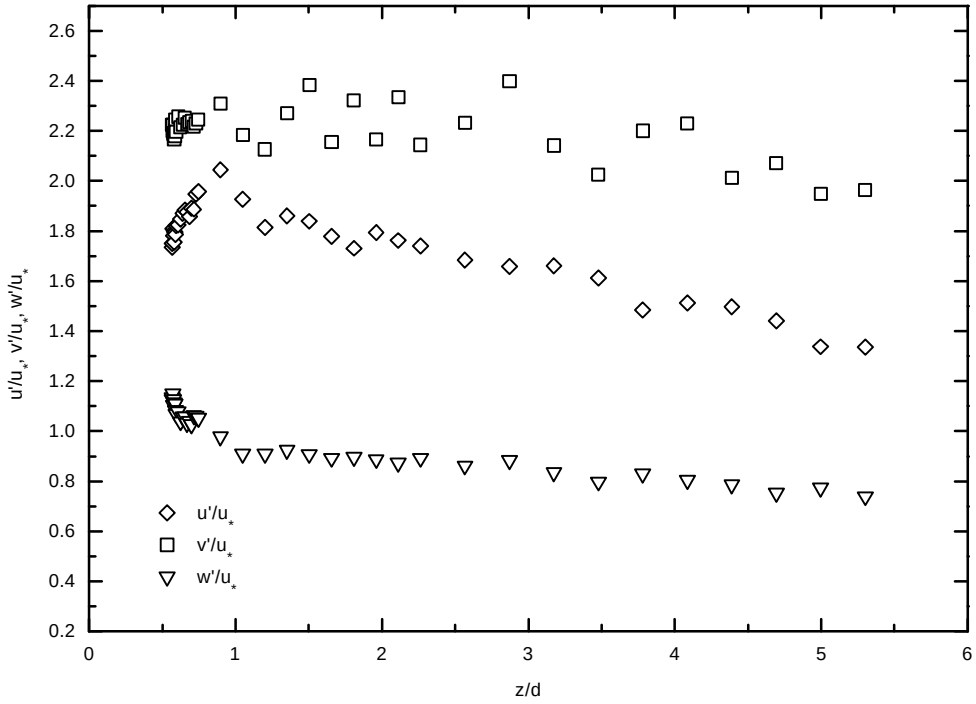

Figure 48(b). Distribution of the turbulent intensities at location E (70% packing condition).

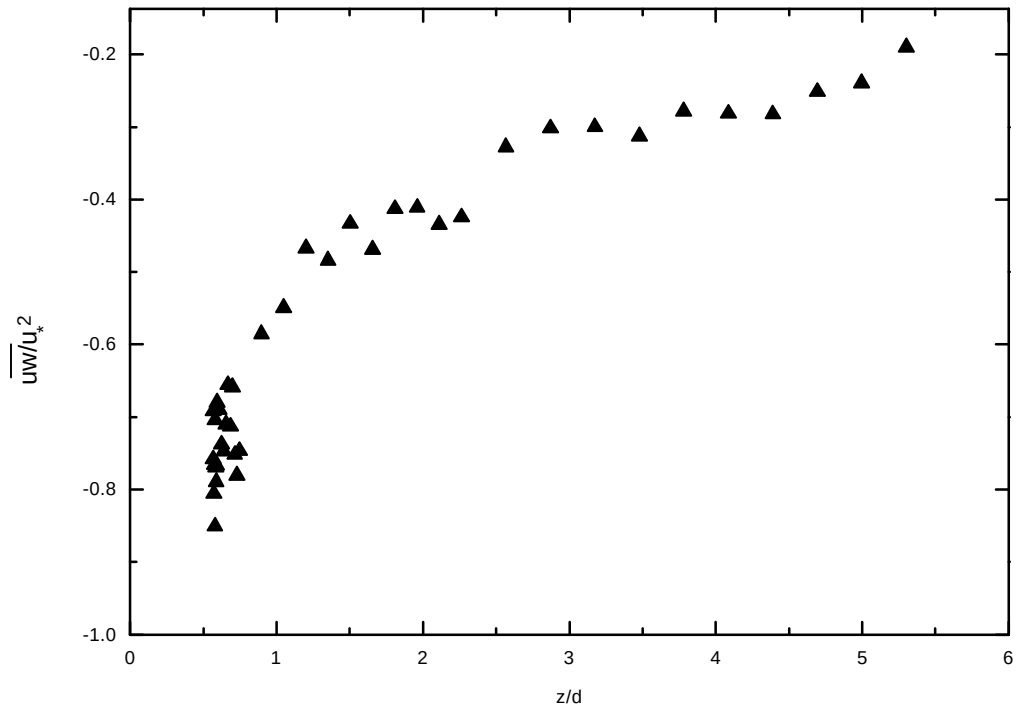

Figure 48(c). The distribution of the time averaged Reynolds stress at location E (70% packing condition).

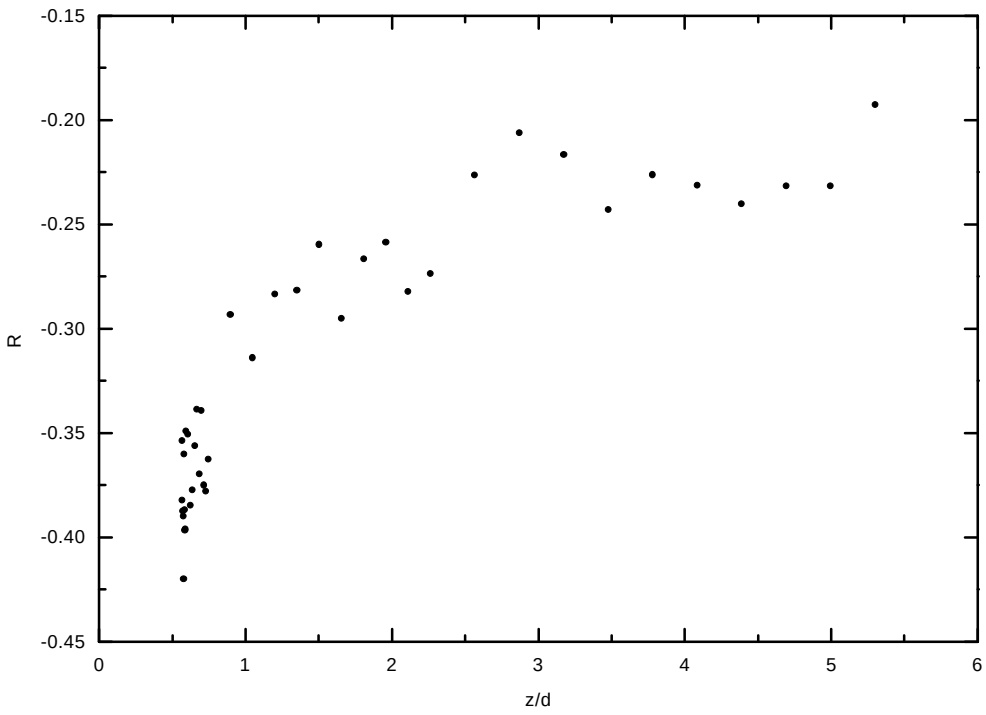

Figure 48(d). The distribution of the correlation coefficient R at location E (70% packing condition).

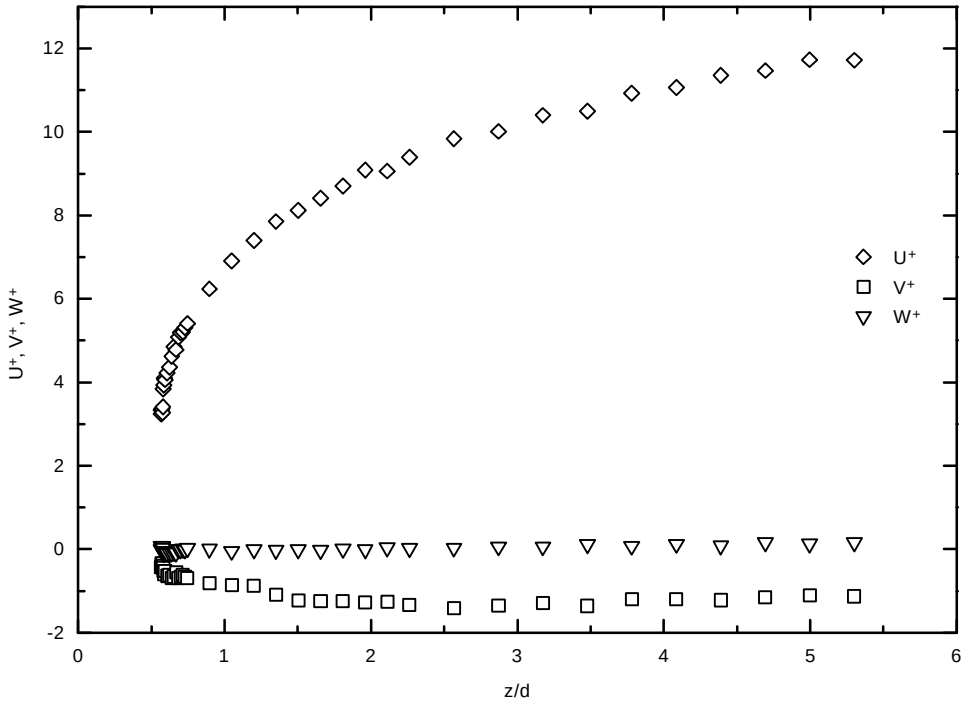

Figure 49(a). The velocity profiles at location D (70% packing condition).

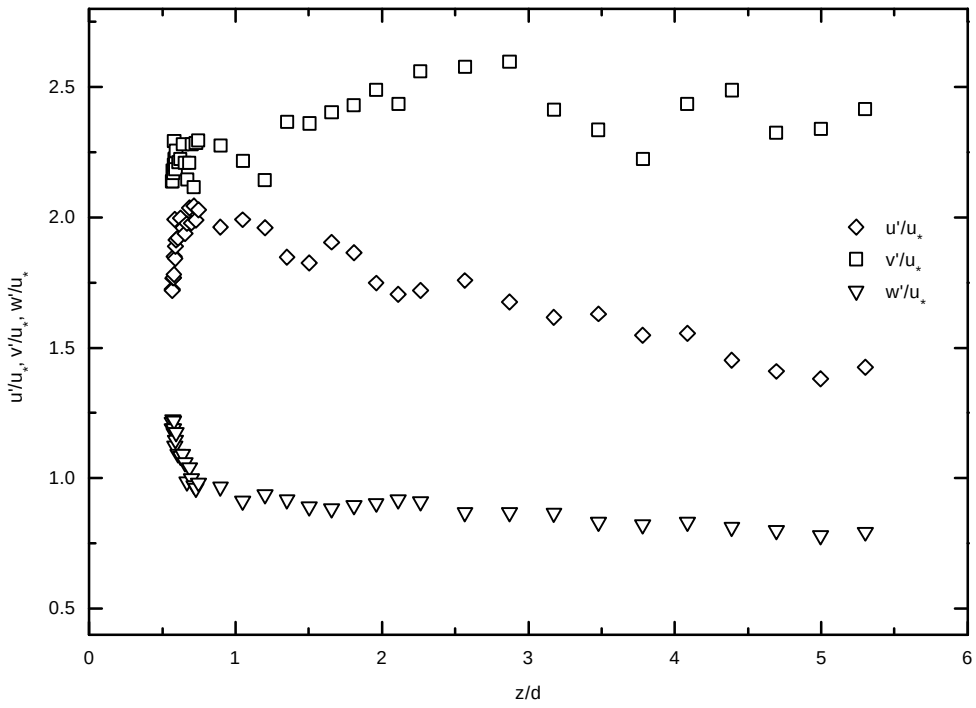

Figure 49(b). Distribution of the turbulent intensities at location D (70% packing condition).

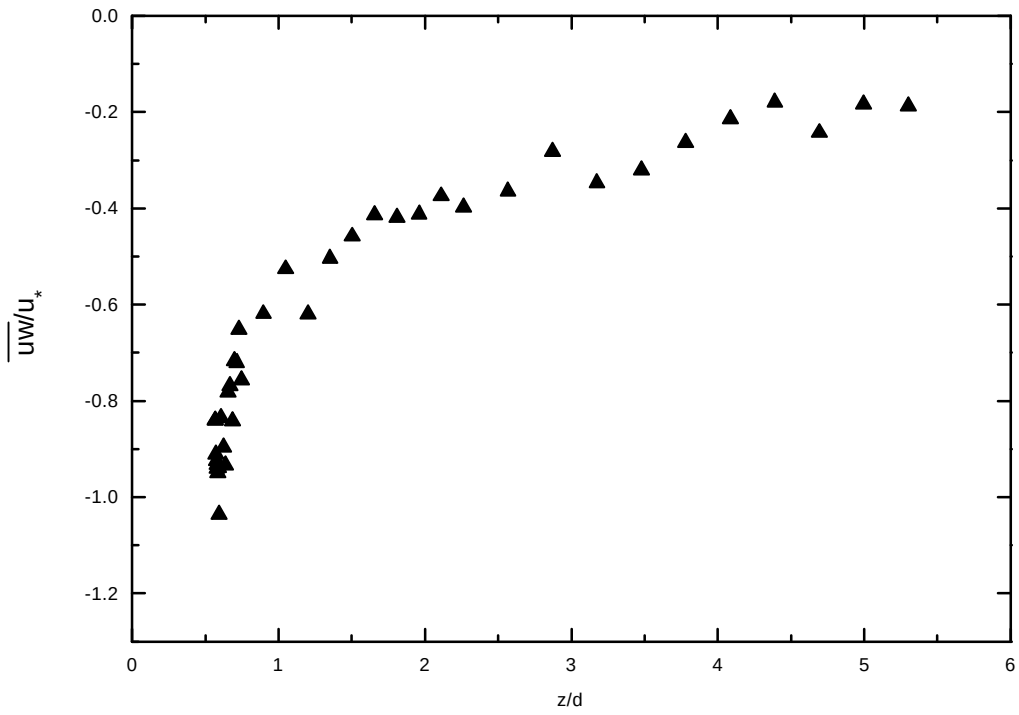

Figure 49(c). The distribution of the time averaged Reynolds stress at location D (70% packing condition).

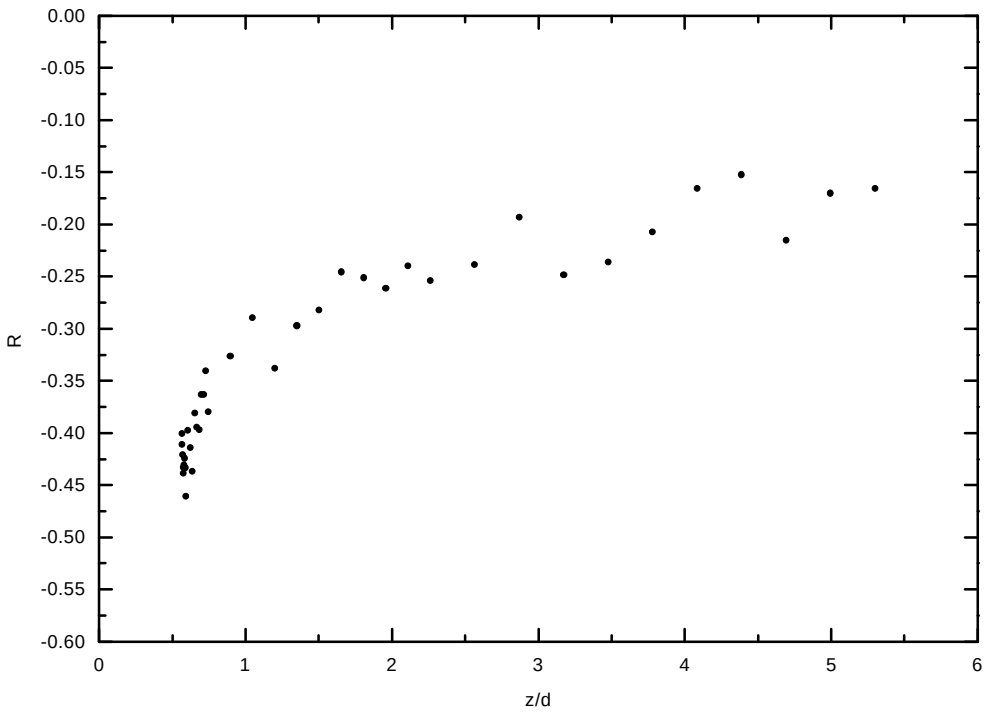

Figure 49(d). The distribution of the correlation coefficient R at location D (70% packing condition).

Chapter 6

The Incipient Condition Model

The objective of this chapter is twofold. First, to evaluate the role that the different instantaneous stress components play in the entrainment of sediment and secondly, to provide a quantitative criterion, which accounts for the role of turbulence on the commencement of sediment motion.

6.1. Representation of turbulent stresses

Over the last twenty years the fluctuating shear stress term (-uw) has been considered as the only stress component that relates with the entrainment of sediment. The systematic exclusion of the other instantaneous stress components (i.e. the normal and the other shear terms) from the study of the entrainment problem indicates that there is a lack of understanding of the mechanisms involved in the interaction of the flow with sediment. Another possible reason for placing a significant emphasis in the study of the (-uw) term is that this term does not get eliminated when the averaging process of the equations of motion takes place. The latter reason reveals that there is an inconsistency in some entrainment models (e.g. Williams et al., 1989). It is not reasonable to say that the role of instantaneous stresses on the sediment motion is accounted for and at the same time use the time averaging process, of the equations of motion, as the basis for the elimination of some of the instantaneous components. To further clarify this statement

let us consider the equations of motion, for example for a 2-D flow, in the following form:

$$\rho \frac{\partial U}{\partial t} = \rho g + \frac{\partial \tau_{xx}}{\partial x} - \rho \frac{\partial U^2}{\partial x} + \frac{\partial \tau_{xz}}{\partial z} - \rho \frac{\partial (UW)}{\partial z} \tag{25a}$$

and

$$\rho \frac{\partial W}{\partial t} = \frac{\partial \tau_{xz}}{\partial x} - \frac{\partial (UW)}{\partial x} + \frac{\partial \tau_{zz}}{\partial z} - \rho \frac{\partial W^2}{\partial z} \tag{25b}$$

where,

$$U = \overline{U} + u \tag{26a}$$

$$W = \overline{W} + w \tag{26b}$$

ρ is the fluid density

$\overline{U}$ is the time average velocity in the x direction

$\overline{W}$ is the time average velocity in the z direction

u is the fluctuating velocity component in the x direction

w is the fluctuating velocity component in the z direction

$$\tau_{xx} = -P_{xx} + 2\mu \frac{\partial U}{\partial x} \tag{26c}$$

$$\tau_{zz} = -P_{zz} + 2\mu \frac{\partial W}{\partial z} \tag{26d}$$

and

$$\tau_{xz} = \mu\left(\frac{\partial U}{\partial z} + \frac{\partial W}{\partial x}\right) \tag{26e}$$

By substituting equations (26a)-(26e) into equations (25a) and (25b) we get:

$$\rho \frac{\partial(\overline{U} + u)}{\partial t} = \rho g + \frac{\partial}{\partial x}\left(2\mu\frac{\partial(\overline{U} + u)}{\partial x} - P_x - \rho\left(\overline{U}^2 + u^2 + 2\overline{U}u\right)\right) + \frac{\partial}{\partial z}\left(\mu\frac{\partial(\overline{U} + u)}{\partial z} + \mu\frac{\partial(\overline{W} + w)}{\partial x}\right.$$

$$\left. - \overline{U}\,\overline{W} - \overline{U}w - \overline{W}u - uw\right) \tag{27a}$$

$$\rho \frac{\partial(\overline{W} + w)}{\partial t} = \frac{\partial}{\partial x}\left(\mu\left(\frac{\partial(\overline{U} + u)}{\partial z} + \frac{\partial(\overline{W} + w)}{\partial x}\right) - \overline{U}\,\overline{W} - \overline{U}w - \overline{W}u - uw\right) +$$

$$+ \frac{\partial}{\partial z}\left(\left(2\mu\frac{\partial(\overline{W} + w)}{\partial z} - P_z\right) - \rho\left(\overline{W}^2 + w^2 + 2\overline{W}w\right)\right) \tag{27b}$$

By averaging equations (27a) and (27b) we get:

$$\rho \frac{\partial \overline{U}}{\partial t} = \rho g + \frac{\partial}{\partial x}\left(2\mu\frac{\partial \overline{U}}{\partial x} - \overline{P}_x - \rho\left(\overline{U}^2 + \overline{u^2}\right)\right) + \frac{\partial}{\partial z}\left(\mu\frac{\partial \overline{U}}{\partial z} + \mu\frac{\partial \overline{W}}{\partial x} - \overline{uw}\right) \tag{28a}$$

and

$$0 = \frac{\partial}{\partial x}\left(\mu\frac{\partial \overline{U}}{\partial z} - \overline{uw}\right) + \frac{\partial}{\partial z}\left(-P_z - \rho\,\overline{w^2}\right) \tag{28b}$$

Equations (27a) and (27b) indicate that there are other fluid stress components viz., u^2, w^2, $\overline{U}u, \overline{U}w$ that possibly may contribute to the initiation of sediment motion. These terms, except u^2 and w^2, get eliminated from the time averaging process (equations 28(a) and 28(b)) and therefore, are ignored in the study of the sediment entrainment problem.

Several authors (e.g. Corrsin, 1973; Bagnold, 1979; Leeder, 1983; Clifford, 1991) have remarked on the importance of the other instantaneous terms that appear in the equations of motion. They suggested that the normal (i.e. u^2, w^2) and instantaneous stresses involving mixed cross-products of mean and fluctuating velocities (i.e. $\overline{U}u, \overline{U}w$) should not be ignored from the study of sediment motion. More recently, Nelson et al. (1995) have indicated a poor correlation between the total momentum flux ρUW and sediment motion and suggested that the UW term may not be the responsible stress component for the sediment motion. They have also shown that U provides the best correlation with the sediment flux.

In the present study the importance of the different stress components is examined by using the data from the existing surface packing condition tests. For this purpose, the time series of the instantaneous normal stress components U^2, W^2, and shear stress UW are constructed. Specifically, for the 2%, 20%, 35%, and 50% packing conditions the time series of U^2, W^2, and UW are plotted for the locations A, B, and C at different distances from the bed (i.e. the locations A, B, and C are defined in figure 34(b)). For the 70% packing condition the times series of the stress terms are plotted for the locations D and E (i.e., these locations are defined in figure 34(b)). The plots in figures 50(a)-50(e) illustrate the variation of the U^2, W^2, and UW terms for the first 1000 measurements (the total number of measurements per point is 3072). The rate of the measurements is

different for each packing condition and it depends on the coincidence rate of the LDV system. Table 13 summarizes the rate of measurements for the different packing conditions tests.

Figure 50(a) illustrates the time series of the U^2, W^2, and UW terms for the 2% packing condition. For all the measuring points U^2 is the most dominant term. The only exemption is observed at the point with z/d=0.089 in location C. This point is located downstream of the ball and is very close to the bed surface. In this case the magnitude of U^2 reduces significantly and becomes of the same order with that of W^2 and UW. Figure 50(a) shows that U^2 has almost the same magnitude for the points that are found in the locations A and B, with z/d =0.9, while it reduces for the corresponding point in location C. The U^2 time series presents more peaks in location A than in location B.

Figure 50(b) shows that U^2 is the most dominant term for the 20% packing condition. U^2 obtains its maximum value in location A (when z/d=0.897). For the points with z/d=0.549, U^2 obtains its maximum value at location B. W^2 is greater in location B (z/d=0.897) while UW obtains its higher values in location C (z/d =0.897) than in A and B.

Figure 50(c) illustrates the dominance of U^2 over the terms W^2 and UW. UW obtains its higher values at locations B and C and is almost equal to zero at location A. U^2 reduces at the points that are closer to the bed surface in locations B and C. W^2 is relatively high at location B comparatively to location A.

In the 50% packing condition (figure 50 (d)) the UW term at location C is greater than in A and B. Similarly, W^2 obtains its higher values at C location. U^2 presents its higher peaks at location B.

Figure 50 (e) presents the time series of the U^2, W^2, and UW terms for the 70% packing condition. The magnitude of UW in the 70% case is higher comparatively to the other packing conditions. Finally, the U^2 term presents its higher peaks at location E.

In summary, figures 50(a)-50(e) show that U^2 is by far greater in magnitude than W^2, and UW. The maximum value of U^2 is on an average 3.5-4 times greater than the maximum value of W^2. This result is in agreement with the findings of Clifford (1991). The magnitudes of W^2 and UW do not differ significantly from each other. The importance of the UW compared to W^2 increases in the 70% case. This may be attributed to the fact that the measuring point in this case is positioned at half a ball diameter above the top of the fifth layer. Finally, figures 50(a)-(e) illustrate that the contributions of the mixed product stress $\overline{U}w$ to the magnitude of the total shear stress, UW, are rather insignificant. It is expected that the term $\overline{U}w$ becomes more important as the distance from the bed increases.

The above results raise many questions regarding the significance of the UW term in the entrainment process. If the magnitude of the stress terms is indeed the criterion that is used to decide which terms should be included in the study of the entrainment problem, then the U^2 term should be considered as the most relevant stress term to sediment motion (instead of UW). Also, there is a lot of uncertainty regarding the form in which the UW stress applies to a sediment particle and if it does the area over which it acts. This uncertainty probably explains why most of the entrainment models that focus on the UW term are rather qualitative.

Traditionally, the uw term is used to identify the fluid interactions associated with the near-bed bursting cycle (i.e., sweeps, ejections, outward and inward interactions).

The quadrant analysis (Lu and Willmarth, 1973) among other techniques (e.g. VITA), is commonly used to isolate the nature of contributions to $\overline{uw}$ from the above events. In the quadrant analysis four discrete categories of momentum exchange are defined on the basis of the signs of u and w (figure 51). A threshold criterion, H, is usually applied, where,

$$\frac{(uw)_i(H)}{\overline{uw}} = \frac{1}{\overline{uw}} \lim_{T\to\infty} \int_0^T uw(t) S_i(t,H) dt \qquad \text{(i=1,2,3,4)} \qquad (29)$$

where, the subscript i refers to the ith quadrant and

$S_i(t,H)=1$ if $|uw(t)| > Huw$

$S_i(t,H)=0$ otherwise

By choosing different H values (H is known in the literature as the hole size (Lu and Willmarth, 1973)), large contributions to Reynolds stress from each quadrant can be extracted leaving the smaller fluctuations in the "hole". The selection of an appropriate threshold parameter H has been the source of considerable ambiguity and inconsistency within published work. In this study H is chosen to be equal to 5 as suggested by Lu and Willmarth, 1973. By using the program "quadrant.for" (Balakrishnan, 1997) the contributions of the different events to the Reynolds stress are computed. Table 14 provides the percentage of time occupied by each kind of turbulence event for the packing condition tests that are performed here. In the 2% case the inward interactions

occupy the highest percentage of the total measuring time (which is about 3 minutes). The outward interactions occupy the second highest percentage of the total time and the sweeps and ejections together cover only 1/3 of the total measuring time.

As the packing density of the particles increases the frequency of occurrence of the ejections and sweeps increases too. Specifically, in the 70% case the period of occurrence of ejections becomes almost twice of that in the 2% case. The frequency of occurrence of the sweeps does not increase at the same rate as of that of ejections. Concomitantly, the percentage of the total time by the interactions occupied is reduced with increasing packing density.

Lu and Willmarth (1973) computed the probability of the uw term normalized by $\overline{uw}$. They considered the bivariate normal distribution of u and w and after some transformations provided an expression for the probability density function of uw,

$$p_t(\mathrm{w}) = \frac{R}{\mathrm{p}} e^{Rx} \frac{K_o|x|}{\left(1-R^2\right)^{1/2}} \tag{30}$$

where,

$$\mathrm{w} \equiv \frac{uw}{\overline{uw}}; \quad R \equiv \frac{-\overline{uw}}{u'w'}; \qquad \mathrm{x} \equiv \frac{\mathrm{Rw}}{1-\mathrm{R}^2} = \frac{-uw}{u'w'\left(1-R^2\right)}$$

$\mathrm{K_o}|\mathrm{x}|$ is the modified Bessel function of zeroth order and is defined as:

$$K_o|x| = -1\left[\ln\left(\frac{|x|}{2}\right) + \overbrace{\lim_{m\to\infty}\left(1+\frac{1}{2}+\frac{1}{3}+\cdots+\frac{1}{m}-\ln(m)\right)}^{\gamma}\right]\sum_{k=0}^{\infty}\frac{|\mathrm{x}|^{2k}}{2^{2k}k!k!} + \frac{1}{2}\sum_{k=1}^{\infty}\frac{|x|^{2k}}{k!k!2^{2k-1}}\left\{1+\frac{1}{2}+\cdots+\frac{1}{k}\right\}$$

Figures 52(a)-(e) illustrate the probability density function (p.d.f) plots of the ω term for all the packing condition tests that are performed here. The pdf's are constructed for the first measuring point in the vertical direction (with z/d=0.89) above the ball (location A). In the 70% case the closest measuring point above the ball is located half of a ball diameter form the top of the fifth layer (location E) (figures 34(a) and (b) illustrate the measuring points above the ball).

Figures 52 (a)-(e) reveal the occurrence of extreme events during the tests. The term uw obtains values that are as high as times $\overline{uw}$ (figure 52 (c)). This result is in agreement with the findings of Lu and Willmarth (1973) for smooth walls. They found that uw can be up to 66 times greater than $\overline{uw}$. The long tail in the positive ω axis of figure 52(a) reveals the dominance in magnitude of the bursts and sweeps over the inward and outward interactions. These high intensity events in the 2% case occupy only 1/3 of the total measuring time (table 14). The distributions become symmetric as the packing density increases (figures 52(b)-(d)). This indicates that the intensity of the sweeps and bursts is almost identical to the intensity of the inward and outward interactions.

7.2. The Stochastic Incipient Motion Model.

In this study the stochastic incipient condition model is derived for two distinct packing configurations (figure 53). The first packing configuration represents the case of a particle that is fully exposed to the flow (i.e. the 2%, 20%, 35%, and 50% cases). The second packing geometry represents the case of a particle that is tightly packed within a bed layer (i.e. the 70% case).

a. Derivation of the threshold model for the first packing configuration.

The instantaneous forces operating on a particle that is fully exposed to the flow (i.e. the 2%, 20%, 35%, and 50% packing conditions) and is in contact with a fixed bed of identical particles in a closely packed three dimensional arrangement are (figure 54):

1. The fluid drag force, which acts at the center of the sphere and is equal to (Yalin, 1977),

$$F_D = 0.125 C_D \rho d^2 U^2 \qquad (31)$$

where, U is the instantaneous streamwise velocity (equation 26(a)), d is the particles' diameter, and C_D is the drag coefficient.

2. The fluid lift force that is acting in the vertical direction and at the center of the sphere (figure 54). The lift force is equal to (Yalin, 1977),

$$F_L = 0.125 C_L \rho d^2 W^2 \qquad (32)$$

where, C_L is the lift coefficient, and W is the instantaneous velocity in the vertical direction (equation 26(b)).

3. The submerged weight of the sphere at its center,

$$G = \frac{1}{6}\pi(\rho_s - \rho) g d^3 \qquad (33)$$

Where, ρ_s is the density of the sphere.

Rolling is considered here as the primary mode of the particle motion. The minimum condition for motion of the ball is determined by taking the balance of moments around the point P_2. The balance of moments of the above forces around the point P_2 yields the following relation:

$$F_D L_3 + F_L \cos\lambda\, L_2 \geq G \cos\lambda\, L_2 \tag{34}$$

where, λ denotes the angle between the flume bed and the horizontal plane.

From the geometry of figure 54 it is obtained that,

$$L_2 = \frac{d}{4\sqrt{3}}$$

and (35)

$$L_3 = \frac{d}{\sqrt{6}}$$

By substituting equations (31), (32), (33), and (35) into (34) we get:

$$A_1U^2+A_2W^2 \geq C \tag{36}$$

Where,

$$A_1 = C_D 0.125 \rho d^3 \frac{1}{\sqrt{6}}$$

$$A_2 = C_L 0.125 \rho d^3 \frac{1}{4\sqrt{3}} \cos\beta$$

and

$C=G\cos\lambda L_2$

C denotes the minimum moment that is required for the commencement of the ball motion in the 2%, 20%, 35%, and 50% packing conditions.

Equation (36) constitutes the threshold equation of sediment motion for an exposed to the flow particle (figure 54). This equation is used as the basis for the development of a stochastic model that will be applicable in the 2%, 20%, 35%, and 50% cases and will be used to determine the minimum magnitude of the instantaneous stress that is necessary to move the ball. For this purpose, next, the statistical characteristics of the terms A_1U^2 and A_2W^2 in equation (36) are examined.

b. Stochastic model for the first packing configuration.

It is recognized in the literature (e.g. Grass, 1983; Lu and Willmarth, 1973; Nezu and Nakagawa, 1993), for both smooth and rough walls, that the histograms of the instantaneous velocities U and W are well approximated by a Gaussian distribution. Also, it is known from statistics (e.g. Olkin et al., 1980) that if a random variable x follows a normal distribution then the square of this variable $y=x^2$ is well represented by

a Gamma distribution. The equation that provides the Gamma density function in this case is the following :

$$P(y) = \frac{1}{\sqrt{2\pi y}} e^{-\frac{y}{2}} \tag{37}$$

According to this remark, U^2 and W^2 in equation (36) follow a Gamma distribution with a density function that is given by equation (37). This does not mean though that the summation of A_1U^2 with A_2W^2 will follow necessarily a Gamma distribution. No proof exists in statistics, which shows that the summation of two Gamma distributions is also a Gamma distribution (Olkin et al., 1980). Another reason that makes the problem more complicated is that U and W are not independent random variables.

In the present study we circumvent the above difficulties by treating the sum $A_1U^2+A_2W^2$ as a new variable, Φ. We focus on the statistical behavior of Φ without considering the statistical characteristics of the terms A_1U^2 and A_2W^2.

Specifically, we assume that the histogram of the new variable Φ is well represented by a two-parameter Gamma density function model. The two variable Gamma density function for the normalized Φ variable, Φ_N is given by,

$$f(\Phi_N | \beta, \delta) = \frac{\beta^{\delta}}{\Gamma(\delta)} \Phi_N^{\delta-1} e^{-\beta\Phi_N} \tag{38}$$

where, Φ_N is the normalized Φ variable and is equal to $\frac{\Phi}{\overline{\Phi}}$, $\overline{\Phi}$ is the mean value of Φ, β is a parameter, and δ defines the shape of the Gamma distribution. Using the method of moments the estimates of the parameters are:

$$d = \Phi'^{2}_{N} b^{2} \tag{39a}$$

$$b = \frac{d}{\overline{\Phi}_N} \tag{39b}$$

Φ'_N is the standard deviation of Φ_N. $\Gamma(d)$ denotes the Gamma function of δ.

To examine the validity of the assumption that is made above (i.e. that Φ follows a Gamma distribution), the data that are obtained in the 2%, 20%, 35%, and 50% packing conditions for the location A (with z/d=0.89) are analyzed. For this purpose the program "phi.for" is written in Fortran language to compare the experimentally determined Φ values with the theoretical Φ values that are computed by means of equations (38) and (39). Table 15 provides the average and standard deviation values of the normalized variable Φ_N, the values of the quantities A_1 and A_2, the average and standard deviation values of Φ, the values of the parameters δ and β that are computed respectively from equations (39a) and (39b), and the values of the $\Gamma(\delta)$ function. Because δ is not an integer number (see table 15) the values of $\Gamma(\delta)$ are computed by using the Stirling formula (Standard Mathematical Tables, 1986).

Figures 55(a)-(d) illustrate the probability density function distributions for the 2%, 20%, 35%, and 50% packing conditions. It is observed, from these figures, that the theoretical distributions fit quite well the experimental data. This happens for all the packing cases despite the fact that the values of δ and β that are used here are determined from the method of moments (equations (39a) and (39b)) and not from a best fit analysis. Figures 55(a)-(d) reveal that the shape of the Φ_N distribution varies from one packing density to another. To maintain consistency during the analysis of data the distribution of Φ_N is constructed for the first measuring point in location A (this is the only location with available data for all the packing conditions). In the 2% case (figure 55(a)) Φ_N follows a "bell-shape" gamma distribution. In the 20% case (figure 55(b)) Φ_N follows a "bell-shape" gamma distribution, which is less pronounced than in the 2% case. In the 35% case (figure 55(c)) the data are approximated with a distribution that almost follows the shape of an exponential. This is reasonable because the shape factor δ in this case is almost equal to 1 (δ=0.836, in table 15); and it is known in statistics that when δ=1 then the gamma distribution becomes exponential (Guttman et al., 1965). The exponential distribution is a special case of a gamma distribution. Finally, in the 50% case the Φ_N distribution obtains a similar shape (i.e. a "bell-shape gamma distribution) to the one in the 20% case. Overall figures 55 (a)-(d) show that the distribution of Φ is well approximated by the two-parameter gamma distribution (equation (38)). The two-parameter gamma distribution is typically used in reliability analysis to determine the time to failure of a system. Recently, Paola (1996) used the two-parameter gamma model to describe the stochastic nature of the bed shear stress in a river bed stream.

c. Derivation of the threshold and stochastic models for the second packing configuration.

The instantaneous forces operating on a particle that is tightly packed (figure 56) within a bed layer are:

1. The fluid lift force that is acting in the vertical direction and at the center of the ball. The lift force in this case is expressed as function of the instantaneous streamwise velocity U (Yalin, 1977) and is equal to,

$$F_L = 0.125 C_L \rho d^2 U^2 \qquad (40)$$

2. The submerged weight of the sphere that is defined in equation (33).

   For the tightly packed ball, movement can occur only as the perpendicular lift exceeds the submerged weight of the particle, i.e.,

$$F_L \geq G\cos\lambda \qquad (41)$$

By substituting equations (33) and (40) to (41) we get,

$$A_3 U^2 \geq G\cos\lambda$$

$$U^2 \geq G\cos\lambda / A_3 \qquad (42)$$

Where, $A_3 = 0.125\rho\pi d^2 C_L$. Equation (42) defines the threshold condition for a particle that is tightly packed within a bed layer.

U^2 in (42) follows a gamma distribution with a density given by equation (37). Figure 57 illustrates the histogram of the normalized U^2, U_N, for the first measuring point (z/d =0.57) in location E (figure 34(b)). The square of the normalized instantaneous streamwise velocity is defined as, $U_N^2 = \left(\frac{U - \overline{U}}{u'} \right)^2$. The values of $\overline{U}$ and u′ are given in table 15.

The linkage of turbulence with the entrainment of sediment is possible in the present study by considering that the probability of entrainment of sediment, P_E (which is defined in equation (7)) is equal to the probability of occurrence of the high energetic stress events that can cause the commencement of sediment motion. Based on this concept the lower bound of the Φ variable (i.e., for the first four packing conditions) or, of the U^2 variable (i.e. for the 70% packing condition) is determined. The sketch in figure 58 depicts the above idea. In the present study, we assume that for relatively large periods of time the probability distribution of Φ or U^2, which is constructed here, based on point measurements have on an average the same spatial characteristics over the test section. The period of the measurements at a point, in this study, is at least 240 times larger of the average bursting period.

Specifically, for the 2%, 20%, 35%, and 50% packing conditions the critical value of Φ is determined from the following equality:

$$1 - P_E = \int_0^{(\Phi_N)_{cr}} f(\Phi_N | \mathrm{b}, \mathrm{d}) d\Phi_N \cong \int_0^{(\Phi_N)_{cr}} \frac{\mathrm{b}^{\mathrm{d}}}{\Gamma(\mathrm{d})} \Phi_N^{\mathrm{d}-1} e^{-\mathrm{b}\Phi_N} d\Phi_N \qquad (44)$$

For the 70% case the critical value of U is determined from the following relation:

$$1-P_E = \int_0^{\left(\frac{U-\overline{U}}{u'}\right)_{cr}} \frac{1}{\sqrt{2p}}\left(\frac{U-\overline{U}}{u'}\right)^{-0.5} e^{-0.5\left(\frac{U-\overline{U}}{u'}\right)} d\left(\frac{U-\overline{U}}{u'}\right) \qquad (45)$$

The integrals in equation (44) and (45) are computed by using the program "Mathematica". The results from the integration process for all the packing conditions are summarized in table 16. The minimum moment C (C denotes the r.h.s. of equation (36)) required to roll the ball in the 2%, 20%, 35%, and 50% cases is equal to 4.67 10^{-6} N-m.

Table 16 shows that the instantaneous value of Φ in the 2% case is almost 4 times greater than its average value $\overline{\Phi}$ and 3.87 times larger than C. In the 20% case Φ is 4.5 greater than $\overline{\Phi}$ and 4.24 than C. In the 35% case Φ is almost 8 times larger than $\overline{\Phi}$ and 5.6 times greater than C. Φ reduces in the 50% case. It becomes 2.87 times greater than its average and 3 times greater than C. In the 70% case the critical value of U is almost 3 times larger than $\overline{U}$ and the corresponding lift force that is computed by means of equation (40) is 2.2 times greater than the submerged weight. The results in table 16 indicate that the critical Φ value is on an average 4 times greater than its average value. Similar results have been reported in the literature (e.g. Gessler, 1965; Lekakis, 1988) about the ratio of the critical bed shear stress with the average bed shear stress.

In summary the results in table 16 reveal that the stochastic model that is constructed here (equations (45) and (46)) can provide consistent results for all the packing conditions. On the average, the critical value of Φ is almost 4 times of the minimum moment, C. In the 70% case the value of the predicted from the model lift

force is almost twice of the submerged weight of the sphere. The difference that is observed in the values of the critical Φ and the minimum moment C may be attributed to the following reasons: 1. The actual point that the effective drag is applied on a particle is not known. The location of this point does not remain the same for the different packing conditions. Subsequently, the length of the moment arm (i.e. L2 in our model) around the support point of the particle (the point P_2 in figure 54) changes for each packing condition. 2. We do not account for the role of the hydrodynamic mass of the fluid. When a body accelerates through a fluid it causes the acceleration of the surrounding fluid. The body behaves as if it is heavier by an amount called the hydrodynamic or added mass of the fluid and requires the application of higher in magnitude fluid forces than the minimum required in order to maintain its motion. For a sphere the coefficient of added mass is 0.5 (Sekine and Kikkawa, 1992). 3. An error may occur in the determination of the probability of sediment entrainment P_E during the analysis of images. Sometimes, when a particle gets entrained may collide with a particle that is located downstream and cause its motion. The image analysis program accounts for the entrainment of both particles in the calculation process of the probability of entrainment. The flow is responsible only for the entrainment of the first particle. 4. The balls may occupy different positions in the flume bed. Depending on their position, some of the balls get entrained more frequently that others.

The above provide some justification for the differentiation that exists in the values of the critical Φ and C. Despite this differentiation the model that is suggested here determines quite well the critical conditions if somebody considers the intermediate steps and assumptions that are involved in the analysis. The Φ seems to be a good

measure for the determination of the initiation of the sediment motion. The present model offers considerable advantages comparatively to the model that is suggested by Naden (1987) because: a. It considers rolling as the primary mode of motion. The Naden's model over - predicts the critical condition by considering that sliding occurs first. b. The Naden model for mathematical expediency considers that w is almost equal to 0.77 of u. While this is valid for the r.m.s quantities of U and W it is not correct for the fluctuating components of the velocities. If we will use the above over simplification in equation (36) we will lead to an overestimation of the critical conditions; and c. The data that are used in the present study are obtained by the LDV system right at the top of the ball for all the packing conditions. No information exists for the location of the measuring point in Naden's data.

Table 13. The rate of the LDV measurements for the different packing conditions.

Tests	$(\frac{\text{number of measurements}}{\text{s}})$
E-2	11
E-20	9
E-35	7
E-50	10
E-70	5

Table 14. The percentage of time that is occupied by each kind of turbulence event.

Tests	Location	Ejections (bursts)	Sweeps	Inward Interactions	Outward Interactions
E-2	A (z/D =0.89)	16.79	20.56	34.9	27.74
E-20	A (z/D=0.89)	27.16	26.25	27.15	19.44
E-35	A (z/D=0.89)	31.32	23.9	22.654	22.102
E-50	A (z/D=0.88)	29.2	25.44	22.97	22.413
E-70	E (z/D=0.566)	33.45	29.65	21.48	15.42

Table 15. The statistical parameters of the Gamma density functions for the packing conditions tests.

Tests	A_1(kg)	A_2(kg)	$\overline{\Phi}_N$	Φ'_N	$\overline{\Phi}$ (N-m)	Φ' (N-m)	β	δ	Γ(δ)
E-2	$6.16\ 10^{-5}$	$1.16\ 10^{-5}$	1	0.52	$4.609\ 10^{-6}$	$2.417\ 10^{-6}$	3.635	3.635	3.869
E-20	$5.91\ 10^{-5}$	$1.16\ 10^{-5}$	1	0.79	$4.365\ 10^{-6}$	$3.436\ 10^{-6}$	1.616	1.616	0.892
E-35	$4.76\ 10^{-5}$	$1.16\ 10^{-5}$	1	1.09	$3.335\ 10^{-6}$	$3.648\ 10^{-6}$	0.836	0.836	1.125
E-50	$4.52\ 10^{-5}$	$1.16\ 10^{-5}$	1	0.88	$4.868\ 10^{-6}$	$4.282\ 10^{-6}$	1.293	1.293	0.839

E-70	$\overline{U}$	u'	β	δ
	0.3456	0.1613	0.5	0.5

Table 16. The ratios of the critical value of Φ (or U) with their average values and the minimum moment C (or lift force).

Tests	$\frac{\Phi_{cr}}{\overline{\Phi}}$	$\frac{\Phi_{cr}}{C}$
E-2	3.923	3.87
E-20	4.5419	4.24
E-35	7.887	5.63
E-50	2.8752	3
E-70	$\frac{U_{cr}}{\overline{U}}$	$\frac{F_L}{G\cos\beta}$
	2.73	2.2

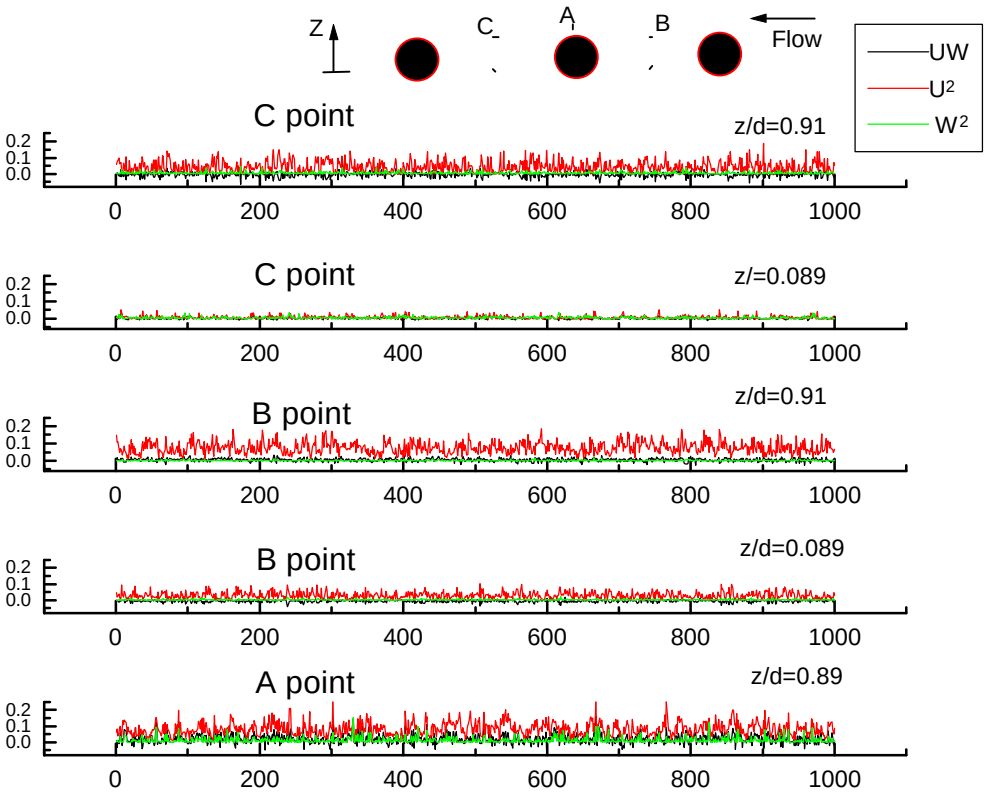

Figure 50(a). Time series plots of U^2, W^2, and UW for the 2% packing condition.

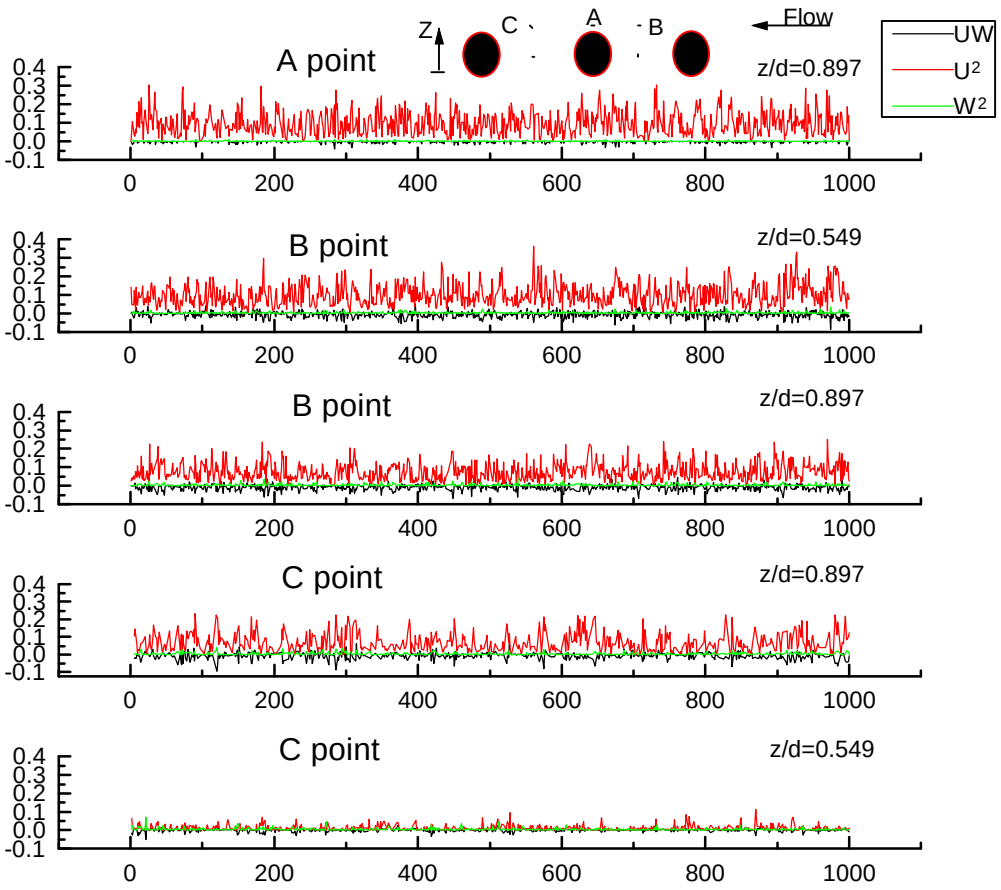

Figure 50(b). Time series plots of U^2, W^2, and UW for the 20% packing condition.

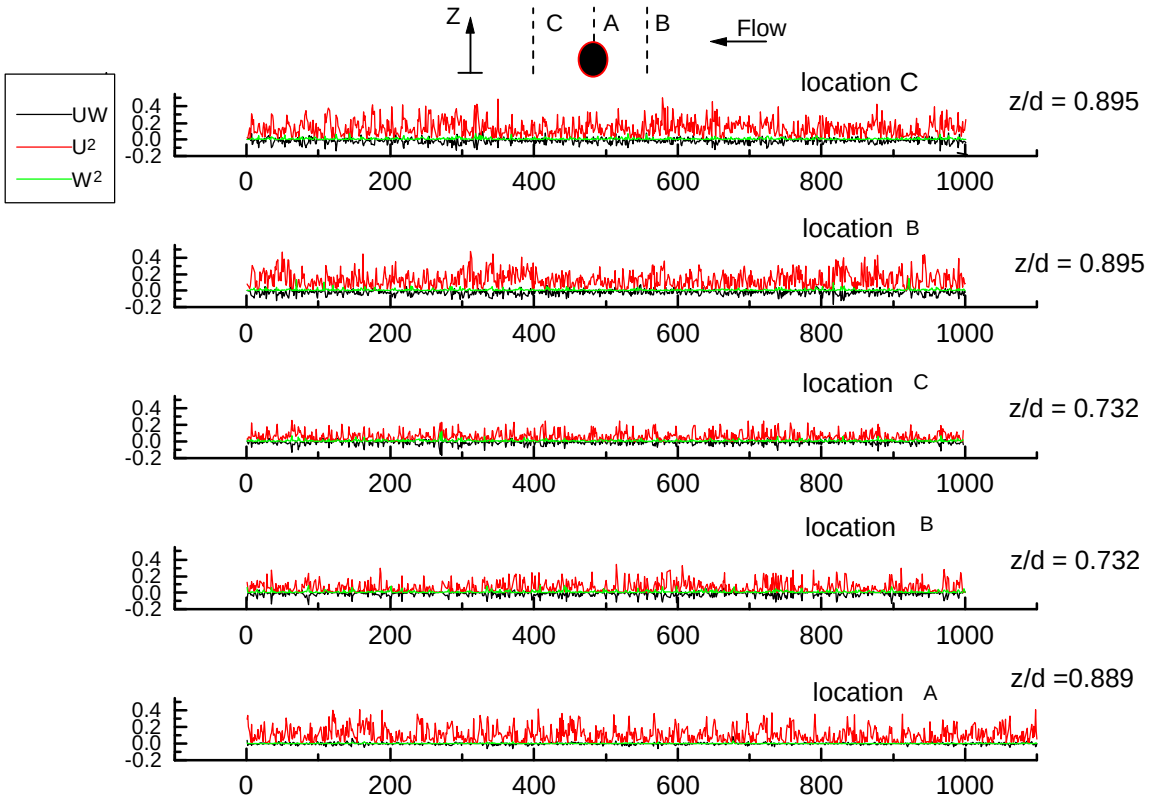

Figure 50(c). Time series plots of U^2, W^2, and UW for the 35% packing condition.

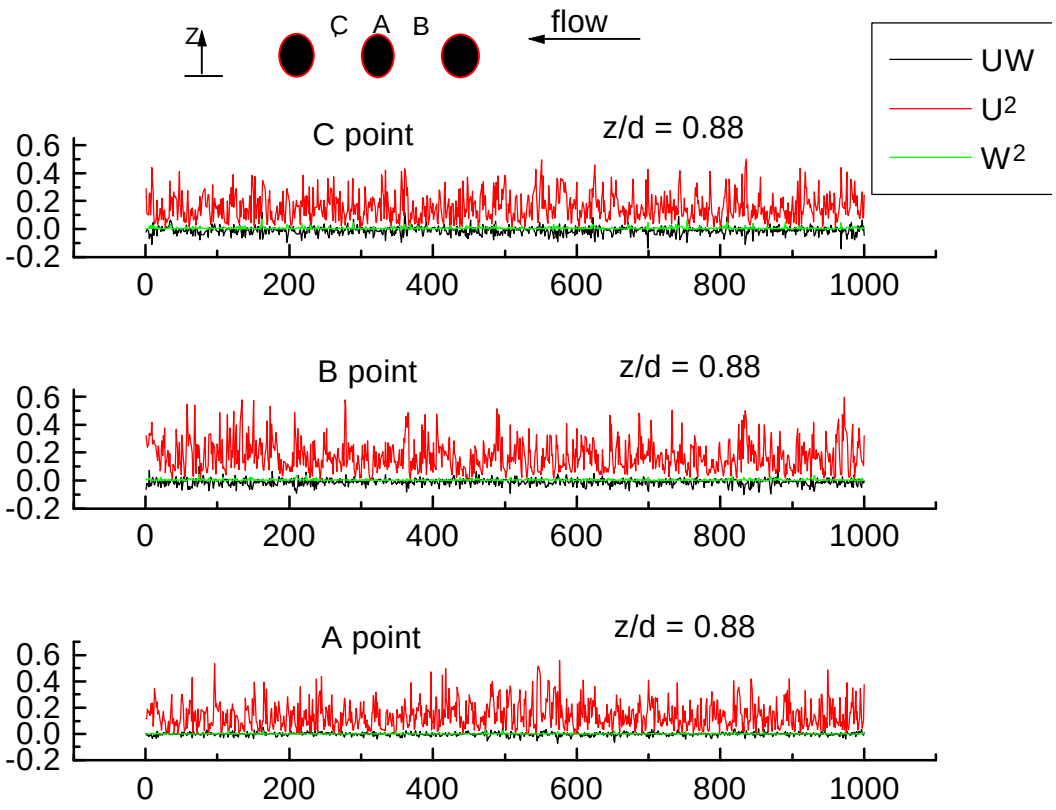

Figure 50(d). Time series plots of U^2, W^2, and UW for the 50% packing condition.

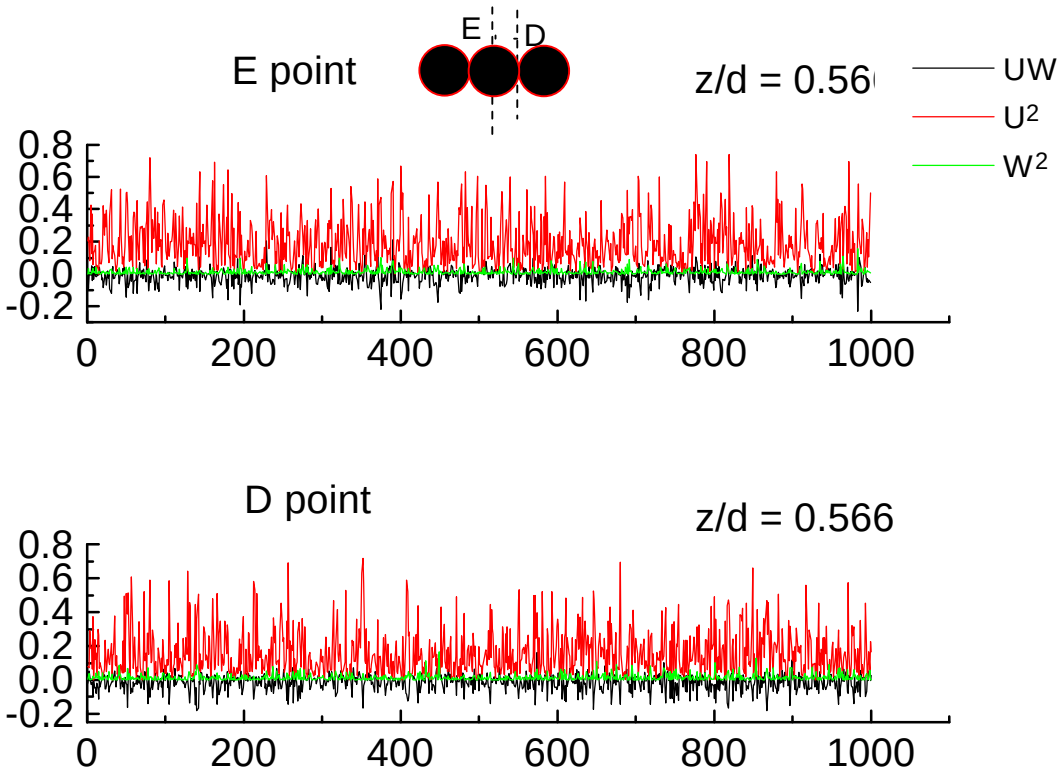

Figure 50(e). Time series plots of U^2, W^2, and UW for the 70% packing condition.

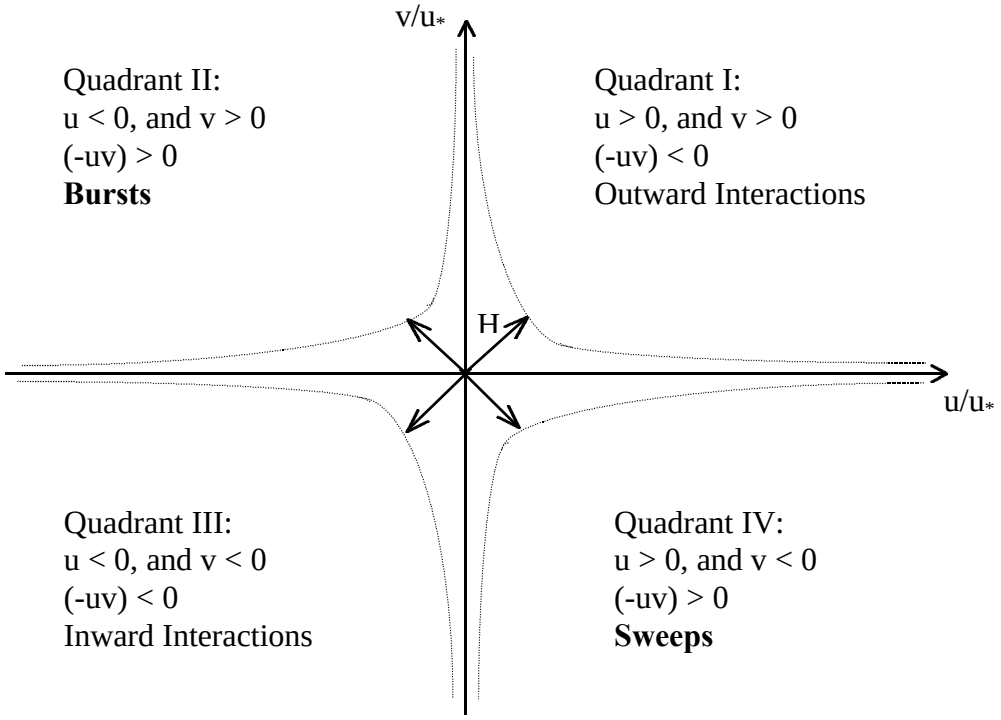

Figure 51. The quadrant method.

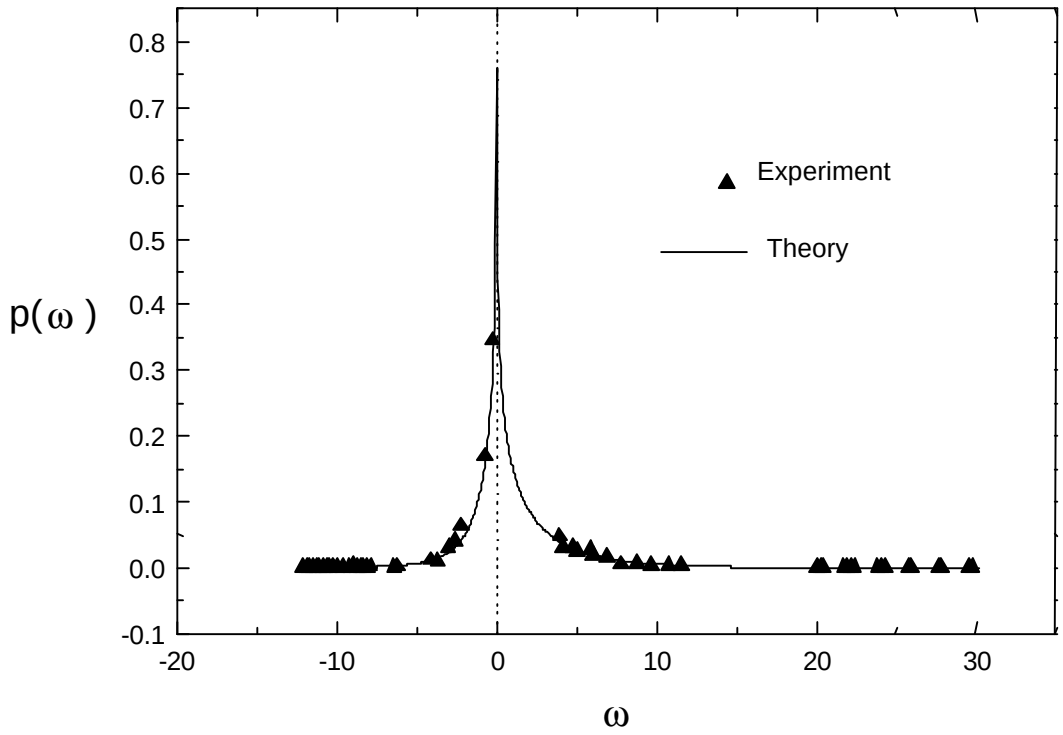

Figure 52(a). The probability density function of the ω term for the 2 % packing condition (location A, z/d=0.89).

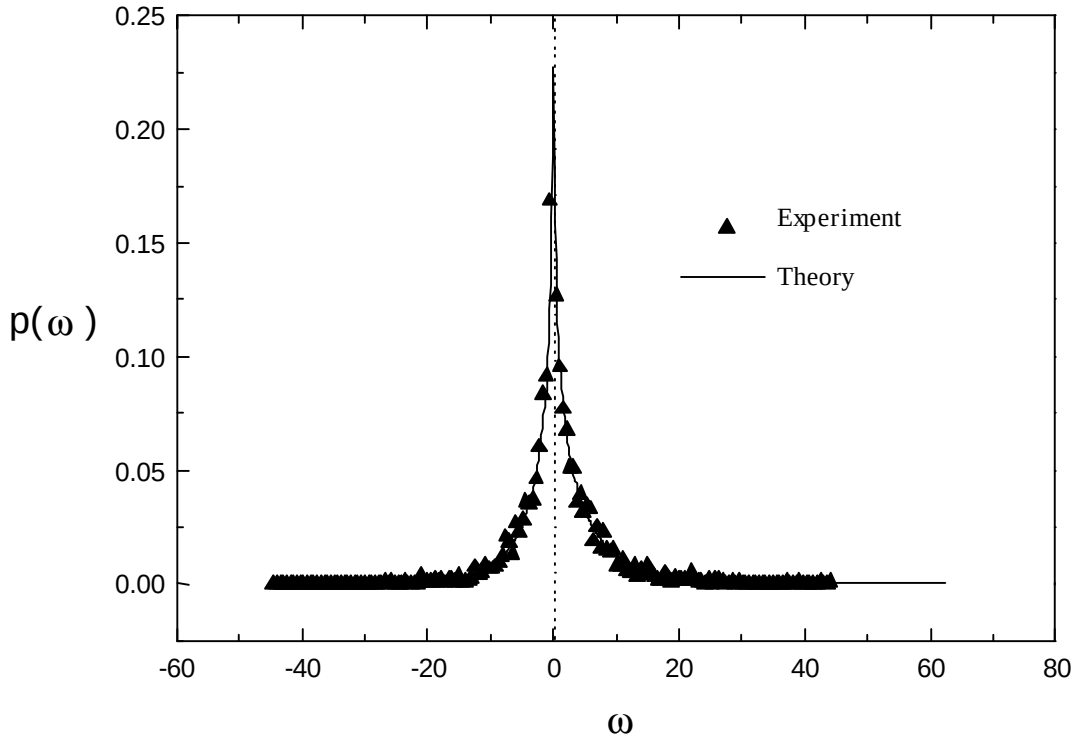

Figure 52(b). The probability density function of the ω term for the 20% packing condition (location A, z/d=0.89).

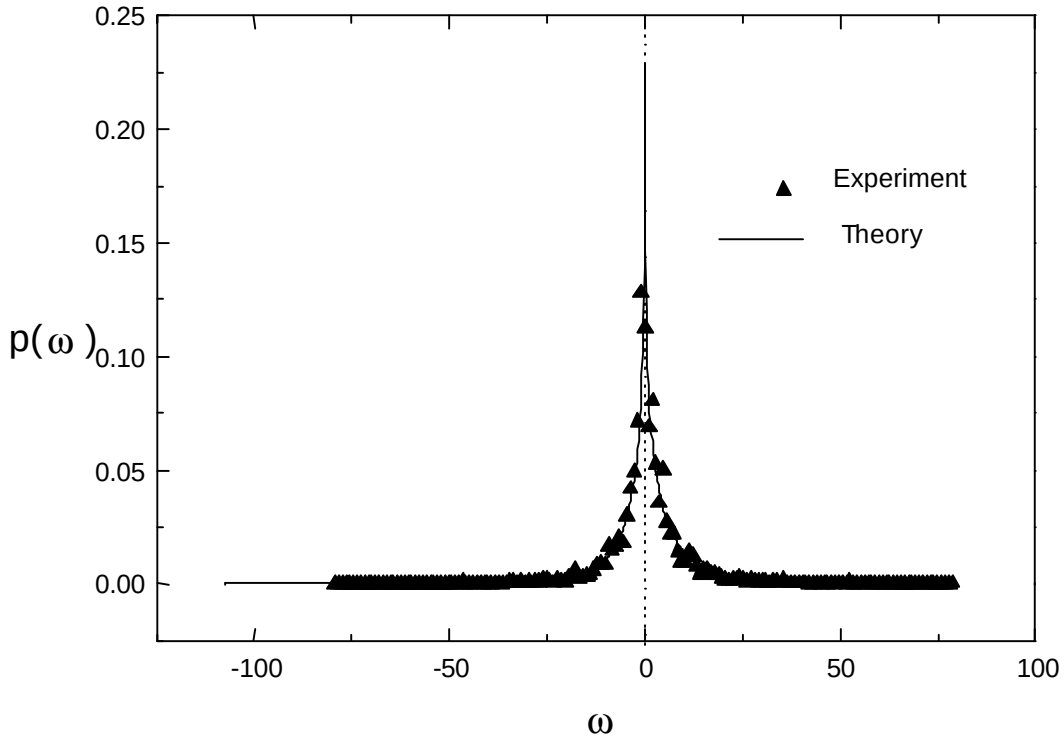

Figure 52(c). The probability density function of the ω term for the 35% packing condition (location A, z/d=0.89).

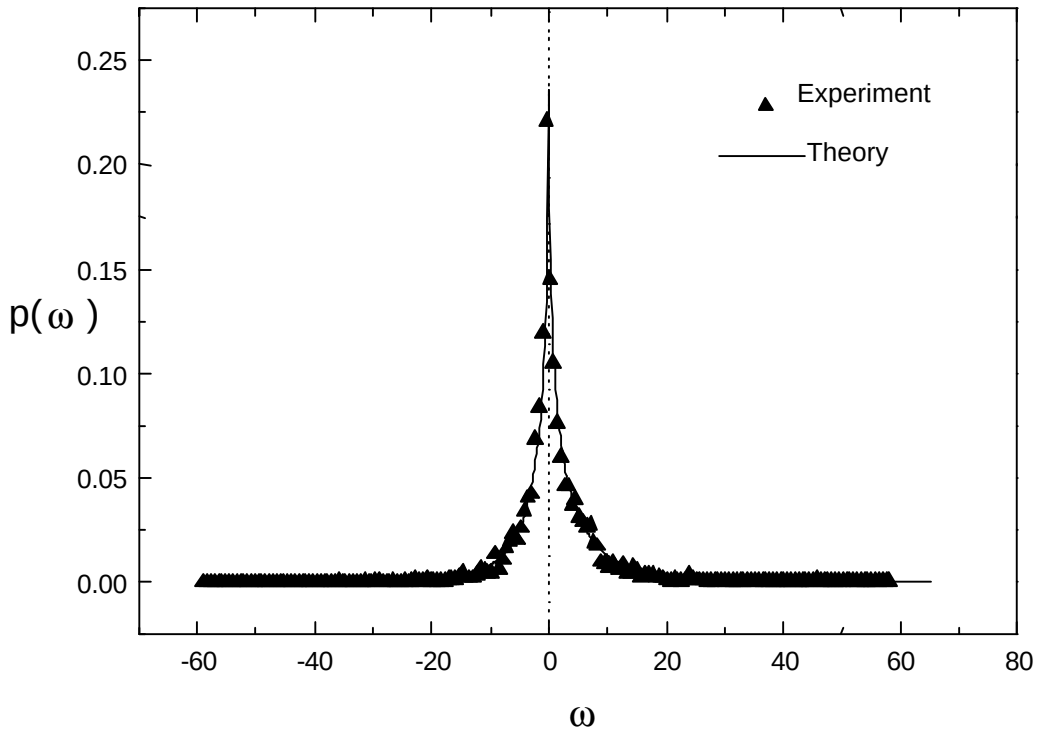

Figure 52(d). The probability density function of the ω term for the 50% packing condition (location A, z/d=0.89).

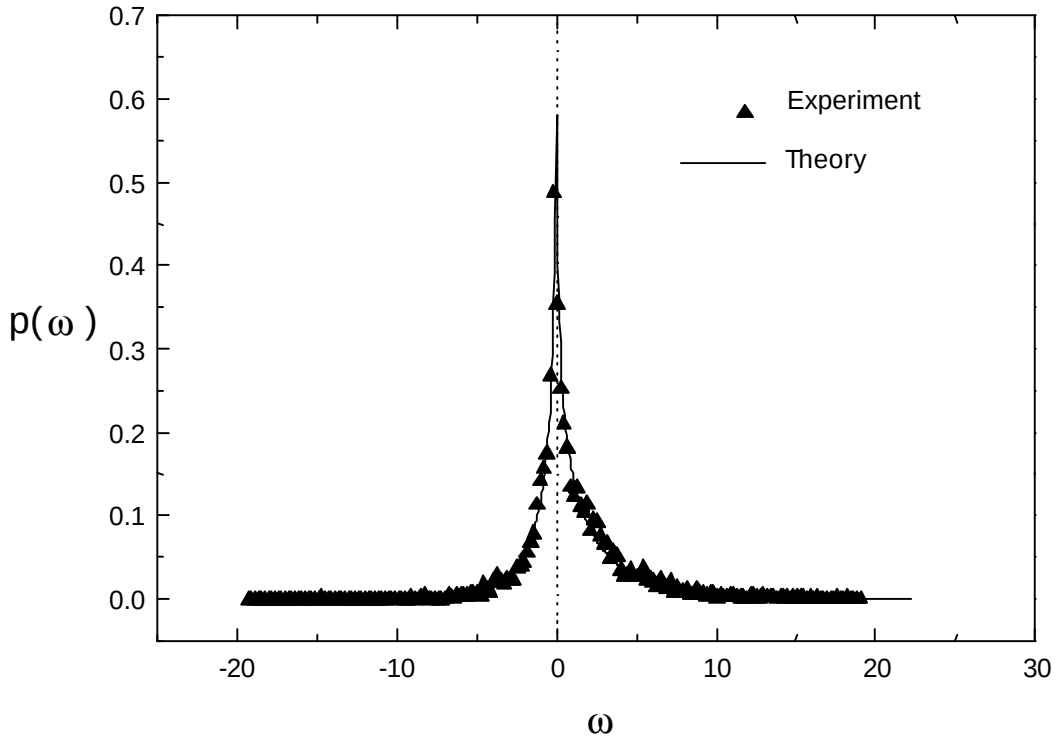

Figure 52(e). The probability density function of the ω term for the 70% packing condition (location E, z/d=0.566).

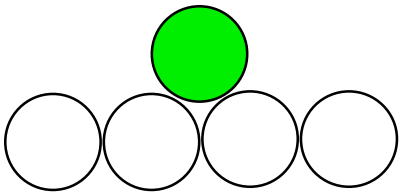

Packing configuration I

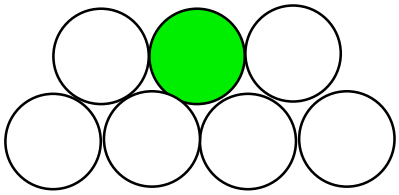

Packing configuration II

Figure 53. The different packing configurations of a particle.

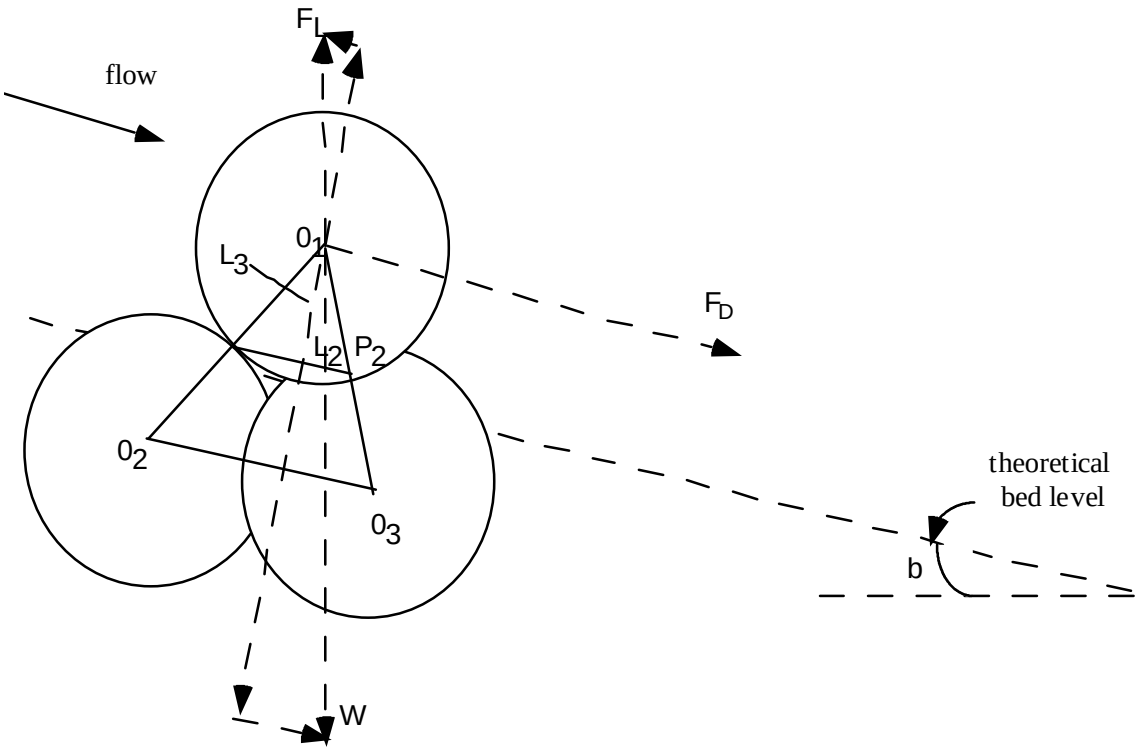

Figure 54. Forces acting on a particle that is fully exposed to the flow.

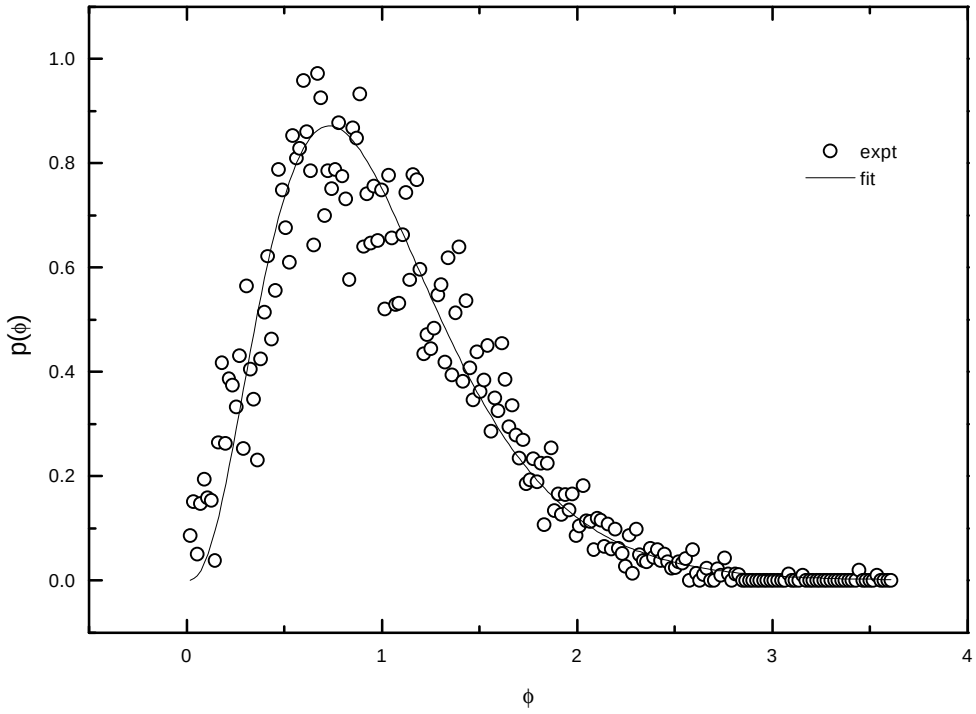

Figure 55 (a). The probability density function plot of the normalized Φ variable for the 2% packing condition.

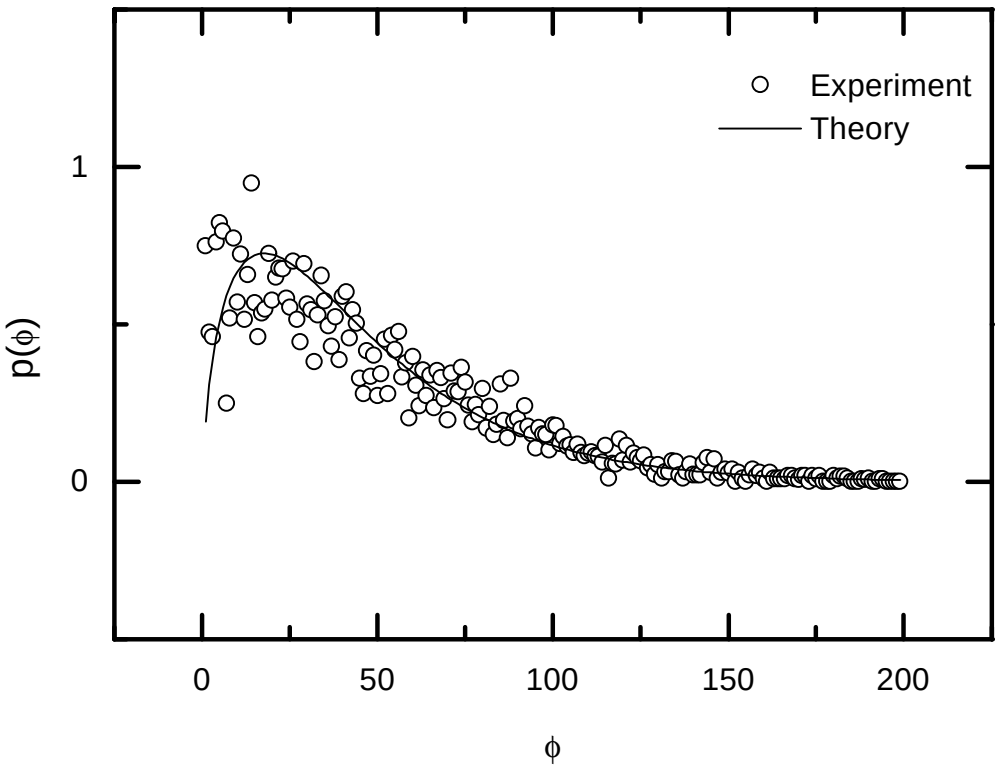

Figure 55 (b). The probability density function plot of the normalized Φ variable for the 20% packing condition.

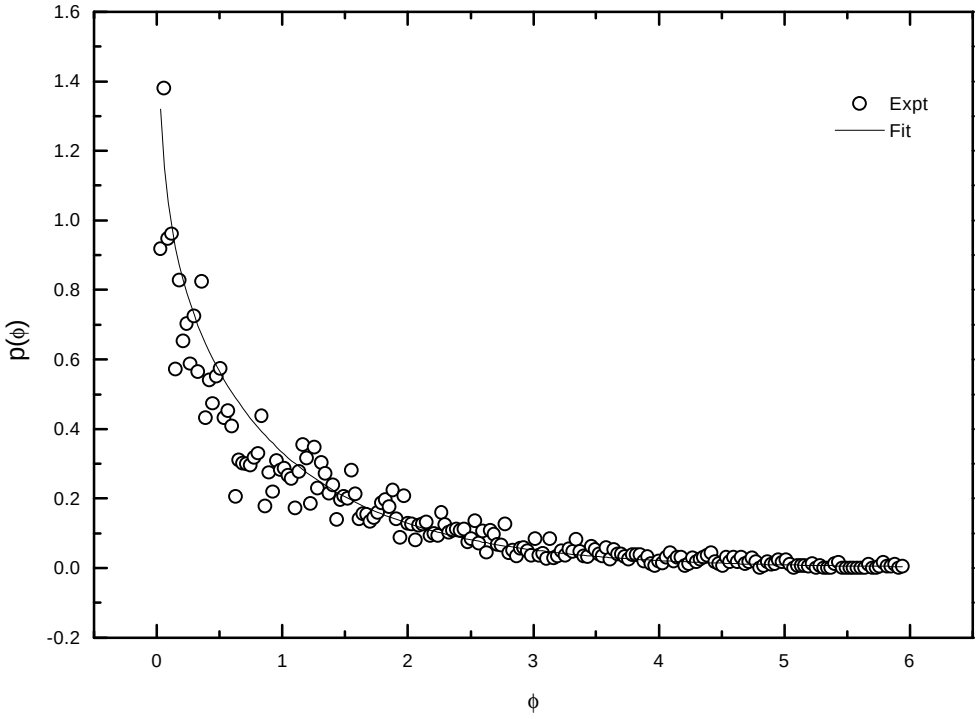

Figure 55 (c). The probability density function plot of the normalized Φ variable for the 35% packing condition.

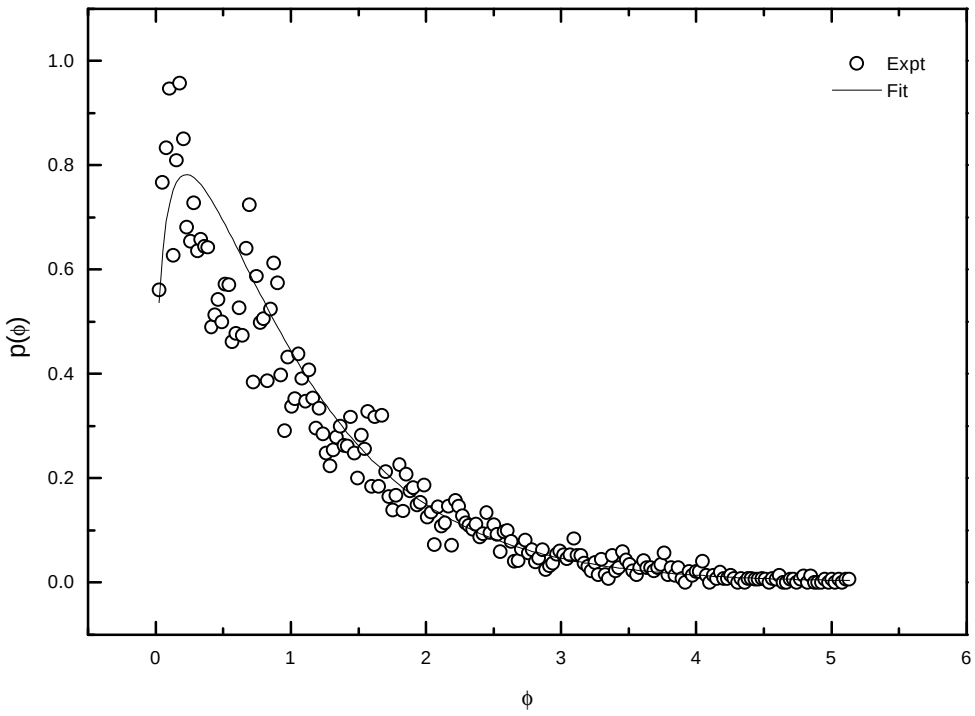

Figure 55 (d). The probability density function plot of the normalized Φ variable for the 50% packing condition.

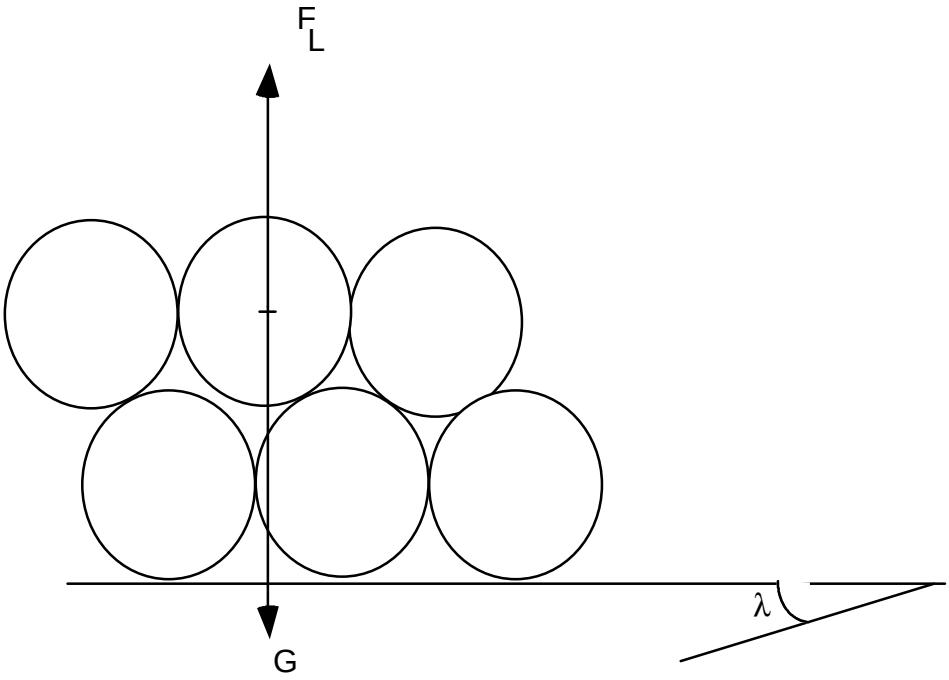

Figure 56. Forces acting on a particle that is tightly packed.

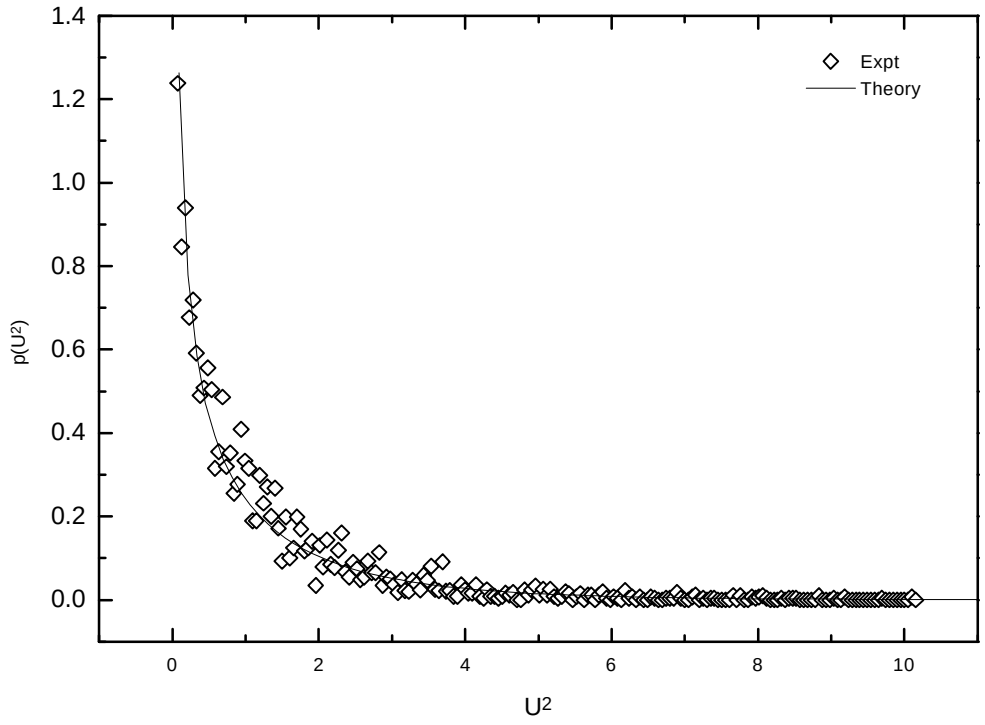

Figure 57. The probability density function plot of the normalized U^2 variable for the 70% packing condition.

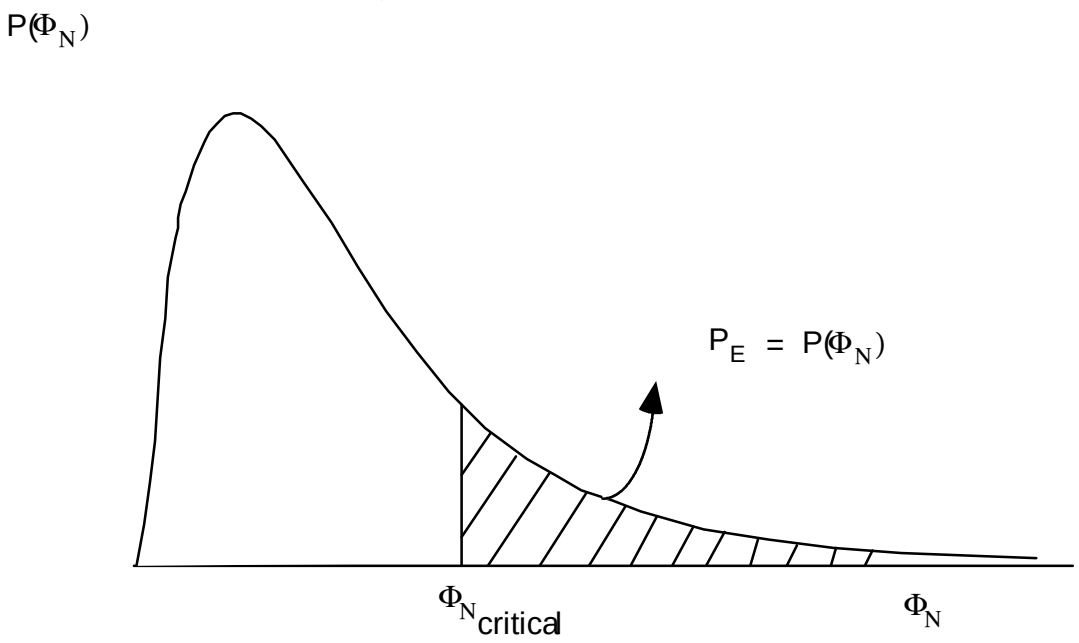

a. Conceptual model for the 2%, 20%, 35%, and 50% packing conditions.

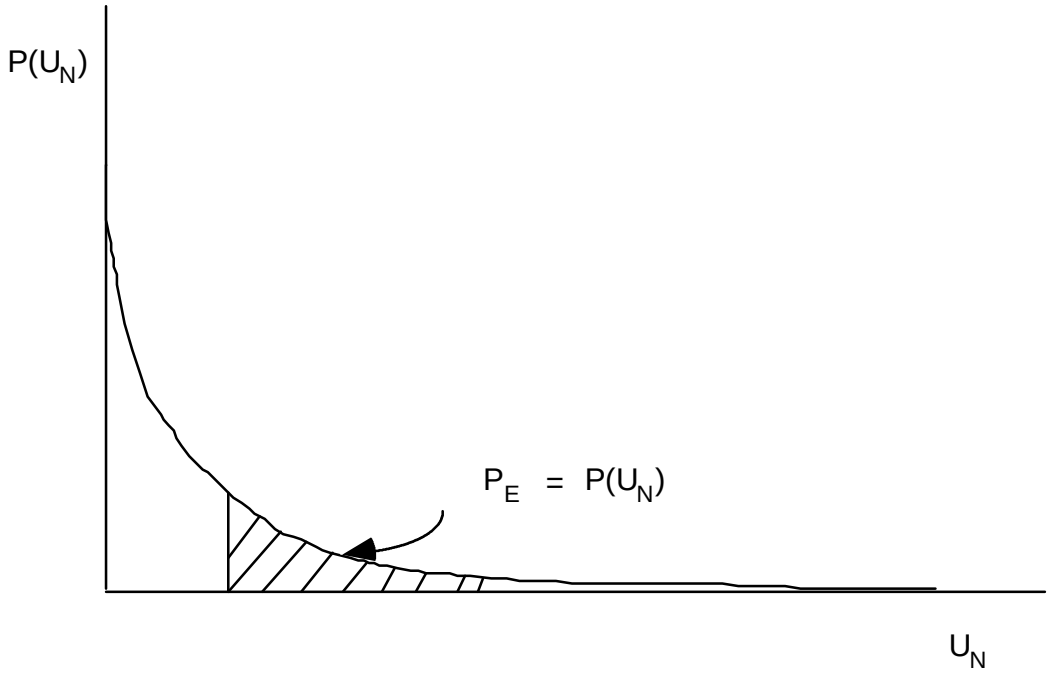

b. Conceptual model for the 70% packing condition.

Figure 58. The linkage of turbulence with sediment entrainment.

Chapter 7

Conclusions

In the present study we examine the role of different instantaneous stress components on the initiation of sediment motion for different bed packing configurations. First, a new methodology is introduced to determine experimentally the critical hydraulic conditions during the tests. To establish these conditions for all the cases, an image analysis tool is used.

It is suggested here that a more rigorous method to predict the commencement of sediment motion is the one that considers the "first displacement" of particles. The main concept behind the determination of the critical conditions for all the packing cases is that the probability of the entrainment of a particle must be the same during a bursting period.

In the present study the events of a bursting cycle are considered as the primary mechanisms responsible for the initiation of sediment motion. The contributions of these events to the Reynolds stress are calculated for the different packing conditions. It is shown that the sweeps and ejections are larger in magnitude in comparison to the interactions for the 2% case.

To investigate the changes in magnitude of the normal stresses U^2 and W^2 and shear stress UW , their time series is constructed for locations close to a ball. It is shown that U^2 is the most dominant term of the stress tensor for all the packing conditions.

In the present study we related the flow data that are obtained from the LDV system with the aerial information obtained from the image analysis tool in order to develop a stochastic tool to predict the threshold conditions of sediment entrainment. It is considered here that the spatial characteristics of the stress do not vary for long time periods.

A new variable (Φ) is introduced to describe the probabilistic nature of turbulence in conjunction with the sediment motion. The balance of moments for two distinct packing configurations is obtained to compute the minimum moment that is necessary for the rolling of a sphere. It is shown that the new variable is a good predictor of the entrainment of a particle. The new variable is well represented by a gamma distribution. The critical value is determined here based on the idea that the probability of the entrained particles should be ideally equal to the probability of the turbulent energetic events that cause the motion. This value can be used as the lower bound in different probabilistic bed load models.

The existing method does not provide any detailed information for the flow events causing the entrainment of particles. This information most probably can be extracted from observations during the interaction of a sphere with the flow field.

References

Ackers, P., and W. R. White (1973). "Sediment Transport: New Approach and Analysis." Journal of Hydraulic Engineering, Vol. 99, HY11, pp. 2041-2060.

Advanced Imaging (1995). "Imaging Development Tools On-Line?" September, pp. 40-42.

Alfredsson, P. H., and A. V. Johansson (1984). "On the Detection of Turbulence-Generating Events." Journal of Fluid Mechanics, Vol. 139, pp. 325-345.

Antonia, R. A. (1981). "Conditional Sampling in Turbulence Measurement." Annual Review of Fluid mechanics, Vol. 13, pp. 131-156.

Bagnold, R. A. (1979). "Sediment Transport by Wind and Water." Nordic Hydrology, Vol. 10, pp. 309-322.

Balakrishnan, M. (1997). Ph.D. Dissertation, in Press, Department of Mechanical Engineering, Virginia Polytechnic Institute and State University, Blacksburg, Virginia.

Balakrishnan, M., and C. L. Dancey (1994). "An Investigation of Turbulence in Open-Channel Flow via Three-Component Laser Doppler Anemometry." ASCE Conference, August 1-6, Buffalo, NY.

Bettess, R. (1984). "Initiation of Sediment Transport in Gravel Streams." Proceedings of the Institution of the Civil Engineers, Part 2, March, pp. 79-88.

Billi, P. (1988). "A Note on Cluster Bedform Behavior in a Gravel-Bed River." Catena, Vol. 15, pp. 473-481.

Blackwelder, R. F., and J. H. Haritonidis (1983). "Scaling of the Bursting Frequency in Turbulent Boundary Layers." Journal of Fluid Mechanics, Vol. 132, pp. 87-103.

Blackwelder, R. F., and R. E. Kaplan (1976). "On the Wall Structure of the Turbulent Boundary Layer." Journal of Fluid Mechanics, Vol. 76, pp. 89-112.

Brayshaw, A. C., L. E. Frostick, and I. Reid (1983). "The Hydrodynamics of Particle Clusters and Sediment Entrainment in Coarse Alluvial Channels." Sedimentology, Vol. 30, pp. 137-143.

Bridge, J. S., and Bennett, S. J. (1992). "A Model for the Entrainment and Transport of Sediment Grains of Mixed Sizes, Shapes, and Densities." Water Resources Research, Vol. 28, No. 2, pp. 337-363.

Browand, F. K., and Plocher, D. A. (1985). "Image Processing for Sediment Transport." International Association for Hydraulic Research, 21st Congress, August, Melbourne, Australia.

Cantwell, B. J. (1981). "Organized Motion in Turbulent Flow." Annual Review of Fluid Mechanics, Vol. 13, pp. 457-515.

Carling, P. A. (1983). "Threshold of Coarse Sediment Transport in Broad and Narrow Natural Streams." Earth Surface Processes and Landforms, Vol. 8, pp. 1-18.

Clifford, N. J., J. McClatchey, and J. R. French (1991). "Measurements of Turbulence in the Benthic Boundary Layer Over a Gravel Bed and Comparison Between Acoustic Measurements and Predictions of the Bedload Transport of Marine Gravels." Sedimentology, Vol. 38, pp. 161-171.

Cline, C., and S. Deutsch (1993). "On Elevated RMS Level in Wall-Bounded Turbulent Flows When Measured by Laser Doppler Velocimeter." Experiments in Fluids, Vol. 15, pp. 130-132.

Coleman, N. L. (1967). "A Theoretical and Experimental Study of Drag and Lift Forces Acting on a Sphere Resting on Hypothetical Stream Bed." Paper Presented at the 12th Congress, International Association for Hydraulics Research, Fort Collins, Colorado.

Corrisin, S. (1973). "Comment on Statistical Characteristics of Reynolds Stress in a Turbulent Boundary Layer." Physics of Fluids, Vol. 16, p 341.

Dancey, C. L. (1990). "Measurement of Second Order Turbulence Statistics in an Axial Flow Compressor via 3-component LDA." AIAA Journal, Vol. 90, p 2017.

Diplas, P., and G. Parker (1992). "Deposition and Removal of Fines in Gravel-Bed Streams," Dynamics of Gravel-Bed Rivers. Edited by P. Billi, R. D. Hey, C. R. Thorne, and P. Tacconi.

Drain, L. E. (1980). The Laser Doppler Technique. John Wiley & Sons, Chichester.

Drake, T. G., R. L. Shreve, W. E. Dietrich, P. J. Whiting, and L. B. Leopold (1988). "Bedload Transport of Fine Gravel Observed by Motion-Picture Photography." Journal of Fluid Mechanics, Vol. 192, pp. 193-217.

Duboys, P. (1879). "Le Rhone et les Rivieres a Lit Affouillable." Annales des Ponts et Chaussees, Series 5, Vol. 18, pp. 141-195.

Economicos, L., C. Shoemaker, K. Russ, R. Brodkey, and D. Jones (1990). "Toward Full-Field Measurements of Instantaneous Visualizations of Coherent Structures in Turbulent Shear Flows."" Experimental Thermal Fluid Science, Vol. 3, pp. 74-86.

Edwards, R. V. (1987). Report of the Special Panel on Statistical Particle Bias Problems in Laser Anemometry." Journal of Fluids Engineering, Vol. 109, pp. 89-93.

Egiazaroff, I. V. (1965). "Calculation of Non-Uniform Sediment Concentration." Journal of Hydraulic Division, ASCE, Vol. 91, pp. 225-247.

Einstein, H. A., and E. A. El-Samni (1949). "Hydrodynamic Forces on a Rough Wall." Review of Modern Physics, Vol. 21, pp. 520-524.

Fenton, J. D., and J. E. Abbott (1977). "Initial Movement of Grains on a Stream Bed: The Effect of Relative Protrusion." Proceedings of the Royal Society of London, Series A, Vol. 352, pp. 523-537.

Gessler, J. (1965). "The Beginning of Bedload Movement of Mixtures Investigated as Natural Armoring Channels." Ph.D. Thesis at the Swiss Federal Institute of Technology.

Graf, W. H., and G. C. Pazis (1977). "Les Phenomenes de Deposition et d'Erosion dans un Canal Alluvionnaire." Journal of Hydraulic Research, Vol. 15, pp. 151-165.

Grass, A. J. (1971). "Structural Features of Turbulent Flow Over Smooth and Rough Boundaries." Journal of Fluid Mechanics, Vol. 50, Part 2, pp. 233-255.

Grass, A. J. (1983). The Influence of Boundary Layer Turbulence on the Mechanics of Sediment Transport. Edited by B. M. Sumer, and A. Muller, pp. 3-17, A. A. Balkema, Rotterdam, Netherlands.

Grass, A. J., R. J. Stuart, and M. Mansour-Tehrani (1991). "Vortical Structures and Coherent Motion in Turbulent Flow Over Smooth and Rough Boundaries." Journal of Fluid Mechanics, Vol. 336, pp. 35-65.

Gupta, A. K., and R. E. Kaplan (1972). "Statistical Characteristics of Reynolds Stress in a Turbulent Boundary Layer." Physics of Fluids, Vol. 15, No. 6, June, pp. 981-985.

Gyr, A. (1983). "Towards a Better Definition of the Three Types of Sediment Transport, Journal of Hydraulic Research, Vol. 21, pp. 1-15.

Haralick, R. M., and L. G. Shapiro (1991). "Glossary of Computer Vision Terms." Pattern Recognition, Vol. 24, No. 1, pp. 69-93.

He, M., and Q. Han (1982). "Stochastic Model of Incipient Sediment Motion." Journal of Hydraulic Division, ASCE, Vol. 108, No. HY2, February, pp. 211-224.

Jain, R., R. Kasturi, and B. G. Schunck (1995). Machine Vision. McGraw-Hill Series in Computer Science, McGraw-Hill, Inc.

Kalinske, A. A. (1947). "Movement of Sediment as Bed Load in Rivers." Transactions, American Geophysical Union, Vol. 28, No. 4, pp. 615-620.

Kline, S. J., W. C. Reynolds, F. A. Schraub, and P. W. Runstadler (1967). "The Structure of Turbulent Boundary Layers." Journal of Fluid Mechanics, Vol. 30, pp. 741-773.

Komar, P. D., and Z. Li (1986). "Pivoting Analyses of the Selective Entrainment of Sediments by Shape and Size with Application to Gravel Threshold." Sedimentology, Vol. 33, pp. 425-436.

Kramer H. (1935). "Sand Mixtures and Sand Movement in Fluvial Models." Transactions, ASCE, Vol. 100, pp. 798-878.

Krogstad, P. A., R. A. Antonia, and L. W. B. Browne (1992). "Comparison Between Rough and Smooth Wall Turbulent Boundary Layers." Journal of Fluid Mechanics, Vol. 245, pp. 599-617.

Kuhnle, R. A. (1995). "Incipient Motion of Sand-Gravel Sediment Mixtures." Journal of Hydraulic Engineering, Vol. 119, No. 12, pp. 448-449.

Lavelle, J. W., and H. O. Mofjeld (1987). "Do Critical Stresses for Incipient Motion and Erosion Really Exist?" Journal of Hydraulic Engineering, Vol. 113, No 3, March, pp. 370-385.

Lee, B. E., and B. F. Soliman (1977). "An Investigation of the Forces on Three Dimensional Bluff Bodies in Rough Wall Turbulent Boundary Layers." Fluids Engineering, Transactions of the ASME, September, pp. 503-510.

Leeder, M. R. (1983). "On the Dynamics of Sediment Suspension by Residual Reynolds Stress-Confirmation of Bagnold's Theory." Sedimentology, Vol.. 30, pp. 485-491.

Ling, C.H. (1995). "Criteria for the Incipient Motion of Spherical Sediment Particles". Journal of Hydraulic Engineering, ASCE, Vol.. 121(6), pp.. 472-478.

Lu, S. S., and W. W. Willmarth (1973). "Measurement of the Structure of the Reynolds Stress in a Turbulent Boundary Layer." Journal of Fluid Mechanics, Vol. 60, Part III, pp. 481-511.

Luchic, T. S., and W. G. Tiederman (1987). "Timescale and Structure of Ejections and Bursts in Turbulent Flows." Journal of Fluid Mechanics, Vol. 174, pp. 529-552.

Magalhaes, L., and T. S. Chau (1983). "Initiation of Motion Conditions for Shale Sediments." Canadian Journal of Civil Engineering, Vol. 10, pp. 549-554.

Mantz, P. A. (1980). "Low Sediment Transport Rates Over Flat Beds." Journal of the Hydraulic Division, ASCE, Vol. 106, No. HY7, July, pp. 1173-1190.

McQuivey, R. S. (1973). "Summary of Turbulence Data from Rivers, Conveyance Channels and Laboratory Flumes." U. S . Geological Survey, Paper 802-B.

McQuivey, R. V., and E. V. Richardson (1969). "Some Turbulence Measurements in Open-Channel Flow." Journal of Hydraulics, ASCE, Vol. 95, HY1, pp. 209-223.

Meyers, J. F. (1985). "The Elusive Third Component." International Symposium on Laser Anemometry, ASME Winter Annual Meeting, Miami Beach, Florida.

Moore, M. C. (1994). "Bedload Transport: The Effects of Particle Shape and an Investigation of a Wide Range of Transport Rates." M. S. Thesis, Virginia Polytechnic Institute and State University, Blacksburg, Virginia.

Naden, P. (1987). "An Erosion Criterion for Gravel-Bed Rivers." Earth Surface Processes Landforms, Vol. 12, pp. 83-93.

Nakagawa, H., and I. Nezu (1978). "Bursting Phenomenon Near the Wall in Open-Channel Flows and its Simple Mathematical Model." Memoirs, Faculty of Engineering, Kyoto University, Vol. 40, pp. 213-240, Japan.

Nakagawa, H., and I. Nezu (1981). "Structure of Space-Time Correlation's of Bursting Phenomenon in an Open Channel Flow." Journal of Fluid Mechanics, Vol. 104, pp. 1-43.

Neill, C. R., and M. S. Yalin (1969). "Qualitative Definition of Beginning of Bed Movement." Journal of the Hydraulics Division, ASCE, Vol. 95, HY1, January, pp. 585-587.

Nelson, J., R. L. Shreve, S. R, McLean, and T. G. Drake (1995). "Role of Near-Bed Turbulence Structure in Bed Load Transport and Bed Form Mechanics." Water Resources Research, Vol. 31, No 8, pp. 2071-2086.

Nezu, I., and H. Nakagawa (1986). "Investigation of Three-Dimensional Turbulent Structure in Uniform Open-Channel and Closed Duct Flows." Proceedings of the Japanese Society of Civil Engineers, Vol. 369, pp. 89-98.

Nezu, I., and H. Nakagawa (1993). Turbulence in Open Channel Flow. IAHR, A. A. Balkema, Rotterdam.

Offen, G. R., and S. J. Kline (1974). "Combined Dye-Streak and Hydrogen Bubble Visual Observation of a Turbulent Boundary Layer." Journal of Fluid Mechanics, Vol. 62, pp. 223-239.

Paintal A. S. (1971). "Concept of Critical Shear Stress in Loose Boundary Open Channels." Journal of the Hydraulics Division, ASCE, Vol. 9, pp. 91-114.

Paintal, A. S. (1971). "A Stochastic Model of Bed Load Transport." Journal of Hydraulic Research, Vol. 9, No. 4, pp. 527-554.

Papanicolaou, A., M. Balakrishnan, P. Diplas, and C. L. Dancey (1995). "Effects of Particle Packing on Bedload Motion." Proceedings of the First International Conference on Water Resources, San Antonio, Texas, August 14-18, pp. 712-716.

Papanicolaou, A., P. Diplas, M. Balakrishnan, , and C. L. Dancey (1996). "A Note on Incipient Motion of Sediment Particles." Proceedings of the

Parker, G., P. C. Klingeman, and D. G. McLean (1982). "Bedload and Size Distribution in Paved Gravel-Bed Streams." Journal of Hydraulic Division, ASCE, Vol.. 108, 544-571.

Perkins and Hunt (1989). "Particle Tracking in Turbulent Flows", Advances in Turbulence 2. Editors: H. Fernholz and H. Fiedler, Springer-Verlag Berlin, Heidelberg 1989, pp.. 286-291.

Reid, I., and L. E. Frostick (1987). "Toward a Better Understanding of Bedload Transport." Recent Developments in Fluvial Sedimentology, Society of Economic Paleontologists and Mineralogists, Special Publication No. 39, pp. 13-19.

Reynolds, A. J. (1974). Turbulent Flows in Engineering. Wiley & Sons, London, Great Britain.

Rifai, M. F., and K. V. H. Smith (1971). "Flow Over Triangular Elements Simulating Dunes." Journal of Hydraulic Division, ASCE, Vol. 97.

Schlichting, H. (1960). Boundary Layer Theory. McGraw Hill Book Company.

Sekine, M., and H. Kikkawa (1988). "A Fundamental Study on the Sediment Transport in an Open Channel Flow." Memoirs of the School of Science and Engineering, Waseda University, No. 52, pp. 103-141.

Sekine, M., and H. Kikkawa (1992). "Mechanics of Saltating Grains II." Journal of Hydraulic Engineering, Vol. 118, No. 4, pp. 536-558.

Shields, A. (1936). "Anwendung der Ähnlichkeitsmechanik und der Turbulenzforschung auf die Geschiebebewegung." *Mitteilungen der Preussischen Versuchsanstalt für Wasserbau und Schiffbau*, No. 26, Berlin, Germany (English Translation by W. P. Ott and J. C. Uchelon, California Institute of Technology, Pasadena, California, USA).

Song, T., W. H. Graf, and U. Lemmin (1994). "Uniform Flow in Open Channels with Movable Gravel Bed." Journal of Hydraulic Research, Vol. 32, No. 6, pp. 861-876.

Steffler, P. M., N. Rajaratnam, and A.W. Peterson (1985). "LDA Measurements in Open Channel." Journal of Hydraulic Engineering, ASCE, Vol. 111, pp. 119-130.

Steidtman, J. R. (1984). "Size-Density Sorting of Sand-Size Spheres During Deposition from Bedload Transport and Implications Concerning Hydraulic Equivalence." Sedimentology, Vol. 29, pp. 877-883.

Sumer, B. M., and R. Deigaard (1981). "Particle Motions Near the Bottom in Turbulent Flow in an Open Channel." Journal of Fluid Mechanics, Vol. 109, pp. 311-338.

Vanoni, V. A. (1964). "Measurements of Critical Shear Stress for Entraining Fine Sediments in a Boundary Layer." Report KH-R-7, W. M. Keck Laboratory of Hydraulic and Water Resources, California Institute of Technology.

Vanoni, V. A., P. C. Benedict, D. C. Bondurant, J. E. McKee, R. F. Piest, and J. Smallshaw (1966). "Sediment Transportation Mechanics: Initiation of Motion, Progress Report, Task Committee on Preparation of the Sedimentation Manual." Journal of the Hydraulics Division, ASCE, Vol. 92, No. Hy2, March, pp. 291-314.

Wang, Sany-yi, and H. W. Shen (1985). "Incipient Sediment Motion and Riprap Design." Journal Hydraulic Engineering, Vol. 111, No. 3, March, pp. 520-538.

Wark, C. E., and H. M. Nagib (1991). "Experimental Investigation of Coherent Structures in Turbulent Boundary Layers." Journal of Fluid Mechanics, Vol. 230, pp. 183-208.

Weiberg, P. L., and J. D. Smith (1987). "Calculations of Critical Shear Stress for Motion of Uniform and Heterogeneous Sediments." Water Resources Research, Vol. 23, pp. 1471-1480.

Wei, T., and W. W. Willmarth (1991). "Examination of V-Velocity Fluctuations in a Turbulent Channel Flow in the Context of Sediment Transport." Journal of Fluid Mechanics, Vol. 223, pp. 241-252.

White, C. M. (1940). The Equilibrium of Grains on the Bed of a Stream." Proceedings of the Royal Society of London, Series A, 174, pp. 322-338.

Williams, J. J., P. D. Thorne, and A. D. Heathershaw (1989). "Measurements of Turbulence in the Benthic Boundary Layer over a Gravel Bed." Sedimentology, Vol. 36, pp. 959-971.

Wilcock, P. R. (1988). "Methods for Estimating the Critical Shear Stress of Individual Fractions in Mixed-Size Sediment." Water Resources Research, Vol. 24, pp. 1127-1135.

Yalin, M. S. (1977). Mechanics of Sediment Transport. 2nd Edition, Pergamon Press, New York, NY.

Appendices

Appendix I

Settings of the Panasonic recorder

During the digitization process the Panasonic board should be in the following configuration:

1. The search dial should not be at the “menu” position because it will no longer be possible to perform any operations except those of the dial menu function.
2. The input switch should be at the “s-video” position when the signals have been input to the S-video in connectors.
3. The meter switch should be at the “norm” position to provide sound of normal type.
4. The audio monitor should be at the “mix” position.
5. The S-VHS switch off must be off.
6. The control switch is set at the “remote” position for operating the unit by remote control.
7. The Y-DNR (Digital Noise Reducer) switch has to be at level 1.
8. The C-DNR (Reduction of the signal noise) is set at the off position.
9. The video AGC at the “on” position in order the video level to be automatically adjusted during the recording process.
10. The image switch at the “edit” position during editing.
11. The mode switch is at the “EE” position.

12. The VITC switch is on.

13. The REC RUN is selected to activate the time code.

Appendices II-III

II. Video capture using Video Vision Studio and Adobe Premiere 4.0

Select source
set matrix switcher to column 2, row 1

Launch adobe premiere 4.0

Video presets:

select radius studio-Full NTSC screen

Hit F10 to deactivate apple talk

Go to **Movie capture**

Record settings

Record at 640x480 or at 320X240

select input **source**
movie capture: video input
change pop - up menu to source
set digitizer = video input
set input = s-video 1
format NTSC
filter = VCR

select input **image**

select **compression options**
movie capture = video input

change pop - up menu to compression
compressor = radius studio
depth = color
quality = most
frames per second = best or you can make a choice
click “ok”

select image **quality options**

movie capture = video input
change pop - up menu to Image
move sliders to adjust video levels to match output on TV to your right

select **audio parameters**

movie capture = sound input
change pop - up menu to Sample
set to 8 - bit, 22KHZ, stereo
play a portion of video tape and set gain so meters peak with 1 red indicator

locate **video clip**

rewind or forward your tape to find the clip that you desire to capture. You want to capture while the video is playing so leave about a two to five second lead on the frame you want.

Record **video**

click **record**

Stop recording by **clicking the mouse.**

On your screen there is a window that includes your clip. Drag
first the clip to the Project window
save clip - project as e.g., thanos.vvs

second drag the clip to the construction window

make movie

click **output options entire project as Pict files.**
Save movie as, e.g, frame1.movie

At the end of the process you will see at the folder or desktop individual pict files.

The capturing process successfully ends here.

III. Conversion of the of the Pict files to different type of format.

Use of the program debabelizer 1.5

file:batch:save
click on edit
select any files currently in list and click remove
click desktop
double click on users_C
double click on user folder
select files and click append or click append all
click save
click replace
click auto naming options
enter the name for the image files and add **.001**
choose this option (use this and add 1 at the end)
click ok
click set
click desktop
double click on capture array
click on user folder
click select “username”
set file format with the **type** pop-up menu to tiff
set color depth to 8 -bit
click “do it”

Appendix IV

List of the experimental data sets

TEST No. E-2

Date: 9/25/96

Packing condition: 2 %

Total no. of balls used in the test section: 530

Slope, S= 0.2 %

Type of balls.: glass beads, with specific gravity=2.54 and diameter D=0.008 m

Depth in m, H =0.05

Water pressure in mm, Δh = 153

Water discharge in m3/s, Q= 0.0122

Average depth velocity in m/s, V = 0.4

Dimensionless stress, τ^*= HS/RD= 0.008 , ($R = \frac{\rho_s}{\rho} - 1 = 1.54$)

Gate configuration (rods): 4 (3/10)" , 1 (1/4)", and 1 sq.

pump frequency: 27.1 Hz (pump 1)

Total no. of balls collected in the basket: 4

Test duration in min: 30

The camera focal length during the test is 2 m/7 ft.

The camera area of view has length 31 cm and width 41 cm. The test area is 300 cm long and 40 cm wide.

129 lead balls are placed per side.

TEST No. E-20

Packing condition: 20%

Total number of balls used in the test section: 5,300

Slope, S = 0.2%

Type of balls: glass beads, with specific gravity = 2.54 and diameter d = 0.008 m

Depth in m, H = 0.068

Water pressure in mm, Δh = 510 (water - air manometer) or 41 (water - mercury manometer)

Water discharge in m^3/s, Q = 0.02185

Average depth velocity in m/s, V = 0.527

Dimension - less bed shear stress, τ^* = HS/RD = 0.01087

Gate configuration (rods): 1(1/4)", 3(3/16)", and 2 sq.

Total number of balls collected in the basket: 6

Test duration in min: 30

Use of the Laser Doppler Velocimeter: No

Use of the Video Camera: Yes

Observations:

The adjustable frequency pump (i.e. pump 1) was used during the tests. Sediment motion was observed at pump frequency of 26 Hz. The speed of pump 1 was increased gradually to avoid clustering of the particles.

TEST No. E-35

Packing condition: 35 %

Total number of balls used in the test section: 9275

Slope, S = 0.8%

Type of balls: glass beads, with specific gravity 2.54 and diameter d = 0.008 m

Depth in m, H =0.057

Water pressure in mm, Δh = 51 (water-mercury manometer)

Water discharge in m^3/s, Q = 0.02462

Average depth velocity in m/s, V = 0.708

Dimension - less bed shear stress, $\tau^* = HS/RD$ =0.037

Gate configuration (rods): 1(1/4)", 4(3/16)", and 1sq.

Pump Frequency: 47 Hz (pump 1)

Total number of balls collected in the basket: 52

Test duration in min: 20

Use of the Laser Doppler Velocimeter: No

Use of the Video Camera: Yes

Observations:

Due to the initial surge from the pump five balls were collected in the basket. These balls were not considered as part of the bed load material that was collected during the test period.

For the 35 % packing condition we increased gradually the pump frequency until we reached the frequency of 30 Hz. From that frequency to 47 Hz.

TEST No. E-50

Packing condition: 50% packing

Total number of balls used in the test section: 13250

Slope, S = 1%

Type of balls: glass beads, with specific gravity 2.54 and diameter d= 0.008 m

Depth in m, H = 0.057

Water pressure in mm, Δh = 590

Water discharge in m^3/s, Q = 0.0264

Average depth velocity in m/s, V = 0.76

Dimension - less bed shear stress, τ^* = HS/RD = 0.048

Gate configuration: 3 (1/4) + 1(3/16) + 1 sq.

Pump configuration: 50.1 Hz

Total number of balls collected in the basket: 120

Test duration in min: 20

Use of the Laser Doppler Velocimeter: No

Use of the Video Camera: Yes

Observations:

Very similar to the conditions observed at the 35 % packing condition.

TEST No. E-70

Packing condition: 70% packing

Total number of balls used in the test section: 18558

Slope, S = 1.2%

Type of balls: glass beads with specific gravity = 2.54 and diameter d = 0.008m

Depth in m, H = 0.076

Water pressure in mm, Δh = 410

Water discharge in m^3/s, Q = 0.054

Average depth velocity in m/s, V = 1.19

Dimension - less bed shear stress, τ^* = HS/RD = 0.072

Gate configuration: 1 (1/4)", 4(3/16)", and 2 sq.

Total number of balls collected in the basket: 50

Test duration in min: 1

Use of the Laser Doppler Velocimeter: No

Use of the Video Camera: Yes

Observations:

The test was repeated at least 15 times to check the validity of the data. The duration of the test was small since gravel particles were getting entrained from the upstream section of the flume.

VITA

Athanasios N. Papanicolaou was born in Northern Greece. He completed his undergraduate studies in 1989 at the Aristotle's University of Thessaloniki (AUT), Greece. In 1992 he received his Master's of Science degree in Civil Engineering and joined the Ph.D. program of Virginia Tech (V.P.I&SU). A. Papanicolaou has received several awards during the course of his studies. He is interested to continue his research in an academic institution.